



**A 2-D NUMERICAL SIMULATION AND  
ANALYSIS OF A SIMPLE BAND MODEL FOR  
THE PRIZ SPATIAL LIGHT MODULATOR**

DISSERTATION

Gary D. Barmore, Major, USAF

AFIT/DS/ENP/96-05

**DISTRIBUTION STATEMENT A**

Approved for public release;  
Distribution Unlimited

DEPARTMENT OF THE AIR FORCE  
AIR UNIVERSITY  
**AIR FORCE INSTITUTE OF TECHNOLOGY**

Wright-Patterson Air Force Base, Ohio

DTIC QUALITY INSPECTED 1

AFIT/DS/ENP/96-05

**A 2-D NUMERICAL SIMULATION AND  
ANALYSIS OF A SIMPLE BAND MODEL FOR  
THE PRIZ SPATIAL LIGHT MODULATOR**

DISSERTATION

Gary D. Barmore, Major, USAF

AFIT/DS/ENP/96-05

19970210 028

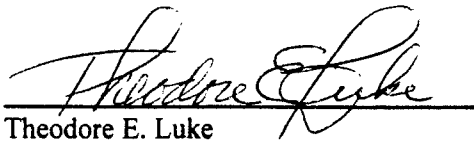
Approved for public release; distribution unlimited

The views expressed in this dissertation are those of the author and do not reflect the official policy or position of the Department of Defense or the U.S. Government.

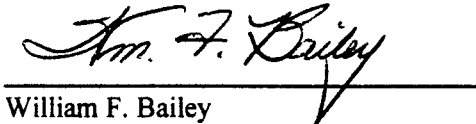
A 2-D NUMERICAL SIMULATION AND ANALYSIS  
OF A SIMPLE BAND MODEL FOR THE  
PRIZ SPATIAL LIGHT MODULATOR

Gary D. Barmore, B.S., M.S.E.E.  
Major, USAF

Approved:

  
Theodore E. Luke

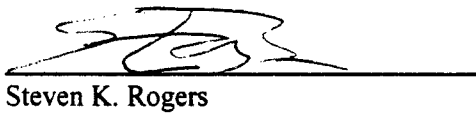
20 Nov 96

  
William F. Bailey

20 Nov 96

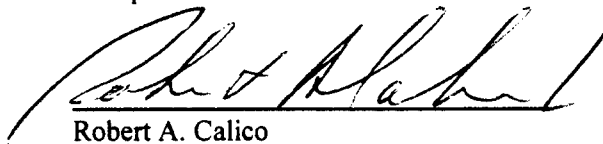
  
David L. Coulliette

20 Nov 96

  
Steven K. Rogers

20 Nov 96

Accepted:

  
Robert A. Calico

Dean, School of Engineering

**A 2-D NUMERICAL SIMULATION AND ANALYSIS  
OF A SIMPLE BAND MODEL FOR THE  
PRIZ SPATIAL LIGHT MODULATOR**

DISSERTATION

Presented to the Faculty of the School of Engineering  
of the Air Force Institute of Technology  
Air University in Partial Fulfillment of the  
Requirements for the Degree of  
Doctor of Philosophy

Gary D. Barmore, B.S., M.S.E.E.

Major, USAF

November 1996

Approved for public release; distribution unlimited

### *Acknowledgments*

I am indebted to my research advisors, Dr. Theodore Luke, Dr. William Bailey, and LtCol David Coulliette. Their advice was invaluable in completing my effort, and I deeply appreciated their quick review of the corrected dissertation after my defense. My supervisor, Dr. Donald Hanson, deserves special thanks for giving me the time and encouragement to complete the dissertation during my current assignment. Finally, I would like to thank my wife, Susan, for her patience and understanding during this extremely long project.

Gary D. Barmore

## *Table of Contents*

	Page
Acknowledgments .....	iii
List of Figures .....	vii
List of Tables .....	xiv
List of Symbols .....	xv
Greek .....	xv
General .....	xvi
Abstract .....	xviii
I. Introduction .....	1
II. Mathematical Model .....	6
Overview – A Verbal Description .....	6
The Input .....	13
Charge Distributions and the Rate Equations .....	13
Poisson's Equation .....	15
Electro-optics .....	17
Diffraction .....	20
Dominance .....	23
Interpretation of Dominance .....	25
Typical Scales .....	27
III. Code Development .....	30
Overview and the Mathematical Model .....	30
Grid, Boundary Conditions, and the External Circuit .....	33
Rate Equations via 4th-Order Runge-Kutta .....	35
Electric Fields via the Full Multi-Grid .....	37
Pockels Effect and the Jones Matrices .....	38
Diffraction of the Read-Beam via the Fast Fourier Transform .....	39
Validation of the Numerical Simulation .....	40
IV. The Literature .....	44
Experiment .....	44
Theory .....	48
Numerical Modeling .....	54
Other Models .....	55
V. Investigation of Device Physics .....	58
Standard Operating Point .....	60

Essential Physical Mechanisms .....	63
Range of Typical Output .....	68
Internal Dynamics .....	68
Typical Output in Terms of the Internal Dynamics. ....	72
Dominance Factors .....	81
Sensitivity to Parameters during Continuous Illumination (CW) .....	83
Sensitivity to Recombination and Detrapping Mechanisms in Pulsed Operation .....	88
Summary of the Device Physics .....	94
Continuous Illumination .....	95
Pulsed Illumination .....	96
VI. Model Evaluation .....	99
Approach .....	100
Diffraction Efficiency as a Function of Modulation Index .....	100
First and Second Order Diffraction Efficiency .....	103
Early and Late Write-Beam Turnoff .....	106
Summary of the Model Evaluation .....	114
VII. Conclusions .....	116
Modeling .....	116
Model Evaluation .....	117
New Predicted Behavior .....	118
Code Enhancements .....	120
Photorefractive Material Evaluation .....	121
Summary .....	122
Appendix A. 2-D Numerical Simulation Parameter Sets .....	124
Appendix B. Qualitative Analysis using Dominance .....	126
Charge and Field Distributions .....	126
Dominance .....	127
Factors in Grating Dynamics .....	129
Longitudinal Slope of the Donor Grating (Absorption) .....	130
Longitudinal Separation in Donor and Trap Gratings (Longitudinal Drift) .....	131
Growth Rate of the Trap Grating (Effective Trapping Rate) .....	132
Transverse Variation in the Donor Grating (Write-beam Modulation) .....	133
Transverse Distortion in the Free Electron Grating (Transverse Drift) .....	134
Appendix C. Jones Matrix Derivation of Output Phase Shift .....	136
Appendix D. Sensitivity Analysis .....	139
Appendix E. Abridged User's Guide .....	154
Introductory Comments .....	154



Installation .....	156
Running the Programs .....	157
Output .....	162
Pitfalls and Difficulties .....	167
Appendix F. Simulation Error .....	169
Appendix G. Asymmetry in Output .....	173
Appendix H. Approximation to Diffraction Efficiency .....	178
Bibliography .....	182
Vita .....	186

## *List of Figures*

Figure	Page
1. Possible PRIZ configuration. BS is a beam splitter. $L_1$ and $L_2$ are crossed polarizers. F is a filter that absorbs the remaining write-beam at wavelength $\lambda_w$ . . . . .	7
2. Simple band model . . . . .	7
3. Physics associated with the write-beam. . . . .	9
4. PRIZ Orientation. If the input is a sinusoidal grating in $x$ , then the operator aligns the input linear polarizer parallel to $y$ . (3:649) . . . . .	11
5. Physics associated with the read-beam . . . . .	11
6. Device representation for Jones matrix calculations. A linear polarizer specifies the input vector, $E_{in}$ . . . . .	19
7. Typical transverse field distribution without significant distortion from drift. The ordinate ( $x = 1$ , $z = 1$ ) is the intersection at the rear, bottom of the plot. The cathode is at $z = 1$ (the left side near the high peaks), and the anode is at $z = 65$ . This is output from the code and shows normalized (unitless) field values. . . . .	26
8. Algorithms associated with PRIZ physics . . . . .	31
9. Code timing . . . . .	32
10. Grid . . . . .	34
11. Boundary conditions . . . . .	35
12. Dependence of the diffraction efficiency on the frequency of the temporal modulation of the light intensity ( $f_z$ ) for two spatial frequencies ( $f_{x1}$ and $f_{x2}$ ). (12:165) . . . . .	45
13. Petrov single pulse experiment. (12:165) . . . . .	46
14. Time dependence of the diffraction efficiency for modulation factors $m=1$ (1), 0.45 (2), and 0.27 (3), $U=1.8$ kV, $v=2.5$ mm <sup>-1</sup> , $\eta_{max}=0.5\%$ . (3:70) . . . . .	52
15. Time dependence of the first- and second-order diffracted light $I_1$ , $I_2$ for $v=0.5$ mm <sup>-1</sup> , $I=500$ $\mu$ W/cm <sup>2</sup> , $\lambda=488$ nm. (3:71) . . . . .	52
16. Energy band diagram for BSO at 300 K. (47:2657; 13:3684; 43:5170) . . . . .	56

17. Energy-gap structure showing hopping transport via tunneling between localized states near the Fermi level (events A and B), and transport by multiple trapping via shallow traps (event D). (11:53) ..... 57
18. First order diffraction efficiency versus time for the standard operating point. The normalizing diffraction efficiency is  $\eta_0 = 1.5625 \cdot 10^{-4}$ . Peak dominance is  $\delta = +2.2/(100 \cdot 65) = 3.4 \cdot 10^{-4}$ . The grid is 65x65. (b32) ..... 62
19. Sensitivity of the simulation to physical mechanisms. (a) Bliznetsov mathematical prediction (4:753), (b) 2-D numerical simulation with only Bliznetsov's mechanisms, (c) 2-D simulation adding all currents, and (d) 2-D simulation adding exponential absorption. Mechanisms are added to the 2-D simulation by adding appropriate expressions to the rate equations. (b64) ..... 66
20. Evolution of the net charge density for the standard operating point. The distributions are at (a) 2 ms and (b) 9 ms. The initial electron transit time is 1 ms. The charge densities ranges in (a) from -0.8 to +5.9 and in (b) from -6.2 to +70.0 in normalized units ( $n_0$ ). (b32) ..... 69
21. Evolution of the longitudinal electric field distribution for the standard operating point. The distributions are at (a) 2 ms and (b) 9 ms. The initial electron transit time is 1 ms. The longitudinal field ranges in (a) from -2.5 to -0.74 and in (b) from -4.4 to -0.24 in units of the initial longitudinal field ( $E_0 = V/d$ ). (b32) ..... 70
22. Evolution of the transverse electric field distribution for the standard operating point. The distributions are at (a) 2 ms and (b) 9 ms. The initial electron transit time is 1 ms. The transverse field ranges in (a) from -0.25 to +0.25 and in (b) from -0.55 to +0.55 in units of the initial longitudinal field ( $E_0 = V/d$ ). The transverse fields are zero at both electrodes. (b32) ..... 71
23.  $\eta_1$  vs t for large p-dominance during continuous illumination. (b32) ..... 74
24.  $\eta_1$  vs t for small p- to n-dominant shift during continuous illumination. The square, ■, indicates the time of the change from positive to negative dominance. (b45) ..... 75
25.  $\eta_1$  vs t for large n-dominance during continuous illumination. (b36) ..... 76
26.  $\eta_1$  vs t for small n- to p-dominant shift during continuous illumination. The square, ■, indicates the time of the change from negative to positive dominance. (b28) ..... 77
27.  $\eta_1$  vs t for p-dominance during pulsed operation, late turnoff. The circle, ●, indicates the turnoff time. No phase reversal occurs. (b48) ..... 77
28.  $\eta_1$  vs t for p-dominance during pulsed operation, early turnoff. The circle, ●, indicates the turnoff time; the square, ■, indicates the time of change from positive to negative dominance. (b48) ..... 79
29.  $\eta_1$  vs t for n-dominance during pulsed operation, late turnoff. The circle, ●, indicates the

turnoff time. (b51) .....	80
30. $\eta_1$ vs t for n-dominance during pulsed operation, early turnoff. The circle, ●, indicates the turnoff time. (b51) .....	80
31. Range of dominance at peak output for changes in variables from the standard operating point (see Appendix D for detailed data). The triangles identify the parameter values for the standard operating point, which produces a dominance of $2.2 \cdot (0.01/N) = 3.38 \cdot 10^{-4}$ . Variable limits are annotated on the respective bar. ....	85
32. Range of dominance for a change in intensity at the standard operating point ( $\alpha = 1000 \text{ m}^{-1}$ ) and a point where $\alpha = 3500 \text{ m}^{-1}$ . ....	86
33. Change in peak diffraction efficiency (in $\eta_0$ ) when the parameter values are doubled at the standard operating point. ....	87
34. Change in the timing of the peak diffraction efficiency (in ms) when the parameter values are doubled at the standard operating point. ....	88
35. Pulsed operation for a donor recombination study when the write-beam is turned off at a) $\infty$ , b) 1, c) 2, d) 5, e) 8, f) 32, and g) 72 ms. Circles, ●, indicate the turnoff time. (b73) .....	90
36. Self-erasure (%) relative to peak diffraction efficiency for single (parameter) changes to a baseline. Patterns indicate changes to a p- (standard operating point) or n-dominant (standard operating point with $\xi_t = 5 \cdot 10^{17} \text{ s/m}^3$ ) baseline. ....	91
37. Reintensification (%) of diffraction efficiency relative to peak output after write-beam turn-off for single (parameter) changes to a baseline. Patterns indicate changes to a p- (standard operating point) or n-dominant (standard operating point with $\xi_t = 5 \cdot 10^{17} \text{ s/m}^3$ ) baseline. ....	93
38. Diffraction efficiency as a function of modulation index. m is (1) 1.0, (2) 0.45, and (3) 0.27 (3:70). ....	101
39. Reproduction of Shlyagin index of modulation experiment (3:70). $\eta_{\text{norm}}$ is the diffraction efficiency for the $m = 0.95$ curve at 100 ms. (b61) .....	102
40. Time dependence of first and second order diffracted light $I_1, I_2$ for $v = 0.5 \text{ mm}^{-1}$ , $I = 500 \text{ } \mu\text{W/cm}^2$ , $\lambda = 488 \text{ nm}$ (3:71). ....	103
41. Simulation of Shlyagin et al.'s plot of first and second order diffraction efficiency (3:71). (b45a) .....	105
42. Oscilloscope traces of the diffraction efficiency for various values of the exposure to the writing light, $W = I_0 t_0$ . $I_0 = 30 \text{ } \mu\text{W/cm}^2$ , $v = 2 \text{ mm}^{-1}$ , the writing is started at time $t = 0$ . a) $t_0 = 1.5 \text{ s}$ , b) 0.125, c) 0.2 s, d) 0.3 s. Peak occurs in (a) between 0.2 and 0.3 s. (4:751) .....	107

43.	Pulsed operation for a large p-dominance with continuous illumination peak at 7 ms. The write-beam is turned off at a) 5 and b) 72 ms. Turnoff times are indicated by circles. (b32) .....	108
44.	The write-beam is turned off at 3 ms for cases of a) $\tau_t = 25$ ms, $n_s = 3.3 \cdot 10^{17}$ , and b) $\tau_t = 10$ ms, $n_s = 3.3 \cdot 10^{17}$ . The small circles indicate turnoff times. (b72 and b71, respectively) .....	110
45.	Strong self-erasure and reintensification. The small circle indicates the turnoff time. (b79) .....	113
46.	Good late turn-off behavior is shown in (a) using the b79 parameter set. Good early turn-off is shown in (b)-(d) using the b83 parameter set. The small circles indicate turnoff times at a) 72, b) 3, c) 7, and d) 11 ms. The output peaks in (a) at 5 ms and in (b)-(d) at 9 ms. ....	114
47.	(a) Sample net charge density, $(x,z,t)$ , and (b) transverse field grating, $E_x(x,z,t)$ at a time $t$ before significant distortions develop. ....	127
48.	Longitudinal cross sections of the charge gratings at a peak in the input write-beam. (a) Net charge density, $\rho(z,t)$ , (b) positive donor grating, $N_d^+(z,t)$ , (c) negative trap grating, $N_t^-(z,t)$ , (d) free electron grating, $n_e(z,t)$ , and (e) longitudinal electric field, $E_z(z,t)$ . $t < \tau$ . ....	128
49.	Longitudinal slope of positive donor grating for (a) low and (b) high absorption. $I \cdot \alpha = \text{constant}$ . ....	131
50.	Spatial separation of donor and trap gratings for (a) short and (b) long trapping time. ....	132
51.	Effective trapping rate for (a) high and (b) low trapping rate. ....	133
52.	Transverse variation in the amplitude of the donor grating for (a) low and (b) high peak input intensity. ....	134
53.	Transverse distortion in the free electron grating in (a) the negative space charge region and (b) the positive space charge region. ....	135
54.	Device representation for Jones matrix calculations neglecting optical activity .....	136
55.	Diffraction efficiency and timing sensitivity to absorption coefficient, $\alpha$ ( $\text{m}^{-1}$ ). (b26) .....	140
56.	Dominance sensitivity to absorption coefficient, $\alpha$ ( $\text{m}^{-1}$ ). (b26) .....	140
57.	Diffraction efficiency and timing sensitivity to electron lifetime, $\tau$ (ms), at $\alpha = 1000 \text{ m}^{-1}$ . (b28) .....	141

58.	Dominance sensitivity to electron lifetime, $\tau$ (ms), at $\alpha = 1000 \text{ m}^{-1}$ . (b28) .....	141
59.	Diffraction efficiency and timing sensitivity to electron lifetime, $\tau$ (ms), at $\alpha = 3500 \text{ m}^{-1}$ . (b45) .....	142
60.	Dominance sensitivity to electron lifetime, $\tau$ (ms), at $\alpha = 3500 \text{ m}^{-1}$ . (b45) .....	142
61.	Diffraction efficiency and timing sensitivity to intensity, $I_0$ ( $\text{W}/\text{m}^2$ ), at $\alpha = 1000 \text{ m}^{-1}$ . (b29) .....	143
62.	Dominance sensitivity to intensity, $I_0$ ( $\text{W}/\text{m}^2$ ), at $\alpha = 1000 \text{ m}^{-1}$ . (b29) .....	143
63.	Diffraction efficiency and timing sensitivity to intensity, $I_0$ ( $\text{W}/\text{m}^2$ ), at $\alpha = 3500 \text{ m}^{-1}$ . (b43) .....	144
64.	Dominance sensitivity to intensity, $I_0$ ( $\text{W}/\text{m}^2$ ), at $\alpha = 3500 \text{ m}^{-1}$ . (b43) .....	144
65.	Diffraction efficiency and timing sensitivity to mobility, $\mu$ ( $\text{m}^2/\text{V}/\text{s}$ ). (b30) .....	145
66.	Dominance sensitivity to mobility, $\mu$ ( $\text{m}^2/\text{V}/\text{s}$ ). (b30) .....	145
67.	Diffraction efficiency and timing sensitivity to trap lifetime, $\tau_t$ (ms), at $\alpha = 1000 \text{ m}^{-1}$ . (b31) .....	146
68.	Dominance sensitivity to trap lifetime, $\tau_t$ (ms), at $\alpha = 1000 \text{ m}^{-1}$ . (b31) .....	146
69.	Diffraction efficiency and timing sensitivity to trap lifetime, $\tau_t$ (ms), at $\alpha = 3500 \text{ m}^{-1}$ . (b52) .....	147
70.	Dominance sensitivity to trap lifetime, $\tau_t$ (ms), at $\alpha = 3500 \text{ m}^{-1}$ . (b52) .....	147
71.	Diffraction efficiency and timing sensitivity to voltage, $V$ (volts). (b42) .....	148
72.	Dominance sensitivity to voltage, $V$ (volts). (b42) .....	148
73.	Diffraction efficiency and timing sensitivity to modulation index, $m$ . (b37) .....	149
74.	Dominance sensitivity to modulation index, $m$ . (b37) .....	149
75.	Diffraction efficiency and timing sensitivity to trap-to-donor recombination coefficient, $\xi_{td}$ ( $\text{s}/\text{m}^3$ ). (b59) .....	150
76.	Dominance sensitivity to trap-to-donor recombination coefficient, $\xi_{td}$ ( $\text{s}/\text{m}^3$ ). (b59) .....	150
77.	Diffraction efficiency and timing sensitivity to donor recombination coefficient, $\xi_d$ ( $\text{s}/\text{m}^3$ ). (b60) .....	151

78.	Dominance sensitivity to donor recombination coefficient, $\xi_d$ (s/m <sup>3</sup> ). (b60) .....	151
79.	Diffraction efficiency and timing sensitivity to injection coefficient, $n_s$ (m <sup>-3</sup> ). (b66) .....	152
80.	Dominance sensitivity to injection coefficient, $n_s$ (m <sup>-3</sup> ). (b66) .....	152
81.	Diffraction efficiency and timing sensitivity to spatial modulation frequency, $\nu$ (lines/mm). (b47) .....	153
82.	Grid to demonstrate data arrangement. ....	156
83.	Creating a new parameter file .....	159
84.	Opening an existing parameter file .....	159
85.	Editing model parameters and program flags .....	160
86.	Menu to run the program and view the output .....	161
87.	Net charge density vs position .....	163
88.	Transverse electric fields vs position .....	164
89.	Longitudinal electric fields vs position .....	164
90.	Slow index of refraction vs position .....	165
91.	Dominance vs time .....	165
92.	Amplitude of output electric field vs x .....	166
93.	First order diffraction efficiency vs time .....	166
94.	Simulation error as a function of grid size and frequency of electric field calculation for large p-dominance. Grid size and update frequency are (a) 65 <sup>2</sup> and normal, (b) 129 <sup>2</sup> and normal, (c) 257 <sup>2</sup> and normal, (d) 65 <sup>2</sup> and always, and (e) 129 <sup>2</sup> and always. (b55) ...	170
95.	Simulation error as a function of grid size and frequency of electric field calculation for small n-dominance. Grid size and update frequency are (a) 65 <sup>2</sup> and normal, (b) 65 <sup>2</sup> and always, and (c) 129 <sup>2</sup> and normal. (b28) .....	171
96.	Simulation error as a function of grid size and frequency of electric field calculation for pulsed operation. Grid size and update frequency are (a) 65 <sup>2</sup> and normal, (b) 65 <sup>2</sup> and always, and (c) 129 <sup>2</sup> and normal. (b32) .....	172
97.	Transverse distributions in a brief simulation showing worst case error in potential. Plots (a) through (c) are taken at the sixth of thirty-three longitudinal points. The distributions	

	are (a) the net charge density input to the FMG, (b) the potential output from the FMG, (c) the transverse fields calculated from the potential, and (d) the output field distribution proportional to the longitudinal integral of the transverse fields. ....	174
98.	Output electric field versus transverse location showing typical amount of asymmetry. This corresponds to 33 transverse points and an input of 2 sine periods. ....	175
99.	Output electric field (modified) versus transverse location. The asymmetry has been effectively removed. ....	176
100.	FFT of unmodified output electric field. First order output corresponds to $k=2$ . ....	176
101.	FFT of modified output electric field. First order output corresponds to $k=2$ . ....	177



### *List of Tables*

Table	Page
1. Normalization constants (15:759) .....	36
2. Illumination and dominance combinations for typical output .....	73
3. Parameter sets b26 to b54 .....	124
4. Parameter sets b55 to b89 .....	125
5. Simulation error for continuous illumination and large dominance.(b55) .....	169

## *List of Symbols*

### **Greek**

$\alpha$	Absorption coefficient (1/m).
$\delta$	Dominance identifies whether the positive space charge region ( $\delta > 0$ ) or negative space charge region ( $\delta < 0$ ) dominates the phase shift between the fast and slow electro-optic axes in the PRIZ.
$\Delta\varphi$	Phase difference between the fast ( $\varphi_f$ ) and slow ( $\varphi_s$ ) phase shifts in the electric field.
$\epsilon$	Permittivity (F/m).
$\varphi_f$	Phase shift induced in the fast component of the read-beam's electric field during longitudinal transmission through the crystal.
$\varphi_s$	Phase shift induced in the slow component of the read-beam's electric field during longitudinal transmission through the crystal.
$\eta$	Two definitions used according to context. Diffraction efficiency is the most common use. If subscripted it designates the diffraction efficiency of the respective order. Less often it is used as the quantum efficiency or conversion efficiency of photons absorbed to generate ionized donors.
$\eta_n$	Nth order diffraction efficiency.
$\eta_0$	Constant diffraction efficiency equal to $1.5625 \cdot 10^{-4}$ .
$\lambda_r$	Read-beam wavelength (m).
$\lambda_w$	Write-beam wavelength (m).
$\mu$	Electron mobility ( $\text{m}^2/\text{V/s}$ ).
$\nu_w$	Write-beam frequency (Hz).
$\nu_x$	Spatial modulation frequency of the write-beam (lines/mm).
$\rho$	Net charge density ( $\text{C/m}^3$ ).
$\xi_d$	Donor recombination coefficient ( $\text{s/m}^3$ ).
$\xi_t$	Trap recombination coefficient ( $\text{s/m}^3$ ).

$\xi_{td}$	Trap-to-donor recombination coefficient ( $\text{s/m}^3$ ).
$\tau$	Trapping time (sec).
$\tau_d$	Donor recombination time constant (sec).
$\tau_t$	Detrapping time or trap lifetime (sec).
$\omega$	Temporal frequency of the electric field (Hz).

### General

BSO	Bismuth silicate or $\text{Bi}_{12}\text{SiO}_{20}$ .
CW	A mode of operation of the PRIZ where the write beam illumination is left on continuously.
d	Longitudinal extent of the PRIZ crystal (m).
D	Diffusion coefficient ( $\text{m}^2/\text{s}$ ).
e	Electron charge (C).
$E_{\text{out}}$	Output electric field after the output polarizer (V/m).
$E_x$	Transverse electric field (V/m).
$E_z$	Longitudinal electric field (V/m).
$\mathcal{F}_x$	Spatial Fourier transform in the transverse direction.
g	Generation coefficient for photon absorption, equal to $(I_0 \alpha \eta) / (h\nu_w)$ in ( $\text{photons/m}^3/\text{s}$ ).
h	Planck's constant, $6.63 \times 10^{-34}$ J/sec.
I	Write-beam intensity or output intensity in the far field, depending on context ( $\text{W/m}^2$ ).
$I_n$	Nth order output intensity in the far field ( $\text{W/m}^2$ ).
$I_0$	Peak write-beam intensity ( $\text{W/m}^2$ ).
$I_{\text{out}}$	Output intensity after the output polarizer ( $\text{W/m}^2$ ).
$I_r$	Read-beam intensity ( $\text{W/m}^2$ ).
J	Current density ( $\text{A/m}^2$ ).

$k$	Magnitude of the wave vector of the intensity grating ( $\text{m}^{-1}$ ).
$m$	Spatial modulation index of the input write-beam.
$n_e$	Free electron density ( $1/\text{m}^3$ ).
$n_o$	Index of refraction in the absence of an electric field.
$n_f$	Index of refraction seen by the fast component of the electric field.
$n_s$	Injection coefficient, used to determine the electron flux across the cathode ( $1/\text{m}^3$ ) or the index of refraction seen by the slow component of the electric field.
$N$	Number of grid points in one (either) direction.
$N^-$	Net negative charge density ( $1/\text{m}^3$ )
$N_d$	Donor density ( $1/\text{m}^3$ ).
$N_d^+$	Ionized donor density( $1/\text{m}^3$ ).
$N_t$	Trap density ( $1/\text{m}^3$ ).
$N_t^-$	Ionized (filled) trap density ( $1/\text{m}^3$ ).
$q$	Charge of the electron (C).
$r_{41}$	Electro-optic coefficient.
$t$	Time (sec).
$U$	Potential (V).
$V$	Applied, external voltage (V).
$x$	Transverse coordinate (m).
$y$	Transverse coordinate perpendicular to the x-axis (not simulated).
$z$	Longitudinal coordinate (m).

## *Abstract*

This dissertation discusses the development of and analyzes the first complete, 2-D numerical simulation of the PRIZ. The simulation is based upon a simple band model of the PRIZ: a single donor, a single trap, and free electron carriers. Modeled mechanisms include photogeneration, energy level transitions, injection, drift currents, diffusion currents, photorefraction and diffraction. The model goes beyond the previous charge and field dynamics of 1-D numerical models to include optical effects, and it eliminates the oversimplifications and assumptions used in earlier mathematical models with closed solutions. Sensitivity analyses and selected simulations provide a better understanding of the dynamic imaging phenomena.

The device output depends on the relative dominance or strength of the fields in the positive or negative space charge region. Transverse drift is as important as charge mirror imaging and injection current in determining peak output and self-erasure.

The simulations show a broad range of unreported behavior both before and after write-beam turnoff, including sharp transients; reintensification with and without phase reversals; and even strong intensification after a turnoff. Finally, the 2-D model is shown to be a reasonable representation of the PRIZ by comparing simulated output with experimental data from the literature.

# **A 2-D NUMERICAL SIMULATION AND ANALYSIS OF THE PRIZ SPATIAL LIGHT MODULATOR USING A SIMPLE BAND MODEL**

## ***I. Introduction***

The PRIZ spatial light modulator is basically a cubic, photorefractive, wide-bandgap semiconductor sandwiched between two electrodes. Understanding the physics of the PRIZ spatial light modulator will enhance understanding of related devices and could open the way for development of optical applications.<sup>1</sup> Research in the 1980s concentrated on experiment and mathematical modeling associated with the dynamic, versus storage, aspects of PRIZ image processing (1; 2; 3; 4).<sup>2</sup> The most sophisticated numerical model developed was a 1-D solution that provided information only on charge distributions and electric fields; it could not model the photorefractive effects (5; 6). The literature reports a 2-D mathematical model that did include the photorefractive process, but numerous assumptions and approximations were used to simplify the

---

<sup>1</sup> The PRIZ can include or omit insulators between the electrodes and the semiconductor. The literature sometimes labels the configurations as either a conducting or an insulated PRIZ. This dissertation investigates only the conducting PRIZ.

<sup>2</sup> The PRIZ is basically a photorefractive crystal, usually  $\langle 110 \rangle$  or  $\langle 111 \rangle$  BSO, with an external voltage source. Absorbed photons from a write-beam generate free electrons. Those electrons drift under the local electric fields. Drift, diffusion, injection, and trapping cause charge redistribution that in turn modify the local electrical fields and, through the electro-optic effect, the indices of refraction. The varying indices of refraction in turn modulate a read-beam to produce an output image.

mathematics (3; 4). By 1990, the research on the PRIZ and its most commonly used photorefractive material, BSO, had shifted to new materials and new applications.

Advances in computer technology enable a 2-D numerical model which can relax and examine the validity of previous assumptions and simplifications and still run in reasonable times. This dissertation describes the numerical modeling and investigation of the PRIZ using a simple band model – a single trap level, a single donor level, and one free carrier type, electrons.

The dissertation has two goals: understanding the device's physics and evaluating the usefulness of the 2-D model. The first goal is to enhance understanding of the physics associated with the PRIZ's optical processing. Some devices can store images for long periods. Others enhance the moving portions of an image while suppressing static background (4:751). Like previous investigations, the work here concentrates on understanding the dynamic imaging aspects of the device, a mode of operation where the static parts of an input image are suppressed in the output while moving parts are enhanced.

The second goal is to evaluate the usefulness of the simple band model in creating a realistic numerical simulation of the PRIZ. The evaluation is done without any new experiments; the dissertation compares the simulation results with the sketchy data from the few experiments reported in the literature. The PRIZ numerical model supplements the simple band model of the material with various mechanisms: photogeneration of electrons; drift and diffusion of those free electrons; electron injection across the electrodes; trapping; detrapping; donor recombination; and direct trap to donor recombination. The standard Pockels effect equations represent photorefraction.<sup>3</sup>

Since understanding the dynamics of the PRIZ is the heart of the investigation, a few words on dynamic imaging are appropriate. An image is processed in the PRIZ when a write-

---

<sup>3</sup> The literature includes more complicated models (7; 8; 9; 10; 11).

beam generates, and internal dynamics evolve, a complex set of index gratings. That set of gratings then diffracts a (planar) read-beam to produce the observed/processed image. Interestingly, the PRIZ can suppress a static background while enhancing a moving object (1:3091-3092; 2:3850-3853). Reported times for achieving suppression of static background, sometimes called self-erasure, are long, lasting seconds (3:71; 4:751). For such long time constants, applications such as moving target indicators are impractical. Before this work, the mechanisms for suppressing static backgrounds and enhancing moving objects were not well understood. Researchers published a significant amount of work in the 1980s on such dynamics, often called dynamic imaging; but the basic physics remained obscured by the complexity of the mathematical models and the over simplifications required for obtaining mathematical solutions (3; 4; 12). This work clarifies the physics behind dynamic imaging.

To accomplish the above goals and clarify the physics, this work takes a straightforward approach. First, the simple band model was selected and then coded. The code uses (defaults to) a perfect sinusoidal intensity distribution for the write-beam that keeps distortion analysis simple and corresponds to the most common experiments. The code solves for charge densities via a 4th-order variable step size Runge-Kutta (RK) algorithm. Fields are evaluated via a Full Multi-Grid (FMG) Poisson solver from the two dimensional charge distributions. Drift, diffusion, and injection currents modify carrier motion. The influence of the spatial modulation of the indices of refraction was evaluated via Jones matrices to produce the output field distribution. Finally, a Fast Fourier Transform (FFT) diffracts the output to the far field.

After testing code components and validating the whole program against a known 1-D solution, the numerical model's sensitivity to selected parameters was analyzed using continuous illumination. That analysis provided enough data to understand background suppression. Contrast enhancement was studied by relating phenomena after write-beam turnoff to phenomena seen near



trailing edges in a dynamic image. The combination of sensitivity simulations and turnoff (or pulsed) simulations provided enough data to understand the device physics.

Using the sensitivity and write-beam turnoff simulations as a foundation, the research then investigated the usefulness of the model. The investigation was specifically interested in gaining confidence in the simple band model's representation of the PRIZ; confidence in the physical insight obtained from the simulations; and in the new phenomena predicted by the model.

To develop this confidence, the code generated results comparable to experimental data reported in the literature. New experiments were left for a follow-on investigation. The simulations demonstrated most of the characteristics reported in the literature, which produced a strong confidence in the results of the numerical model.

The above work produced the following contributions to the body of knowledge on the PRIZ:

- The first complete, 2-D, numerical simulation of the PRIZ that includes charge and field dynamics, the transverse linear electro-optic effect, and output diffraction.
- A conceptual technique for analyzing internal device dynamics and relating those dynamics to the observed output.
- Predictions of new device behavior, including several new types of transient effects that occur after turning off the device's illumination.
- A demonstration that the mathematical theory of Bliznetsov et al. produces incorrect quantitative output due to the neglect of two significant physical mechanisms.
- Evidence that the simple band model used here is a reasonable representation of the physics in a real device.

The remainder of this dissertation provides the details of the above work. Chapter II begins by describing the mathematical model that is the basis for the numerical simulation. Chapter III describes the model's coding and validation. After providing a foundation for the reader in previous chapters, Chapter IV surveys relevant work in the literature. Chapter V

discusses the heart of the investigation; the sensitivity and pulsed simulations that investigate the physical processes. Chapter VI evaluates the model's usefulness by comparing simulations with experiments reported in the literature. Chapter VII lists conclusions. Because of the scope of the work, numerous appendices describe related topics of interest.

## ***II. Mathematical Model***

The 2-D numerical simulation of the PRIZ is based upon a relatively simple mathematical model. The work starts with a cubic,  $\langle 111 \rangle$ , photorefractive crystal (typically bismuth silicate (BSO)) sandwiched between two conductors. The combination of a single donor, a single trap, and a free electron carrier represents the crystal – a simple band model. A metal-semiconductor barrier at the cathode limits current flow through the device. The following paragraphs describe the physical mechanisms, such as photogeneration, injection, drift, photorefraction and diffraction, used to simulate a complete PRIZ. The description is first presented verbally and then mathematically.

### **Overview – A Verbal Description**

The PRIZ is a spatial light modulator. It can store and read out holograms in the usual way, but it can also suppress the static background in an image and enhance moving objects. To find out why and how the suppression and enhancement occurs, this research created a model of the device, ran simulations, and analyzed the results. This chapter's overview describes the physical arrangement of the device; the material properties selected for modeling; and the physical processes that occur during device operation.

Figure 1 shows the geometry of the PRIZ. The crystal width,  $d$ , is typically between 0.4 and 0.5 mm while the transverse extent of the crystal is about 1 cm by 1 cm. The electrodes are transparent. The write-beam is normally incident to the device and may contain a static or dynamic image. Both write- and read-beams are usually monochromatic. Input ( $L_1$ ) and output ( $L_2$ ) linear polarizers select specific orientations of the electric field, and a filter (F) on the output

permits transmission of only the read-beam. A voltage source (V) provides an external field throughout the device.

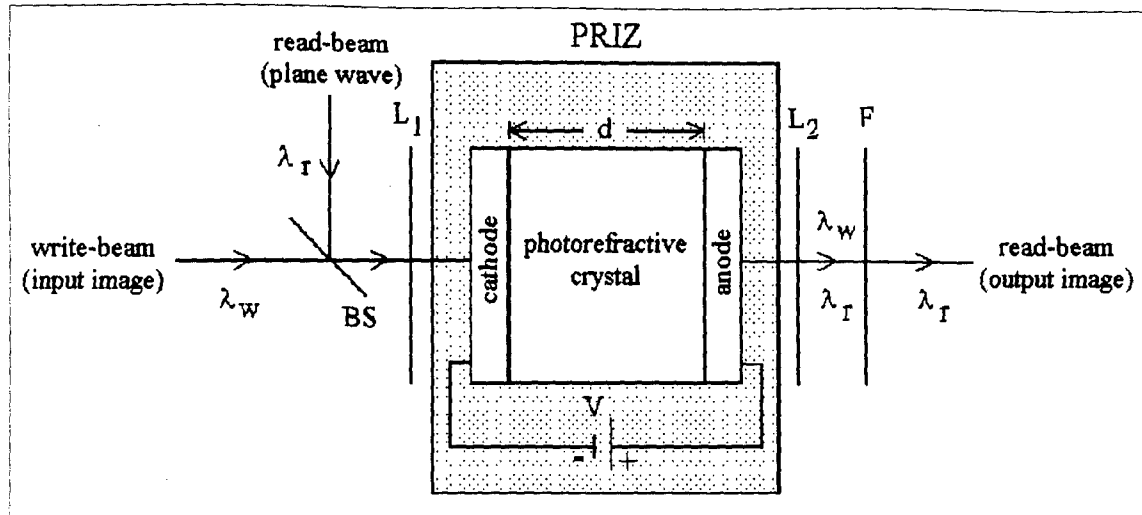


Figure 1. Possible PRIZ configuration. BS is a beam splitter.  $L_1$  and  $L_2$  are crossed polarizers. F is a filter that absorbs the remaining write-beam at wavelength  $\lambda_w$ .

Figure 2 illustrates the model of the photorefractive material used throughout this work.

This simple band model is similar to those models used extensively in the literature (13:3686-3690; 14:878; 15:234).

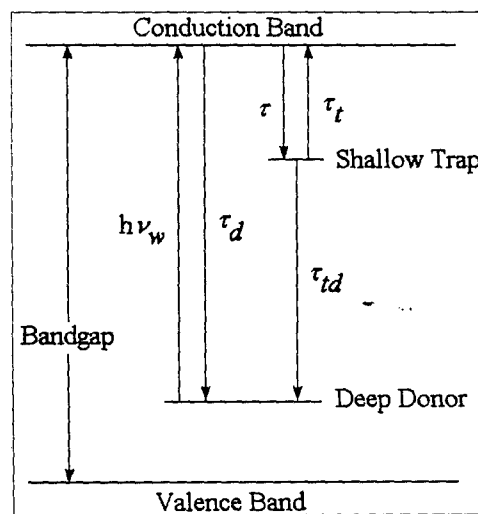


Figure 2. Simple band model

As shown in Figure 2, the forbidden band contains a single deep donor level and a single relatively shallow trap level. Only free electron carriers are considered. In Figure 2,  $h$  is Planck's

constant;  $\nu_w$  is the write-beam frequency;  $\tau_d$  is a time constant associated with recombination of a free electron with an ionized donor (donor recombination lifetime);  $\tau$  is the free electron lifetime;  $\tau_t$  is the trap lifetime; and  $\tau_{td}$  is a lifetime associated with the transition of an electron from a filled trap to an ionized donor (trap to donor recombination). In the mathematical model, the only lifetime that is constant is the trap lifetime, the other lifetimes take into account changing local charge densities. The mathematical model represents the other lifetimes with recombination coefficients; e.g.,  $\tau_d$  becomes  $\xi_d/N_d^+$ , the ratio of a constant donor recombination coefficient to the local density of the ionized donors. That is, the modeler obtains an effective lifetime by dividing the recombination coefficient by the appropriate local (in both space and time) charge density. With injection, drift, and diffusion of the free electron carriers, the values of the lifetimes change throughout the device. By assumption, the donors and traps are immobile.

Before considering the physical processes within the device, the simple write-beam used throughout this dissertation is described. The write-beam input to the device could be almost anything: a static photographic image, a dynamic image from a video camera, or something simpler. Just as a one dimensional square pulse consists of an infinite sum of sine waves of different periods, an arbitrary two-dimensional image can consist of a very complex combination of sinusoidal gratings of different periods and orientations. Since any image is a linear superposition of these gratings, this work uses a single sinusoidal grating with a fixed spatial orientation. The use of a single sinusoidal grating has the advantage of reducing the imaging problem from two dimensions to an effective one dimension. The use of a single sinusoidal grating also has the advantage of experimental simplicity. Such a grating is easily formed by the interference of two plane waves and the storage within the device of that grating can be confirmed by simple diffraction of a read-beam.

Given the above device and material description, and assuming the intensity distribution in the write-beam is a single frequency sinusoidal grating, a brief preview of the physical processes in the PRIZ follows.

Figure 3 and Figure 5 show the sequence of the physical events beginning with an input from a write-beam. To clarify the separate effects of the write- and read-beam, Figure 3 illustrates the physical processes beginning with the write-beam and Figure 5 illustrates those processes associated with the read-beam. In both figures, the coordinate dependencies assume only a two dimensional representation of the device (a slice in the  $xz$  plane, see Figure 4). Since the input image (write-beam) is only two-dimensional, a slice at any  $y$  value creates the same 1-D distribution,  $I(x)$ . The PRIZ is not sensitive to write-beam phase information, only intensity.

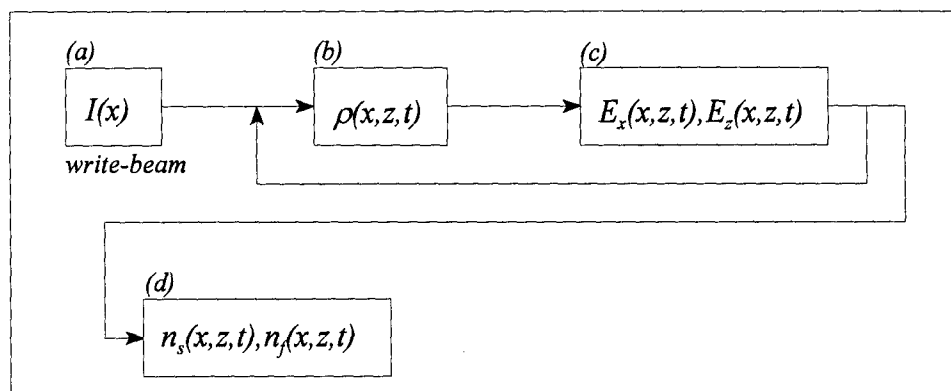


Figure 3. Physics associated with the write-beam.

In Figure 3, block (a), immobile donors in the crystal absorb photons from the sinusoidal write-beam,  $I(x)$ , photogenerating free electron carriers. These free carriers drift under the local electric field. Traps may capture the electrons or the electrons may recombine with a donor site. Diffusion and injection across the cathode will also affect the local free electron density. Filled (immobile) traps may give up their electron and either create a free carrier or fill an ionized donor site. In Figure 3, block (b),  $\rho(x,z,t)$  represents the net charge density that results from the photogeneration and subsequent charge redistribution.

The net charge distribution, which is a function of space and time, is the source of a scalar potential throughout the volume of the device. Poisson's equation relates the scalar potential to a given charge distribution. The transverse and longitudinal electric fields,  $E_x(x,z,t)$  and  $E_z(x,z,t)$ , are at a given time the negative gradient of the scalar potential (Figure 3, block (c)). The fields generated from the local charge partially modify the externally imposed field and affect the drift of the local charge, thus modifying the prior charge distribution.

The longitudinal and transverse electric fields also influence the crystal's indices of refraction. The PRIZ uses a photorefractive crystal that displays the transverse electro-optic or Pockels effect. In that effect, the local electric fields modify the optical properties of the crystal creating a set of fast and slow indices of refraction,  $n_f(x,z,t)$  and  $n_s(x,z,t)$  (Figure 3, block (d)). In other words, the electric fields cause the crystal to become optically anisotropic. Thus, the anisotropy characterizes the space and time varying electric fields and net charge densities.

The mathematical dependence of the change in the indices of refraction on the electric fields varies with the relative orientation of the electric fields to the device's optical axes. Figure 4 shows the crystal orientation chosen for this work.<sup>4</sup> In addition to the specific orientation, the crystal is assumed to be cubic and photorefractive.

While the write-beam is needed to alter the indices of refraction in the device; it is the indices of refraction that effectively store the input image. To observe the transformed output image, the experimenter must apply a read-beam. An output filter eliminates the write-beam after it traverses the crystal, and lets the experimenter see only the output read-beam. The following paragraphs show how the indices of refraction affect the read-beam (see Figure 5).

---

<sup>4</sup> To obtain optimum output contrast, the  $\langle 111 \rangle$  PRIZ requires the input linear polarizer to be parallel to the y axis when device orientation creates transverse fields in the x direction. Given transverse fields in the x direction, the principal axes of the photorefractive crystal are  $45^\circ$  from the  $\langle 11\bar{2} \rangle$  and the  $\langle \bar{1}10 \rangle$  crystallographic directions.

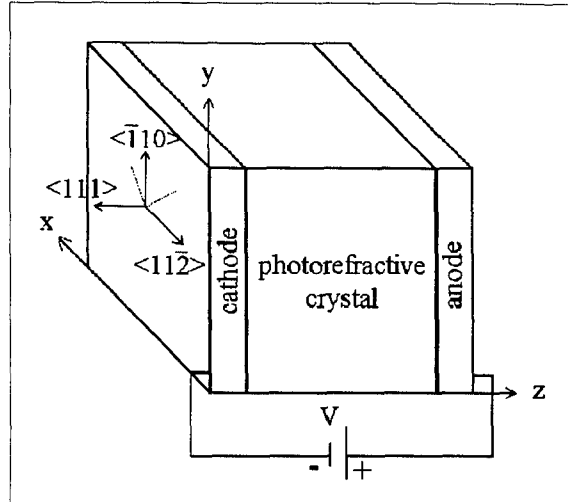


Figure 4. PRIZ Orientation. If the input is a sinusoidal grating in  $x$ , then the operator aligns the input linear polarizer parallel to  $y$ . (3:649)

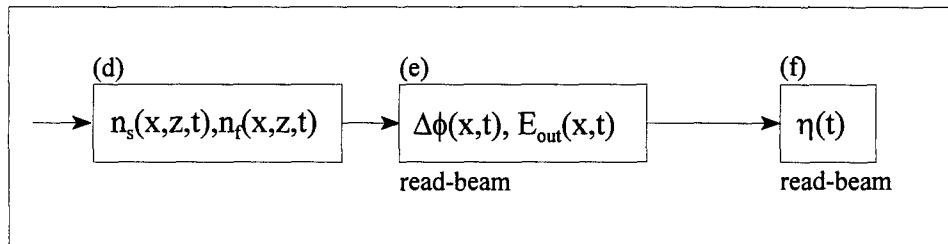


Figure 5. Physics associated with the read-beam

The experimenter selects the wavelength of the read-beam to minimize absorption. By assumption, the read-beam does not affect the internal charge and field dynamics. Rather, the index of refraction distribution in the PRIZ affects the read-beam much as a volume hologram affects a beam of light. However, in the present case, one can reduce the volume hologram to an equivalent thin hologram by adding the effects of the induced anisotropy of the indices of refraction in any given  $z$ -directed filament (i.e., along a longitudinal path through the device). Thus, to a first order approximation, the net effect of the induced anisotropy is diffraction of the read-beam from a thin phase grating. To correspond to experiment, and for simplicity, the read-beam is a simple plane wave.



Thus, the indices of refraction altered by the write-beam modulate the read-beam as it passes through the device. In the device configuration described above,<sup>5</sup> the indices of refraction (Figure 5, block (d)) cause one orthogonal component of the read-beam's electric field to slow with respect to the other component. The electric field induced index of refraction distribution (created by the write-beam) thus creates a phase shift,  $\Delta\phi(x,t)$ , between the components of the read-beam's electric field at the output. The observer identifies this phase shift at the device output as a function of transverse location (Figure 5, block (e)). The output linear polarizer eliminates most of the output electric field,  $E_{out}(x,t)$ , leaving only those components associated with the phase difference. Thus, the output field distribution is an 'image' of the phase shift.

The ratio of intensity in the first order of the diffracted output in the far field to the input intensity after the input polarizer is the first order diffraction efficiency,  $\eta_1(t)$  or just  $\eta(t)$  (Figure 5, block (f)).

The physics described above may differ in an experimental PRIZ. The PRIZ is not limited to the  $\langle 111 \rangle$  orientation shown in Figure 4; it can also use an alternate  $\langle 110 \rangle$  orientation (16:649). In the  $\langle 110 \rangle$  PRIZ, the cathode would be plated to a surface parallel to the (110) plane. The illumination would still be incident to the cathode.

The photorefractive material may also differ in an experimental device. Bismuth silicate ( $\text{Bi}_{12}\text{SiO}_{20}$ ) has the desired optical properties, but  $\text{Bi}_{12}\text{GeO}_{20}$  and  $\text{Bi}_{12}\text{TiO}_{20}$  have also been used (25:325). The initial modeling done in this work used published numerical values of the material properties of BSO since it is the most commonly used material in the PRIZ; the later modeling used values which may not correspond to any known material.

---

<sup>5</sup> The relevant device configuration is a read-beam propagating normal to the cathode with crossed linear polarizers on either end of the device.

The following paragraphs describe the mathematics of the above physical processes in detail.

### The Input

As mentioned previously, the input write-beam is a static, sinusoidal 1-D intensity grating. Previous researchers used a sinusoidal write-beam for much of their work (3:68; 4:750). Thus, using the same input here makes comparison with earlier work straightforward. The expression for that intensity grating is

$$I(x) = I_o' [1 + m \cos(kx + \pi)] = \left( \frac{I_o}{1 + m} \right) [1 + m \cos(kx + \pi)] \quad (1)$$

where  $I_o'$  is the mean input intensity;  $I_o$  is the peak input intensity;  $m$  is the index of modulation;  $k$  is the magnitude of the wave vector of the intensity grating;  $x$  is the transverse coordinate; and  $I(x)$  is the resulting write-beam intensity distribution. The write-beam is assumed constant in the  $y$  direction, the transverse direction orthogonal to the  $x$  axis (see Figure 4).

### Charge Distributions and the Rate Equations

A standard set of rate equations (see Equations (2) to (4)) uses the input intensity distribution,  $I(x)$ , and a set of initial conditions to provide a solution of the charge distribution (17:82; 18:1159; 19:758; 5:28). In this work, the initial conditions are zero densities for the ionized donor ( $N_d^+$ ), traps ( $N_t^-$ ), and free electrons ( $n_e$ ) and a constant local electric field ( $V/d$ ) from the external voltage source. These conditions do not necessarily correspond to the those for a device in the presence of background illumination; however, they are reasonable approximations for an unilluminated (dark) device.

The following rate equations show nearly all of the physical mechanisms in the mathematical model (injection across the cathode is a special case of the drift current, see Equation

(12)). The physical processes are identified below their mathematical expressions. The equations are

$$\frac{\partial N_d^+(\bar{x},t)}{\partial t} = \underbrace{\frac{I(x)\alpha\eta e^{-\alpha z}}{h\nu_w} \left( \frac{N_d - N_d^+(\bar{x},t)}{N_d} \right)}_{\text{photogeneration}} - \underbrace{\frac{n_e(\bar{x},t) N_d^+(\bar{x},t)}{\xi_d}}_{\text{donor recombination}} - \underbrace{\frac{N_t^-(\bar{x},t) N_d^+(\bar{x},t)}{\xi_{td}}}_{\text{trap-to-donor recombination}} \quad (2)$$

$$\frac{\partial N_t^-(\bar{x},t)}{\partial t} = \underbrace{\frac{n_e(\bar{x},t) [N_t - N_t^-(\bar{x},t)]}{\xi_t}}_{\text{trapping}} - \underbrace{\frac{N_t^-(\bar{x},t)}{\tau_t}}_{\text{detrapping}} - \underbrace{\frac{N_t^-(\bar{x},t) N_d^+(\bar{x},t)}{\xi_{td}}}_{\text{trap-to-donor recombination}} \quad (3)$$

$$\frac{\partial n_e(\bar{x},t)}{\partial t} = \frac{\partial N_d^+(\bar{x},t)}{\partial t} - \frac{\partial N_t^-(\bar{x},t)}{\partial t} + \underbrace{\nabla \cdot [n_e(\bar{x},t) \mu \bar{E}(\bar{x},t)]}_{\text{drift}} + \underbrace{\nabla^2 [D n_e(\bar{x},t)]}_{\text{diffusion}} \quad (4)$$

where  $\bar{x}$  represents the spatial position (x,z); x is the transverse coordinate; z is the longitudinal coordinate; t is time;  $\alpha$  is the absorption coefficient;  $\eta$  is the quantum efficiency, a fraction representing the ratio of the number of photons absorbed to produce one ionized donor;  $N_d$  is the unionized donor density;  $N_t$  is the unionized (empty) trap density;  $\xi_d$  is the donor recombination coefficient;  $\xi_{td}$  is the trap to donor recombination coefficient;  $\xi_t$  is a trapping or trap recombination coefficient;  $\mu$  is mobility;  $\bar{E}$  is the vector electric field; and D is the diffusion coefficient.

Besides the obvious photogeneration and loss mechanisms, the rate equations include longitudinal and transverse drift in one term and diffusion in both directions in another term. At any point in space, the equation of continuity specifies the change in the net charge density,  $\rho$ , due to the current density,  $J$  (20:127) as

$$\frac{\partial \rho(\bar{x},t)}{\partial t} = -\nabla \cdot J(\bar{x},t) = -\nabla \cdot [e \mu n_e(\bar{x},t) \bar{E}(\bar{x},t)] - \nabla^2 [e D n_e(\bar{x},t)] \quad (5)$$

This equation must be modified to account for a metal-semiconductor barrier at the cathode (see Equation (12) below). A barrier also exists at the anode, but the voltage bias is reversed so that the barrier does not impede electron flow through the anode. Thus, at the anode, the longitudinal drift term in Equation (4) or (5) is calculated by using extrapolated free electron charge densities and electric fields. The extrapolated densities and fields at the anode are found by assuming longitudinal, linear distributions extend from the region immediately adjacent to the anode right to the surface of the electrode.

The model calculates the diffusion coefficient,  $D$ , for electrons via the Einstein equation (21:20)

$$D = \mu \frac{kT}{q} \quad (6)$$

The third rate equation, Equation (4), is just a rearrangement of the time rate of change of the net local charge which is

$$\rho(\bar{x}, t) = e \left[ N_d^+(\bar{x}, t) - N_t^-(\bar{x}, t) - n_e(\bar{x}, t) \right] \quad (7)$$

### Poisson's Equation

The charge distribution, obtained from the rate equations, is the source needed to obtain the potential,  $U$ , from Poisson's equation. Poisson's equation is

$$\nabla^2 U(\bar{x}, t) = - \frac{\rho(\bar{x}, t)}{\epsilon} \quad (8)$$

where  $\epsilon$  is the permittivity of the photorefractive material and any variation of  $\epsilon$  from a constant is negligible. In turn, the local electric field,  $\bar{E}$ , is

$$\bar{E}(\bar{x}, t) = -\nabla U'(\bar{x}, t) \quad (9)$$

where  $U'$  is the sum of the potential,  $U$ , created by the local charge and the ramp potential,  $U_r$ , created by the constant external voltage. The ramp potential is

$$U_r(\bar{x}) = \left( \frac{x}{d} \right) [V(x=d) - V(x=0)] + V(x=0) \quad (10)$$

Therefore  $U'$  and  $\bar{E}$  describe the local charge shielding of the external field.

The above rate and field equations, the initial conditions of the charge species and electric fields, and the boundary conditions determine the charge and field at every internal position of the crystal.

At this point, the discussion must take into account that the mathematics only model a 2-D slice of the device. Since the simulated crystal is only a two-dimensional slice, there are only four boundaries to consider. In the transverse  $x$  direction, one assumes that the crystal is infinite in extent and only a periodic portion, corresponding to a periodic slice of the input intensity grating, is modeled (i.e.,  $x = 0$  to  $d$ ). Thus, the boundaries at  $x = 0$  and  $x = d$  are periodic in charge flow, charge distribution, and potential

$$U(0,z,t) = U(d,z,t), \quad \rho(0,z,t) = \rho(d,z,t), \quad \left. \frac{\partial \rho}{\partial x} \right|_{x=0} = \left. \frac{\partial \rho}{\partial x} \right|_{x=d} \quad (11)$$

The electric field (mostly from the external voltage) always appears to cause electrons to exit the crystal at the anode. The model assumes that flow at the anode is unimpeded by potential barriers. The external voltage is assumed to maintain a constant potential difference between the anode and cathode. The model does not treat the cathode junction as a pure ohmic contact; it uses the following simplified model of the metal-semiconductor barrier for electron injection (22:375):

$$j_{in}(x,z=0,t) = e \mu n_s [E_z(x,z=0,t) - E_z(x,z=0,t=0)] \quad (12)$$

where  $j_{in}$  is the injected current density;  $n_s$  is an injection coefficient or effective charge density; and  $z$ , the cathode's longitudinal coordinate, is 0. The right hand side of Equation (12) is the argument of the divergence in Equation (5) when Equation (5) is calculated at the cathode. This simple injection model states that when the changing electric field at the cathode exceeds the

initial, externally imposed field at the cathode, current will flow across the metal-semiconductor barrier. The rate equations use Equation (12) in place of the longitudinal drift term (see Equation (4)) when the model calculates densities adjacent to the cathode.

### Electro-optics

When given the time and space dependent fields, the model can determine their effects on the optical output. The cubic photorefractive crystals in the PRIZ display a transverse linear electro-optic or Pockels effect (23:221; 24:399-411). In the words of Yariv and Yeh:

According to the quantum theory of solids, the optical dielectric impermeability tensor depends on the distribution of charges in the crystal. The application of an electric field will result in a redistribution of the bond charges and possibly a slight deformation of the ion lattice. The net result is a change in the optical impermeability tensor. This is known as the electro-optic effect. (24:221)

A detailed discussion of the application of the impermeability tensor to cubic, photorefractive materials can be found in the work by Yariv and Yeh (23:221-238). However, the mathematics here account for the application of the impermeability tensor to the  $\langle 111 \rangle$  PRIZ. In essence, in the Pockels effect, two orthogonal (linear) polarizations of a light beam propagate at different speeds through a photorefractive crystal in the presence of an electric field. Knowing the electric field and the crystal orientation, the physics identifies two orthogonal 'fast' and 'slow' axes. Associated with these two axes is a pair of fast and slow refraction indices. If the applied electric field depends on spatial position, one obtains spatial distributions for both refraction indices. This work sometimes calls these distributions 'index gratings.' In a  $\langle 111 \rangle$  photorefractive crystal, the fast and slow index gratings obtained from the Pockels effect are (16:649; 25:331)

$$n_f(\bar{x}, t) = n_o - \frac{n_o^3 r_{41}}{2} \left[ \sqrt{\frac{2}{3}} E_x(\bar{x}, t) - \frac{E_z(\bar{x}, t)}{\sqrt{3}} \right] \quad (13)$$

$$n_s(\bar{x},t) = n_o - \frac{n_o^3 r_{41}}{2} \left[ -\sqrt{\frac{2}{3}} E_x(\bar{x},t) - \frac{E_z(\bar{x},t)}{\sqrt{3}} \right] \quad (14)$$

where  $n_o$  is the index of refraction in the absence of an electric field;  $n_f$  is the modified index in the fast direction;  $n_s$  is the modified index in the slow direction;  $r_{41}$  is the appropriate electro-optic coefficient for this orientation;  $E_x$  is the transverse electric field; and  $E_z$  is the longitudinal electric field.

Given normal incidence for the read-beam, either component of the electric field at a given transverse point will see the phase shift (25:331)

$$\varphi_i(x,t) = \frac{2\pi}{\lambda_r} \int_0^d n_i(\bar{x},t) dz \quad (15)$$

where the index  $i$  represents either the slow,  $s$ , or fast,  $f$ , index;  $\varphi_i$  is the change in phase imposed on the respective component of the beam along its optical path;  $n_i$  is the appropriate index of refraction; and  $\lambda_r$  is the wavelength of the beam being effected. The assumption here is that the fields change slowly enough in time that any point on the read-beam sees a static pair of index gratings during its half millimeter of travel.

Thus, the Pockels effect will shift the orthogonal fast and slow components of a wave with respect to each other. Since the only difference between the two index expressions (Equations (13) and (14)) is the sign in front of the transverse electric field, *only the transverse field* creates a phase shift between the two components. This work assumes a normally incident read-beam and a specific alignment of the input linear polarizer (see Figure 4 and its caption).

Thus, the net phase shift between the two orthogonal components is

$$\Delta\varphi(x,y,t) = \varphi_s(x,y,t) - \varphi_f(x,y,t) = \frac{2\pi n_o^3 r_{41}}{\lambda_r} \sqrt{\frac{2}{3}} \int_0^d E_x(\bar{x},t) dz \quad (16)$$

While this represents the phase shift seen by a read-beam propagating through the crystal, it does not include the effects of the polarizers applied to a real device. To include the polarizers, start by representing the electro-optic and polarization effects on the read-beam as Jones matrices (see Figure 6).<sup>6</sup>

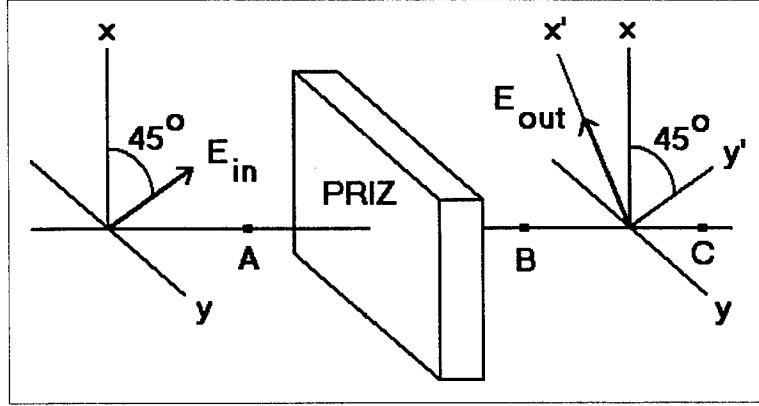


Figure 6. Device representation for Jones matrix calculations. A linear polarizer specifies the input vector,  $E_{in}$ .

The expression for the output electric field is

$$\begin{bmatrix} E_{out,\perp} \\ E_{out,\parallel} \end{bmatrix} \equiv \begin{bmatrix} E_{x'} \\ E_{y'} \end{bmatrix} = \begin{bmatrix} \frac{1}{\sqrt{2}} & -\frac{1}{\sqrt{2}} \\ \frac{1}{\sqrt{2}} & \frac{1}{\sqrt{2}} \end{bmatrix} \begin{bmatrix} e^{i\varphi_s} & 0 \\ 0 & e^{i\varphi_f} \end{bmatrix} \begin{bmatrix} \frac{1}{\sqrt{2}} \\ \frac{1}{\sqrt{2}} \end{bmatrix} = \frac{1}{2} \begin{bmatrix} e^{i\varphi_s} - e^{i\varphi_f} \\ e^{i\varphi_s} + e^{i\varphi_f} \end{bmatrix} \quad (17)$$

where  $\perp$  indicates the direction perpendicular to the input polarizer and  $\parallel$  indicates a direction parallel to it. Equation (15) describes the slow and fast phase shifts ( $\varphi_s$  and  $\varphi_f$ ). The Jones vector for the output field shows only the complex amplitudes of the field components (23:62). The expression is valid immediately after the output crossed polarizer at any transverse location (see Appendix C). These complex amplitudes are not 'real' expressions of the wave, but

---

<sup>6</sup> Note the axes shown here are not those used elsewhere in this paper; the axes here were selected to simplify the matrices. For the actual crystal and polarizer orientations, see the discussion for Figure 4.



representations of the relative phase between the components. Adding the time dependence to the component of the output in the direction of the crossed polarizer gives the following expression for the field after the output crossed polarizer:

$$E_{out}(x,t) \equiv E_{out,\perp}(x,t) = \frac{1}{2} \left( e^{i\varphi_s(x,t)} - e^{i\varphi_f(x,t)} \right) e^{-i\omega t} \quad (18)$$

where  $x$  is now the true transverse coordinate of the PRIZ shown in Figure 4;  $t$  is time; and  $\omega$  is the frequency of the read-beam.

The intensity distribution right after the crossed polarizer is

$$I_{out}(x,t) \propto E_{out}(x,t) E_{out}^*(x,t) = |E_{out}(x,t)|^2 \quad (19)$$

This result assumes an input field of unit amplitude and the corresponding proportional intensity.

Another effect will also modify the output – optical activity. Optical activity causes right and left circularly polarized light to travel at different speeds. This phenomenon is wavelength dependent and causes a large phase shift in BSO (26:201; 27:260-274; 15:235). With the polarizations described above, optical activity causes an additional phase shift to both the fast and slow components, but no significant phase shift between the two. Researchers often negate this effect by simply rotating the output (originally crossed) polarizer (28:1687). This work assumes the output linear polarizer is rotated to remove the effects of optical activity.

## Diffraction

The above mathematics show how the write-beam creates charge and field distributions that modify the indices of refraction. The equations also show how the indices phase modulate a read-beam and what effect the polarizers have on the output. The output intensity in Equation (19) is equivalent to a contact photo immediately after the output polarizer.

The experimenters investigate the device output by examining the diffraction pattern (image) in the far field or Fraunhofer region. Given an analytical expression for the field after the

output crossed polarizer, the expression for the power spectrum of the diffracted beam is (29:376-377)

$$I(f_x) \propto \left( \frac{1}{\lambda z} \right)^2 \left| \mathcal{F}_x \{ E_{out}(x, t) \} \right|_{f_x = \frac{x'}{\lambda z}}^2 \quad (20)$$

where  $I(f)$  is the irradiance or intensity in the power spectrum in the far field corresponding to a spatial frequency of  $f_x$ ;  $\lambda$  is the wavelength of the read-beam;  $z$  is the distance from the output polarizer to the observation plane;  $x$  is the transverse coordinate after the output polarizer;  $x'$  is the transverse coordinate in the observation plane; and  $\mathcal{F}_x$  is the spatial ( $x$ ) Fourier transform.

In a numerical solution, only discrete samples (at discrete values of  $x$ ) of the output field after the polarizer are available. This suggests the need for a discrete Fourier transform; yet discrete Fourier transforms do not provide measurable spatial locations for the output.<sup>7</sup> Thus, a scale factor must be chosen to get the correct output power, irradiance, or intensity.

*Numerical Recipes* suggests different scaling factors based upon different definitions of total power (30:550). The following logic makes selection straightforward. The discrete form of Parseval's theorem relating the Fourier coefficients in the space domain to the Fourier coefficients in the spatial frequency domain (30:504) is

$$\sum_{k=0}^{N-1} |h_k|^2 = \frac{1}{N} \sum_{n=0}^{N-1} |H_n|^2 \quad (21)$$

---

<sup>7</sup> A standard spatial Fourier transform would operate on a function of some spatial coordinate. The result would be a function of spatial frequency. When this transform is performed via optical diffraction on an image (input function), the viewer can measure intensity in the far field (output function) at spatial locations. Different spatial locations, depending on how far away the observation point is from the image, correspond to different spatial frequencies. When the input function is discretized by sampling at regular spatial intervals, a discrete Fourier transform provides a set of similar discrete values corresponding to the output function at discrete spatial frequencies. If the distance between samples is known, so are the spatial frequencies of the output. However, the discrete Fourier transform by itself does not tell the user where to look in an optical experiment to find those frequencies. Rather, scale factors or normalization methods are used to guarantee that power is conserved from the input to the output.

where  $h_k$  are the coefficients in the space domain (discrete values of  $E_{out}$ );  $H_n$  are the coefficients in the spatial frequency domain (discrete values of  $\mathcal{F}_x\{E_{out}(x,t)\}$ ); and  $N$  is the number of discrete samples. The goal is to equate the total power in both domains, before and after the Fourier transform. A selected definition of total power in the space domain is the “mean squared amplitude” (30:550)

$$P = \frac{1}{N} \sum_{k=0}^{N-1} |h_k|^2 \quad (22)$$

where  $P$  is total power in the space domain. If the model used another definition, e.g., “sum squared” without the  $1/N$  factor, the power would be dependent on the sampling interval or grid size. Combining these two expressions, with conservation of energy or power, suggests a relationship for the output intensity at the respective spatial frequency given by

$$I_n(t) \propto \frac{1}{N^2} |H_n|^2 = \frac{1}{N^2} |F_{x,n,N}\{E_{out}(x,t)\}|^2 \quad (23)$$

where  $I_n$  is the intensity in the  $n$ th harmonic;  $F_{x,n,N}$  represents the output of the discrete Fourier transform corresponding to the  $n$ th harmonic; and  $N$  is the number of transverse samples.

Given the output intensity in the various orders ( $n$ ), one can determine the  $n$ th order diffraction efficiency (31:182) by

$$\eta_n(t) \equiv \frac{I_n(t)}{I(t)} \quad (24)$$

where  $n$  is the order;  $I$  is the intensity of the input linearly polarized read-beam; and  $I_n$  is the output intensity of that component of the output beam corresponding to the  $n$ th harmonic. This is one way to measure the distortion and loss in the read-beam.

Assuming the input read-beam intensity is unity, or noting the linearity of the diffraction process, one obtains the following expression for  $n$ th order diffraction efficiency:

$$\eta_n(t) = \frac{1}{N^2} |F_{x,n,N}\{E_{out}(x,t)\}|^2 \quad (25)$$

Thus, using the above mathematical models for photoconductivity, nonlinear optics, and diffraction, one obtains expressions for the diffracted read-beam and for a measure of loss and distortion, diffraction efficiency. That is, given a sinusoidal input at a spatial modulation frequency  $\nu$ ,  $\eta_1$  represents the output energy at frequency  $\nu$ ,  $\eta_2$  the output energy at  $2\nu$ , etc. Thus,  $\eta_1 = 1.0$  would represent no loss or distortion between the input and output. Anything less shows varying degrees of combined loss and distortion.

### **Dominance**

Besides evaluating the intensity output in a diffraction order, one can also analyze internal charge or field distributions. To do this, a new quantity called dominance ( $\delta$ ) was devised. Dominance identifies whether the fields created in the positive or in the negative space charge region dominate the phase shifts that affect the read-beam and the output. The next section explains dominance intuitively and shows an example of the fields. If the fields in the positive space charge region dominate, the device is p-dominant ( $\delta > 0$ ). When the fields in the negative space charge region dominate, the device is n-dominant ( $\delta < 0$ ).

Dominance is a tool for analyzing gross, internal, charge and field dynamics. Simulations revealed that when a sinusoidal intensity grating (write-beam) was input, before transverse drift changes the charge distribution, the transverse distribution of the charges and transverse electric fields were periodic with the same period as the input. The peaks and valleys corresponded to the same locations as the input. After longer periods of illumination, these symmetrical distributions became more complicated, although they remained periodic. Although a longitudinal slice at some transverse point would seem an obvious method to represent the overall behavior of the charge and

field distributions, the distortions make such a conclusion questionable. Thus, the research needed some way of measuring an average change in the distributions.

To use the periodicity information, this work started by defining

$$c(x) \equiv \text{sign}\{\cos(kx + \pi)\} \quad (26)$$

The sign function,  $c(x)$ , essentially identifies a sign associated with the input intensity distribution.

This function will flip the sign of the transverse fields in alternating transverse half periods ( $\pi/k$ ) (see Equation (1)).

Next, the research used this function to define dominance,  $\delta$ , as the ‘average’ magnitude of the output phase shift. Using Equation (16) for the phase shift, dominance is defined as

$$\delta(t) \equiv \frac{1}{m} \sum_{i=1}^m [c(x_i) \Delta\phi(x_i, t)] = \frac{2\pi n_o^3 r_{41}}{m\lambda_r} \sqrt{\frac{2}{3}} \sum_{i=1}^m \left[ c(x_i) \int_0^d E_x(x_i, z, t) dz \right] \quad (27)$$

where  $m$  is the number of transverse points sampled and  $x_i$  is the value of the  $x$  coordinate at each of those sampled points.

The data showed that the products of the sign function,  $c(x_i)$  and the longitudinal integral of the transverse fields were mostly either all positive or all negative at any given time. This led to a more intuitive expression for dominance

$$\begin{aligned} \delta(t) &= \frac{2\pi n_o^3 r_{41}}{m\lambda_r} \sqrt{\frac{2}{3}} \sum_{i=1}^m \left[ c(x_i) \int_0^d E_x(x_i, z, t) dz \right] \\ &\approx \pm \frac{2\pi n_o^3 r_{41}}{\lambda_r} \sqrt{\frac{2}{3}} \left| \int_0^d E_x(x_i, z, t) dz \right|_{ave} \end{aligned} \quad (28)$$

This equation shows dominance to be proportional (with a sign uncertainty) to the average value of the magnitude of the longitudinal integral of the transverse field. Using the approximation developed in Appendix H for first order diffraction efficiency, which is

$$\eta_1(t) \propto \left[ \left| \int_0^d E_x(\bar{x}, t) dz \right|_{ave} \right]^2 \quad (29)$$

gives

$$\eta_1(t) \sim \delta(t)^2 \quad (30)$$

Thus, a numerical calculation of the square of dominance should provide a value proportional to the first order diffraction efficiency. The assumptions here include small phase shifts, occurrence of most of the energy in the first order output, and symmetry of the transverse field distribution mostly undistorted by drift.

The next two sections depart from the pure physical and mathematical approach used in the earlier parts of this chapter. Even readers familiar with the basics of photorefractives might not be comfortable with dominance or with the specific scales (times, velocities, etc.) of the PRIZ. The following sections use results from the simulations to enhance the reader's understanding of the mathematical model.

### **Interpretation of Dominance**

As mentioned above, dominance is approximately an average of the magnitude of either the output phase shift or the longitudinal integral of the transverse field. The square of dominance is proportional to the first order diffraction efficiency. Unfortunately, the mathematical description may not make clear the relationship between dominance and the internal charges and fields. A visual approach is the easiest way to understand the concept. Consider the typical transverse field distribution in Figure 7.

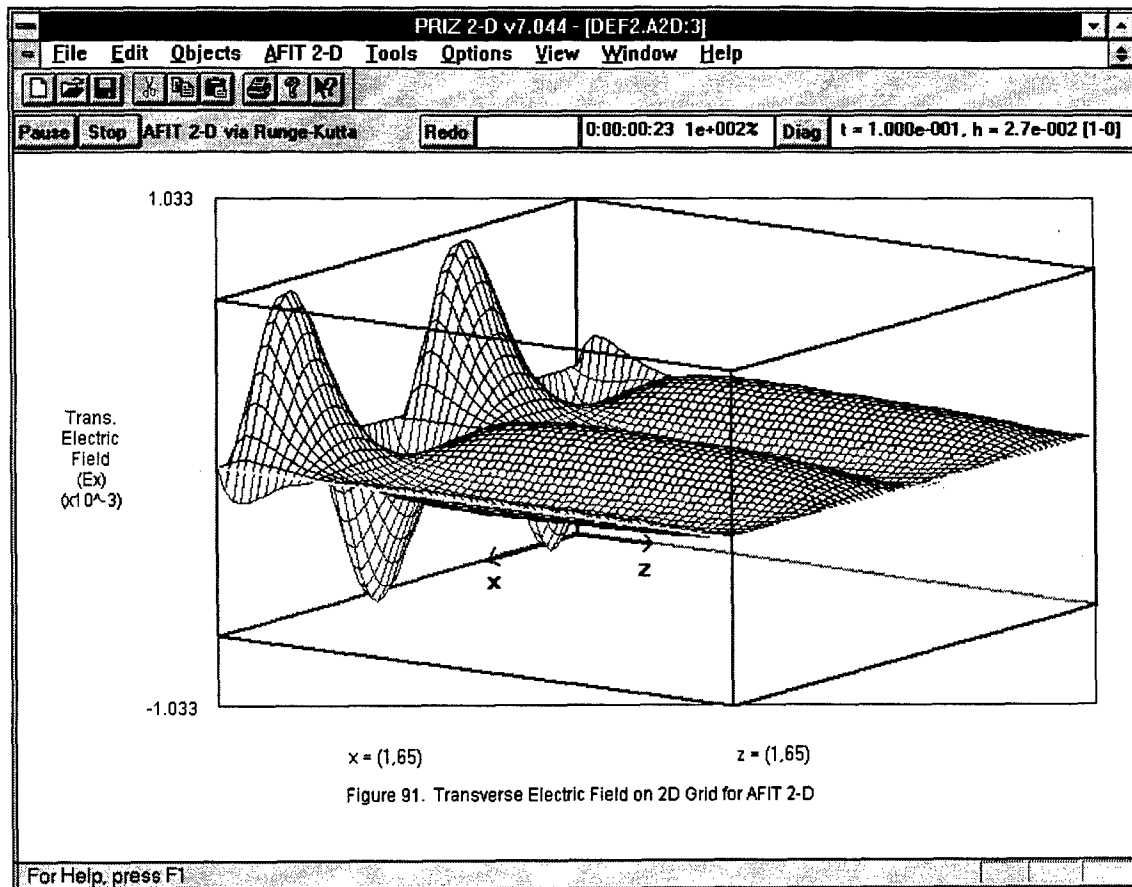


Figure 91. Transverse Electric Field on 2D Grid for AFIT 2-D

Figure 7. Typical transverse field distribution without significant distortion from drift. The ordinate ( $x = 1, z = 1$ ) is the intersection at the rear, bottom of the plot. The cathode is at  $z = 1$  (the left side near the high peaks), and the anode is at  $z = 65$ . This is output from the code and shows normalized (unitless) field values.

To better understand dominance, slice the simulated region into four equal-sized, parallel strips running from the cathode to the anode and flip over the strips that contain large negative peaks. The flip is equivalent to multiplying longitudinal integrals by  $c(x)$ . Now mentally do the longitudinal integrals. The big peaks near the cathode dominate those integrals, so each integral is a positive number ( $\delta > 0$ ). If the peaks near the cathode were relatively small, the integrals could turn out to be negative ( $\delta < 0$ ). During a period of illumination, the signs of the integrals may

change (positive to negative or vice versa), indicating a phase reversal. This procedure helps to better understand the relationship between dominance and the internal charge and fields.

A slightly more rigorous method of relating dominance to internal charge distributions starts with Gauss' law

$$\nabla \cdot \bar{E}(\bar{x}, t) = \frac{\rho(\bar{x}, t)}{\epsilon} = \frac{\partial E_x(\bar{x}, t)}{\partial x} + \frac{\partial E_z(\bar{x}, t)}{\partial z} \quad (31)$$

Without knowing how the fields change in the longitudinal direction, the mathematics will not generate an algebraic relationship between the charge and the transverse fields. However, when the net charge distribution becomes large, so will the transverse fields, since the divergence (change) in the field vector must also become large. Thus, large charges will create large transverse fields compared with the fields generated by small charge densities. Thus, larger charge densities should create large dominances, either positive or negative. While this method is an approximation, it has proven to be an accurate description of what happens internally.

### Typical Scales

Since simulation of the device via computer coding of the above equations is the approach used in this work, the reader may appreciate a brief description of the various scales for the crystal's charge and field dynamics. This work usually selected initial parameter values from the literature for BSO, a typical photorefractive material used in PRIZ construction. Typical parameters would be an external voltage of 1 kV, a crystal width of 1 mm, and a mobility of  $10^{-6} \text{ m}^2/\text{V}\cdot\text{s}$ . The use of such parameters creates a constant longitudinal field of  $10^6 \text{ V/m}$  ( $E_0$ ), which in turn results in a typical electron velocity of 1 m/s, or a time of 1 ms for the electron to transit the device. For a 65x65 grid, an electron would move from one grid point to the next in 15.6  $\mu\text{s}$ . After charge redistribution, longitudinal fields near the cathode will range from about 1.5 to 15  $E_0$ .



depending on various parameters. Transverse fields will usually be smaller. Thus, local velocities vary considerably throughout the device.

As for charge density,  $N_d$  is typically around  $10^{24} \text{ m}^{-3}$  and  $N_t$  is about  $10^{22} \text{ m}^{-3}$ . A peak write-beam intensity of  $10 \text{ W/m}^2$  on a sinusoidal distribution results in  $N_d^+$  and  $N_t^-$  reaching nearly  $5 \cdot 10^{21} \text{ m}^{-3}$  at peak locations for a run of 180 ms; however, the free electron density,  $n_e$ , never rises much above  $10^{19} \text{ m}^{-3}$ .<sup>8</sup>

Since the free electron density, out of the three charge species, is the most susceptible to quick change, it is the most likely species to create difficulties during solution of the rate equations. A small change in a very small number ( $n_e$ ), can be a large source of error. Thus, problems may occur where the free electron density is smallest.

Other potential problems might be associated with charge transport distances versus calculation step times. As mentioned above, if the simulation uses a  $65 \times 65$  grid, then an electron will move from one grid location to the next in about  $15 \text{ } \mu\text{s}$ . This time will be much shorter in the higher fields near the cathode. If the solution does not update the charge distribution at least every  $15 \text{ } \mu\text{s}$ , field calculations will lag behind charge calculations and shielding effects will be incorrect.

Summarizing the theory, several equations describe the dynamics of charge, field, and index grating formation. Those equations specify the time rate of change of the densities of the three charge species, the field given those charge distributions, and the indices of refraction given the electric fields. Using those expressions, the above paragraphs showed how the indices affect the phase modulation of the read-beam and how the linear polarizers convert that phase modulation to amplitude modulation. Because of the nonlinear charge redistribution, which adds nonlinearities to the phase shifts, the output beam shows nonlinearities also. The above

---

<sup>8</sup> Note that the charge densities were taken from typical simulations performed and reported later in this work.

mathematics also derive an expression for diffraction efficiency, a simple method for measuring the distortion and modulation loss in the output. Finally, the mathematics define a function called dominance that simplifies analysis of internal charge and field dynamics.

### ***III. Code Development***

The previous chapter described the mathematical model of the PRIZ. This chapter describes the implementation of that model in software, first by providing an overview of the code describing module integration, then describing each module or algorithm in detail, and finally wrapping up with a description of the validation process.

#### **Overview and the Mathematical Model**

The computer code implements the mathematical model in object oriented C++. The author was familiar with the language, it was available for both Windows and UNIX, and its object oriented structure promised significant coding efficiencies. To save time, the code modifies and uses canned routines from *Numerical Recipes*<sup>TM</sup> whenever possible (30). The following paragraphs do not describe the actual software except where needed to identify simplifications or approximations to the physics. Instead, the text describes only the algorithms that implement the model. The validation process ensures that the code accurately implements the mathematical model of the physics and the respective algorithms.

The previous chapter's equations and flow charts (Figure 3 and Figure 5) suggested how one would model the physics. Figure 8 pulls the physics together and relates each process to the selected algorithm.

The new acronyms in Figure 8 include i.c. for initial conditions, b.c. for boundary conditions, R.K. for Runge-Kutta with adaptive step-size control, and FFT for the fast Fourier transform. The loop back in Figure 8 indicates where the code feeds the electric fields back into the Runge-Kutta routine that solves the rate equations.

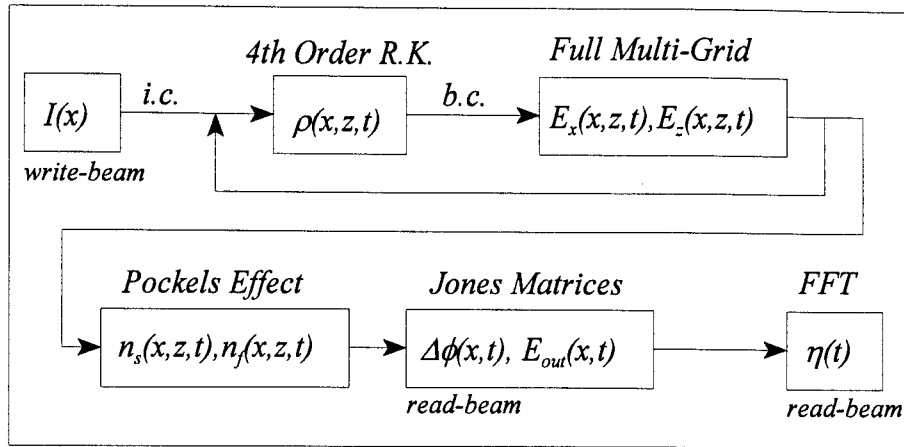


Figure 8. Algorithms associated with PRIZ physics

Note that the Runge-Kutta routine actually solves the rate equations (see Equation (2) to Equation (4)) for the densities of the ionized donors, ionized traps, and free electrons. Equation (7) sums the local densities to get the net charge density at every location at a given time,  $\rho(x,z,t)$  in Figure 8.

To save time, and because the user does not need a truly continuous output, the software does not solve the complete system of equations at every small time step. The Runge-Kutta routine selects small time steps, e.g., 1  $\mu$ s, to keep the error down. In a 100 ms run, that step size results in calculating data 100,000 times. Such a large amount of data would be very hard to use, store, and present. The Runge-Kutta and the Full Multi-Grid (FMG) calculations must be done frequently to minimize errors. However, the refraction indices, output fields, phase shifts, and diffraction efficiency can be calculated at a sparse rate, e.g., once every 1 ms, since they result in output that does not feed back into the model. Figure 9 shows the timing of the various calculations.

The user specifies both the model parameters and the inputs that describe how the simulation will run. Simulation inputs include the number of intervals at which the output is reported, how long each interval is (e.g., 1 ms each for an 80 ms run), and the electric field update

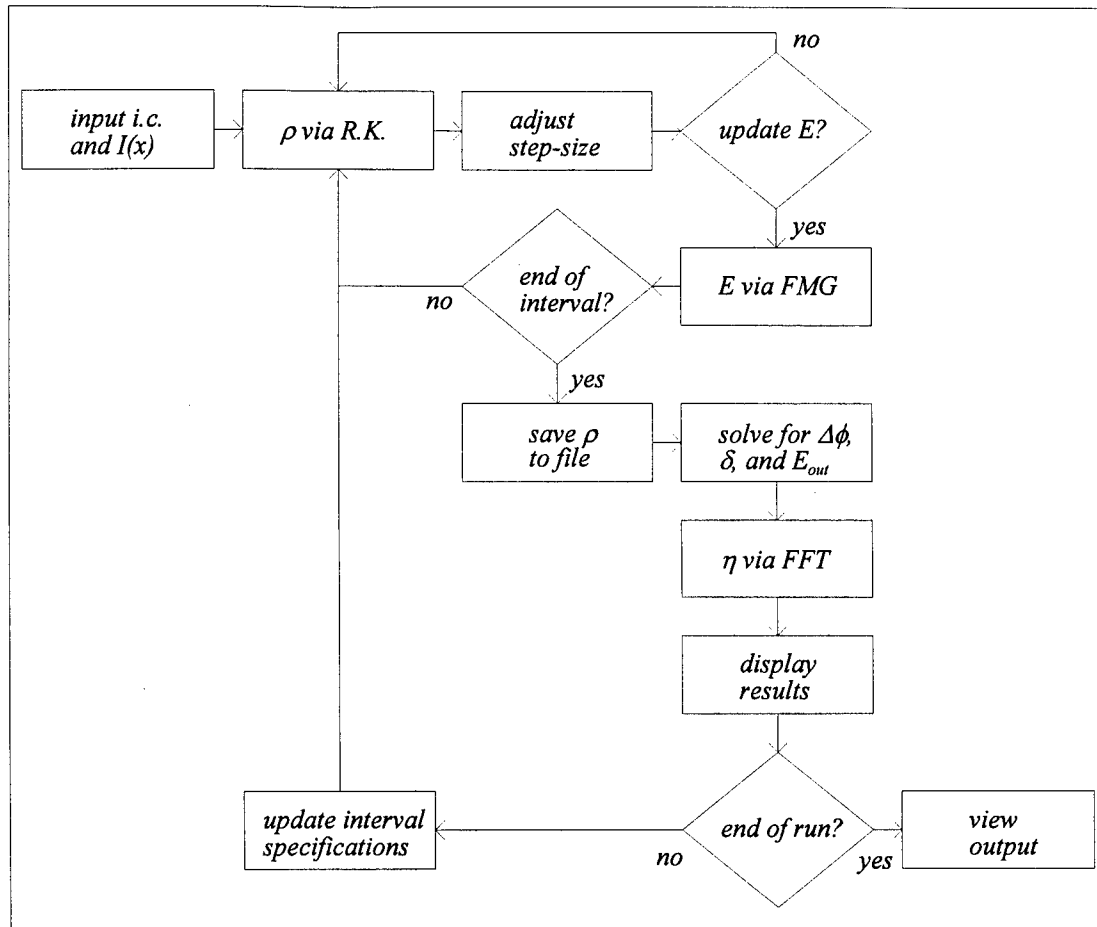


Figure 9. Code timing

frequency within each interval (e.g., after every RK step). At the end of each interval, the program saves the charge density distributions to disk (one file per interval) and displays user selected plots on the computer monitor. Saving the charge distributions permits a user to rerun<sup>9</sup> a simulation that originally took from 40 minutes to 2 weeks in less than 30 seconds. This allows the user to examine, as the simulation evolves, functions or distributions that the software does not store for viewing at the end of a run. The program saves in memory data like current, diffraction efficiency, and dominance at the end of each interval so that the user can later view plots of those variables versus time.

<sup>9</sup> Rerunning a simulation recalculates, only at the specified reporting times, the electric fields (based upon the saved charge distributions from the original run), the phase shifts, and the output distributions.

The current method of running the program is to use the Microsoft Windows™ version (with full graphical capability) to create a parameter specifications file (\*.a2d). The user uploads that file to a fast UNIX system and then runs the simulation remotely (40 minutes to 2 weeks). Next, the researcher downloads the data files output by the program, the charge density distributions (\*.dat), back to the Windows system. The user then reruns the simulation without the lengthy Runge-Kutta calculations (less than 30 seconds total). Finally, the user views and prints selected plots from Windows. See Appendix E for details on how to run the program.

The following paragraphs provide details on the code's implementation and validation.

### **Grid, Boundary Conditions, and the External Circuit**

Selection and implementation of specific algorithms are interdependent. For example, the *Numerical Methods* Full Multi-Grid (FMG) Poisson solver, which calculates potentials faster than competing algorithms such as successive over-relaxation (30:866) and Fourier methods (30:858), requires a square grid ( $2^N+1$  points per side,  $N$  being an integer) with points equally spaced in both directions. A typical transverse input intensity distribution is two periods of a sinusoidal grating. The two periods cover a width of 1 mm for a spatial frequency of 2 lines per mm. The minimum number of transverse points to represent two sines would be about 9 to 17 (9 points can represent only the local maxima/minima and the zeros of the 2 sine waves). This assumes no fine structure develops in the charge and fields during operation. The expected charge and field distributions are the only drivers in selecting the minimum number of points in the longitudinal direction. Previous 1-D simulations at AFIT suggested that a grid needed 50 to 100 points for adequate resolution. Thus, the typical run uses a square grid of 65 x 65 points and solves for 11,907 charge densities (excluding boundaries). Figure 10 shows the grid layout. See Appendix F for an analysis of the errors associated with the grid resolution.

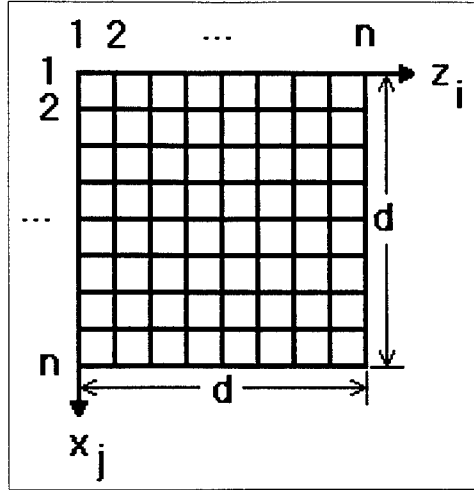


Figure 10. Grid

The mathematical model assumes that an external voltage source maintains a constant potential difference between the cathode and anode ( $U = -V$  at  $z = 0$  and  $U = 0$  at  $z = d$ ). This specifies the longitudinal boundary conditions. The grid points are indexed  $i = 1, 2, \dots, n$  as the coordinate goes from 0 to  $d$ , where  $n$  is the number of grid points. Thus  $U = -V$  at  $z_1$  and  $U = 0$  at  $z_n$ .

In the transverse direction, the periodic, pseudo-infinite input creates a periodic potential. The simulations' input of an 'infinite' sinusoidal intensity grating requires the code to enforce periodicity. Thus, the code assumes non-sinusoidal inputs are also periodic. The code conforms to the following relations:

$$\begin{aligned} U(x_2, z_i, t) &= U(x_{n-1}, z_i, t), \\ U(x_1, z_i, t) &= U(x_{n-2}, z_i, t), \text{ and} \\ U(x_3, z_i, t) &= U(x_n, z_i, t), \forall i \in \{1, 2, \dots, n\} \end{aligned} \quad (32)$$

Figure 11 shows the boundary conditions.

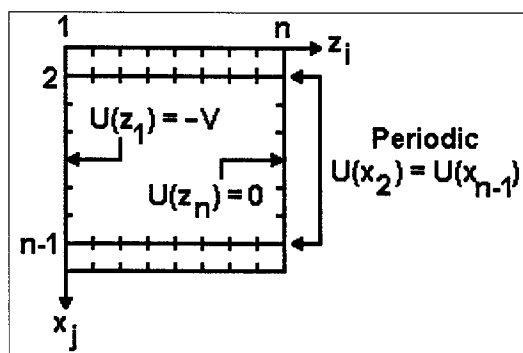


Figure 11. Boundary conditions

Although the FMG algorithm enforces a constant potential between the electrodes, in truth the potential across the electrodes will deviate slightly. To assure that potential deviation is negligible (e.g., less than 10%), the software models a simple circuit where the PRIZ is a current source in series with a voltage source that has a large impedance. To determine the current density out of a 3-D device, the program assumes that longitudinal drift at the anode is identical at every (unmodeled) transverse  $y$  direction and is periodic in the transverse  $x$  direction. These assumptions permit extrapolation of the anode current to a 1 cm x 1 cm (transverse face) crystal. The circuit passes this anode current through a 1 M $\Omega$  (user selectable) impedance to generate a voltage drop. Given the applied voltage (typically 1 to 2 kV), the code calculates the percentage drop for the user. The program does *not* feed the voltage drop back to the boundary conditions of the FMG. The user is expected to examine the voltage drop versus time to determine the validity of the constant voltage assumption enforced by the FMG.

#### Rate Equations via 4th-Order Runge-Kutta

The code must solve the rate equations (Equations (2) to (4)) at every interior grid point in the crystal. In a 65 x 65 grid, the software must find 11,907 charge densities ( $N_d^+$ ,  $N_t^-$ , and  $n_e$  at



63<sup>2</sup> points). Computer processing limitations prevent doing a full 3-D simulation, which would require solving over 800,000 simultaneous differential equations.

Initial conditions for solving the rate equations include zero values for initial time, ionized donor density, ionized trap density, free electron density, and transverse field. The potential at the cathode is a constant  $-V$ ; the potential at the anode is 0; and the longitudinal field is  $-V/d$  everywhere inside the crystal.

Before solving the rate equations, the program converts all variables to relatively small, unitless quantities to minimize numerical problems. Table 1 shows the normalization constants. In normalizing the equations, combinations of these constants are frequently necessary. The only change to the rate equations is that mobility,  $\mu$ , disappears from the current terms. Of course, all variables become unitless.

Table 1. Normalization constants (15:759)

<u>Variable</u>	<u>Normalization</u>	<u>Interpretation</u>	<u>Units</u>
time	$\frac{d^2}{\mu V}$	initial electron transit time	sec
distance	$d$	longitudinal width of crystal	m
density	$\frac{\epsilon V}{ed^2}$	density where the Maxwellian relaxation time equals the initial electron transit time	m <sup>-3</sup>
voltage	$V$	external voltage	volts

After discretizing and normalizing the rate equations, one still needs algorithms to approximate the drift, diffusion, and injection currents. The software uses three-point central difference equations to convert potentials (the FMG solution) to electric fields. The current expressions use the resulting fields and previously calculated (or initial) charge densities. The program uses a three-point central difference equation in the transverse direction to approximate

the drift term (actually its divergence). A one-sided difference equation showed no savings in time or accuracy.

Calculation of the longitudinal drift term requires use of a forward difference approximation to avoid numerical instability (oscillation). The code modifies the current expression at points adjacent to the cathode to include electron injection across the cathode. This is the equivalent of a forward differencing scheme, and appears to be the source of the instability when interior current calculations use central differencing. The forward differencing scheme that avoids the numerical instability is the same method used in earlier AFIT 1-D simulations (5:30).

The software calculates diffusion by a standard central differencing approximation to the second derivatives.

Given the drift, diffusion, and injection currents, any standard ODE solver can solve the rate equations. After testing several algorithms, fourth-order Runge-Kutta with adaptive step-size control was selected (30:710-722). Other algorithms, e.g., Bulirsch-Stoer, were slower on a full size simulation. Stiff versions of both algorithms did not appear to solve even one time step in a reasonable period.<sup>10</sup> Since the Runge-Kutta algorithm typically solves for 11,907 variables, while a stiff routine finds (a sparse)  $1.42 \cdot 10^8$  variables, this result is reasonable.

### **Electric Fields via the Full Multi-Grid**

When the model needs to calculate the electric fields, it calls a Full Multi-Grid (FMG) Poisson solver to obtain the scalar potentials everywhere on the grid (30:871-889). Testing of other algorithms, such as Fourier techniques, revealed none had the accuracy or speed of the FMG.

---

<sup>10</sup> It was unclear whether the stiff code was working correctly. However, the expected rate for *working* code was slow enough for the extremely large number of variables ( $12,000^2$ ) that additional effort was not expended.

The effort modified the *Numerical Recipes* FMG routine to specify periodic boundary conditions on the longitudinal edges and fixed potentials ( $U$ ) on the transverse edges (electrodes).

After obtaining the scalar potential, the code uses the finite difference approximations mentioned above to get the electric fields in both directions. Again, alternative one-sided and even five point schemes showed no improvement in accuracy or speed.

Compared with a single solution (at any specific time) of the rate equations via the Runge-Kutta algorithm, the FMG solution for potential is time consuming. Thus, the simulation allows the user to specify whether the code updates the electric field every time the Runge-Kutta routine calculates the derivatives (rate equations), or whether to wait until the Runge-Kutta finishes a time step. The program defaults to calculating the electric fields at the end of each Runge-Kutta step. This default calculation frequency degrades accuracy slightly but saves significant runtime (see Appendix F).

### **Pockels Effect and the Jones Matrices**

Given the electric fields throughout the device, one can find the fast and slow indices of refraction. Although the calculation of diffraction efficiency does not require the indices of refraction (the calculation uses longitudinal integrals instead), the program calculates the indices for the user at the end of each interval. On the other hand, the phase shift between the fast and slow axes of the read beam is an essential part of the optical output. The expression for the phase shift, Equation (16), requires calculation of the longitudinal integral of the transverse electric field. A relatively simple approximation is used to calculate the integral: the rectangle rule

$$\int_0^d E_x(\bar{x}, t) dz \approx \sum_{i=2}^{k-1} [E_x(x, z_i, t) \Delta z] \quad (33)$$

where the interval from 0 to  $d$  is split into  $k-1$  subintervals each with length  $\Delta z$ . The larger error inherent in the rectangle rule than in other approximations does not result in any noticeable

degradation in the output (i.e., 'jaggedness' in the transverse distribution of  $E_{out}$ ). The calculation uses the electric field,  $E_x$ , sampled at transverse location  $x$ , time  $t$ , and various longitudinal positions  $z_i$ . The summation is across only the interior points where charge, fields, and the indices of refraction are well defined. The boundary points ( $i = 1$  and  $i = k$ ) are at the electrodes and do not have well defined indices of refraction. Since the resulting phase shifts appear very smooth across adjacent transverse locations (integrations), the coding process did not examine more accurate algorithms such as Simpson's rule.

The program also calculates dominance at this point using Equation (27) and the rectangle rule described above. In the code, the longitudinal integral of the transverse electric field is calculated only once and then reused.

After finding the phase shift at every transverse position, the software calculates the amplitude of the output electric field just after the output polarizer via Equation (54) from Appendix H. Earlier versions of the code used the unnecessarily complex expression of Equation (18).

### **Diffraction of the Read-Beam via the Fast Fourier Transform**

To obtain the diffracted read-beam in the far field, the program feeds the amplitudes of the output electric field after the output crossed polarizer, see Equation (54) in Appendix H, into a fast Fourier transform (FFT) from *Numerical Recipes* (30:507). The code then uses Equation (25) on page 23 to scale the output from the FFT. Assuming an input read-beam intensity of unity, the software assigns the appropriate scaled components out of the FFT to the first and second order diffraction efficiencies.

The calculation of diffraction efficiency completes the coding of the model. The code neglects optical activity; losses in the polarizer and output filters; losses and reflections in the transparent electrodes; and losses and reflections in the photorefractive crystal. In addition, it is

currently limited to one crystal orientation and one arrangement of the polarizers. However, the code is applicable to any cubic, wide-bandgap semiconductor with similar photorefractive properties. This work uses the refraction index ( $n_o$ ) and the electro-optic coefficient ( $\eta_{41}$ ) reported for BSO by Petrov (15:243-269).

The above flow charts and descriptions of the code explain what, why, and how each calculation occurs. The descriptions do not really give the reader a sense of what the program produces for the user or a sense of the code's potential for analysis. To do so, Appendix E shows plots of selected output early in a simulation (before significant transverse drift). This is only a sampling of the output; it does not do justice to the many data types and display options available.

### **Validation of the Numerical Simulation**

At this time, no well characterized experimental data exists for comparison with the code's output; i.e., no method exists for testing the 'correctness' of the code as a whole. Such a test would require data from an experiment in which each variable modeled in the simulation had known values. No such experiment currently exists. The best validation available is to check the various modules for proper operation, make certain that the code reflects the mathematical equations that describe the device, and compare the output with results from earlier 1-D simulations (which also were not completely validated).

The limited validation in this work began by testing each major algorithm for correct performance. The validation tested the Runge-Kutta, the Full Multi-Grid, and the fast Fourier transform with known functions and verified correct performance. The Runge-Kutta test was a one-dimensional quadratic. The FMG test involved two-dimensional sinusoidal functions of varying spatial frequencies. The FFT test used single and summed sinusoidal inputs at multiple frequencies. Modified versions of the Runge-Kutta and FMG routines were also used to produce a 1-D code with output identical to earlier AFIT 1-D codes created with MATHLIB (5).

At a more detailed level, the validation examined the impacts of alternative approximations to some simpler algorithms. For example, the effort considered two, three, and five point finite differences as alternative expressions for derivatives. These investigations found no significant difference in the results (values for the electric fields and currents) for any of these methods. However, the validation process identified an oscillation (instability) when the code combined two (boundary) and three point (interior) differencing schemes. Since the cathode boundary allows only a longitudinal, one-sided two point scheme, the process selected forward differencing for the longitudinal current calculation.

Ideally, the code should update the electric field as often as the charge distributions. However, the Runge-Kutta routine does calculations at frequent time points (intervals) to get a result over a 'large' step and then backs up and uses smaller intervals if the error is too big. This can result in many time-consuming FMG calculations. To save time, the investigation looked at the impact on diffraction efficiency of calculating the electric field less frequently. Appendix F shows that only minor effects (1% error) occurred when the code updated the electric field less often than the charge (i.e., at the end of a Runge-Kutta step). The process examined several different types of runs to avoid looking only at an easy case.

To check the size of the error introduced by the Runge-Kutta algorithm, the validation process reduced the allocated relative error three orders of magnitude to  $10^{-6}$ . The simulation with the smaller error showed no significant difference in the results (charge, field, phase shifts, and diffraction efficiency). Because of a long runtime, the research included only one such test.

The Full Multi-Grid algorithm does not permit specifying an error; however, it does permit the user to change the number of v-cycles executed at each step in the algorithm (see 30:875). Changing the number of v-cycles, i.e., approximating the solution at a different grid resolution, effectively changes the amount of smoothing the routine performs, and will implicitly

change its error. The investigation tested various numbers of v-cycles and, again, found no significant differences in the results (the potential distribution).

The validation process also looked at the impact of using a finer grid. A finer grid produced a small but significant change in the output, up to 6% in diffraction efficiency. The difference is usually quantitative and not qualitative in nature (see Appendix F). Memory requirements prevented running the simulation at grid sizes above 256 by 256, and time requirements limited the number of simulations at that size. From the grid tests, one could estimate a maximum error of about 10% on a 65x65 grid.

Tests determined that the implementation of the periodic boundary conditions was acceptable for the potential. The program maintained periodicity. However, the output phase shifts showed a spatial modulation (see Appendix G) at a wavelength twice that of the simulated extent of the crystal ( $\lambda = 2d$ ). Energy at that frequency will not affect diffraction efficiencies at harmonics of the input ( $\lambda = d, d/2, d/3, \dots$ ), the frequencies this effort is interested in. The source of the modulation appears to be related to the enforcement of the periodic boundary conditions in the Full Multi-Grid. Given an input periodic charge distribution (two sines) in the transverse direction, the FMG outputs a transverse potential distribution that is periodic in  $d$  (the same potential at  $x = 0$  as at  $x = d$ ) but not in  $d/2$ . That is, the potential is not the same at  $x = d/2$  as it is at  $x = 0$  and  $x = d$ . Paradoxically, the size of this error decreases at larger exposures.

The validation process compared the electric fields and diffraction efficiencies generated in a typical run to reported experimental values. The comparison showed that the simulated diffraction efficiencies were smaller,  $10^{-3}$  versus  $10^{-2}$ . A reexamination of the literature suggested that the experimental PRIZ devices may have used insulators or just poor electrode to semiconductor contacts to achieve the 1% diffraction efficiencies. That is, the experiments with higher diffraction efficiencies than those achieved in the present simulations may have had some

measure of insulation between the cathode and the photorefractive crystal (see Appendix D). Additional simulations confirm that as the user decreases the injection coefficient (going from no insulator toward total insulation), diffraction efficiency rises. The code is unable to simulate a complete insulator at the cathode (no injection) because the Runge-Kutta routine's error control slows the calculations down to almost a dead stop when the injection coefficient becomes small. Thus, experimental data is probably consistent with the behavior of the simulation.

Finally, the investigation compared previous 1-D simulations with a 2-D simulation using a constant input intensity (in the  $x$  direction). This is probably the most comprehensive test possible on the numerical model. The earlier 1-D code used at AFIT is consistent with the Bryksin's 1-D numerical work (19:757-761); the community has accepted its results. If the 2-D code is performing correctly, the results should be the same for both 1-D and constant input 2-D simulations. For a constant input intensity, the results were effectively the same for both 1-D and 2-D simulations.

A final test validated the calculation of diffraction efficiency and confirmed again that the field calculations are correct. The mathematics of Bliznetsov et al. (4:751) were used to produce 2-D charge distributions and first order diffraction efficiencies as functions of time. A longitudinal cut of that charge distribution is a positive step adjacent to the cathode that increases in amplitude and contracts towards the cathode in time; the width ( $z_0(x)$ ) and amplitude depend on the input intensity distribution (see Equation 40 on page 64). The 2-D numerical code in this work used Bliznetsov's charge distribution to calculate first order diffraction efficiency. The mathematical and numerical calculations produced peak efficiencies that varied by less than 1%.

Thus, the validation process made every reasonable effort to ensure that the numerical 2-D code is a correct solution of the mathematical equations. The code is not perfect; however, the measurable inaccuracies are small (less than 10%) under most conditions (see Appendix F).



#### *IV. The Literature*

Throughout the 1980s, a group of mostly Russian investigators<sup>11</sup> took a detailed look at the PRIZ. Their strengths were theory and experiment. The Russian researchers would typically develop some mathematical expressions based upon simplifying assumptions and then show how closely their mathematical predictions compared with experimental data. Unfortunately, they tended not to report the values of the variables they used to solve their equations, which makes their results hard to reproduce.

The previous researchers started with experiments that showed that the PRIZ's output depended on both the temporal and spatial frequencies of the input – something they named dynamic image selection (DIS). These early experiments initiated an intense search for the theoretical basis of the observed phenomena. The theoretical work started with a simple linear theory valid for short illumination times and progressed to include the nonlinear response indicative of longer illumination times. During this period, researchers used experiments to confirm their theory. Near the end of their investigations, the Soviets produced a numerical 1-D model (9:757-759) which AFIT researchers later reproduced (6; 5).

The following paragraphs report on previous work in the categories of experiment, theory, and numerical modeling. The research mentioned here is limited to that applicable to this work.

##### **Experiment**

The first reports of PRIZ experimentation were published around 1979. A previous device, the PROM, had used a BSO crystal in another crystallographic orientation, taking

---

<sup>11</sup> The names V.V. Bryksin, M.P. Petrov, M.G. Shlyagin, A.M. Bliznetsov, A.V. Khomenko, and L.I. Korovin recur repeatedly in the literature.

advantage of the longitudinal electric fields to modulate the output of the device (32:432-433).

The PRIZ uses an orientation in which transverse electric fields control the output of the crystal.

In late 1979 Petrov et al. reported using the PRIZ spatial modulator as, among other things, a simple spectrum analyzer (33:752-753). As in all early experiments, they compared diffraction efficiency for both the PRIZ and the PROM, which showed the superiority of the PRIZ.

In 1980, Petrov et al. reported on the temporal and spatial frequency dependence of the PRIZ (12:165-166). When they applied a sinusoidal intensity grating to the PRIZ, the diffraction efficiency showed a peak when plotted against both temporal and spatial frequency (see Figure 12). The literature often calls the PRIZ a space-time light modulator because of this dual dependency.

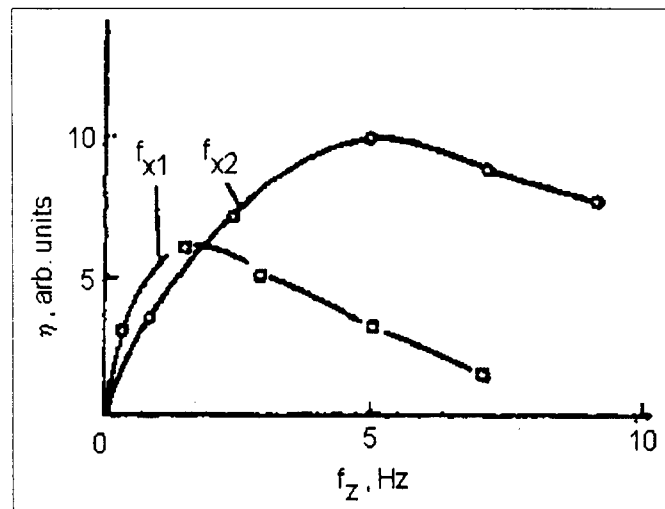


Figure 12. Dependence of the diffraction efficiency on the frequency of the temporal modulation of the light intensity ( $f_z$ ) for two spatial frequencies ( $f_{x1}$  and  $f_{x2}$ ). (12:165)

Also, when Petrov et al. imaged a moving bar of light onto the device, the read-beam showed enhancement of the leading and trailing edges of the bar. The brightness of the two edges displays peaks when plotted against the speed of the bar. Petrov et al. suggested that the dimensions and speed of the moving bar are just alternative ways of looking at varying spatial and

temporal frequencies. They named the PRIZ's performance in response to varying temporal and spatial input frequencies "dynamic image selection."

In the same experiment, the authors also illuminated the PRIZ with a single pulse of a sinusoidal write-beam (see Figure 13). The output peaked after the researchers turned the write-beam on and again after they turned it off. Some self-erasure occurred after each peak. The authors reported a phase reversal at the time they turned off the write-beam (12:185).

Although the results were qualitative, they correspond closely with the numerical results reported in this dissertation. Both works have a sinusoidal write-beam input, and both show a peak in the output followed by self-erasure. Also, after write-beam turnoff, both show reintensification followed by a second period of self-erasure.

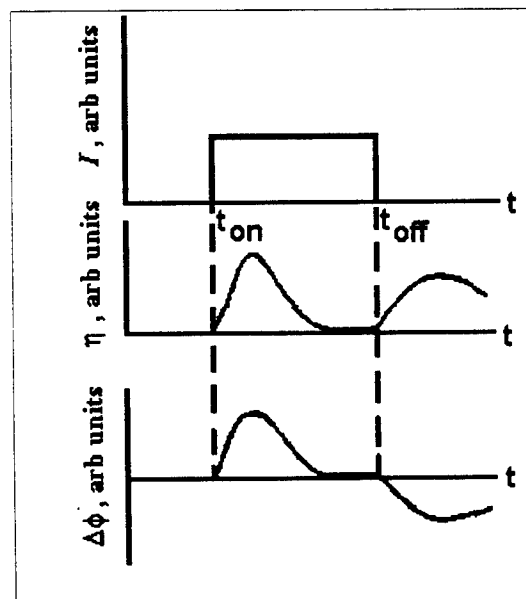


Figure 13. Petrov single pulse experiment.  
(12:165)

Later in 1980, Petrov's group continued its experimentation with the PRIZ (34:816-821). They reported on holographic experiments (not comparable to the simulations here) and showed the dependence of diffraction efficiency on crystal orientation. Their paper ended the early experimental work with the PRIZ.

Shortly after the initial experiments, Petrov and Khomenko collaborated with Casasent and Caimi of Carnegie-Mellon to reproduce some of those experiments at Carnegie-Mellon. They published two articles that summarized or reproduced the early work, using some figures from the earlier articles (1:3090-3092; 2:3846-3854). These reports described the experimental setup much better than the earlier literature. They also reported the phenomenon of suppression of a stationary, non-zero background via dynamic image selection. These reports led scientists to believe that the PRIZ could be used as a moving target indicator.

The Carnegie-Mellon experiment in moving target detection showed an output contrast between the moving object and the background of between 5 and 50. When the input intensity of the moving object and the stationary background were equal,  $r_{in} \equiv I_{mo} / I_b = 1$ , the output contrast,  $r_{out}$ , was 5. This contrast is considered the magnitude of background suppression. When the researchers increased  $r_{in}$  to 2.5,  $r_{out}$  increased to 50 (2:3854). At  $r_{in}$  higher than 2.5,  $r_{out}$  did not increase above 50.

In 1987, Bliznetsov et al. showed that reciprocity<sup>12</sup> holds in the PRIZ only for low exposures (22:374-376). They used one dimensional numerical simulations to support a claim that at high exposures where linearity does not hold, the failure of reciprocity is due to the injection current.

---

<sup>12</sup> Reciprocity is the phenomena where the total output of the device has a linear relationship to exposure, the product of input intensity and time. In the region where reciprocity holds, increasing intensity from one experiment to a second will cause a phenomenon to occur earlier in the second than the first.

## Theory

After the initial experimentation, there followed a period in which the researchers performed intense theoretical work to explain the observed phenomena. This period started with a theoretical description of the charge and field dynamics by a group led by V.V. Bryksin.

In 1981, Bryksin and his group started with the basic rate and field equations, linearized them, and obtained an expression for the first spatial Fourier component of the longitudinal integral of the transverse field,  $I_1$  (17:82-86). This might be considered a theoretical equivalent of dominance, although Bryksin et al.'s intent at the time was to show the time dependence of electro-optic phase shifts (17:83).

When plotted,  $I_1$  showed a peak and then a fall-off modulated by various sized oscillations. The plots show that the peak  $I_1$  value can be either positive or negative. Bryksin et al. also noted, not in the text of his work but in the caption of a figure, that diffraction efficiency is proportional to  $I_1^2$ . This relationship,  $\eta \sim I_1^2$ , looks very similar to the relationship in this work between dominance and first order diffraction efficiency,  $\eta_1 \sim \delta^2$ . In fact, the previous chapters showed that dominance is very closely related to the first order component of the longitudinal integral of the transverse fields.

Many of the later papers use Bryksin et al.'s theoretical approach (17:83). In later works, the rate and field equations change as do the assumptions used to simplify the solution, such as linearity. Thus, in early 1982, Bryksin and Korovin (18:1159-1163) developed expressions for charge and field distributions using a derivation very similar to Bryksin et al.'s (17:83). Their development provided the basis for determining the transverse fields in the linear operating region. Later in 1982, Bryksin et al. used this theory to compare analytically calculated electric fields with experimental data for short periods of illumination (28:1686-1689).

After the initial theoretical work, specialized investigations began in several different areas. These included dynamic image selection, charge and field dynamics, light transmission, and crystallographic orientation.

As already mentioned, Petrov et al. did some early work on crystallographic orientation in 1980 (34:818) and 1981 (35:789-792). In 1983, Owechko and Tanguay studied in detail the effect of crystal orientation on the electro-optic phase modulation (36:239-242). In that paper they developed a theory on how the linear electro-optic effect creates harmonic distortion.

In 1984, Owechko and Tanguay expanded their investigation of crystallographic orientation (16:644-652). Their theory is an essential part of the foundation for the 2-D numerical simulation in this dissertation. It includes Equations (13) and (14), defining the indices of refraction as modified by the Pockels effect (16:649).

A substantial body of the literature examines the theoretical foundation of the charge and field distributions within the PRIZ. In 1983, Bryksin and Korovin published their early work on the nonlinear theory of field dynamics within the PRIZ (37:30-33). They assumed that the net charge distribution is a positive step charge adjacent to the cathode and ignored any negative charge. They provided expressions for the width of the positive step and for the electric field at the cathode.

Later that year, they added an exponential curve for light absorption (instead of a constant throughout the device).<sup>13</sup> They stated that the exponential dependency must be considered "when absorption is substantial" (38:686-689).

---

<sup>13</sup> The transmission function of light through the crystal has an exponential dependence,  $I(z) = I_0 e^{-\alpha z}$ . Thus, the number of photons absorbed per unit distance must also have an exponential dependence. The absorption *coefficient* is of course a constant for a given wavelength.

In 1984, Bryksin et al. revisited the linear operating mode of the PRIZ to develop an expression for diffraction efficiency similar to Equation (57) of Appendix H (14:878)

$$\eta_1(t) = \left[ \frac{\Delta\varphi_1(t)}{4} \right]^2 \quad (34)$$

In that paper, they derived an expression for the longitudinal integral of the first harmonic of the transverse electric field ( $P_1$ ) and a dimensionless function proportional to  $P_1$ ,  $G$ . They noted that this “integrated characteristic” may be negative for low modulation frequencies.

The early research has touched upon a quantity very similar to dominance. However, the literature identifies these pseudo-dominance quantities only with longitudinal integrals of the transverse field. They do not attempt to relate the quantities to charge dynamics in any fashion. Furthermore, the derivations are generally too complex to obtain an intuitive understanding from the mathematics. The driving force in developing the dominance concept was the need to analyze the charge and field dynamics intuitively.

In 1984, Bryksin and Korovin also looked at the nonlinear theory of charge formation near the cathode and the resulting electric field in that region (39:2051-2057). They published another paper on the dependence of the charge distribution on light absorption, this time using their nonlinear theory (40:2195-2199).

The culmination of the Soviets’ theory on charge and field in the nonlinear regime of the PRIZ came in 1985. At that time, Shlyagin et al. developed the basis of the final theory on the nonlinear performance region of the PRIZ (3:68-72). Because of the complexity of the derivation, the group made numerous limiting assumptions. These assumptions included a positive step charge distribution, Equation (40) on page 64; an inequality to enforce that charge distribution, Equation (41) on page 64; and a zero time rate of change of the free electron density,  $\partial n_e / \partial t$ . Their expression for the  $n$ th harmonic of the phase shift of the ordinary wave was

$$\varphi_{o,n} = \frac{16\pi egt(1-a)B_o}{\epsilon n^2} \int_0^\infty \cos(nx) (1+m \cos(x)) F_n(x) dx, \quad (35)$$

$$F_n(x) = nkz(x) - \frac{1 + e^{-nk(d-z_o(x))} - e^{-nkd} - e^{-nkz_o(x)}}{1 + e^{-nkd}}, \quad g = \frac{I\alpha f}{h\nu}$$

where  $n$  is the order;  $e$  is the charge of the electron;  $g$  is the rate of photoelectron production from donor levels;  $\alpha$  is the absorption coefficient for light at frequency  $\nu$ ;  $h$  is Planck's constant;  $I$  is the intensity of the writing light;  $f$  is the quantum efficiency;  $t$  is time;  $a = n_s/(g\tau)$ ;  $B_o$  is a constant that depends on the angle between the transverse fields and the optical axes of the crystal;  $x$  is the transverse coordinate;  $z$  is the longitudinal coordinate;  $m$  is the modulation index;  $z_o$  is the width of the positive step charge;  $k$  is the magnitude of the wave vector of the input intensity distribution; and  $d$  is the longitudinal extent of the crystal.

Although the group plotted diffraction efficiency in many different ways, they did not identify a clear relationship between an expression for diffraction efficiency and  $\varphi_{o,n}$ . Yet, the group claimed an almost exact correspondence between their experimental and analytical results for diffraction efficiency. Even if the group had clearly stated an expression for diffraction efficiency, the failure to identify all of the parameters involved in the plots makes the plots difficult if not impossible to reproduce. Figure 14 and Figure 15 are two of their plots. Both figures show characteristics similar to those produced by the simulations discussed in the chapter that evaluates the simple band model.

During the period when the Bryksin group was developing the theory of charge and field dynamics, they also began applying the theory to dynamic image selection. Typically, the investigators of dynamic imaging explain basic phenomena and suggest that the more complex phenomena, e.g., dynamic imaging, are just combinations of the simpler phenomena. In 1982, Bryksin's group reported on the theory of dynamic image selection (41:193-196). The group



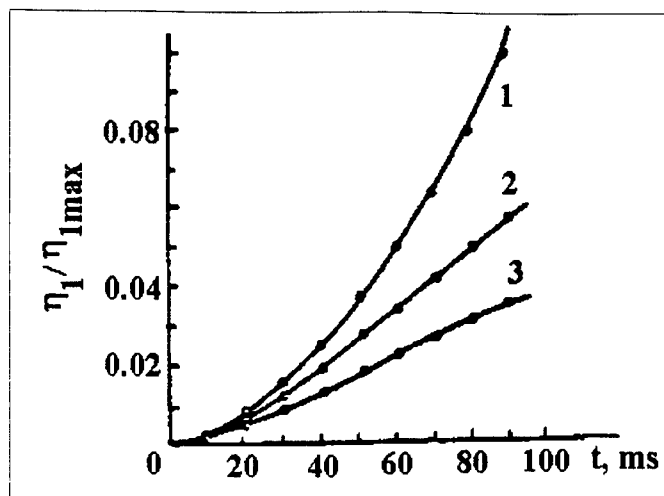


Figure 14. Time dependence of the diffraction efficiency for modulation factors  $m=1$  (1),  $0.45$  (2), and  $0.27$  (3),  $U=1.8$  kV,  $v=2.5$  mm $^{-1}$ ,  $\eta_{\max}=0.5\%$ . (3:70)

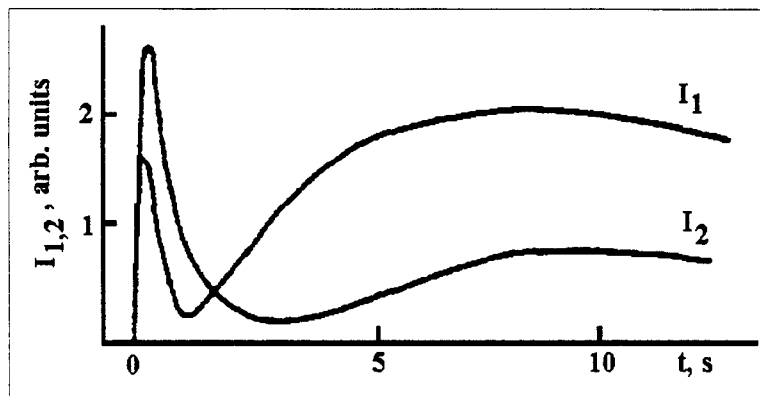


Figure 15. Time dependence of the first- and second-order diffracted light  $I_1$ ,  $I_2$  for  $v=0.5$  mm $^{-1}$ ,  $I=500$   $\mu$ W/cm $^2$ ,  $\lambda=488$  nm. (3:71)

related dynamic imaging both to a dependence of diffraction efficiency on the spatial modulation frequency of the illumination and to the effects of terminating the illumination. In 1983, Bryksin and Korovin developed a theory relating injection current to dynamic imaging (42:1347-1351). They claimed that the existence of an injection current through the cathode is critical in describing the positive charge region near the cathode and its effect on the self-erasure of the output.

In 1987, Bliznetsov et al. concluded their theory of dynamic image selection by developing the theory of what happens immediately after write-beam turnoff (4:750-754). They

reported that the injection of electrons across the cathode is a major factor in what happens after turnoff. Their analytical expression for diffraction efficiency immediately after turnoff is

$$\begin{aligned}
 \eta(t) &= B E_o^2 l^2 I_1^2(t), \quad I_1 = \frac{1}{\pi} \int_0^\lambda d\xi \cos(x\xi) \left\{ \mathcal{F}_o + \frac{n_s(t-t_o)}{n_o \tau} \mathcal{F}_1 \right\}, \\
 \mathcal{F}_o &= \frac{g_o}{x} \left\{ x \zeta_o - D [1 - e^{-x \zeta_o} + e^{-x(d-\zeta_o)} - e^{xd}] \right\}, \\
 \mathcal{F}_1 &= D \int_0^{\zeta_o} d\zeta \left( 1 - \frac{\zeta}{Q} \right)^{-1 + \frac{1}{g_o}} \left( e^{-x\zeta} + e^{-x(d-\zeta)} - \frac{1}{D} \right) + g_o Q \left[ \frac{g_o Q}{\zeta_o} (1 + \gamma) \right]^{-\frac{1}{g_o}} \\
 &\quad \cdot \left\{ -1 + e^{-M} + D \left[ \frac{e^{-x\zeta_o} - e^{-xd-M}}{1 + (1 + \gamma)x\zeta_o} + \frac{e^{-x(d-\zeta_o)} - e^{-M}}{1 - (1 + \gamma)x\zeta_o} \right] \right\}, \\
 \lambda &= \frac{1}{vl}, \quad x = 2\pi vl, \quad \frac{1}{D} = 1 + e^{-xd}, \quad \zeta_o = \frac{z_o}{l}, \quad d = \frac{d_o}{l}, \\
 Q &= \zeta_o \frac{g_o + 1 + \gamma}{g_o}, \quad M = \frac{d - \zeta_o}{\zeta_o(1 + \gamma)}, \quad l = \mu \tau |E_o|, \quad n_o = \frac{\epsilon}{4\pi e \mu \tau}, \\
 g_o &= \frac{(g - \frac{n_s}{\tau}) t_o}{n_o}, \quad g = \frac{I_w \alpha f}{\hbar \omega}, \quad I_w = I_o (1 + m \cos(2\pi v y))
 \end{aligned} \tag{36}$$

where B depends on the orientations of the crystal axes, the direction of the transverse fields, and the polarization direction of the readout light;  $E_o$  is the field generated by the external voltage;  $\mu$  is the electron mobility;  $\tau$  is the electron lifetime;  $n_s$  is the density of free electrons in the cathode region;  $t$  is time;  $t_o$  is the time when the write-beam is turned off;  $e$  is the electron charge;  $\epsilon$  is the dielectric constant;  $z_o$  is the width of the positive step charge region;  $y$  is the transverse coordinate;  $\hbar$  is Planck's constant;  $\omega$  is the frequency of the write-beam;  $v$  is the spatial modulation frequency of the write-beam;  $d_o$  is the longitudinal extent of the crystal;  $\alpha$  is the absorption coefficient;  $f$  is the quantum efficiency;  $m$  is the modulation index; and  $I_o$  is the input intensity.  $\gamma$  is not defined in the article; however, recreating the derivation shows  $\gamma = \frac{1}{\alpha z_o} - 1$ .

Besides relying on the assumptions in the 1985 work by Shlyagin et al. (3), Bliznetsov et al. used only the first term in an infinite series expansion about the time of turnoff ( $t - t_0$ ) to describe device behavior after turnoff. One would expect the use of only the first term in the expansion to limit the derivation's validity to a short linear period immediately after turnoff. Thus, it is not surprising to find that the group's mathematical predictions completely fail to match their nonlinear experimental data. This failure is perhaps the biggest gap in their work.

### Numerical Modeling

In 1987, Bryksin's group developed a one dimensional numerical model of the charge and fields within the PRIZ (19:757-759). The charge redistribution was described as

$$\begin{aligned} \rho &= e(n_+ - n_t - n), \quad \frac{\partial E}{\partial x} = \frac{4\pi\rho}{\epsilon} \\ \frac{\partial \rho}{\partial t} + e\mu \frac{\partial(nE)}{\partial x} &= 0, \quad \frac{\partial n_t}{\partial t} = \frac{n}{\tau} \\ n_+ &= N_d \left[ 1 - e^{-\frac{g\alpha t}{N_d} e^{-\alpha x}} \right], \quad g = \frac{If}{\hbar\omega} \end{aligned} \quad (37)$$

where  $\rho$  is the net charge density;  $e$  is the electron charge;  $n_+$  is the ionized donor density;  $n_t$  is the filled trap density;  $n$  is the free electron density;  $E$  is the electric field;  $x$  is the longitudinal coordinate;  $\epsilon$  is the static permittivity;  $\mu$  is the photoelectron mobility;  $\tau$  is trap lifetime;  $t$  is time;  $\alpha$  is the absorption coefficient;  $N_d$  is the donor density;  $I$  is the input intensity;  $f$  is the quantum efficiency; and  $\omega$  is the frequency of the light.

They also give an expression for the injection at the cathode that becomes

$$n(0, t) = n_s \left[ 1 - \frac{E(0, 0)}{E(0, t)} \right] \quad (38)$$

where the first 0 in each argument of  $E$  refers to  $x = 0$ , and the second argument of  $E$  is the time.

They solve these expressions by a finite difference scheme.

At AFIT, Luke et al. reproduced that 1-D numerical model, modified it, applied a different solution algorithm, and then performed a variety of investigations (6; 5). The result of the AFIT 1-D effort is a similar, but simplified, version of the current work. The 1-D numerical simulations were limited in various ways, including the lack of any simulation of the electro-optic effects of the device.

### **Other Models**

The simple band model is not the only model of BSO or similar crystals reported in the literature. Other models include multiple traps, hole carriers, and even hopping transport. The following is just a brief sampling.

A number of articles emphasize the existence of multiple electron traps. Astratov et al. performed some experimental work with charge transfer in 1983 using both shallow and deep traps (8:1244-1247). Attard and Brown in 1986 explored the decay dynamics of laser-induced phase gratings and developed a model that included multiple shallow and deep trapping levels as well as electron and hole trapping (10:3253-3259). In 1988, Attard investigated photoconductivity in BSO. The model in Figure 16 uses multiple traps and hopping mechanisms (43:5169-5174).

Other articles emphasize more complex models. In 1989, Attard proposed a model that used very long-lived electron and hole traps. Attard uses this model to explain a technique for restoring faded holographic images (44:3211-3219). In 1990, Attard examined a multiple defect/impurity transport model (see Figure 17) with both hopping bands and immobile carriers in traps (11:44-55).

Attard in 1991 examined the hopping band structure again and extended his work on the associated quasi-Fermi levels (9:933-936). Further work could modify the numerical model developed in this dissertation to include any of the above mechanisms.

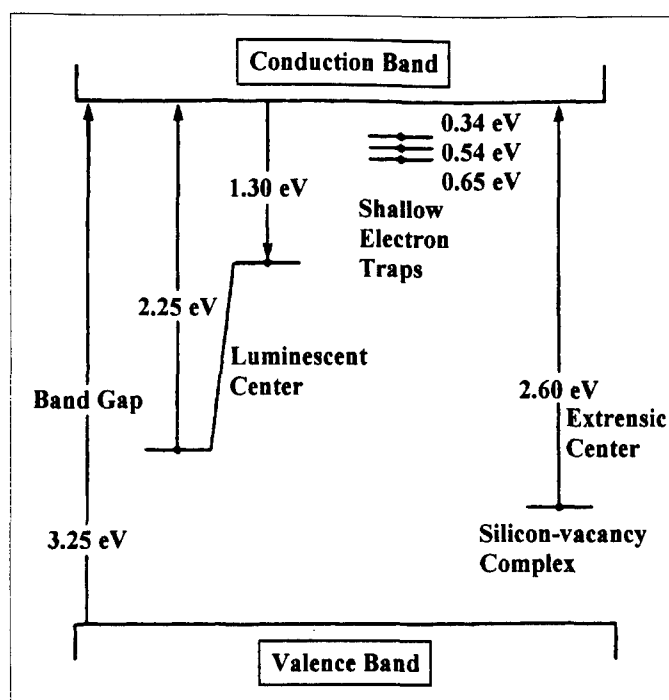


Figure 16. Energy band diagram for BSO at 300 K.  
(47:2657; 13:3684; 43:5170)

Finally, it is worth mentioning two general surveys dealing with BSO and the PRIZ. In 1989 Petrov and Khomenko produced an excellent report which summarized most of the work that had been done on the PRIZ at that time (25:325-352). If that work misses something, Petrov's book (and its mind-boggling bibliography) catches it (15:243-269).

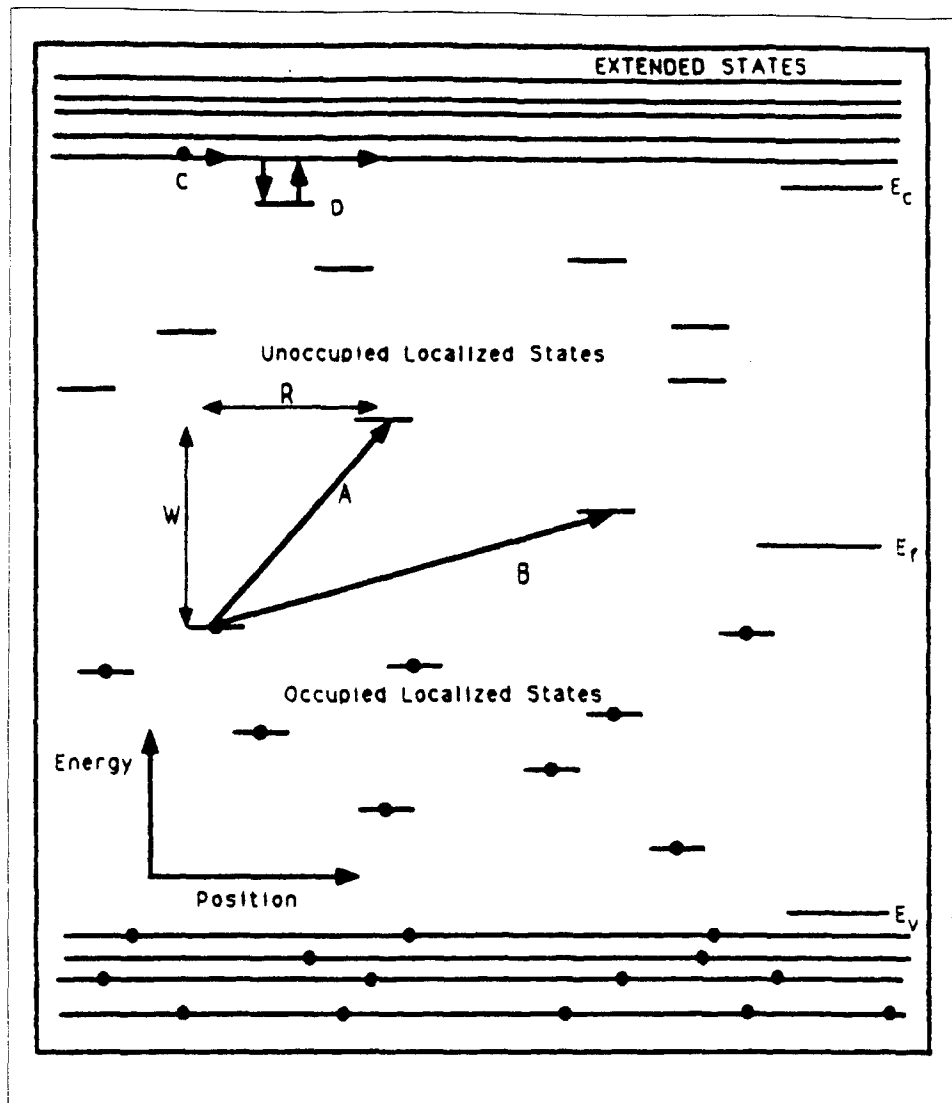


Figure 17. Energy-gap structure showing hopping transport via tunneling between localized states near the Fermi level (events A and B), and transport by multiple trapping via shallow traps (event D). (11:53)

## *V. Investigation of Device Physics*

This chapter describes the investigation into the basic processes that control the PRIZ's performance and how that performance varies as the device's physical parameters are changed. The device performance of interest is that demonstrated during dynamic imaging rather than holography or long-term storage. Thus, desirable output characteristics are fast self-erasure and a large peak amplitude for a change in the input. This work selected a set of parameters, called the standard operating point, that minimized the time of the output peak, maximized the ratio of peak amplitude to amplitude at the point of greatest self-erasure, and coincidentally minimized the code's runtime.<sup>14</sup> The description of device physics in this chapter starts with a more detailed description of how the standard operating point was selected.

Using the standard operating point, which specifies the rates of the physical processes, the simulations of this work show that the latest model in the literature did not include all essential physical processes. A minimum set of essential physical processes is determined by comparing the output of the latest mathematical model in the literature with output from the numerical model in this work. The comparison indicates that exponential absorption and transverse drift are essential physical processes not modeled in the literature (4:752).

With the minimum model or set of processes established, a sensitivity analysis was performed by varying one parameter at a time about the standard operating point. From that sensitivity analysis, the text first shows typical output for parameter sets near the standard

---

<sup>14</sup> The model includes all of the physical processes in expressions in the rate equations (see Equations (2) to (4)). However, selection of proper parameters can reduce processes' rates so low that they are effectively non-operative. It is also possible to totally eliminate processes from the model by setting a flag that forces use of a subset of the rate equations with selected processes' expressions omitted; however, that flag is used rarely and when it is used, it is clearly identified in the text.

operating point (p-dominant) and an alternate operating point (n-dominant). The phenomena displayed in the output plots are explained via an analysis built around charge and field dominance. After the plots, selected knowledge gained from the sensitivity analysis is summarized in a short discussion on the major factors affecting dominance. The plots, their analysis, and the discussion of dominance should provide some qualitative understanding of how the device works.

Thereafter, quantitative data from the sensitivity analysis shows how doubling the model's parameters, one at a time, affects device performance during continuous illumination. The effects of doubling the parameters at the standard operating point are shown in terms of the magnitude and timing of the peak output. The continuous illumination phenomena demonstrate what could happen to the static portion of an image during dynamic imaging in a PRIZ.

Relating write-beam turnoff (pulsed operation) to the trailing edge of a moving object in an image provides some insight into what happens to the dynamic portions of an image processed by the PRIZ. The changing charge distributions after write-beam turnoff change the device's output. The standard and alternate operating points use parameters that specify very low rates for thermal ionization, donor recombination, and trap-to-donor recombination, three processes that can change the charge distributions after turnoff. The text shows the effects of increasing, one at a time, the rates of those mechanisms. The output for pulsed operation is characterized by the degree of self-erasure before write-beam turnoff and the amount of reintensification after turnoff.

In summary, this chapter discusses the following concepts: the minimum set of physical processes needed for an accurate 2-D numerical simulation; how the device works internally to produce the observed output; and a quantitative measure for the range of performance achievable by the modeled device near the standard operating point. These concepts, and the data used to implement them, will be the foundation for validating the model in the next chapter. In that



chapter, model validity is evaluated by comparing the predictions of numerical simulations to experimental data reported in the literature.

### **Standard Operating Point**

Part of the motivation behind this research was the possibility of designing a PRIZ that operates fast enough for a practical moving target indicator (MTI). This effort implements the simple band model numerically, and then performs simulations and analyses. The emphasis was on creating a device that operated quickly and demonstrated short time constants in its output, a device with good dynamic imaging characteristics.

The parameters were selected from parameter sets used in previous AFIT 1-D simulations. The earlier AFIT researchers chose their parameters from published BSO values and from values estimated for the PRIZ by previous experimenters in the open literature (4:750-752). The AFIT parameter set chosen was the one that showed the quickest fall-off in the longitudinal integral of the transverse fields.<sup>15</sup>

In the 2-D simulation, the selected set ran slowly in terms of computer runtime. This work tested a series of parameter variations until a set was found that created a peak in diffraction efficiency in under 40 ms. This set of parameters was a starting set for the body of the investigation and is identified in this chapter as the standard operating point. The set showed a peak in output at 7 ms. It also ran for over an hour on a 66 MHZ 486/DX2 and about 15 minutes on a Sun SPARC 20 (using the UNIX code created later) to reach a simulated time of about 80 ms. This was more than fast enough to produce a large number of simulations for extensive analysis.

During coding, testing, and debugging, the work always emphasized producing software to handle parameter sets (devices) that displayed fast self-erasure. Thus, the code was not

---

<sup>15</sup> The AFIT 1-D model estimated the transverse fields by assuming a sinusoidal charge distribution in the transverse direction.

designed to simulate the minutes or hours of real-time that would be needed for long-term storage. The 10 second observation period reported in some Soviet papers could be simulated with multi-week or longer runs.

Thus, the code produces results for devices operating for 10's or 100's of milliseconds, and is capable of handling reasonable deviations in parameters about the standard operating point:  $I_o=10 \text{ W/m}^2$ ,  $m=0.9$ ,  $v_x=2 \text{ lines/mm}$ ,  $\lambda_w=488 \text{ nm}$ ,  $V=1 \text{ kV}$ ,  $d=1 \text{ mm}$ ,  $\alpha=1000 \text{ m}^{-1}$ ,  $n_s=1.38 \cdot 10^{18} \text{ m}^{-3}$ ,  $\mu=10^{-6} \text{ m}^2/\text{V/s}$ ,  $\xi_t=5 \cdot 10^{18} \text{ s/m}^3$ ,  $\xi_d=10^{22} \text{ s/m}^3$ ,  $\xi_{td}=\infty \text{ s/m}^3$ ,  $\tau_t=10 \text{ s}$ ,  $\eta=1$ ,  $N_t=10^{22} \text{ m}^{-3}$ ,  $N_d=2.76 \cdot 10^{24} \text{ m}^{-3}$ , and  $\epsilon=4.43 \cdot 10^{-10} \text{ F/m}$ .

In the set of parameters comprising the standard operating point, the trap to donor recombination coefficient of infinity is created by a flag that deletes the trap to donor recombination expression from the rate equations. The peak intensity of  $10 \text{ W/m}^2$  is a compromise between reducing the runtime required to see a peak followed by self-erasure in diffraction efficiency and limiting the exposure to avoid theoretical crystal damage (45:21). The spatial modulation frequency was chosen to provide a high diffraction efficiency (3:69) while meeting numerical grid and crystal size limitations in the code. The trap recombination coefficient produces an initial electron lifetime of  $\tau=0.5 \text{ ms}$  which is half a transit time. The absorption coefficient is probably lower than that found for most experimental write-beams wavelengths. The above parameters effectively create almost no thermal ionization, donor recombination, or trap-to-donor recombination.

The continuous illumination output for the standard operating point is displayed in Figure 18. This output is a typical plot of first order diffraction efficiency versus time with limiting values shown on the appropriate axis.<sup>16</sup> The constant  $\eta_o = 6.25 \cdot 10^{-4}$  normalizes the diffraction

---

<sup>16</sup> Each figure caption specifies a parameter set name, e.g., b32. This name refers to a specific set of values characterizing the device and its various physical processes and mechanisms.

efficiency.<sup>17</sup> This and later plots show the peak value of dominance within the plot.<sup>18</sup> If the dominance changes sign during a simulation, additional local peak or end-point dominance values are annotated. This allows the reader to know whether a run is p- or n-dominant, how large the peak dominance is, and whether phase reversals occur during the time shown.

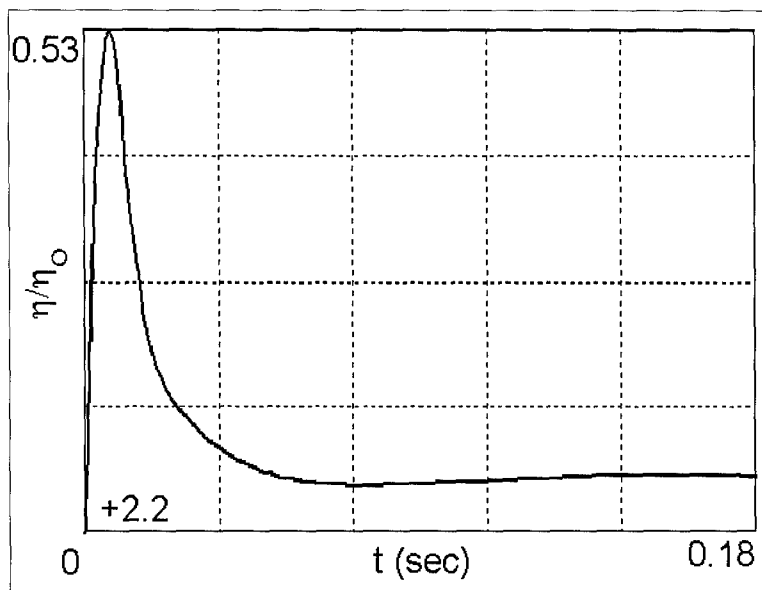


Figure 18. First order diffraction efficiency versus time for the standard operating point. The normalizing diffraction efficiency is  $\eta_0 = 6.25 \cdot 10^{-4}$ . Peak dominance is  $\delta = +2.2/(100 \cdot 65) = 3.4 \cdot 10^{-4}$ . The grid is 65x65. (b32)

As a reminder, the expression for dominance (Equation (28) on page 24) is

---

A figure may show a sequence of simulations (plots) that model variations from the parameter set either by varying parameters or deleting mechanisms in the model. The caption identifies or quantifies the mechanism or parameter variation, respectively. For any figure, the parameter values that do not change are found in Appendix A.

<sup>17</sup> The value of  $\eta_0$  is arbitrary, but it keeps the plot labeling simple and easy to compare.  $\eta_0 \equiv 0.04/N$  with  $N = 64$ , the typical number of points in the FFT.

<sup>18</sup> Dominance values provided on the plots are scaled by  $100N$  to keep the number of digits encumbering the plots to a minimum.  $N$  is the number of grid points in either direction, and is always 65 in the text. Thus a dominance value plotted as +2.2 is really  $\delta = 2.2/(100 \cdot 65) = 3.38 \cdot 10^{-4}$ .

$$\begin{aligned}\delta(t) &= \frac{2\pi n_o^3 r_{41}}{m\lambda_r} \sqrt{\frac{2}{3}} \sum_{i=1}^m \left[ c(x_i) \int_0^d E_x(x_i, z, t) dz \right] \\ &\approx \pm \frac{2\pi n_o^3 r_{41}}{\lambda_r} \sqrt{\frac{2}{3}} \left| \int_0^d E_x(x_i, z, t) dz \right|_{ave}\end{aligned}\quad (39)$$

This expression defines dominance as an average of the longitudinal integrals of the transverse electric field (1/m times the sum of m integrals). The second expression uses a  $\pm$  sign to show that the result may be either positive or negative. When the sign is positive, the device is p-dominant. When the sign is negative, the device is n-dominant.

### Essential Physical Mechanisms

Although the model in this work accounts for most of the physical processes one would expect to affect the device's performance, the comparable models used in the literature omitted several of those physical processes – processes known to occur in a real device (3; 4). Thus, it is logical to question whether the omission of those processes significantly affects the predicted output. The following paragraphs show that the omission by Bliznetsov et al. of transverse drift and exponential absorption, both known to occur in the PRIZ, results in predictions that are not quantitatively correct (4:750-754).

The predecessor to the model used in this work was the mathematical theory developed by Shlyagin et al. (3) in 1985 and Bliznetsov et al. (4) in 1987. Their mathematical results were not limited to the linear region of operation of the PRIZ or to a linear index of refraction distribution. However, Shlyagin et al.'s and Bliznetsov et al.'s models do not include all of the physical processes used in this work's model or all of the physical processes known to occur in real devices.

The mechanisms used by Shlyagin et al. (3) and Bliznetsov et al. (4) are photogeneration of electrons, longitudinal drift, trapping, injection of electrons across the cathode, and uniform

absorption.<sup>19</sup> They also assumed a constant potential across the electrodes. Equation (36) on page 53 illustrates their final expressions. Mechanisms such as exponential absorption, transverse drift, diffusion, thermal ionization of traps, and donor recombination were excluded. Bliznetsov et al. further assumed that the time rate of change of the free electron density,  $\partial n_e / \partial t$ , is zero, and that the net charge distribution is a positive step region adjacent to the cathode (4:752), resulting in the equation

$$\begin{aligned}\rho(x,t) &= e t \left( g(x) - \frac{n_s}{\tau} \right) H(z_o(x,t) - z) \\ &= e t g_o \left( 1 + m \cos(kx) - \frac{n_s}{g_o \tau} \right) H(z_o(x,t) - z)\end{aligned}\quad (40)$$

where  $g = g_o(1 + m \cos(kx))$ ,  $g_o = I_o \alpha \eta / h \nu_w$ ;  $H$  is the Heavyside function; and  $z_o$  is the longitudinal extent of the positive step region at transverse location  $x$  and time  $t$ .

Bliznetsov et al. imposed the following inequality which guarantees, by making the right-hand side of Equation (40) positive, that their assumption of a positive step charge near the cathode is valid for every transverse location during continuous illumination (4:753):

$$1 - m \geq \frac{h \nu_w n_s}{I_o \alpha \eta \tau} \quad (41)$$

While this inequality is consistent with their assumed charge distribution, the inequality limits the theory's mathematical predictions by artificially restricting the choice of parameter values.

The remainder of this section will evaluate the significance of the omissions and assumptions in the mathematics of Bliznetsov et al. by comparing the output of their theory

---

<sup>19</sup> Uniform absorption is modeled when the photogeneration term in Equation (2) does not include the  $e^{-\alpha z}$  expression. Do not confuse uniform absorption with a constant absorption coefficient, i.e.,  $\alpha = \text{constant}$ . Hereafter, when reference is made to adding exponential absorption to the rate equations, the  $e^{-\alpha z}$  expression is included in Equation (2).

(Equation (36) on page 53) with the output from the 2-D numerical model in Chapter II. The model in Chapter II includes several of Bliznetsov's omitted processes, and contains no assumptions of charge distribution or rates of change in the free electron density. Hence the model in Chapter II represents a more complete and accurate simulation of the PRIZ than the earlier model by Bliznetsov et al. (4).

The comparison starts by selecting a common parameter set for both sets of calculations (models). To satisfy the inequality in Equation (41), the standard operating point was altered with a modulation index of  $m = 0.74$  and an absorption coefficient of  $\alpha = 800 \text{ m}^{-1}$  (set b64). The standard operating point uses an electron lifetime equal to half the initial transit time, the same ratio suggested by Bliznetsov et al. (4:752). The modulation index, 0.74, is the largest value that satisfies Equation (41). The extremely low absorption coefficient,  $800 \text{ m}^{-1}$ , corresponds to a write-beam wavelength of 488 nm in BSO (15:233). The low absorption coefficient also creates a slow exponential decay of the transmitted write-beam that is as close as practical to the uniform absorption assumed by the model of Bliznetsov et al. (4).

The output of the two models is shown in Figure 19. The prediction of Bliznetsov et al. (Equation (36) on page 53) is shown in Figure 19a, a plot of first order diffraction efficiency versus time. Figure 19b shows the results of the model in Chapter II, where the rate equations are modified to include *only* photogeneration, uniform absorption, trapping, longitudinal drift, and injection. This is the complete set of processes used in Bliznetsov et al.'s mathematics (4), but without their incorrect assumptions of a positive step charge distribution and a time independent free electron distribution. Figure 19c shows the result of adding transverse drift to the set of processes in the rate equations. Figure 19d shows the effect of adding the exponential absorption. Both processes are known to exist in the PRIZ. Figure 19 shows that both processes have a significant effect.

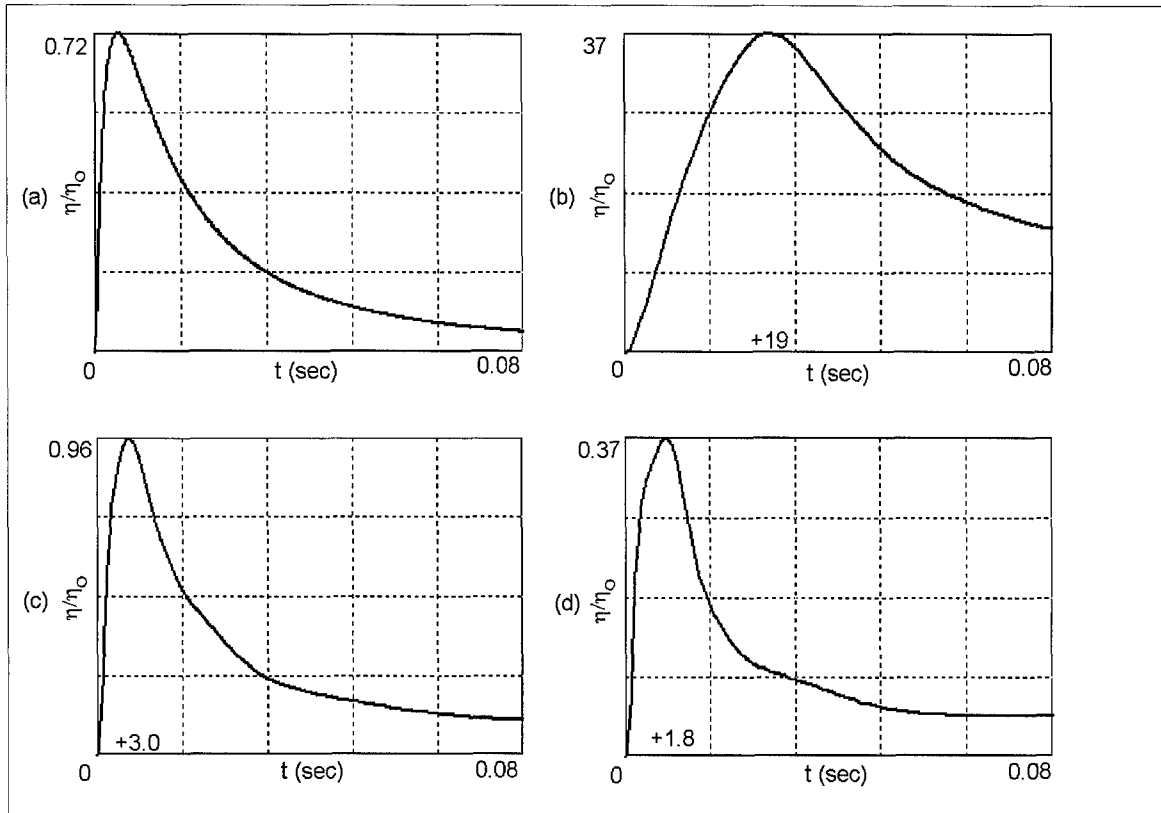


Figure 19. Sensitivity of the simulation to physical mechanisms. (a) Bliznetsov mathematical prediction (4:753), (b) 2-D numerical simulation using only Bliznetsov's mechanisms, (c) 2-D simulation adding transverse drift, and (d) 2-D simulation adding exponential absorption. Mechanisms are added to the 2-D simulation by changing the rate equations (b64)

One might expect the calculation by Bliznetsov et al. in Figure 19a to be very similar to the numerical 2-D calculation in Figure 19b that uses the same physical mechanisms. However, Bliznetsov et al. approximate the charge distribution as a positive step adjacent to the cathode, ignoring any charge beyond their  $z_0$ . The actual distribution is positive throughout much of the device, not just adjacent to the cathode, and is of significant amplitude beyond  $z_0$ . Thus within the interior of the device ( $z > z_0$ ), significant positive fields exist and grow over time that are not taken into account by Bliznetsov et al. These fields continue to grow after Bliznetsov's charge distribution collapses to the cathode and produces the fall in Figure 19a. The growing fields in the center of the device produce the higher diffraction efficiency in Figure 19b.

The addition of the processes of transverse drift and exponential absorption in Figure 19c and 19d were selected for two reasons. First, both processes exist in a real device. The transverse fields must cause transverse drift of the electrons. Also, the exponential dependence of photogeneration in the longitudinal direction from a 440 nm write-beam in BSO with its absorption coefficient of  $3500\text{ m}^{-1}$ , is far from uniform (15:233). The second reason these two processes were chosen is that they can be easily characterized. The transverse drift term does not depend directly on any new or unknown parameters, although the transverse drift's local magnitude will depend on all the other processes that affect the local charge distributions. The absorption coefficient is well characterized from numerous investigations reported in the literature. In contrast to these two processes, the remaining physical processes in this work's model (see Equations (2) and (3) on page 14) depend on parameter values that are not known. Since the rates of those processes, e.g., donor recombination and thermal ionization, are not known, it was not reasonable to make their inclusion or exclusion a factor in analyzing the completeness and accuracy of Bliznetsov et al.'s mathematics (4).

Returning to the comparison, Figure 19c shows that adding transverse drift causes the output to peak sooner and at a much lower value than in Figure 19b. The transverse drift causes electrons to flow towards the positive charge regions (in the x direction) while they flow towards the anode. The result is zero or negative charge in the interior of the device where significant positive charge exists when no transverse drift occurs. The absence of the interior positive charge peaks in Figure 19c causes opposite (from the fields near the cathode) or zero fields in the interior that produce a much smaller output. With transverse drift limiting fields in the interior of the device, processes associated with charge and fields near the cathode cause the output to peak much sooner in Figure 19c (see the section on page 68). The diffraction efficiency at 4 ms in Figure 19b is only about 6 times larger than at 4 ms in Figure 19c. However, since Figure 19b continues to



rise for a longer period, the difference eventually reaches a large factor of about 39.

Adding an exponential dependence to absorption produces Figure 19d. With less photons absorbed, fewer ionized donors are produced. This results in smaller charge densities, fields, and diffraction efficiency. The reduction in the total absorption produced by the relatively low  $800\text{ m}^{-1}$  absorption coefficient produces the relatively small, but significant, change from Figure 19c.

Thus, Figure 19 shows that the approximation used for the charge distribution by Bliznetsov et al. neglects significant positive charge in the body of the device. Figure 19b shows the result when that positive charge is not ignored. When transverse drift is added to the set of physical mechanisms (Figure 19c), most of that interior positive charge is neutralized and the output drops to something near the estimate of Bliznetsov et al. in Figure 19a. Adding exponential absorption further reduces the amount of positive charge and the output (Figure 19d).

### **Range of Typical Output**

After comparing this effort's model with its predecessor (4), a sensitivity analysis was run near the standard operating point (see the data in Appendix D). In this section, plots of general output from that analysis (see Table 2) will demonstrate the range of behavior achievable with the simple band model and the numerical code. Each type of behavior will be explained in terms of changes in the internal charge and field distributions. To make that explanation easier to understand, a brief introduction explains the device's internal dynamics.

**Internal Dynamics.** Before presenting the plots of diffraction efficiency versus time, it will be useful to explain the internal charge and field dynamics that drive the output. Figure 20 shows the net charge distributions after two and nine transit times (one transit time is one millisecond) for the standard operating point. the input intensity distribution at the cathode was sinusoidal, and the output diffraction efficiency peaked at seven transit times. The plots are normalized to their maximum and minimum values to show as much detail as possible.

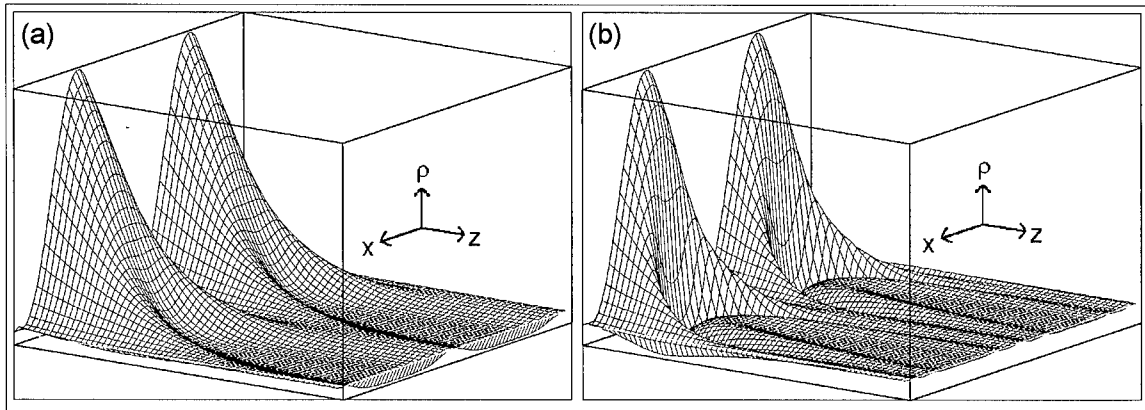


Figure 20. Evolution of the net charge density for the standard operating point. The distributions are at (a) 2 ms and (b) 9 ms. The initial electron transit time is 1 ms. The charge densities ranges in (a) from -0.8 to +5.9 and in (b) from -6.2 to +70.0 in normalized units ( $n_0$ ). (b32)

Photogeneration and drift create the initial charge distribution seen in Figure 20a.

Photogeneration produces positively ionized donors and free electrons. The donors are immobile; the electrons initially drift toward the anode in the longitudinal electric field due to the external voltage and are trapped after an electron lifetime ( $\tau$ ). The resulting separation of charges creates the two large positive peaks in Figure 20a near the cathode and the much smaller negative peaks from filled traps near the anode. The shapes of the distributions reflect the transverse sinusoidal input and the longitudinal exponential absorption curve ( $\alpha d = 0.8$ ). After only two transit times, distortion is already seen in the differing z-coordinate of the transition from positive to negative charge. Thus, even this early, the simulation is no longer linear.

As time proceeds, photogeneration creates larger and larger positive and negative peaks. The growing positive peaks create larger fields that in turn increase injection of electrons across the cathode and transverse drift of the free electrons. Both mechanisms result in electrons moving toward the positive peaks. The presence of the increased electron densities at the peaks increases trapping at the positive peaks and generally slows down the growth of those peaks.

As the positive and negative charge separates longitudinally, a minima is created in the longitudinal electric field; the field becomes smallest near the transition region between the positive and negative charge (see Figure 21). The smaller fields in that region result in slower moving electrons and thus more trapping in the transition region. These additional trapped negative charges force the transition region away from the anode; the net positive region is effectively compressed towards the cathode. This effect is observed in comparing Figure 20a and Figure 20b. The longitudinal electric field also forces electrons into the device across the cathode and out of the device across the anode.

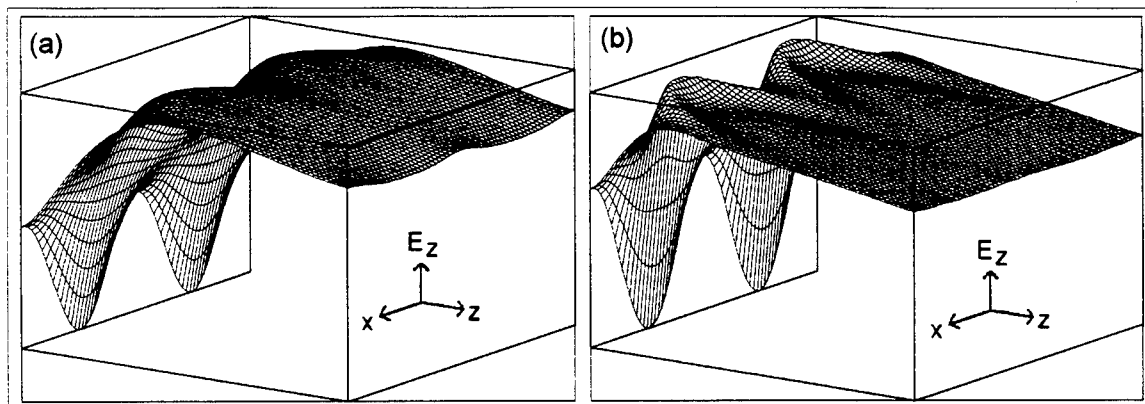


Figure 21. Evolution of the longitudinal electric field distribution for the standard operating point. The distributions are at (a) 2 ms and (b) 9 ms. The initial electron transit time is 1 ms. The longitudinal field ranges in (a) from -2.5 to -0.74 and in (b) from -4.4 to -0.24 in units of the initial longitudinal field ( $E_0 = V/d$ ). (b32)

Transverse drift does not affect only the positive charge region; it also exists in the negative charge region. Near the negative peaks, the transverse fields force the electrons away from the regions of large negative charge densities and toward the valleys between the peaks. In time, this slows down the growth of the negative peaks and increases the negative charge in the valley region.

Since the output electric field distribution is proportional to the longitudinal integral of the transverse fields (see Appendix H), it is also important to have some understanding of the

transverse fields created by the changing net charge distributions. Figure 22 shows the transverse electric field distributions at the same times as the net charge distributions in Figure 20. The transition between the field generated in the positive and negative charge regions moves towards the cathode in Figure 22 just as it does in Figure 20.

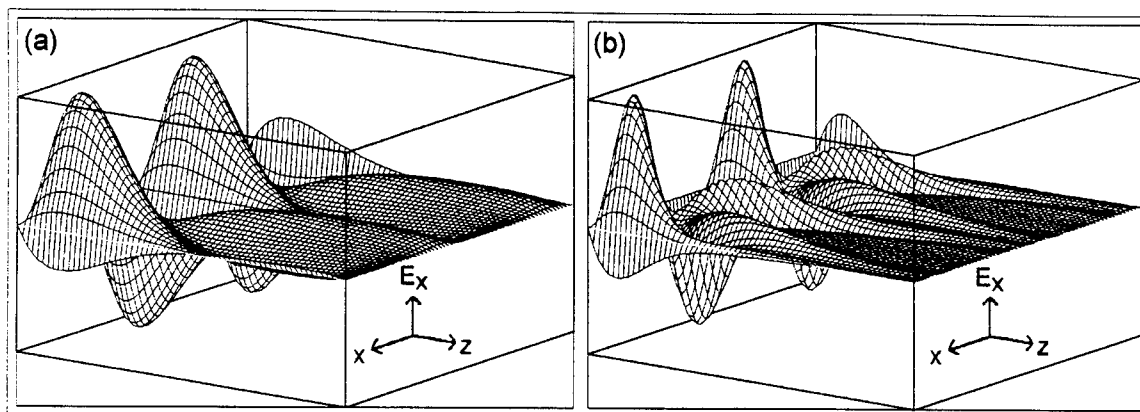


Figure 22. Evolution of the transverse electric field distribution for the standard operating point. The distributions are at (a) 2 ms and (b) 9 ms. The initial electron transit time is 1 ms. The transverse field ranges in (a) from -0.25 to +0.25 and in (b) from -0.55 to +0.55 in units of the initial longitudinal field ( $E_0 = V/d$ ). The transverse fields are zero at both electrodes. (b32)

The shapes of the fields in Figure 22a suggested the definition for dominance. Because of the periodicity, if one creates four equal sized slices perpendicular to the electrodes (from left to right in Figure 22), and then one flips over alternating slices to produce four identical slices (via the sign function,  $c(x)$ , in Equation (27)), the result is four large positive peaks near the cathode and four smaller negative peaks near the anode. Given that the output field is proportional to the longitudinal integral of the transverse field, and that the positive charge region's and negative charge region's contribution to the integral are of opposite signs, either the positive charge region or the negative charge region must dominate the integral and the output. In a device characterized by the standard operating point, the positive charge region dominates the output.

There is one additional significant effect, called charge mirror imaging, associated with the transverse fields near the cathode. An equipotential surface or an infinite conducting plane

(e.g., each electrode) affects the electric fields that arise from nearby charges. An equivalent way of looking at the effect of the conducting plane on the charge's electric field is to position a charge of opposite sign and equal magnitude at a mirror image location and then remove the conducting plane. That is, the electric field distribution produced by a charge and its mirror image is the same as that produced by a charge and the infinite conducting plane. By definition, a line from the original charge to its mirror image is bisected at right angles by the infinite conducting plane. The electric field at any point near the conducting plane is found by vector addition of the electric fields created by the charge and its mirror image in the absence of the conducting plane. The vector sum reduces the size of the transverse fields close to the conducting plane, and makes the transverse fields zero on the plane. Thus, when the positive charge region is compressed toward the cathode, charge mirror imaging reduces the size of the transverse fields and the positive charge region's contribution to dominance and the output. The code implicitly produces this effect when the Full Multi-Grid enforces its equipotential boundary conditions at the electrodes.

**Typical Output in Terms of the Internal Dynamics.** Each figure shown in this section, see Table 2, plots first order diffraction efficiency along the ordinate (y-axis) and time along the abscissa (x-axis). Since the plots are representative of only general behavior, the numerical values for the axes are not provided. The parameter sets for each simulation are near the standard operating point and thus do not include significant donor recombination, thermal detrapping, or trap-to-donor recombination.

In order to show and explain a representative sample of the observed behavior, it is necessary to show devices that are both p- and n-dominant. Although there are many ways to achieve n-dominance, the method used here was to reduce the electron lifetime from 0.5 transit times to 0.05 transit times. This operating point will be called the alternate operating point.

Table 2. Illumination and dominance combinations for typical output

<b>Figure</b>	<b>Illumination</b>	<b>Dominance</b>	<b>Operating Point</b>
Figure 23	continuous	p	standard
Figure 24	continuous	$p \rightleftharpoons n$	standard + $I_0=6 \text{ W/m}^2$ , $\alpha=3500 \text{ m}^{-1}$
Figure 25	continuous	n	alternate
Figure 26	continuous	$n \rightleftharpoons p$	standard + $\xi_t=10^{18} \text{ s/m}^3$
Figure 27	late turnoff	p	standard + $\tau_t=0.1 \text{ s}$
Figure 28	early turnoff	$p \rightleftharpoons n$	standard + $\tau_t=0.1 \text{ s}$
Figure 29	late turnoff	n	alternate + $\tau_t=0.1 \text{ s}$
Figure 30	early turnoff	n	alternate + $\tau_t=0.1 \text{ s}$

Since the output is different for p-dominance versus n-dominance, for continuous versus pulsed illumination, and for early versus late turnoff in pulsed operation, a complete exposé requires six plots. Another two plots show transitions from low p- to n- dominance and low n- to p-dominance during continuous illumination. These transition plots require variations from the standard operating point as shown in Table 2.

In Table 2, the pulsed or turnoff cases use a trap lifetime of 0.1 second instead of the 10 seconds in the standard or alternate operating points. This variation was selected merely to enhance the change seen after turnoff, e.g., the reintensification peak in Figure 27 is larger than it is in a run with  $\tau_t = 10$  seconds.

The first plot, Figure 23, shows a p-dominant device under continuous illumination where the positive net charge peaks control the device. The output rises, peaks, and then self-erases.

The initial rise in the output is caused by the quickly growing positive charge peaks near the cathode. Increasing injection and transverse drift force electrons to the positive region's peaks where increased trapping slows down the growth in the peaks. Compression of the positive region

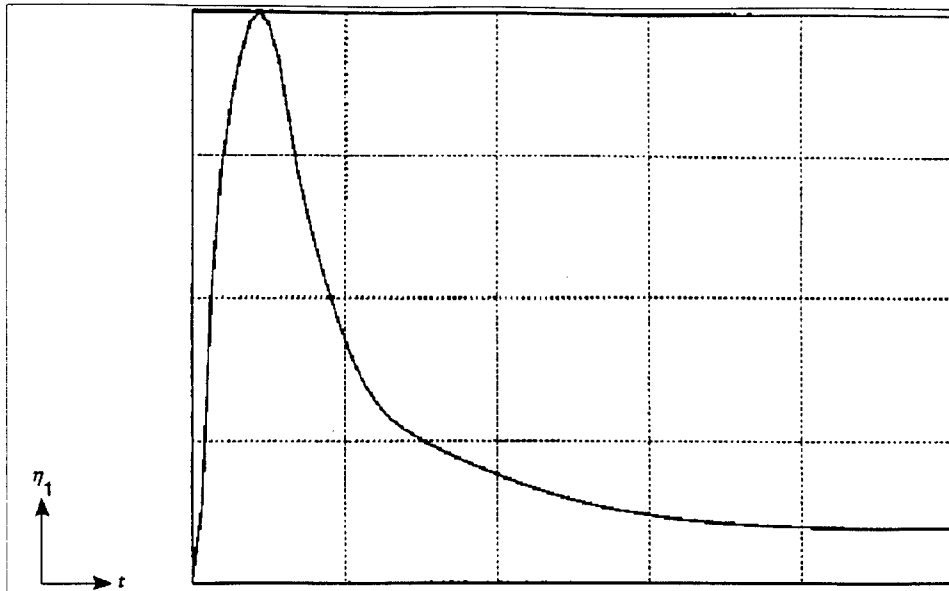


Figure 23.  $\eta_1$  vs  $t$  for large p-dominance during continuous illumination. (b32)

toward the cathode continually reduces the positive charge region's contribution to dominance. This compression of the positive region and charge mirror imaging at some point become significant enough to cause the positive charge region's contribution to dominance to peak and begin falling. At no time in this simulation is the contribution from the negative charge region significant.

The primary factors in the final self-erasure seem to be the motion of the charge boundary toward the anode combined with charge mirror imaging. When the simulation restricts the positive charge to one grid point adjacent to the cathode, the results become questionable. This occurs near the last 25% of this run.

Figure 24 shows a smaller initial p-dominance. The same mechanisms operate here as in Figure 23 during the initial rise, peak, and fall. However, the positive charge region's dominance falls far enough that a phase reversal or change in the sign of the dominance occurs, and the negative charge region becomes dominant. The primary factor in the fall again appears to be the motion of the charge boundary toward the cathode. Because the *square* of dominance is roughly

proportional to first order diffraction efficiency, a smooth shift of dominance from a positive value through zero to a negative value corresponds to a fall to zero and a reintensification in diffraction efficiency.

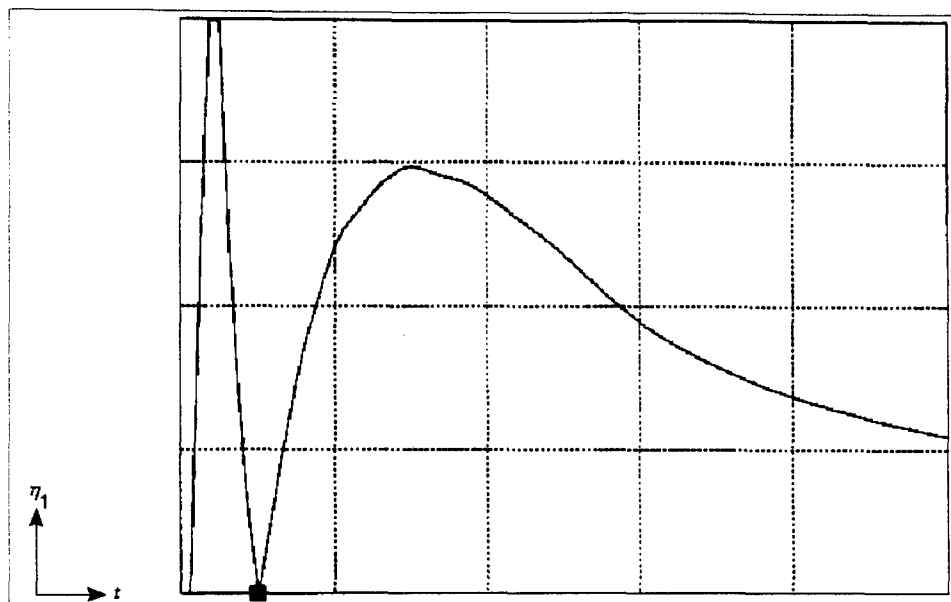


Figure 24.  $\eta_1$  vs  $t$  for small p- to n-dominant shift during continuous illumination. The square, ■, indicates the time of the change from positive to negative dominance. (b45)

The new phenomenon in Figure 24 is actually the peak and fall in the output after the phase reversal. When the dominance indicated a phase reversal, the negative charge region became dominant. By the time of the second peak, the positive region's contribution is nearly steady-state but is not yet limited to the first bin, while transverse drift has stopped the negative peaks from rising and has increased the negative charge in the negative region's valleys. The continued rise in the negative region's valleys drives the final self-erasure in Figure 24.

When the parameters create an initial n-dominance, the result is similar to that shown in Figure 25 for the alternate operating point. The short electron lifetime of the alternate operating point causes this effect by creating relatively small positive peaks near the cathode that allow the



fields from the negative charge region to dominate the device. The output rises as trapping creates increasingly larger charge peaks in the negative charge region. The peak and subsequent self-erasure occur when the negative peaks stop rising and the negative valleys start filling.

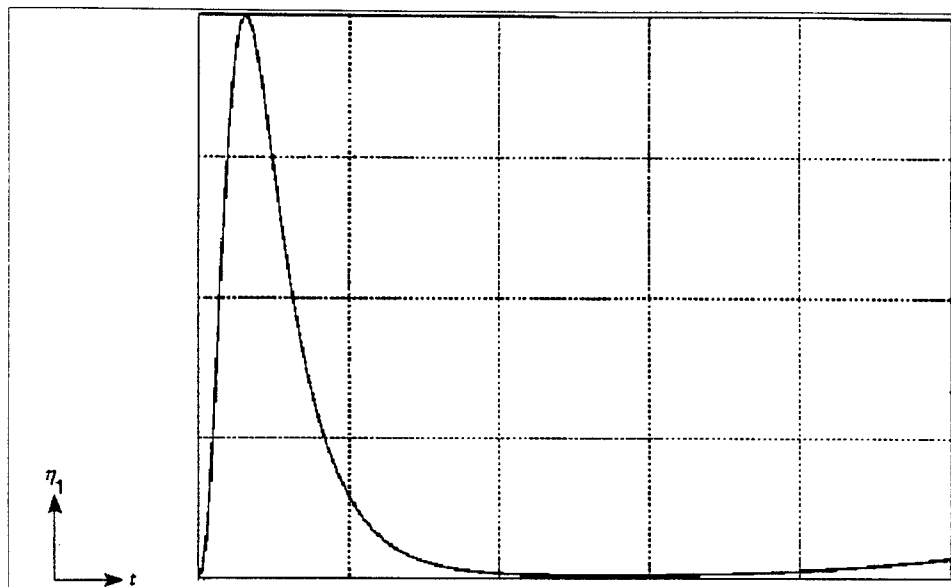


Figure 25.  $\eta_1$  vs  $t$  for large n-dominance during continuous illumination. (b36)

Figure 26 shows another small dominance transition during continuous illumination, this time from n- to p-dominance (versus the p- to n-dominance shift of Figure 24). The primary mechanisms causing the rise and fall in the output are the same as those in the strong n-dominance plot of Figure 25. The difference here is that the positive charge region's contribution to the dominance is large enough that as the negative region's contribution falls, the output falls through a zero dominance level. The change through the zero dominance level causes a phase reversal and, of course, the zero diffraction efficiency in Figure 26.

Turning off the write-beam illumination creates additional types of behavior. Figure 27 shows a device that is p-dominant while the illumination is on. The simulation turns off the write-

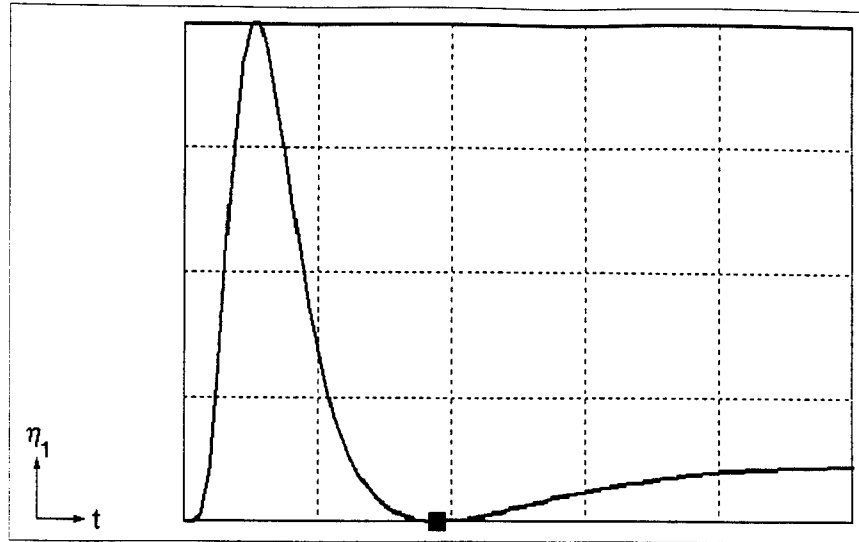


Figure 26.  $\eta_1$  vs  $t$  for small n- to p-dominant shift during continuous illumination. The square, ■, indicates the time of the change from negative to positive dominance. (b28)

beam at a relatively late time.<sup>20</sup> The same processes described above for Figure 23 control the device while the write-beam is on.

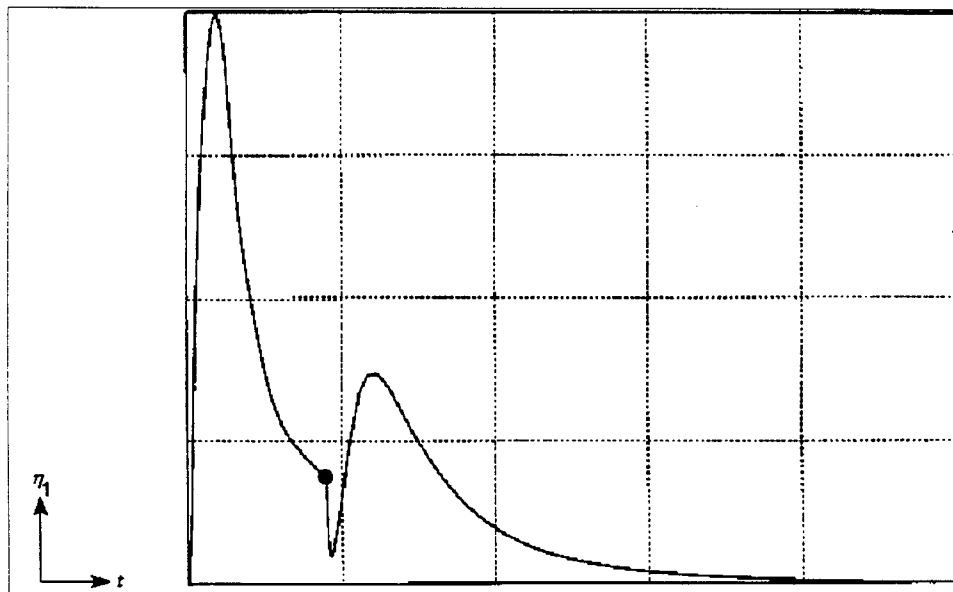


Figure 27.  $\eta_1$  vs  $t$  for p-dominance during pulsed operation, late turnoff. The circle, ●, indicates the turnoff time. No phase reversal occurs. (b48)

<sup>20</sup> A late turnoff occurs when the write-beam is turned off after the output has peaked and fallen to less than 50% of the peak value. Of course, early turnoff is any write-beam turnoff before that time. In the cases here, early turnoff is before the output peak.

When the illumination stops, a number of interesting things happen. Photogeneration ceases immediately. Without absorption, the device creates no more positive donors or photogenerated free carriers. However, injection and transverse drift still occur. Electron trapping also continues. It is trapping that creates the initial transient. When the user turns off the write-beam, the delicate balance between the positive donors and negative traps is upset. Suddenly, trapping still occurs, but donor generation does not, and the net negative contribution quickly increases. This shows up as a trapping transient; e.g., the short, steep drop in diffraction efficiency immediately after the turnoff in Figure 27.

Since the electron lifetime is much shorter than the trap lifetime, detrapping or thermal ionization will become significant at a time later than the initial trapping transient. The electrons leave filled traps, drift toward the anode, and refill new traps or leave the device through the anode. The flow of electrons toward and through the anode exposes a larger positive charge near the cathode and causes the reintensification seen in Figure 27. Injection of electrons across the cathode starts falling when photogeneration ceases, no longer offsetting the electron ejection through the anode. After trapping and detrapping reach an equilibrium (final peak region), and injection and drift slow down, the ever diminishing supply of free electrons slowly fills traps to create the final self-erasure.

When the user turns off the write-beam earlier, as in Figure 28, the positive donor and negative trap densities are not yet much larger than the free electron density. Thus, the initial trapping transient has a much larger relative impact on the output. In Figure 28, the transient is large enough that a phase reversal occurs (the zero value followed by reintensification). In this simulation, electron drift through the anode and detrapping effects cause the final self-erasure. The directions of the shifts in dominance (not diffraction efficiency) are similar to those of Figure

27, but the device state at the turnoff this time is a much smaller p-dominance so that the trapping transient creates a phase reversal. Because of the early turnoff, which results in relatively few charged donors, traps, and carriers, no other effects follow the final self-erasure.

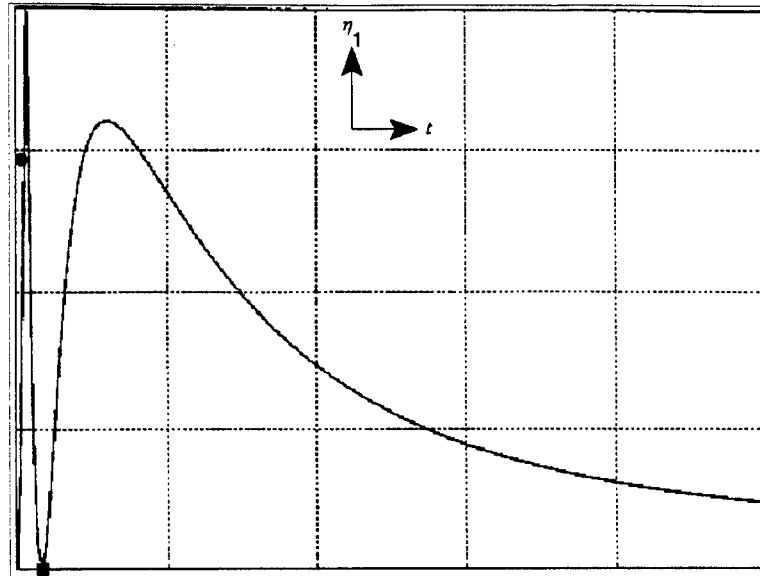


Figure 28.  $\eta_1$  vs  $t$  for p-dominance during pulsed operation, early turnoff. The circle, ●, indicates the turnoff time; the square, ■, indicates the time of change from positive to negative dominance. (b48)

When the device is n-dominant during continuous illumination, one observes a different behavior. The most significant difference is that the initial trapping transient, instead of creating a fall in the output, causes an immediate rise in the output. As before, the trapping transient causes a shift toward n-dominance, but now it starts from a net n-dominant state. Figure 29 shows the intensification from trapping followed by a self-erasure for an n-dominant device. In this situation the negative peaks are large enough that drift continues to reduce the negative charge region's contribution. This reduction plus detrapping creates the final self-erasure.

Figure 30 shows an n-dominant device when the user turns off the write-beam early, before the physical processes create relatively large donor and trap densities and before the

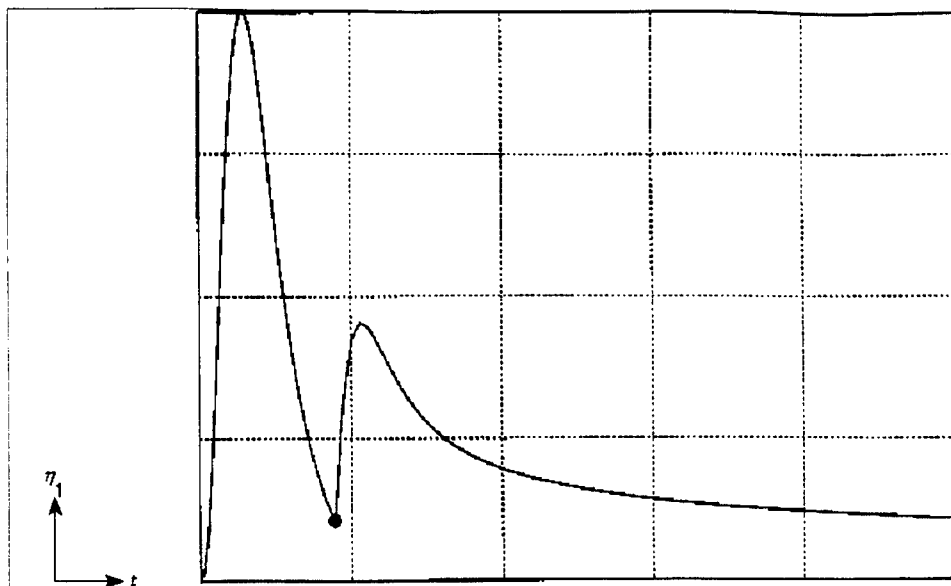


Figure 29.  $\eta_1$  vs  $t$  for n-dominance during pulsed operation, late turnoff. The circle, ●, indicates the turnoff time. (b51)

continuous illumination peak occurs. The initial trapping transient causes the output to keep rising. Detrapping reverses the output and in this case creates the final self-erasure.

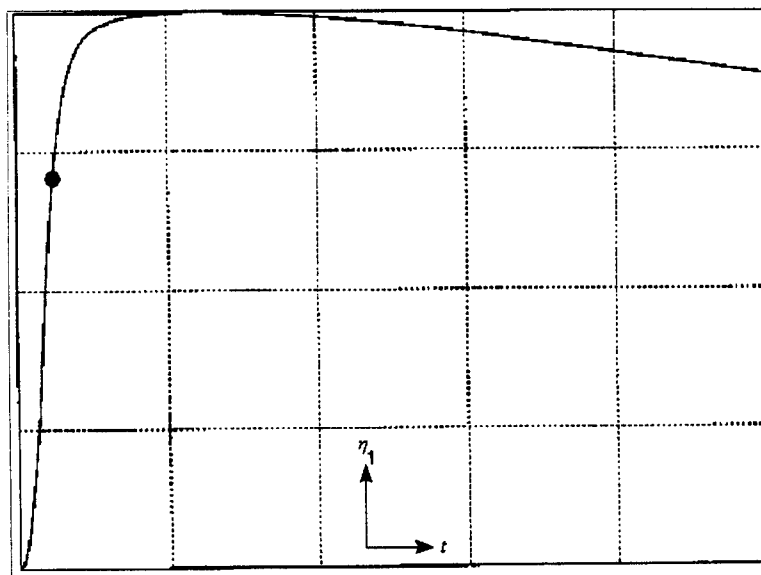


Figure 30.  $\eta_1$  vs  $t$  for n-dominance during pulsed operation, early turnoff. The circle, ●, indicates the turnoff time. (b51)

The literature is devoid of any report of several of the phenomena in the above simulations in either previous experiments or modeling. In particular, the literature reports neither the intensification after write-beam turnoff in n-dominant devices (see Figure 30) or the quick phase reversal and strong reintensification after early turnoff in p-dominant devices (see Figure 28). In addition, there are no reports of rapid short transients immediately after turnoff in  $\langle 111 \rangle$  PRIZ devices (as in Figure 29). Since each of these types of behavior distinguish the dominance state of the device, this knowledge could help researchers to evaluate new photorefractive materials.

### **Dominance Factors**

The brief explanations of the above phenomena used the concept of dominance between either the two charge regions or the integrals of the transverse fields from the two regions. Thus, dominance as described in the preceding section explains the output. But the analysis of the detailed sensitivity data also led to an understanding of the underlying factors that create the dominance states. Appendix B provides a detailed explanation of those factors; this section only summarizes that knowledge.

Dominance basically identifies whether the longitudinal integral of the transverse fields in the positive space charge region of the device or the negative space charge region dominates the output, i.e., which subintegral is the largest. Since larger charge concentrations tend to create larger fields, it is possible to associate larger subintegrals with larger net charge densities. Thus, if the positive charge near the cathode is much larger than the negative charge near the anode, the device should be p-dominant considering spatial extent and Gauss' law. As the charge and field distributions change, so will the dominance.

At least five significant factors affect the charge distribution and the dominance state: (1) the longitudinal slope of the positive donor distribution created by the absorption coefficient; (2)

the longitudinal separation between the positive donor and negative trap distributions created by longitudinal drift and the electron lifetime; (3) the growth rate of the negative trap distribution resulting from the electron lifetime; (4) the transverse variation in the positive donor distribution resulting from transverse modulation of the write-beam; and (5) the transverse distortion in the free electron distribution generated by transverse drift. The following paragraphs briefly touch on each of these.

A large absorption coefficient creates a large positive donor density near the cathode and a smaller density near the anode. A small absorption coefficient creates a more uniform positive donor density throughout the device. Considering that the external voltage source moves the generated free electrons toward the anode, devices with different absorption coefficients will show very different densities of exposed positive donors near the cathode. For a given input intensity, the large absorption coefficient produces a large positive charge and the small coefficient produces a smaller charge.

To get the charges separated, longitudinal drift of the free electron carriers plays an essential role. If the traps did not capture the electrons, the device would quickly become very positively charged. With an extremely short electron lifetime, the net positive charge is very small, ignoring injection at the cathode. The magnitude of the lifetime controls how wide the spatial separation between positive and negative net charges will become. Considering the longitudinal slope in the positive donor distribution created by the exponential absorption of photons, it is obvious the longer separation creates larger net charges in the two regions.

The electron lifetime will have a second effect. A longer lifetime will result in fewer filled traps at a given location. Hence, the more slowly growing negative trap distribution will reduce the overall contribution from the negative charge.

Of course, the change in the *transverse* charge distribution is also important. That distribution originates with the transverse modulation of the write-beam. In this work, the write-beam modulation is typically sinusoidal. Thus, a larger modulation index will create a larger variation in the charge and larger fields, given the same modulation period.

Transverse drift can also affect the transverse charge distribution. The charge distribution directly creates the fields controlling transverse drift, so device parameters only *indirectly* control drift. However, the positive and negative charge regions shaped by the preceding four factors generate transverse fields that generally force electrons toward the net positive charge and away from the net negative charge. Thus, transverse drift reduces the net charge density in both the positive and negative space charge regions.

Clearly, the composite effect of all five factors will determine the particular dominance state and trajectory of diffraction efficiency for a given device and time. The above analysis was used successfully to predict the effects of changing selected parameters. Thus, the usefulness of dominance and the approximation that relates it to charge density distribution were confirmed.

### **Sensitivity to Parameters during Continuous Illumination (CW)**

The plots of typical output presented earlier in this chapter demonstrate that a numerical solution of the equations representing the simple band model can achieve a broad range of behavior. The plots in the earlier section comparing mechanisms showed the advantages of the numerical model over the mathematical approximation used in the literature. This section will describe the quantitative changes in performance that are achieved by varying the model's parameter values around the standard operating point in a sensitivity analysis. To allow comparison of the effects of individual parameter changes, only those simulations based upon the standard operating point (see Appendix A) are covered here. Once again, it is important to remember that the parameter set for this data effectively excludes thermal ionization, donor



recombination, or trap-to-donor recombination. If the reader is interested, Appendix D provides a more comprehensive presentation of the total set of simulations created in the sensitivity study.

Figure 31 shows the range of dominance values achieved by changing the model's parameters one at a time starting at the standard operating point. The selected ranges were chosen for a number of reasons. Since the recombination coefficients have little effect, they were varied until a change was observed. The trap lifetime range was selected from numerous simulations to show a wide variation in output; no values for trap lifetimes are reported in the literature. The absorption coefficient range slightly exceeds the numbers corresponding to possible write-beam wavelengths (15:233). The intensity and voltage ranges approximate those reported in multiple experiments in the literature. The injection coefficient, like the mobility, extends for about an order of magnitude to either side of the reported value for BSO (22:375; 15:234). The electron lifetime extends from a value four times that estimated in the literature (4:752 estimates the electron lifetime as half a transit time) to a time that lets the electron travel only 2/3 of a grid spacing on a 65x65 grid in the field imposed by the external voltage. Using those ranges, Figure 31 shows the effect each variable can have on the amplitude of the output and also shows whether the variable is capable of changing the dominance from positive to negative.

Clearly, most of the parameters have the potential to cause large shifts in the output. Also, in the operating region of this data, most of the combinations of parameters create p-dominant devices. The p-dominant devices also tend to create larger peak output. Finally, Figure 31 also shows it is also possible to create n-dominant devices with moderate changes to the absorption coefficient, the electron lifetime, or the intensity.

The magnitude of the dominance changes seen in Figure 31, e.g., the -1.1 to +2.2 (x 0.01/N) range caused by varying intensity, can change significantly when the operating point changes. Appendix B explains how changing the intensity, for a given modulation index, changes

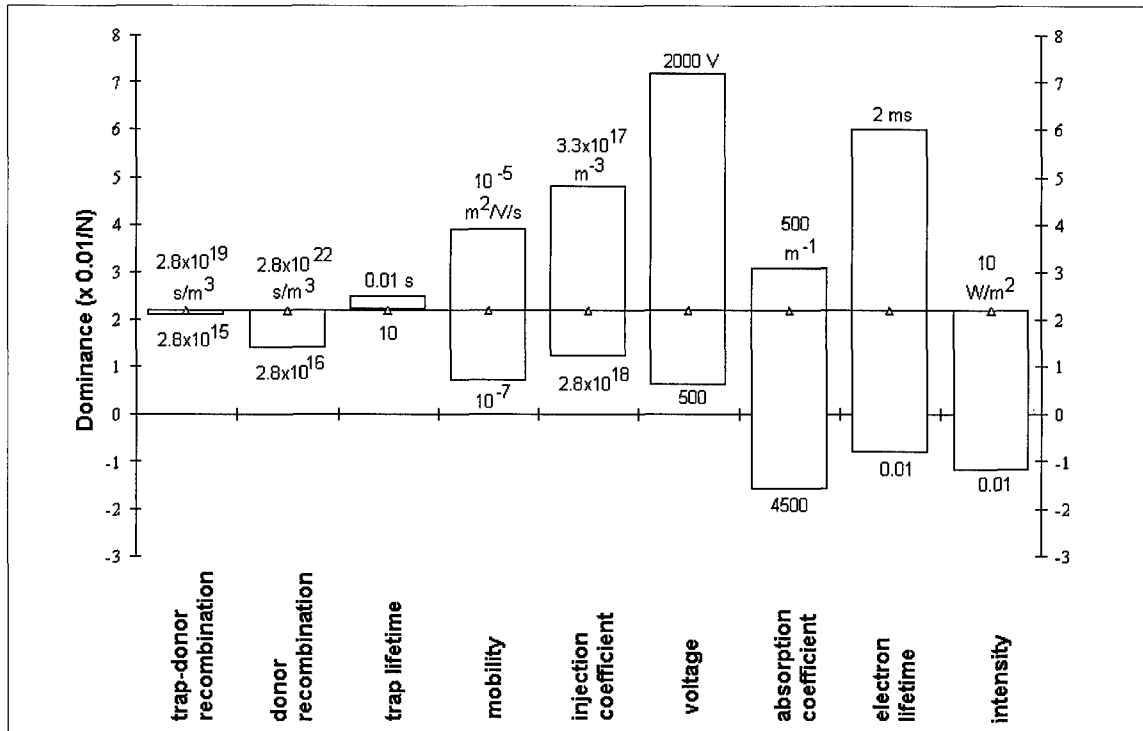


Figure 31. Range of dominance at peak output for changes in variables from the standard operating point (see Appendix D for detailed data). The triangles identify the parameter values for the standard operating point, which produces a dominance of  $2.2 \cdot (0.01/N) = 3.38 \cdot 10^{-4}$ . Variable limits are annotated on the respective bar.

the variation in the transverse charge distributions. Without changing other parameters, higher intensity results in large positive charge densities and a shift towards p-dominance. That relationship between intensity and dominance was shown in Figure 31. Figure 32 shows the same range of intensity (0.01 to 10  $\text{W/m}^2$ ) for both the standard operating point and one where the absorption coefficient and write wavelength were changed to  $\alpha = 3500 \text{ m}^{-1}$  and  $\lambda_w = 442 \text{ nm}$ . The write-beam wavelength was adjusted to be more consistent with the new absorption coefficient.

The data in Figure 32 suggests that the modeler must carefully consider the effects of changing an operating point. The device may behave very differently in a new operating region where only a single parameter is changed. In the example here, changing the absorption coefficient produces an n-dominant device over the entire range of intensity. At 1000  $\text{m}^{-1}$  and 10

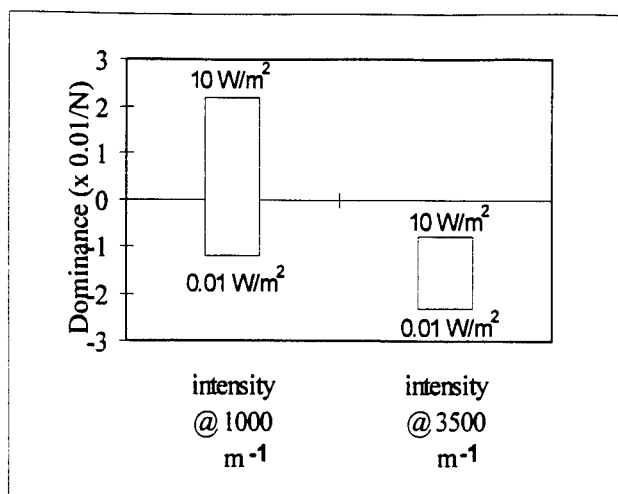


Figure 32. Range of dominance for a change in intensity at the standard operating point ( $\alpha=1000 \text{ m}^{-1}$ ) and a point where  $\alpha=3500 \text{ m}^{-1}$ .

$\text{W/m}^2$ , the p-dominant output could be expected to drop after an early write-beam turnoff because of the initial trapping transient's shift towards n-dominance. On the other hand, at  $3500 \text{ m}^{-1}$  and  $10 \text{ W/m}^2$ , one would see the output diffraction efficiency rise.

Figure 33 shows how the peak diffraction efficiency changed when the parameter values were doubled, one at a time, at the standard operating point. The direction of the change has been retained. None of the parameter changes resulted in a change from p- to n-dominance.

Changes in the trap-to-donor and donor recombination coefficients showed no significant effect on the amplitude of the output at the selected operating points. Since these recombination rates were very low to begin with at the standard operating point, this is not unexpected. The recombination rates at these values appear negligible compared to photogeneration and trapping.

Figure 33 shows that changes in the external voltage or the electron lifetime have large impacts at the standard operating point. This makes sense since both of these parameters dramatically affect the free electron distribution, which over time creates the negative trap distribution. Since the positive donor distribution changes little for a given input, the trap

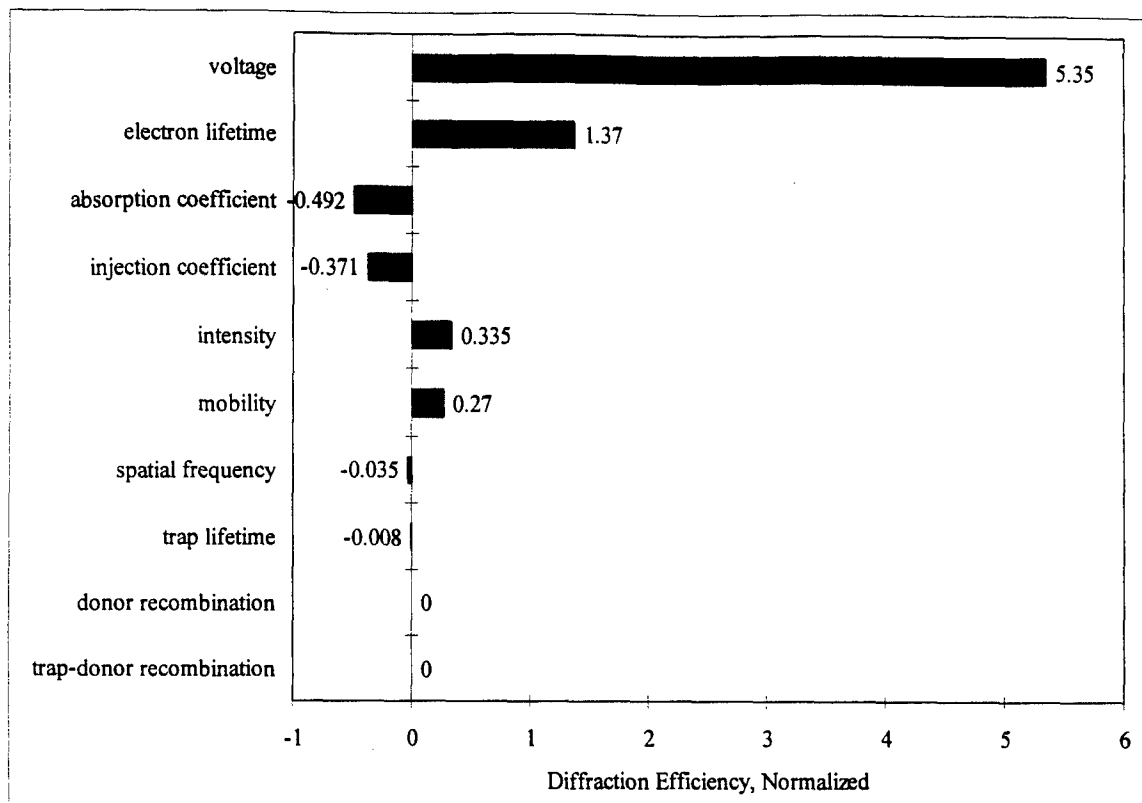


Figure 33. Change in peak diffraction efficiency (in  $\eta_0$ ) when the parameter values are doubled at the standard operating point.

distribution is the primary factor in modifying the electric fields, the indices of refraction, and the output diffraction efficiency.

Figure 34 shows how the timing of the peak output changes with the same doubling of the parameters as in Figure 33, again at the standard operating point. Thus, this figure shows the complementary change in the device's response time to the output amplitude data in Figure 33.

In this case, the temporal resolution of the simulation was typically 1 ms in a 180 ms run. The zeros in the figure indicate an unresolved ( $< 1$  ms) level of change. Since these devices are p-dominant, the peak in output is controlled by injection, transverse drift, charge mirror imaging, and compression of the positive region toward the cathode. The data indicates that compression of the positive region toward the cathode is one of the primary causes of the peak and subsequent fall in

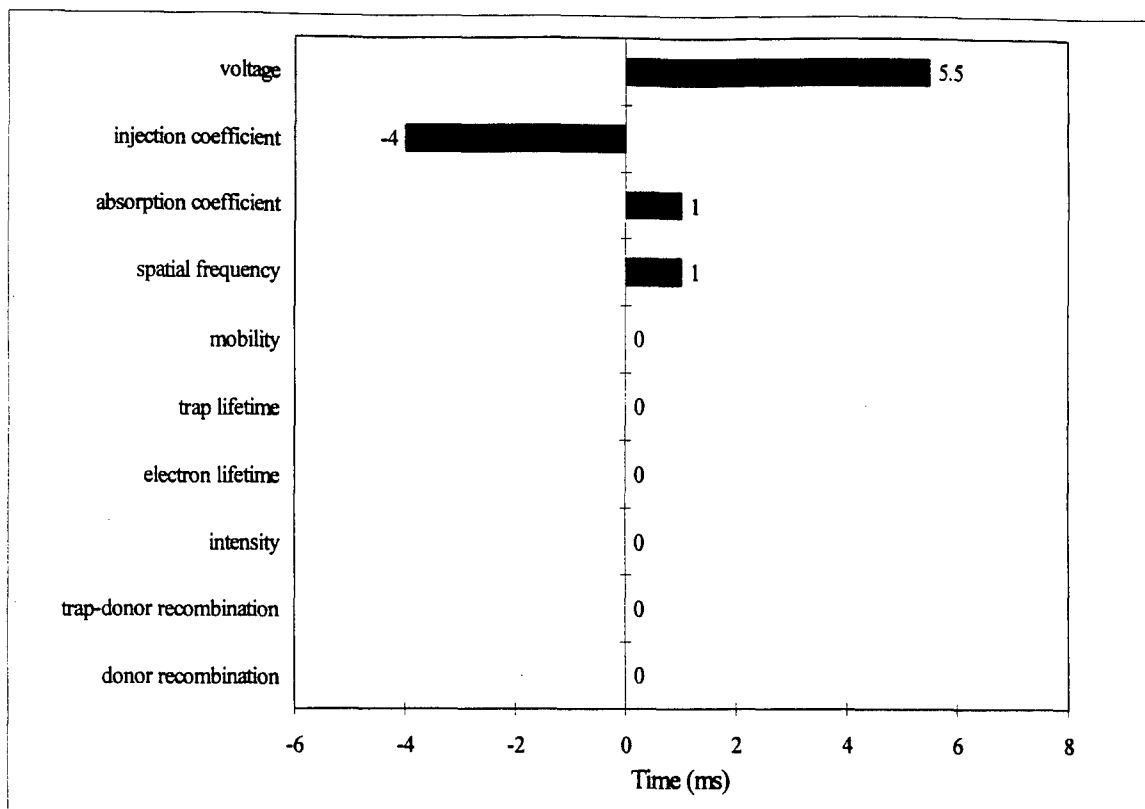


Figure 34. Change in the timing of the peak diffraction efficiency (in ms) when the parameter values are doubled at the standard operating point.

the output diffraction efficiency (see page 70). Since a higher voltage moves the electrons further towards the anode before they are trapped, the compression of the positive region is delayed, and the large impact of voltage in Figure 34 is reasonable. Since injection is another significant factor in causing the controlling positive charge region's contribution to dominance to peak, its large effect in Figure 34 is also reasonable (4; 22).

### Sensitivity to Recombination and Detrapping Mechanisms in Pulsed Operation

The previous section quantified the continuous illumination sensitivity of the modeled PRIZ in terms of peak dominance, peak diffraction efficiency, and timing of the peak output. The ideal follow-on would be to quantify the sensitivity to parameter variations in a pulsed mode of operation where the write-beam is turned off at some point. Since the output before write-beam turnoff in a pulsed simulation is no different than the output in the same period in a continuous

illumination run, the behavior of interest occurs after turnoff. There lies the problem. Depending on when the modeler turns off the write-beam, the behavior differs drastically. Figure 35 shows the range of data for a set of parameters (b73). The operating point, b73, deviates from the standard operating point only in the magnitude of the donor recombination coefficient,  $\xi_d = 2.77 \cdot 10^{16} \text{ s/m}^3$  versus  $10^{22} \text{ s/m}^3$ . The range of performance seen in Figure 35 is typical of pulsed mode simulations. Because of the difficulty of characterizing the nearly infinite range of behavior in just one sequence of pulsed simulations, only a few sequences were run for the sensitivity analysis. More pulsed simulations were run to evaluate the model (by comparing performance with experiments in the literature) and are discussed in the next chapter.

The motivation behind the pulsed simulations was to determine how the charge distributions decayed after the write-beam was turned off. The approach is to study the sensitivity of the model to mechanisms that can destroy the charge distributions created by the write-beam. Since thermal ionization, donor recombination, and trap-to-donor recombination are mechanisms that can destroy the charge distributions, the sensitivity analysis looked at  $\tau_t$ ,  $\xi_d$ , and  $\xi_{td}$ .<sup>21</sup>

Arguably, the primary characteristics for pulsed operation are the amount of output decay before turnoff and the level of reintensification demonstrated after turnoff. To examine these characteristics, the investigation again used both p-dominant (standard operating point) and n-dominant (**alternate operating point**) baselines.

---

<sup>21</sup> Donor recombination occurs when a free electron recombines with an ionized donor. Trap-to-donor recombination occurs when an electron from an ionized trap transitions to an ionized donor. Thus, both recombination mechanisms reduce or destroy charge species distributions. Thermal ionization, on the other hand, occurs when a free electron is generated from a filled, ionized trap. Thus, the ionized trap distribution is reduced, but the free electron concentration is increased. However, the free electron is mobile, and some of those eventually leave the device. Hence, thermal ionization can be thought of as a means of effectively reducing the negative charge distribution.

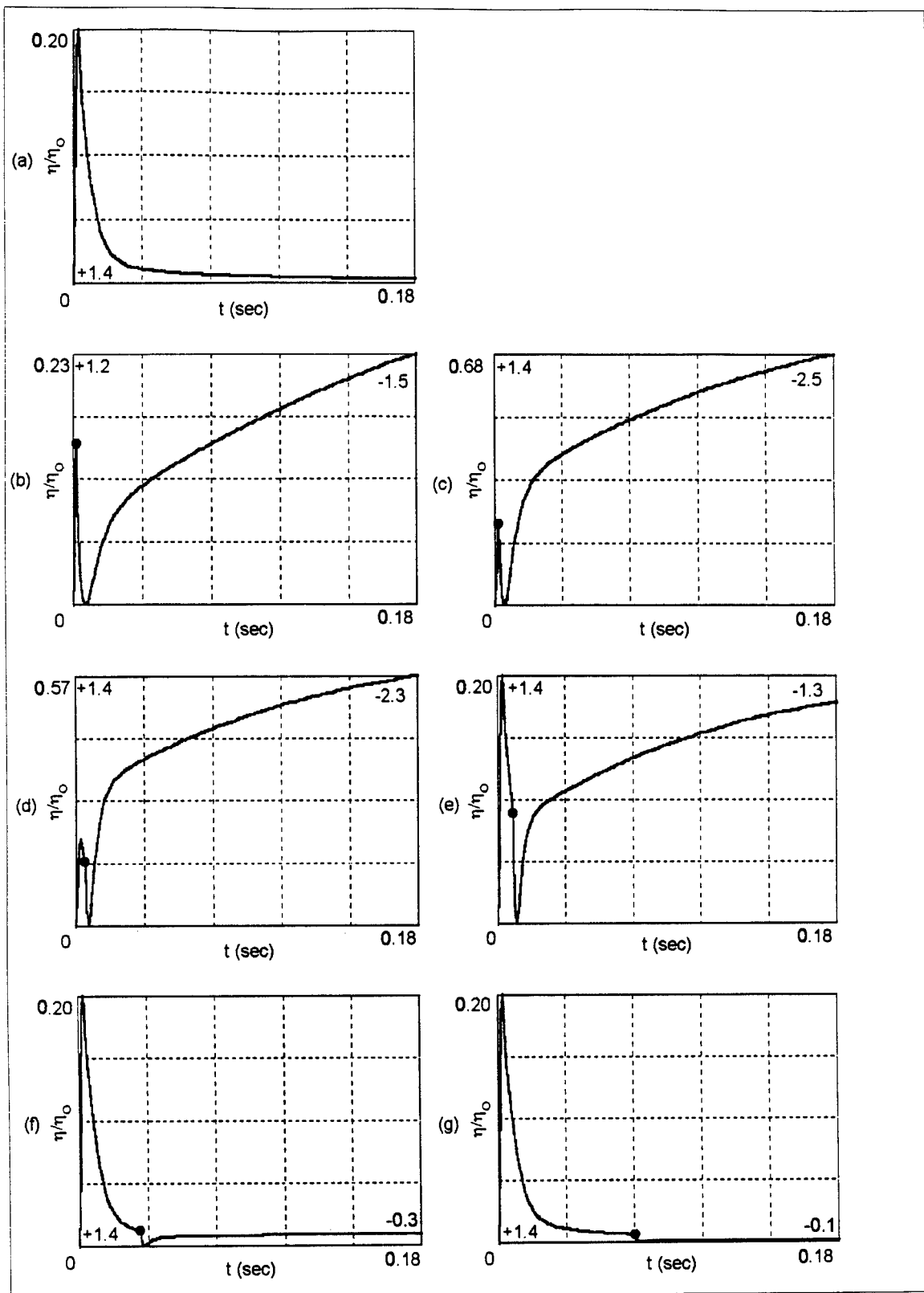


Figure 35. Pulsed operation for a donor recombination study when the write-beam is turned off at a)  $\infty$ , b) 1, c) 2, d) 5, e) 8, f) 32, and g) 72 ms. Circles, ●, indicate the turnoff time. (b73)

Figure 36 shows the self-erasure observed for the p- and n-dominant baselines and then adds the effects of separately changing the different mechanisms. The baseline uses  $\tau_t = 10$  s,  $\xi_{td} = \infty$ , and  $\xi_d = 10^{22}$  s/m<sup>3</sup>. When mechanisms are added, the simulation changes the respective parameter, one at a time, to either  $\tau_t = 0.1$  s,  $\xi_{td} = 2.77 \cdot 10^{18}$  s/m<sup>3</sup>, or  $\xi_d = 2.77 \cdot 10^{16}$  s/m<sup>3</sup>.

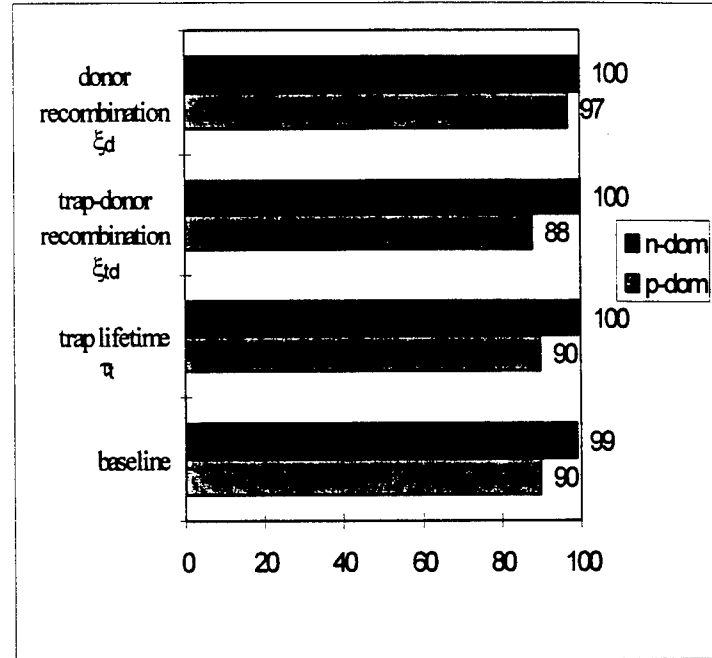


Figure 36. Self-erasure (%) relative to peak diffraction efficiency for single (parameter) changes to a baseline. Patterns indicate changes to a p- (standard operating point) or n-dominant (standard operating point with  $\xi_t = 5 \cdot 10^{17}$  s/m<sup>3</sup>) baseline.

The worst case self-erasure, 88%, is inadequate when the experimenter wants *total* self-erasure. Total self-erasure would cause the static portion of an image applied to a PRIZ to disappear totally on the output. On the other hand, a level of only 88% self-erasure would leave a relatively strong, unwanted, ghost image. In some of the runs used in the next chapter (runs not made for the sensitivity analysis), the self-erasure was as little as 60% of peak.



Notice that in Figure 36, n-dominant devices show larger amounts of self-erasure than the p-dominant devices. In the p-dominant devices simulated in Figure 36, the positive charge region's contribution is very large compared to the negative charge region, and a steady state condition is reached well above zero dominance. On the other hand, the n-dominant simulations have a large enough positive space charge effect that zero dominance is reached as the negative charge region's contribution falls. From the range of behavior shown in Figure 23 to Figure 26, it would appear that the fact that n-dominant devices showed more self-erasure in Figure 36 is purely chance and is based upon the two parameter sets. Since both p- and n-dominant cases exist where transition occurs to the other dominance state during continuous illumination, there must also exist two sets of parameters, one p-dominant and one n-dominant, that both show 100% self-erasure.

Figure 37 shows the maximum observed degree of reintensification for the same cases as in Figure 36. One observes a much larger degree of variation in the reintensification than was observed in the self-erasure. The baseline cases, without strong recombination and thermal ionization mechanisms to destroy or change the charge distributions that build up, demonstrate relatively large reintensifications (20% and 68% for the p- and n-dominant devices). Since the degree of self-erasure for the baseline n-dominant case is 99%, one would expect the large 68% reintensification to be caused in large part by an increase in ionized traps from the free electron distribution via the initial trapping transient.

Increasing the thermal ionization rate, which decreases the trap lifetime, can be expected to reduce the negative charge region's contribution to dominance by the reduction of the number of filled traps and by the eventual loss of electrons from longitudinal drift through the anode or through donor recombination. Thus, one would expect a net shift towards p-dominance after the initial transient. The result should be a larger reintensification on a p-dominant device and a smaller reintensification on an n-dominant device. Figure 37 shows the expected change.

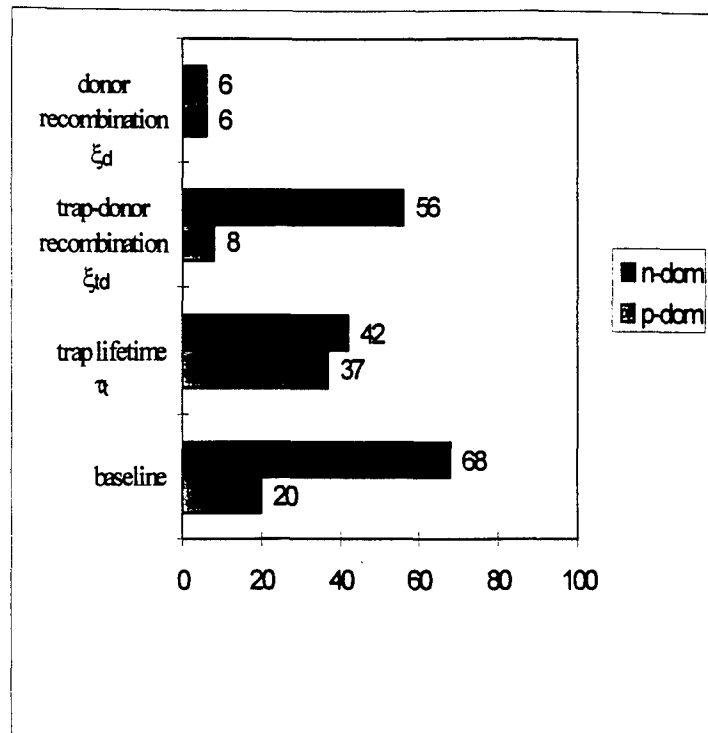


Figure 37. Reintensification (%) of diffraction efficiency relative to peak output after write-beam turn-off for single (parameter) changes to a baseline. Patterns indicate changes to a p- (standard operating point) or n-dominant (standard operating point with  $\xi_t = 5 \cdot 10^{17} \text{ s/m}^3$ ) baseline.

Increasing the trap-to-donor recombination rate should decrease both the donor and trap distributions equally. Thus for a first order effect, one would expect to see no change. However, both cases show a 12% decrease in the reintensification level. No straightforward reason for the change is obvious. One could speculate that increasing the number of empty traps by trap-to-donor recombination might increase the trapping rate slightly, but one would not expect this to cause the observed 12% changes.

Finally, increasing donor recombination deletes more free electrons and more ionized donors. If one again assumes the non-dominant regions (the charge regions that do not control the output) have negligible contributions, then a p-dominant device would lose more of its ionized donor distribution and reduce its level of reintensification. Figure 37 shows that effect. An n-

dominant device would see negligible change from losing ionized donors. To obtain the large drop in reintensification observed in Figure 37, one would have to assume that the electrons are creating ionized traps and are a very large factor in the 68% reintensification observed in the n-dominant baseline. In that case, donor recombination will deplete those free electrons and cause a large reduction in reintensification. That reduction is observed: 68% to 6%.

One should emphasize a final point with respect to pulsed operation. The device is very sensitive to the injection coefficient. By changing  $n_s$  or the injected current density an order of magnitude (from the default value of  $n_s = 1.38 \cdot 10^{18} \text{ m}^{-3}$ ), reintensification can range from a high of 90% down to near zero when no other parameter is changed. If  $n_s$  is zero, the device becomes an insulating PRIZ (no injection) instead of the conducting PRIZ modeled in this work. The data suggests that the absolute value of the reintensification in diffraction efficiency after write-beam turnoff remains nearly unchanged for a change in  $n_s$ , but the peak output during continuous illumination changes drastically. That is, the absolute changes in the charge distributions that cause reintensification are not significantly affected by changing the injection coefficient, and those charge distribution changes are probably spread throughout the device rather than only being located adjacent to the cathode.

This chapter was intended to give some feel for the qualitative and quantitative behavior of the modeled device and its internal processes. Because of the extent of the information in this chapter, a brief summary is provided.

### **Summary of the Device Physics**

The research used simulations of both continuous illumination (CW) and pulsed operations to learn how the device functioned. To develop an intuitive understanding of the physics, the work evaluated the internal charge and field dynamics in terms of a newly defined quantity: dominance. While dominance is an average magnitude (over the transverse direction) of

the longitudinal integral of the transverse field, one can intuitively relate dominance to an average longitudinal integral of the net charge. Thus, the sign of dominance tells whether the transverse fields in the positive space charge region (near the cathode) or the negative space charge region (nearer the anode) dominate the optical output. The mathematics (see Appendix H) and simulations show that the square of dominance is roughly proportional to first order diffraction efficiency. The next few paragraphs organize the summary depending on whether the simulations used continuous or pulsed illumination. The comments emphasize the new knowledge gained from the investigation.

**Continuous Illumination.** In p-dominant devices, the output rises until a combination of transverse drift, injection, charge mirror imaging, and compression of the positive region toward the cathode cause a peak. Transverse drift and injection across the cathode move electrons toward the positive peaks adjacent to the cathode and thus increase the trapping rate in those regions. Also, the positive charge region draws in toward the cathode with time, effectively reducing the transverse fields mirrored at the cathode. During these events, the negative charge region's contribution to dominance in a p-dominant device is usually insignificant. The literature fails to identify transverse drift as a significant factor in this process.

Once the p-dominant output peaks, continued compression of the positive region is the primary phenomenon causing subsequent self-erasure. If the parameter set is chosen so that the peak p-dominance is not too large, the self-erasure after the initial peak output can be great enough to create a phase reversal followed by an intensification in diffraction efficiency. In the case of the phase reversal, the contribution from the negative charge region to the dominance actually becomes bigger than the contribution from the positive charge region. While the positive region was growing and then shrinking, trapping in the negative charge region continued. After some period of operation, transverse drift in the negative space charge region (which pushes free

electrons away from the negative peaks) causes the negative peaks to stop rising and causes the negative valleys to fill. That rise in the negative valleys can result in a final self-erasure in the output.

Simulations show that initially n-dominant devices also show a peak and then self-erasure. Trapping of electrons in the negative charge region causes the negative peaks to grow and creates the initial rise in the output. In n-dominant devices, the peak and subsequent self-erasure occurs primarily from an increase in transverse drift in the negative space charge region. The relative peak-to-valley amplitude stops rising and begins falling. Essentially, drift causes the trapping rate to be higher in the valleys than in the peak regions. The accumulation of positive net charge near the cathode occurs just as in the p-dominant devices. However, its effect may be insignificant or may appear only as a brief oscillation in the output.

While published experimental work may have used n-dominant devices, the literature does not associate any results during continuous illumination with n-dominant states. If n-dominant devices have existed, devices where the output is controlled by negative charge densities, their creators either have not realized it or have not reported it.

The sensitivity analysis shows that the significance of each parameter depends on which output characteristic is of interest. Voltage and injection coefficient create the largest changes in the diffraction efficiency. Intensity and mobility have the greatest effect on timing. The absorption coefficient, electron lifetime, and intensity create the widest range of p- to n-dominant devices. The simulations also show that the variation in the output for a single parameter change depends on the state of all the other parameters. That is, the model of the device does not behave the same at different operating points and regions of the parameter space.

**Pulsed Illumination.** This research shows that pulsed operation exhibits a range of behavior far beyond what the literature reports. The growth of the positively ionized donor

distribution stops when the code (or researchers) turns off the write-beam. Without photogeneration of electrons, the dynamics are limited to recombination, injection, drift, trapping and detrapping. Thus, one expects to see fewer and fewer free electrons that correspond to an ever slowing trapping rate.

Dominance shifts easily explain the various transient effects observed after write-beam turnoff. The simulations show a very fast shift toward n-dominance when photogeneration stops. This occurs because the 'uncovering' of *newly* ionized donors stops instantaneously. The electric fields still force electrons away from the large ionized donor sites near the cathode (uncovering the donors), but the drift now uncovers no *new* ionized donors. Thus, a mechanism shifting the device toward p-dominance instantaneously disappears, and the result is a continuous shift toward n-dominance. But as the electron concentration falls, so does the trapping rate, causing the shift toward n-dominance to slow. If at some point the trapping rate drops below the thermal ionization (detrapping) rate or the ejection rate out the anode becomes dominant, the output shifts toward p-dominance.

The parameter set and the time of turnoff drive the dominance state of the device at the end of the write-beam pulse. For p-dominant devices, the transient shift toward n-dominance is a quick self-erasure. If the p-dominance at turnoff is small enough, the self-erasure leads to a phase reversal and reintensification. For early turnoffs, this reintensification can go higher than the initial peak. The literature does not report this stronger level of reintensification.

The simulated behavior of pulsed, n-dominant devices is explainable, but published reports of similar behavior do not exist. The initial transient shift toward n-dominance produces an immediate *intensification* after write-beam turnoff. Thermal ionization produces a later measure of self-erasure. Thus, while CW operation of an n-dominant device produces behavior

similar to that of p-dominant devices, the n-dominant device's pulsed operation is drastically different.

## *VI. Model Evaluation*

The numerical simulations in the preceding chapter demonstrated a wide range of possible device performance. In this chapter, simulations are used to demonstrate the ability of the model to generate output similar to published experimental data. The experimental data chosen shows: (1) the relationship of diffraction efficiency to modulation index (3:70); (2) the relative behavior of first and second order diffraction efficiency as a function of time (3:71); and (3) device behavior after early and late write-beam turnoff (4:751). The selected data represents a large part of all of the experimental data in the literature. Most published data reports only relative values of diffraction efficiency, and none includes all of the material parameters necessary to fully specify a parameter set in this work.

The simple band model in this effort is very successful at predicting behavior similar to the chosen experimental data, failing to reproduce only one characteristic. The discrepancy can be explained by noting either the different time domains imposed by the multi-week runtimes required to simulate seconds of device time or the likely differences in parameter values between the simulated devices and the unknown parameters of the experimental devices. The research stopped evaluating the model when it reached a point of diminishing returns; i.e., when the promising numerical investigations had been run; the literature suggested no further avenues of approach; and new experimental data was needed for further direction. The evaluation should continue when experimental feedback is available to supplement and guide the numerical simulation.



## **Approach**

The first step was to select an initial operating point for each experimental simulation. The selection was achieved by reviewing the body of previous simulations for comparable characteristics, examining that simulation's parameter set, and reviewing the selected article from which the experimental data was taken. Thereafter, a simulation was run using the selected initial set of parameters and the results analyzed. If necessary, the initial set was modified and additional simulations run. This process was repeated until the runs produced a satisfactory set of simulations or there existed no reason to expect better performance with further changes.

After a simulation with characteristics similar to those in the literature was produced, an analysis was made of the success of the simulation. The analysis specifically considered whether the final operating point was consistent with the previously developed understanding of the device physics. In some cases, the analysis was used to supplement that understanding.

## **Diffraction Efficiency as a Function of Modulation Index**

In 1985, Shlyagin et al. published experimental data on the behavior of diffraction efficiency as a function of modulation index (3:70). Figure 38 reproduces that data. Shlyagin et al. used an operating voltage  $V = 1.8$  kV, an input spatial modulation frequency  $\nu_x = 2.5$  mm<sup>-1</sup>, and a write-beam wavelength  $\lambda_w = 488$  nm. The product of the mean input intensity,  $I_0$ , and the modulation index,  $m$ , was reportedly held constant; however, no value for the product was given. Shlyagin et al. further reported a maximum diffraction efficiency of 0.5%. The diffraction efficiency clearly peaked much later than 100 ms. The simulations suggest that for such a high diffraction efficiency, Shlyagin et al. may have been experimenting with a PRIZ with a relatively

high barrier at the cathode ( $n_s$ , much less than the values used in this work).<sup>22</sup> If so, the code is unable to investigate that region of parameter space because of the extremely small time steps (long runtimes) the Runge-Kutta routine uses to handle changes in the extremely small electron densities near the cathode.

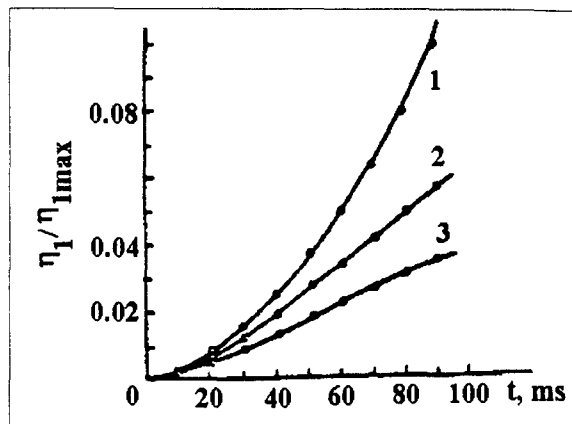


Figure 38. Diffraction efficiency as a function of modulation index.  $m$  is (1) 1.0, (2) 0.45, and (3) 0.27 (3:70).

In an attempt to produce similar data, the investigation created parameter set b61. Set b61 is similar to that reported by Shlyagin et al., with  $V = 1.8$  kV,  $v_x = 2$  mm<sup>-1</sup> (versus the experimental 2.5 mm<sup>-1</sup>),  $\lambda_w = 488$  nm, and  $\alpha = 800$  m<sup>-1</sup>. Its largest change from the standard operating point is the higher voltage. The absorption coefficient came from Petrov's absorption spectrum (15:233). The work adjusted the trapping and detrapping times to achieve the results in Figure 39. The electron lifetime is approximately 70  $\mu$ s (or 0.5 transit times) and the trap lifetime is 7.5 ms.

<sup>22</sup> The sensitivity analysis indicates that lower injection coefficients result in larger output. In this effort, diffraction efficiencies greater than 0.2% were not observed. The code would not (noticeably) run near the standard operating point with  $n_s$  much lower than  $10^{17}$  m<sup>-3</sup>.

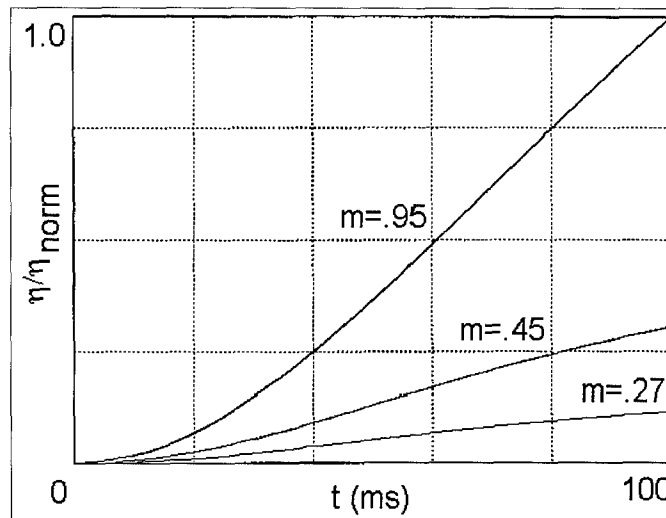


Figure 39. Reproduction of Shlyagin index of modulation experiment (3:70).  $\eta_{\text{norm}}$  is the diffraction efficiency for the  $m = 0.95$  curve at 100 ms. (b61)

The electron lifetime of 0.5 transit times used in b61 was suggested by Bliznetsov et al. (4:752). The much shorter trap lifetime in b61, 7.5 ms, than the 10 s of the standard operating point means that thermal ionization is now a significant mechanism in a 100 ms run. The higher thermal ionization rate drastically reduces the effective trapping rate and causes a strong shift toward p-dominance. Since the b61 device is p-dominant anyway, reducing the trap lifetime reduces the effective trapping rate which results in delaying the peak output and increasing its amplitude. This causes the 100 ms period shown in Figure 39 to represent an early, more linear portion of the output, more characteristic of Figure 38. In theory, reducing injection across the cathode would produce a similar effect.

The only significant difference between Figure 38 and Figure 39 is the difference in peak diffraction efficiency (about a factor of three) between the experimental device and the simulated device. The simulated device's peak output was much lower than that of the experimental device. Since the size of the peak depends on injection, transverse drift, charge

mirror imaging, and compression of the positive charge region toward the cathode (see page 70), there are a number of parameters that could create the difference. The parameter that seems most likely is the injection coefficient. The barrier height is likely to depend upon the technique used to apply the electrodes to the crystal. Thus, construction of the experimental device could have increased the barrier, reducing the injection current and causing a larger peak output. As mentioned previously, because of the Runge-Kutta algorithm's error control, low levels of injection could not be simulated to test this hypothesis.

Thus, the results in Figure 39 are a fair qualitative reproduction of the Shlyagin et al. data. A normalizing diffraction efficiency,  $\eta_{\text{norm}}$ , was selected to create a range of 0 to 1.0 in Figure 39. The results are also consistent with the dominance concept developed earlier. As the modulation index increases, so does the transverse variation in the charge densities. This produces larger transverse fields that produce larger output.

### First and Second Order Diffraction Efficiency

Figure 40 shows the experimental relationship between first and second order diffraction efficiency reported by Shlyagin et al. in 1985 (3:71). In the measurements of Shlyagin et al., the first order intensity,  $I_1$ , is always bigger than the second order intensity,  $I_2$ . Thus, although the  $I_2$  peak in Figure 40 is drawn higher than the  $I_1$  peak, the true peak value of  $I_2$  is less than  $I_1$ .

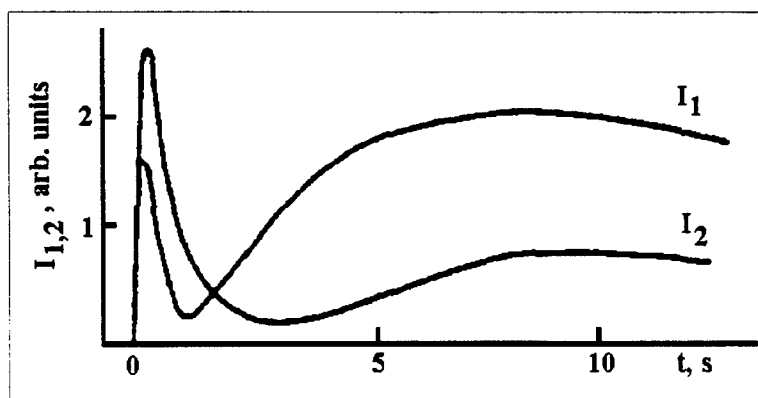


Figure 40. Time dependence of first and second order diffracted light  $I_1$ ,  $I_2$  for  $v=0.5 \text{ mm}^{-1}$ ,  $I=500 \text{ } \mu\text{W/cm}^2$ ,  $\lambda=488 \text{ nm}$  (3:71).

This work reviewed existing simulations to see if any showed the continuous illumination behavior of Figure 40. The best qualitative reproduction found was from parameter set b45, the standard operating point altered to values of  $I_0 = 6 \text{ W/m}^2$  (versus the experimental value of  $5 \text{ W/m}^2$ ),  $\alpha = 3550 \text{ m}^{-1}$  (versus an experimental value near  $1000 \text{ m}^{-1}$  (3:71; 15:233)), and  $\tau \approx 1 \text{ ms}$ . This set differs from the parameters specified by Shlyagin et al. in the caption of Figure 40. Since Shlyagin et al.'s parameters included a spatial modulation frequency of  $0.5 \text{ mm}^{-1}$ , and the code as written can not simulate a frequency below  $1.0 \text{ mm}^{-1}$ , a device with Shlyagin et al.'s parameter set could not be simulated.<sup>23</sup>

However, the simulation shown in Figure 41 is a reasonable qualitative reproduction of Shlyagin et al.'s data in Figure 40. The relative timing and height of the first and second order peaks are very similar. The initial first order peaks occur before the initial second order peaks in both figures. The first order minimum followed by the second order minimum occur next in both figures. Finally, both figures show the final first order and then second order peaks occurring last. The time domains are different because of the effects of different parameter sets.

Since the diffraction efficiencies in Figure 41 are just the ratios of the output intensities to the input intensity, there is no difference in the arbitrary units of that plot and the arbitrary units of the output intensity in Shlyagin et al.'s Figure 40. The amplitude of the second order output in Figure 41 is approximately an order of magnitude lower than the output of the first order, consistent with the results reported by Shlyagin et al. (3:71).

---

<sup>23</sup> The simulated device is sized  $d \times d$ . If one assumes that at least one full period of the input intensity distribution must be simulated, the minimum simulation frequency,  $\nu_{\min}$ , is 1 line per  $d$  millimeters. In a real device  $d$  is approximately  $0.5 \text{ mm}$ . Using that value in a simulation produces  $\nu_{\min} = 2 \text{ mm}^{-1}$ . In the simulations in this effort,  $d$  may be as high as  $1 \text{ mm}$ , giving  $\nu_{\min} = 1 \text{ mm}^{-1}$ .

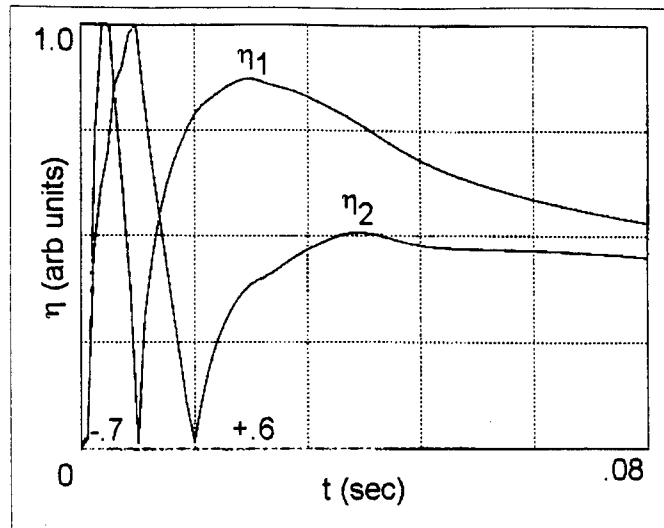


Figure 41. Simulation of Shlyagin et al.'s plot of first and second order diffraction efficiency (3:71). (b45a)

The effort ran additional simulations with data sets more consistent with Shlyagin et al.'s values. Those efforts did not produce results as close as Figure 41. The reader should note that simulations using most parameter sets do not display the particular behavior shown in Figure 40. Most simulations show only a single peak in first order diffraction efficiency and the subsequent self-erasure; few simulations were run long enough to see a second peak.

A concern in comparing Figure 40 and Figure 41 is whether Shlyagin et al.'s data shows marked oscillations or actual phase reversals (passage through zero dominance). Shlyagin et al.'s theory clearly predicts phase reversals after the first order peak (3:71). If Shlyagin et al.'s experimental data in Figure 40 is just marked oscillations (no phase reversals), similar behavior would likely not have been observed in this work's simulations. Few of the continuous illuminations runs in this effort were long enough to show second peaks.

If the minima in Figure 40 do not reach zero, Shlyagin et al.'s experimental data did not produce the phase reversals expected by their own mathematics, which tends to challenge the reasonableness of their theory. However, the body of simulations produced in this work support

their theoretical predictions with several instances of similar phase reversals and no instances of large second peaks without a phase reversal. Once a charge region's contribution peaks, there seem to be no mechanisms available to cause a *large* second peak without a phase reversal. The positive region peaks when it is compressed to the cathode; the negative region peaks when transverse drift reduces the charge variation in the negative charge region (see the discussion on pages 68-70). The two regions' contributions to the output are opposite so that *small* oscillations or second peaks without phase reversals can and do occur.

However, Shlyagin et al.'s data in Figure 40 show *large* oscillations, which one would assume are either too large to exist without phase reversals, exist in only a small region of parameter space, or are produced by some unmodeled physical mechanism. In either case, there are enough similarities between Figure 40 and Figure 41 that one can conclude the 2-D model produces results comparable to the experimental data of Shlyagin et al.

### **Early and Late Write-Beam Turnoff**

Bliznetsov et al.'s Figure 42 demonstrates experimental PRIZ behavior reported nowhere else in the literature (4:751). Because Bliznetsov et al. were unable to produce a closed form solution that yielded similar results, and because this work's numerical inputs and outputs closely match Bliznetsov et al.'s experimental data, this work made an extensive effort to produce similar data.

Bliznetsov et al.'s oscilloscope traces examine the variation of first order diffraction efficiency as a function of time. They turn off the write-beam at 0.125, 0.2, 0.3, and 1.5 seconds. During continuous illumination, the output peaks at about 0.275 seconds and then falls to near zero at about 1.5 seconds. The plots do not indicate the absolute amplitudes of the output, and the oscilloscope traces before about 0.2 seconds are very 'fuzzy'. In the three early turnoff cases, when Bliznetsov et al. turned off the write-beam before or just after peak, the traces show varying

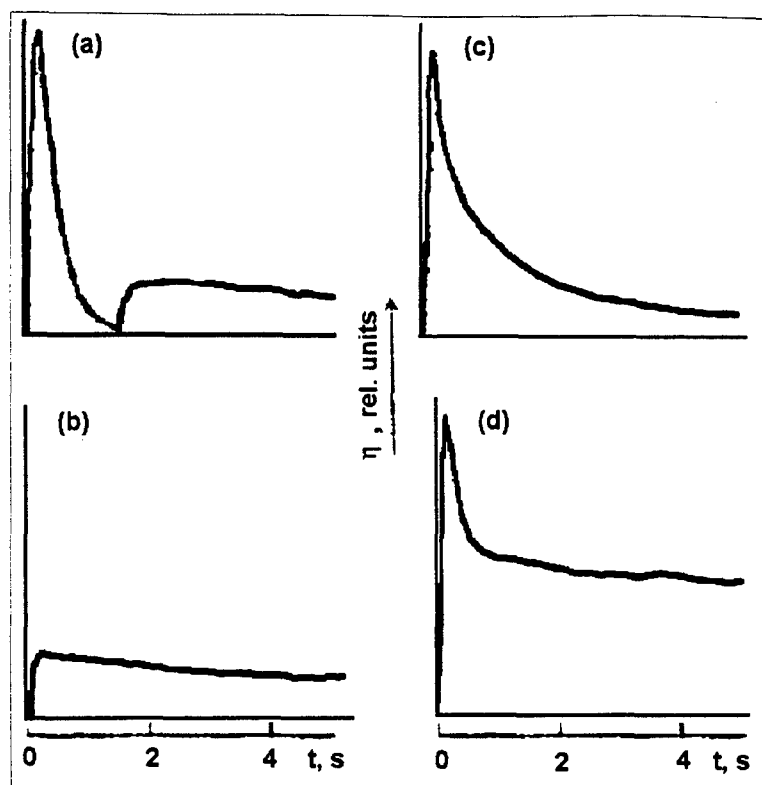


Figure 42. Oscilloscope traces of the diffraction efficiency for various values of the exposure to the writing light,  $W=I_0 t_0$ .  $I_0=30 \mu\text{W}/\text{cm}^2$ ,  $v=2 \text{ mm}^{-1}$ , the writing is started at time  $t=0$ . a)  $t_0=1.5 \text{ s}$ , b)  $0.125$ , c)  $0.2 \text{ s}$ , d)  $0.3 \text{ s}$ . Peak occurs in (a) between  $0.2$  and  $0.3 \text{ s}$ . (4:751)

amounts of self-erasure after write-beam turnoff. No phase reversals are apparent in these early turnoff cases, although they could exist in the fuzzy  $0.2$  seconds (4:751).

In the late turnoff case, the trace shows almost total self-erasure before the experimenter turns off the write-beam and reintensification to about 15% of peak afterwards. Bliznetsov et al. assert that a phase reversal occurs after late turnoff, but only refer to previous literature for that conclusion. They do not indicate that phase reversal was experimentally verified for the data presented. Bliznetsov et al. also state that after late turnoff "diffraction efficiency . . . falls to zero and then starts to grow again." The absence of any fall in diffraction efficiency after write-beam turnoff (no trapping transient) in Figure 42a suggests that the zero value on the oscilloscope trace



might not have coincided with the bottom of the oscilloscope trace, i.e., they might not have achieved the full self-erasure shown in Figure 42a.

Bliznetsov et al. identified the following parameters:  $I_0 = 0.3 \text{ W/m}^2$ ,  $d = 0.4\text{-}0.5 \text{ mm}$ ,  $\lambda_w = 442 \text{ nm}$ ,  $\lambda_r = 633 \text{ nm}$ , and  $V = 2 \text{ kV}$ . From their article, one can also infer some physical parameters:  $\alpha \approx 3500 \text{ m}^{-1}$  and  $\tau \approx 50 \text{ }\mu\text{s}$ . Obviously, these values do not specify a complete parameter set in terms of this work's model; they also result in multi-week runtimes. Bliznetsov et al. did not report the use insulators between the electrodes and the semiconductor; but they also did not provide an experimentally verified value for the injection coefficient,  $n_s$ .

Simulations were first run at the standard operating point to determine if Bliznetsov et al.'s device performance required a specific operating region. Pulsed operation using the standard operating point showed several differences compared to Figure 42 (see Figure 43) and showed that Bliznetsov et al.'s device behavior was not characteristic of all regions of parameter space.

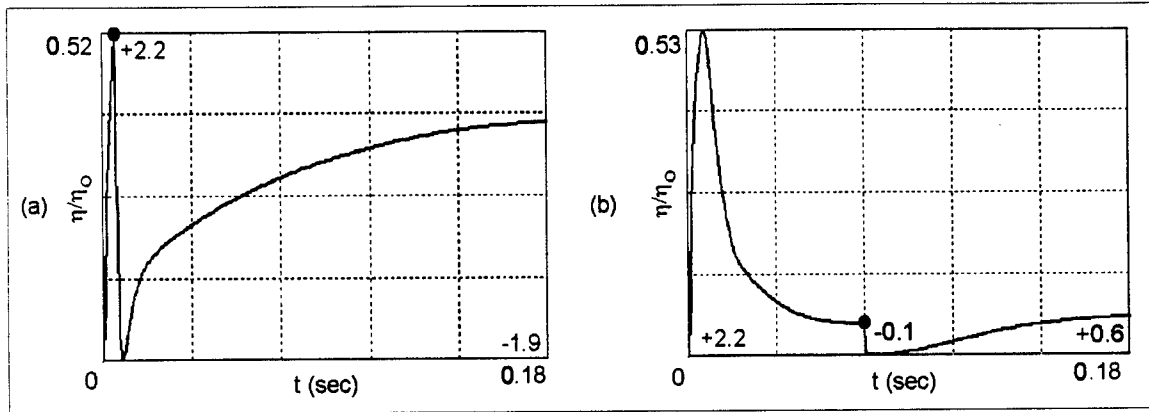


Figure 43. Pulsed operation for a large p-dominance with continuous illumination peak at 7 ms. The write-beam is turned off at a) 5 and b) 72 ms. Turnoff times are indicated by circles. (b32)

In the early turnoff case in Figure 43a, the standard operating point's output displays a quick phase-reversal followed by an extremely large amount of reintensification rather than Bliznetsov et al.'s mild self-erasure. At late turnoff, the self-erasure before and the

reintensification after turnoff are both extremely limited. The desired late turnoff output is near total self-erasure followed by about 15% reintensification.

After some unsuccessful simulations with parameter sets closer to Bliznetsov et al.'s, the search for similar performance took a different approach. According to their writings, Bliznetsov et al. thought their continuous illumination device was p-dominant. Such a conclusion was reasonable for several reasons: (1) the Russian researchers were looking at the PRIZ because it achieved large diffraction efficiencies and the sensitivity analysis of this work suggests p-dominant devices may create larger peak diffraction efficiencies; (2) n-dominant devices show intensification after turnoff instead of self-erasure; and (3) p-dominant devices with a significant trapping transient after turnoff will demonstrate some self-erasure. However, Bliznetsov et al.'s data showed none of the sharp transients seen immediately after turnoff in the simulations of this work. Clearly, the parameter sets for earlier simulations need some mechanism to remove (or slow) those sharp transients.

In an attempt to remove the sharp transients, a known p-dominant device with poor early turnoff performance was selected and the injection coefficient decreased to increase the continuous illumination p-dominance. A dominance analysis predicts that changing the injection across the cathode should not strongly affect the transient fall after turnoff since the transient occurs from trapping throughout the device. However, since a smaller  $n_s$  delays the output peak in a p-dominant device (see Figure 79 in Appendix D), decreasing  $n_s$  will increase the magnitude of the dominance at turnoff, and the *relative* transient shift should be smaller. If the relative size of the transient becomes small enough, no phase reversal will occur, only a slow self-erasure. Changing the detrapping rate, which can cause a significant shift towards p-dominance after turnoff, might fine-tune the output after the modeler obtains a satisfactory, but approximate, result.

Starting from the standard operating point, the injection coefficient was decreased. The amount of drop in diffraction efficiency after turnoff improved (the trapping transients no longer produced phase reversals), but runtime became excessive, probably because of the extremely small free electron density near the cathode and the resultant response from the Runge-Kutta algorithm's error controller. The simulation of devices with less and less injection was stopped at  $n_s = 3.3 \cdot 10^{17} \text{ m}^{-3}$ , and further simulations run with smaller detrapping times. The final two steps in this sequence went from  $\tau_t = 0.025 \text{ s}$  (b72) to  $\tau_t = 0.01 \text{ s}$  (b71), bracketing the desired output in Figure 42b. Figure 44 shows that self-erasure jumps from too much to too little.

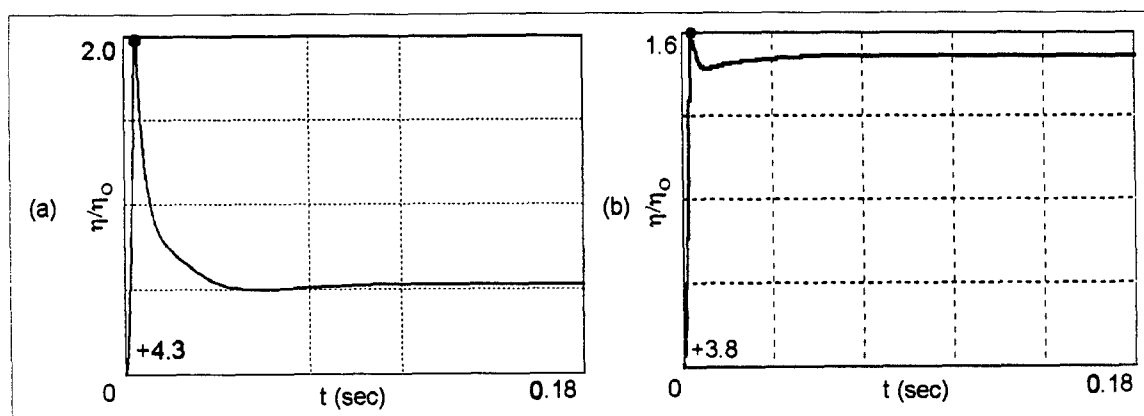


Figure 44. The write-beam is turned off at 3 ms for cases of a)  $\tau_t = 25 \text{ ms}$ ,  $n_s = 3.3 \cdot 10^{17}$ , and b)  $\tau_t = 10 \text{ ms}$ ,  $n_s = 3.3 \cdot 10^{17}$ . The small circles indicate turnoff times. (b72 and b71, respectively)

Since the early turnoff with  $\tau_t = 0.025 \text{ s}$  is reasonably similar to that of Bliznetsov et al., a continuous illumination run was made as a preliminary to a late turnoff simulation (using set b72). Unfortunately, all of the changes that produced acceptable early turnoff (a fall in diffraction efficiency without a phase reversal) caused the continuous illumination output to change. Although the peak output still occurred at around 12 ms, the output fell only 35% in 180 ms. Clearly, at this operating point, the simulations do not show the near total self-erasure observed by Bliznetsov.

Thus, the next problem to address was obtaining strong reintensification after a near total self-erasure. Previous simulations had not shown this behavior; however, the literature suggested an approach. Bliznetsov et al. indicated that latent imaging<sup>24</sup> and dynamic imaging tend to be mutually exclusive, and that dynamic imaging could be associated with strong reintensification (4:751). Thus, a parameter set that prevents good latent imaging might cause strong reintensification. Assuming success with strong, late reintensification, perhaps the early turnoff would correspond to that shown in Figure 42.

Donor recombination combined with thermal ionization should prevent latent image formation by destroying the positively ionized donor and negatively charged trap distributions created by the write-beam before the experimenter applies the read-beam. Other mechanisms might also produce poor latent imaging. For example, trap-to-donor recombination alone might destroy the charge distributions. However, previous simulations had not suggested that this mechanism created strong reintensification. A combination of all three mechanisms also seems likely, but the relative parameter values would be difficult to predict.

To find suitable parameters for donor recombination ( $\xi_d$ ) and thermal ionization ( $\tau_t$ ), the 1-D rate equations were solved using continuous write-beam illumination to obtain a steady-state in ionized donors, filled traps, and free electrons with no external voltage. This simulated writing the latent image. With the steady-state charge densities as starting points, the rate equations were then solved without photogeneration or an applied voltage. This corresponded to allowing the device to sit undisturbed with no applied voltage. In accordance with the criteria of Petrov et al. (46:1332), if the charge densities fell to 1/e of their steady-state values within 10 seconds after

---

<sup>24</sup> In latent imaging, the researcher writes an image to the device without an external voltage source, creating negligible separation of the positive and negative charge densities. After some time, determined by the storage requirements, the experimenter applies the external voltage and reads the image with the read-beam (25:348). If the read-beam does not contain the image, the device does not demonstrate good latent imaging.

turning off the write-beam, then the device was considered to possess poor latent imaging characteristics. The solution indicated various combinations of donor recombination and trap lifetimes that would work. Emphasizing donor recombination in light of the sensitivity analysis, suggested values of  $\xi_d = 2.77 \cdot 10^{16} \text{ s/m}^3$  and  $\tau_t = 0.1 \text{ s}$  (see Appendix D, Figure 67 to Figure 70 and Figure 77 to Figure 78, pp. 146-151).

Simulations using the standard operating point modified with the above donor recombination coefficient and trap lifetime did show some increase in reintensification. It was hypothesized that the absolute reintensification increased significantly, but that the relative reintensification, due to a large peak dominance, did not turn out to be as large as desired.

Earlier results suggested variations in the absorption and injection coefficients might change only the relative degree of reintensification. Additional runs confirmed this hypothesis. Figure 45 shows strong self-erasure and strong reintensification using the b79 parameters that include the new donor recombination coefficient and trap lifetime:  $n_s = 6.917 \cdot 10^{17} \text{ m}^{-3}$ ,  $\tau_t = 0.1 \text{ s}$ ,  $\xi_d = 2.77 \cdot 10^{16} \text{ s/m}^3$ ,  $\lambda_w = 442 \text{ nm}$ , and  $\alpha = 2000 \text{ 1/m}$ . This produced a p-dominant peak at 5 ms, self-erasure to 12% of peak at 72 ms (turnoff), and reintensification to 31% of the peak after turnoff.<sup>25</sup>

Early turnoff behavior was also examined for set b79. The simulations again showed undesirable quick phase reversals followed by strong reintensification, although the transient shift toward n-dominance was not quite as strong as that seen in earlier p-dominant cases.

---

<sup>25</sup> By increasing the injection coefficient to  $1.38 \cdot 10^{18} \text{ m}^{-3}$ , the reintensification rose to 90% of peak after a self-erasure to 22% of peak. In changing from the higher to lower value of the injection coefficient, the peak diffraction efficiency before turn-off changed by a factor of 2.98 while the peak reintensification changed only by a factor of 1.12. That is, the absolute magnitude of the reintensification remained practically unchanged. Only the relative size of the reintensification changed.

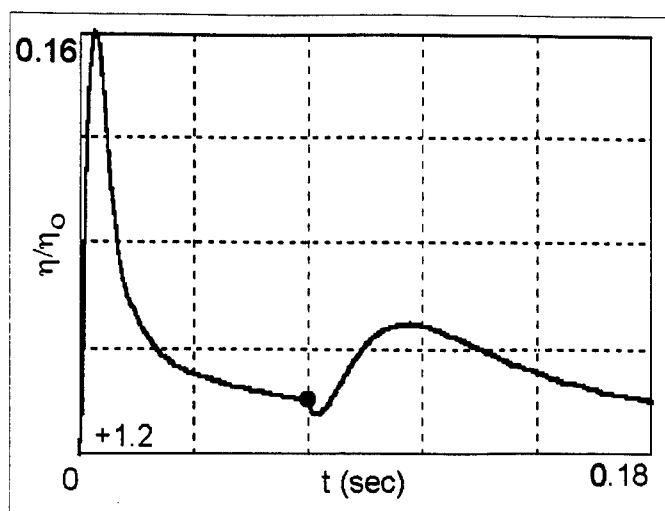


Figure 45. Strong self-erasure and reintensification. The small circle indicates the turnoff time. (b79)

Next, the injection coefficient was decreased in the simulations to remove the phase reversals in the early turnoff cases while still obtaining some reintensification after late turnoff. While set b82, with  $n_s = 10^{17} \text{ m}^{-3}$ , was the last change that still gave recognizable reintensification after late turnoff, set b83, with  $n_s = 2.77 \cdot 10^{16} \text{ m}^{-3}$ , was the first to produce acceptable results for early turnoff. The results were either good early turnoff performance or good late turnoff performance, but not both for the same parameter set.

At this point, the investigation into Bliznetsov et al.'s pulsed behavior ceased. Figure 46 shows behavior, produced by two different parameter sets, that is comparable to Bliznetsov et al.'s data in Figure 42.

In producing behavior similar to Bliznetsov et al.'s reported data (4), considerable understanding was developed of how changing device parameters affected a complex set of characteristics. In removing phase reversals after turnoff, it was found that the effects of injection and thermal ionization were similar on both the absolute amplitude of the output and the relative sizes of the transients. To obtain strong reintensification, it was necessary to investigate and develop some insight into latent imaging; donor recombination and thermal ionization were both

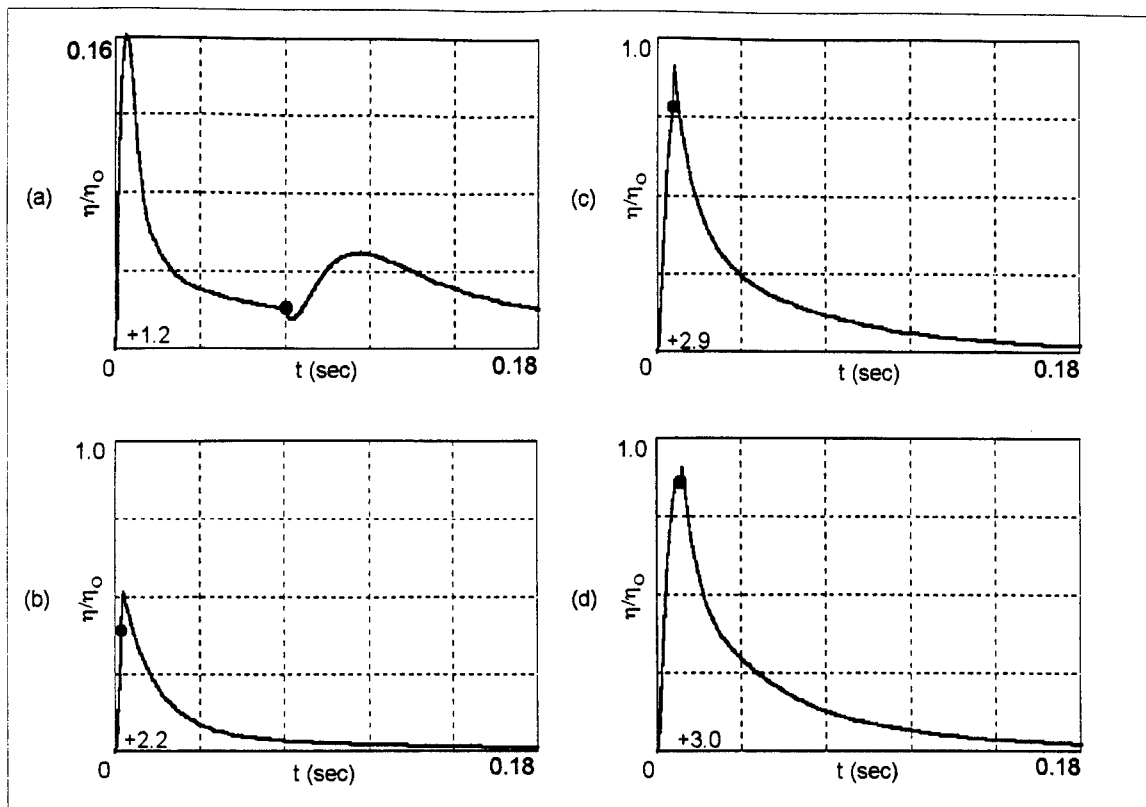


Figure 46. Good late turn-off behavior is shown in (a) using the b79 parameter set. Good early turn-off is shown in (b)-(d) using the b83 parameter set. The small circles indicate turnoff times at a) 72, b) 3, c) 7, and d) 11 ms. The output peaks in (a) at 5 ms and in (b)-(d) at 9 ms.

needed to destroy latent imaging or to produce strong reintensification. But even 'good' combinations of donor recombination and thermal ionization could be masked with the wrong choice of absorption coefficient. Thus, it became apparent that to simulate complex device behavior, it is necessary to consider the interdependencies of most or all of the model's parameters.

### Summary of the Model Evaluation

To decide the extent to which the simple band model represents a real device, computer runs generated results comparable to those reported in the literature. Considering the simplicity of the model, the code produces simulations comparable to a remarkable portion of the experimental behavior reported in the literature. The selected approach optimized the parameter sets, not to simulate the slow devices in the literature, but to produce quick output peaks (and short runtimes)

comparable to those of a good, hypothetical, dynamic imaging device. Thus, the time scales differ from those of published experiments where the phenomena took seconds.

The model is effective at producing output very similar to that of Shlyagin et al. (3:70). In Shlyagin et al.'s experiment, diffraction efficiency increases with time and with modulation index. Shlyagin et al. also reported the relative behavior of first and second order diffraction efficiency as a function of time (3:71). Both orders peaked, self-erased, and then reintensified during continuous illumination. The model produced results comparable to both of Shlyagin et al.'s experiments, although not on the same time scale.

The final experiment for comparison was Bliznetsov et al.'s oscilloscope traces of diffraction efficiency versus time for three early and one late turnoff (4:751). The traces show varying degrees of self-erasure after early turnoffs, and they show a near total self-erasure before, and a strong reintensification after, late turnoff. The 2-D simulations produced results individually comparable to either Bliznetsov et al.'s early or late turnoff behavior, but no single parameter set produced results comparable to both their early and their late turnoff phenomena. Again, the time scales of the simulations were not those reported in the literature. The difference in time domains may account for the observed differences between model and device behavior.

Thus, the model simulated most of the experimental behavior reported in the literature. The few characteristics it did not show could be due to either looking in the wrong region of parameter space, a difference in the time domains, or to a model that does not include every significant physical mechanism. In either case, the large number of experimental characteristics simulated provides strong confidence in using the model for predicting new as well as known behavior.



## ***VII. Conclusions***

The goals of this paper were to determine and understand how the underlying physical processes in a PRIZ produce dynamic imaging and to evaluate the effectiveness of the simple band model used in the 2-D numerical simulations that led to that understanding of the PRIZ. Those goals were accomplished in the work discussed in the previous chapters. The next few paragraphs cull from those results to emphasize the new work, identify important accomplishments, and point to the implications of this research.

### **Modeling**

This effort created the first 2-D numerical model of the PRIZ. The 2-D code models not only the internal charge and field dynamics in two dimensions, but the transverse linear electro-optic effect, the device's crossed linear polarizers, and the transmission of the output to the far field where the diffraction pattern is analyzed. The model improves on its predecessor in the literature (4) by including additional, significant, physical processes that occur in real devices and by eliminating assumptions. The simulations show that including transverse drift and exponential absorption in the mathematical model is essential in producing good quantitative results.

The code models any cubic, photorefractive, wide bandgap semiconductor oriented in the  $\langle 111 \rangle$  position. Minor changes to the code would permit changing orientations, adding insulators, and modifying the model of the metal-semiconductor barriers at the electrodes. The code already incorporates user specification of material parameters, device parameters, different inputs, and alternate algorithms. A completely portable version of the C++ code was compiled and tested on both Windows NT and UNIX systems.

In addition to the quantitative capabilities of the 2-D numerical model, a concept called dominance was developed to intuitively and mathematically relate the numerically determined internal charge and field dynamics to the output diffraction efficiency. This was the first intuitive method created to explain behavior such as phase reversals and reintensification in terms of the internal dynamics.

### **Model Evaluation**

A large number of simulations were run to determine whether the simple band model and the associated physical processes used in the rate equations (see Equations (2) through (4)) adequately reflect the physics in a real device. The approach compared simulated device behavior with the experimental data reported in the literature (3; 4). Considering the simplicity of the band model, a single donor level, a single trap level, and only free electron carriers, the 2-D numerical model's output was comparable to a remarkable amount of the experimental data in the literature.

The task of comparing the simulated output with the data in the literature was made more difficult by several factors: parameter sets chosen to produce fast (useful) dynamic imaging, unreasonable runtimes for simulations in excess of hundreds of milliseconds, and a time domain of seconds for most of the experimental data. The standard operating point was selected to produce a fast peak (7 ms) and self-erasure (under 40 ms) for quick suppression of static background in a dynamic imaging mode of operation. Variations on this parameter set, when simulated times were run to several seconds, took several weeks for each run. Thus, simulating seconds of device time, when searching for an unknown parameter set, was not feasible. This meant the time domains for the comparison of simulated devices with reported experimental data were not the same: one was tens of milliseconds, the other seconds.

Given the different time domains and the unknown parameters for the experimental devices, the simulated output was very comparable to the reported experimental data. The

simulations showed the same dependence of diffraction efficiency on the spatial modulation index as Shlyagin et al.'s data (3:70). Shlyagin et al.'s reported relationship between the first and second order output during continuous illumination was also simulated (3:71). And finally, comparable behavior was simulated to the early and late turnoff data reported by Bliznetsov et al. (4:750).

The conclusion from the many similarities in the 2-D model's output with that reported in the literature is that the 2-D model is a reasonable representation of the physics in a real device. The differences between the simulations and the reported experimental data can be explained by pointing to the different time domains and the possible differences in the parameter sets that characterize the real and simulated devices.<sup>26</sup>

### **New Predicted Behavior**

To explore device behavior and operation, a parameter sensitivity study was performed near the standard operating point for both continuous illumination and pulsed operation. In addition to providing data that explained how the device worked (see Chapter V), the data also predicted new types of device behavior that had not been previously reported in the literature.

Perhaps the most important behavior is the large peak and self-erasure of an n-dominant device during continuous illumination, a device dominated by negative charge. This continuous illumination output is indistinguishable from that of p-dominant devices. The literature had indicated that experimental devices were controlled only by the positive charge in the device during continuous illumination, and the theory had reflected that charge assumption (4). N-dominant devices can be created by altering the standard operating point with higher absorption coefficients, smaller electron lifetimes, or lower input intensities, none of which are unreasonable

---

<sup>26</sup> One could also speculate on the effects caused by the model's omission of some of the more 'exotic' mechanisms (e.g., multiple trap levels, hopping mechanisms, and additional carriers) hypothesized in the literature (11; 43).

values. Thus it is possible that some experimental devices reported in the literature may have been n-dominant and were not identified as such.

An n-dominant device produces different behavior from that of p-dominant devices during pulsed operations. When the write-beam is turned off, the initial, fast, trapping transient produces an intensification in the output, during any portion of the output's rise, peak, and fall. Intensification, except for that occurring after near total self-erasure, has never been reported in the literature. Because of the short length of the transient (a few transit times at most), if an observer does not have good time resolution and correlation between the input and output data, the transient could easily be overlooked; i.e., the observer would conclude the time of turnoff was at the peak of the transient. A device that shows intensification after turnoff would demonstrate a desirable increase in the output that would enhance the device's dynamic imaging properties.

The trapping transient simulated by the 2-D model exists to some extent in all simulated devices. For n-dominant devices it causes intensification; for p-dominant devices the transient causes an immediate drop in output. The relative size of the transient can be affected by varying model parameters. Interestingly, the literature reports the transient after turnoff only for  $\langle 110 \rangle$  devices (53:1385) and not for the  $\langle 111 \rangle$  devices simulated in this work (4:751). This indicates that the parameters characterizing the 2-D model's devices and those in the literature can vary widely.

In some simulated p-dominant devices (parameter sets), the trapping transient following an early turnoff can produce a drop in output, phase reversal, and reintensification to a peak output higher than that before turnoff. This type of behavior was not reported anywhere in the literature. An early turnoff could be associated with the trailing edge of a small, fast moving object in an input image. After the trailing edge passes, the output drop, phase reversal, and strong reintensification could produce an undesirable effect something like a comet trail.

The literature states that after near total self-erasure and a subsequent write-beam turnoff or when the output drops to zero after any write-beam turnoff, phase reversals occur (12:165). Reports of later experiments suggest that the occurrence of phase reversals in similar scenarios was assumed and may not have been experimentally verified (4:751). The 2-D modeling shows that there is a broad region of parameter space (devices) where phase reversals do not occur in such situations. The trapping transient after turnoff in a p-dominant device often is not large enough to force the output through zero dominance and the output in an n-dominant device after turnoff intensifies without any chance of a phase reversal. Experimental verification of the existence of phase reversals in a device under test would help to identify the device's dominance state and could narrow down the range of possible parameters characterizing its physical properties.

### **Code Enhancements**

Future users of the 2-D numerical model may wish to enhance the code to simulate a broader range of devices. One could start by modifying the Full Multi-Grid Poisson solver to permit non-square grids. This would relax the restrictions on input modulation frequency. The other obvious improvement would be to improve the metal-semiconductor barrier model at the boundaries to more realistically represent a specific device. One might also wish to change the code to allow for a variable number of charge species; this could permit adding additional carriers or traps to the photorefractive material model. It could also be advantageous to allow for multiple crystal orientations. With variable polarizer orientations and a simple model for optical activity, one could use the simulation to show how to remove the effects of optical activity and what happens when the polarizers are rotated. The ambitious software programmer might wish to attempt to implement stiff routines to solve the rate equations; this could remove the problem with the Runge-Kutta slowing down for changes to the very small free electron densities. All of these changes would allow use of the 2-D model for a broader set of applications.

## Photorefractive Material Evaluation

One of the more promising applications of this work is using the 2-D numerical model for photorefractive material evaluation. In optical or electro-optical applications that use photorefractive materials, the list of unknown parameter values characterizing the physical processes in the material is a big impediment to accurate modeling and eventual application improvement. Even if the application is not related to the PRIZ, the 2-D numerical model developed here can assist in identifying the material's unknown parameter values.

The process of identifying those unknown parameter values would begin by using the poorly characterized material to create a PRIZ. Since the material to be tested already exists, the cost of creating a PRIZ would be negligible. The next step would be to use any available experimental methods to obtain the value of as many of the material's parameters as possible. The relevant parameters are the ones identified in the 2-D model, i.e.,  $N_d$ ,  $N_t$ ,  $\xi_t$ ,  $\tau_t$ ,  $\xi_d$ ,  $\xi_{td}$ ,  $\mu$ ,  $\alpha$ , and  $\eta$ . Also, the new PRIZ's metal-semiconductor barriers (created by electrode plating) should be evaluated, and the 2-D code should be updated to reflect those barriers. The next task would be to use the 2-D numerical model to identify the remaining unknown parameter values.

In the near ideal case, the initial research and experimentation will leave unknown just a few parameter values. There should be reasonable limits on the ranges of the remaining unknown values. Using those limits and the known parameter values, a sensitivity study, for both continuous and pulsed operation, would be created with the 2-D numerical model. For comparison and analysis, a similar series of experimental runs would be made on the new PRIZ.

The researcher needs to correlate the experimental tests of the new PRIZ with the results of the simulated sensitivity study. The analysis would take advantage of behavior that identifies dominance states. For example, transients creating intensification after turnoff would indicate an n-dominant device; the sensitivity study would limit the range of parameters values for this n-

dominant device. Simulations show that phase reversals during continuous illumination occur in only small operating regions, further limiting the parameters' possible ranges. In the 2-D numerical model, phase reversals and strong reintensification after an early turnoff indicate a p-dominant device, again a situation limiting parameter values. Other characteristics produce similar limitations on parameters.

The complete analysis may identify reasonable parameter values. In the worst case scenario, the analysis will only limit the possible range of the parameters, allowing for a more effective experimental determination of the remaining unidentified values of the photorefractive material's parameters.

## **Summary**

This work created a first-of-its-kind 2-D numerical model of the PRIZ; used that model to understand the optical processing in the PRIZ; predicted several new types of behavior; and demonstrated that the model is a reasonable representation of a real device. The following bullets summarize this work's contributions to the literature:

- The first 2-D numerical model of the PRIZ with good quantitative output.
- A concept for analyzing internal dynamics in terms of dominance of the positive or negative charge regions and their associated transverse fields.
- The mathematical theory of Bliznetsov et al. (4) is shown to produce incorrect quantitative output due to the omission of both transverse drift and exponential absorption, essential mechanisms included in this work's 2-D model.
- A previously unreported operating region is identified where negative charge controls the PRIZ's output during continuous illumination.
- A broad operating region is identified where no phase reversals occur after write-beam turnoff. The literature identifies phase reversals in similar turnoff situations (12; 4).
- The 2-D model predicts behavior where transients after write-beam turnoff produce intensification (in n-dominant devices) or drops in the output, phase

reversals, and reintensification to larger output than before turnoff (for early turnoff in p-dominant devices). Neither behavior is reported in the literature.

- A comparison of simulated output from the 2-D model with experimental data reported in the literature indicates that the 2-D numerical model is a reasonable representation of the physics in a real device.



### Appendix A. 2-D Numerical Simulation Parameter Sets

To keep the text to a minimum, the complete data sets were not provided with each figure.

The following table shows the deviation of each parameter set discussed in the text from the standard operating point:  $I_o=10 \text{ W/m}^2$ ,  $m=0.9$ ,  $v_x=2 \text{ lines/mm}$ ,  $\lambda_w=488 \text{ nm}$ ,  $V=1 \text{ kV}$ ,  $d=1 \text{ mm}$ ,  $\alpha=1000 \text{ m}^{-1}$ ,  $n_s=1.38 \cdot 10^{18} \text{ m}^{-3}$ ,  $\mu=10^{-6} \text{ m}^2/\text{V/s}$ ,  $\xi_i=5 \cdot 10^{18} \text{ s/m}^3$ ,  $\xi_d=10^{22} \text{ s/m}^3$ ,  $\xi_{id}=\infty \text{ s/m}^3$ ,  $\tau_i=10 \text{ s}$ ,  $\eta=1$ ,  $N_i=10^{22} \text{ m}^{-3}$ ,  $N_d=2.76 \cdot 10^{24} \text{ m}^{-3}$ , and  $\epsilon=4.43 \cdot 10^{-10} \text{ F/m}$ . The initial, at  $t=0$ , electron lifetime is  $\tau=0.5 \text{ ms}$  (half a transit time). In the tables,  $t_{\text{off}}$  refers to the time the write-beam is turned off.

Table 3. Parameter sets b26 to b54

Set	Parameters Varied	Change from standard operating point
b26	$\alpha$	none
b28	$\xi_i$	none
b29	$I_o$	none
b30	$\mu$	none
b31	$\tau_i$	none
b32	$t_{\text{off}}$	none
b36	$t_{\text{off}}$	$\xi_i=5 \cdot 10^{17} \text{ s/m}^3$
b37	$m$	$I_o=6 \text{ W/m}^2$ , $m=0.2$ , $\xi_i=10^{19} \text{ s/m}^3$
b40	$t_{\text{off}}$	$\xi_{id}=2.77 \cdot 10^{18} \text{ s/m}^3$
b42	$V$	none
b43	$I_o$	$\lambda_w=442 \text{ nm}$ , $\alpha=3500 \text{ m}^{-1}$
b45	$\xi_i$	$I_o=6 \text{ W/m}^2$ , $\alpha=3500 \text{ m}^{-1}$
b46	$m$	$I_o=0.3 \text{ W/m}^2$ , $v_x=4 \text{ lines/mm}$ , $\lambda_w=442 \text{ nm}$ , $\alpha=3500 \text{ m}^{-1}$ , $\xi_i=3 \cdot 10^{17} \text{ s/m}^3$ , $\tau_i=0.75 \text{ s}$
b47	$v_x$	none
b48	$t_{\text{off}}$	$\tau_i=0.1 \text{ s}$
b51	$t_{\text{off}}$	$\xi_i=5 \cdot 10^{17} \text{ s/m}^3$ , $\tau_i=0.1 \text{ s}$
b52	$\tau_i$	$I_o=6 \text{ W/m}^2$ , $\alpha=3500 \text{ m}^{-1}$ , $\xi_i=5 \cdot 10^{17} \text{ s/m}^3$
b54	$t_{\text{off}}$	$\xi_i=5 \cdot 10^{17} \text{ s/m}^3$ , $\xi_{id}=2.77 \cdot 10^{18} \text{ s/m}^3$

Table 4. Parameter sets b55 to b89

Set	Parameters Varied	Change from standard operating point
b55	grid size, E updating	none
b59	$\xi_{td}$	none
b60	$\xi_d$	none
b61	$m$	$I_o=0.3 \text{ W/m}^2$ , $V=1.8 \text{ kV}$ , $d=0.5 \text{ mm}$ , $\alpha=800 \text{ m}^{-1}$ , $\xi_t=6.95 \cdot 10^{17} \text{ s/m}^3$ , $\tau_t=7.5 \text{ ms}$
b64	mechanisms	$m=0.74$ , $\alpha=800 \text{ m}^{-1}$
b66	$n_s$	none
b69	$t_{off}$	$\tau_t=0.05 \text{ s}$ , $n_s=3.3 \cdot 10^{17} \text{ m}^{-3}$
b70	max $\eta$	$\alpha=800 \text{ m}^{-1}$ , $\xi_t=10^{18} \text{ s/m}^3$ , $\mu=5 \cdot 10^6 \text{ m}^2/\text{V/s}$ , $\tau_t=0.01 \text{ s}$ , $V=2 \text{ kV}$ , $m=0.95$ , $n_s=3.3 \cdot 10^{17} \text{ m}^{-3}$
b71	$t_{off}$	$\tau_t=0.01 \text{ s}$ , $n_s=3.3 \cdot 10^{17} \text{ m}^{-3}$
b72	$t_{off}$	$n_s=3.3 \cdot 10^{17} \text{ m}^{-3}$ , $\tau_t=0.025 \text{ s}$
b73	$t_{off}$	$\xi_d=2.77 \cdot 10^{16} \text{ s/m}^3$
b74	$t_{off}$	$\xi_d=2.77 \cdot 10^{16} \text{ s/m}^3$ , $\tau_t=0.1 \text{ s}$
b75	reintensification	$\xi_d=2.77 \cdot 10^{16} \text{ s/m}^3$ , $\xi_{td}=2.77 \cdot 10^{16} \text{ s/m}^3$
b76	reintensification	$I_o=6 \text{ W/m}^2$ , $\lambda_w=442 \text{ nm}$ , $\alpha=4000 \text{ m}^{-1}$ , $n_s=6.917 \cdot 10^{17} \text{ m}^{-3}$ , $\xi_d=2.77 \cdot 10^{16} \text{ s/m}^3$ , $\tau_t=0.1 \text{ s}$
b77	reintensification	$\lambda_w=442 \text{ nm}$ , $\alpha=4000 \text{ m}^{-1}$ , $n_s=6.917 \cdot 10^{17} \text{ m}^{-3}$ , $\xi_d=2.77 \cdot 10^{16} \text{ s/m}^3$ , $\tau_t=0.1 \text{ s}$
b78	reintensification	$\lambda_w=442 \text{ nm}$ , $\alpha=3000 \text{ m}^{-1}$ , $n_s=6.917 \cdot 10^{17} \text{ m}^{-3}$ , $\xi_d=2.77 \cdot 10^{16} \text{ s/m}^3$ , $\tau_t=0.1 \text{ s}$
b79	reintensification	$\lambda_w=442 \text{ nm}$ , $\alpha=2000 \text{ m}^{-1}$ , $n_s=6.917 \cdot 10^{17} \text{ m}^{-3}$ , $\xi_d=2.77 \cdot 10^{16} \text{ s/m}^3$ , $\tau_t=0.1 \text{ s}$
b80	$n_s$ , $\xi_d$ , $\tau_t$	$\lambda_w=442 \text{ nm}$ , $\alpha=2000 \text{ m}^{-1}$
b81	$t_{off}$	$\lambda_w=442 \text{ nm}$ , $\alpha=2000 \text{ m}^{-1}$ , $n_s=3.5 \cdot 10^{17} \text{ m}^{-3}$ , $\xi_d=2.77 \cdot 10^{16} \text{ s/m}^3$ , $\tau_t=0.1 \text{ s}$
b82	$t_{off}$	$\lambda_w=442 \text{ nm}$ , $\alpha=2000 \text{ m}^{-1}$ , $n_s=1.0 \cdot 10^{17} \text{ m}^{-3}$ , $\xi_d=2.77 \cdot 10^{16} \text{ s/m}^3$ , $\tau_t=0.1 \text{ s}$
b83	$t_{off}$	$\lambda_w=442 \text{ nm}$ , $\alpha=2000 \text{ m}^{-1}$ , $n_s=2.77 \cdot 10^{16} \text{ m}^{-3}$ , $\xi_d=2.77 \cdot 10^{16} \text{ s/m}^3$ , $\tau_t=0.1 \text{ s}$
b84	$\xi_d$ , $\tau_t$	$\lambda_w=442 \text{ nm}$ , $\alpha=2000 \text{ m}^{-1}$ , $n_s=6.7 \cdot 10^{16} \text{ m}^{-3}$
b85	$\alpha$	$\lambda_w=442 \text{ nm}$ , $n_s=2.77 \cdot 10^{16} \text{ m}^{-3}$ , $\xi_d=2.77 \cdot 10^{16} \text{ s/m}^3$ , $\tau_t=0.1 \text{ s}$
b86	quick peak	$\alpha=500 \text{ m}^{-1}$ , $\xi_t=4 \cdot 10^{18} \text{ s/m}^3$ , $\mu=5 \cdot 10^{-6} \text{ m}^2/\text{V/s}$ , $\tau_t=1 \text{ s}$ , $V=500 \text{ V}$ , $v=1 \text{ line/mm}$ , $m=0.2$ , $n_s=2.75 \cdot 10^{18} \text{ m}^{-3}$ , $\xi_d=3.0 \cdot 10^{16} \text{ s/m}^3$ , $\xi_{td}=10^{18} \text{ s/m}^3$
b87	slow peak	$I_o=0.1 \text{ W/m}^2$ , $\alpha=4000 \text{ m}^{-1}$ , $\xi_t=10^{17} \text{ s/m}^3$ , $\mu=5 \cdot 10^{-7} \text{ m}^2/\text{V/s}$ , $\tau_t=0.5 \text{ s}$ , $V=2 \text{ kV}$ , $m=0.95$ , $n_s=3.3 \cdot 10^{17} \text{ m}^{-3}$ , $\xi_{td}=10^{18} \text{ s/m}^3$
b88	$\tau_t$	$I_o=6 \text{ W/m}^2$ , $\alpha=3500 \text{ m}^{-1}$ , $\xi_t=10^{19} \text{ s/m}^3$
b89	$t_{off}$	$\xi_t=5 \cdot 10^{17} \text{ s/m}^3$ , $\xi_d=2.77 \cdot 10^{16} \text{ s/m}^3$

## ***Appendix B. Qualitative Analysis using Dominance***

To assist in understanding the physics associated with the PRIZ, this appendix describes a qualitative method of analyzing the space charge dynamics of the device. The method identifies five key factors that control the charge dynamics and how they effect dominance and diffraction efficiency. The key quantity is dominance. It's square is roughly proportional to diffraction efficiency. It is defined as an 'average' value of the magnitude of the longitudinal integral of the transverse field. Since large localized charges tend to create large localized fields, dominance can be intuitively (though not completely accurately) related to the size of the local net charge. In this fashion, the output observations (diffraction efficiency) can be related to what happens with the internal charge dynamics.

### **Charge and Field Distributions**

For purposes of this analysis, the input intensity distribution is sinusoidal. The write-beam is normal to the cathode face of the crystal, so that as it is passes through the device, locations farther from the electrode see smaller sinusoidal intensities. At each longitudinal location, photons are absorbed creating positively charged donors and free electrons. The electrons drift through the crystal and are trapped. Over time, the positive donor, negative trap, and free electron distributions evolve. During this evolution, the electric fields also change via Gauss' law in turn effecting the drift of the electron carriers and the redistribution of charge. Soon after the write-beam is turned on (when the charge distributions are small and the only noticeable field is the longitudinal one caused by the external voltage), transverse slices of the charge distributions are sinusoidal just like the input. Longitudinal drift causes separation of the charges such that a net positive charge builds up near the cathode with a negative charge closer to the anode. Figure 47

shows typical charge and field distributions for a short write-beam exposure. Notice that the two period input's length (in the  $x$  direction) is chosen such that minima in the input intensity grating correspond to the edges and the midpoint.<sup>27</sup>

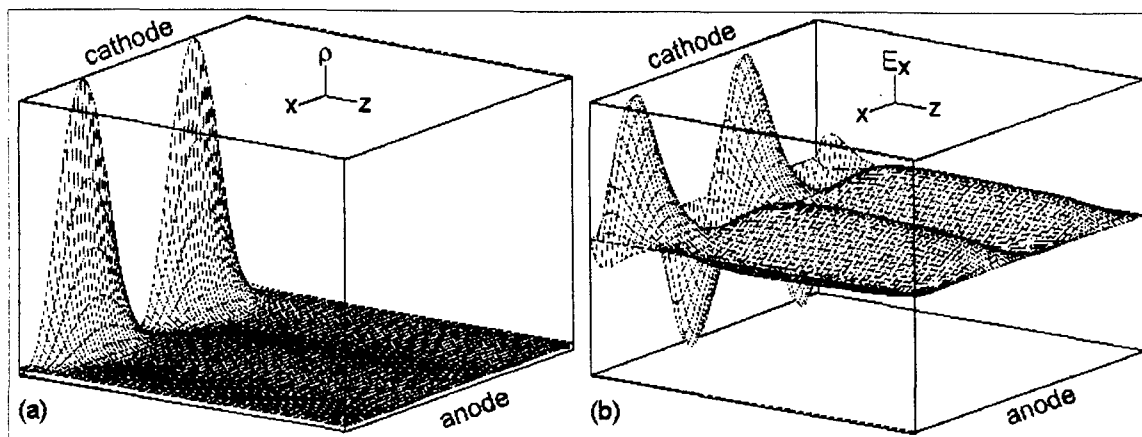


Figure 47. (a) Sample net charge density,  $\rho(x,z,t)$ , and (b) transverse field grating,  $E_x(x,z,t)$  at a time  $t$  before significant distortions develop.

Figure 47 is a very early snapshot of the gratings. The time,  $t$ , was actually less than  $\tau$ , the trapping time. Hence, the negative trap grating and the free electron grating are still about the same size. It is only when time is much greater than  $\tau$  that the free electron grating becomes relatively negligible. Figure 48 shows longitudinal cross sections of the charge gratings at time  $t$  and at a transverse location,  $x$ , corresponding to one of the net charge peaks in Figure 47a. The relative shapes of the gratings in Figure 48 will become important in the next few sections.

### Dominance

The above picture (Figure 47) of the transverse field grating can provide a basis for understanding the physical processes seen in the numerical simulation. Since  $c(x) = \text{sign}\{\cos(kx + \pi)\}$ , and  $\lambda = d/2$ , the dominance is the average value of the longitudinal integral

---

<sup>27</sup> That is, minima are at  $x$  equals  $0$ ,  $d/2$ , and  $d$  where  $d$  is the simulated width and depth of the crystal.

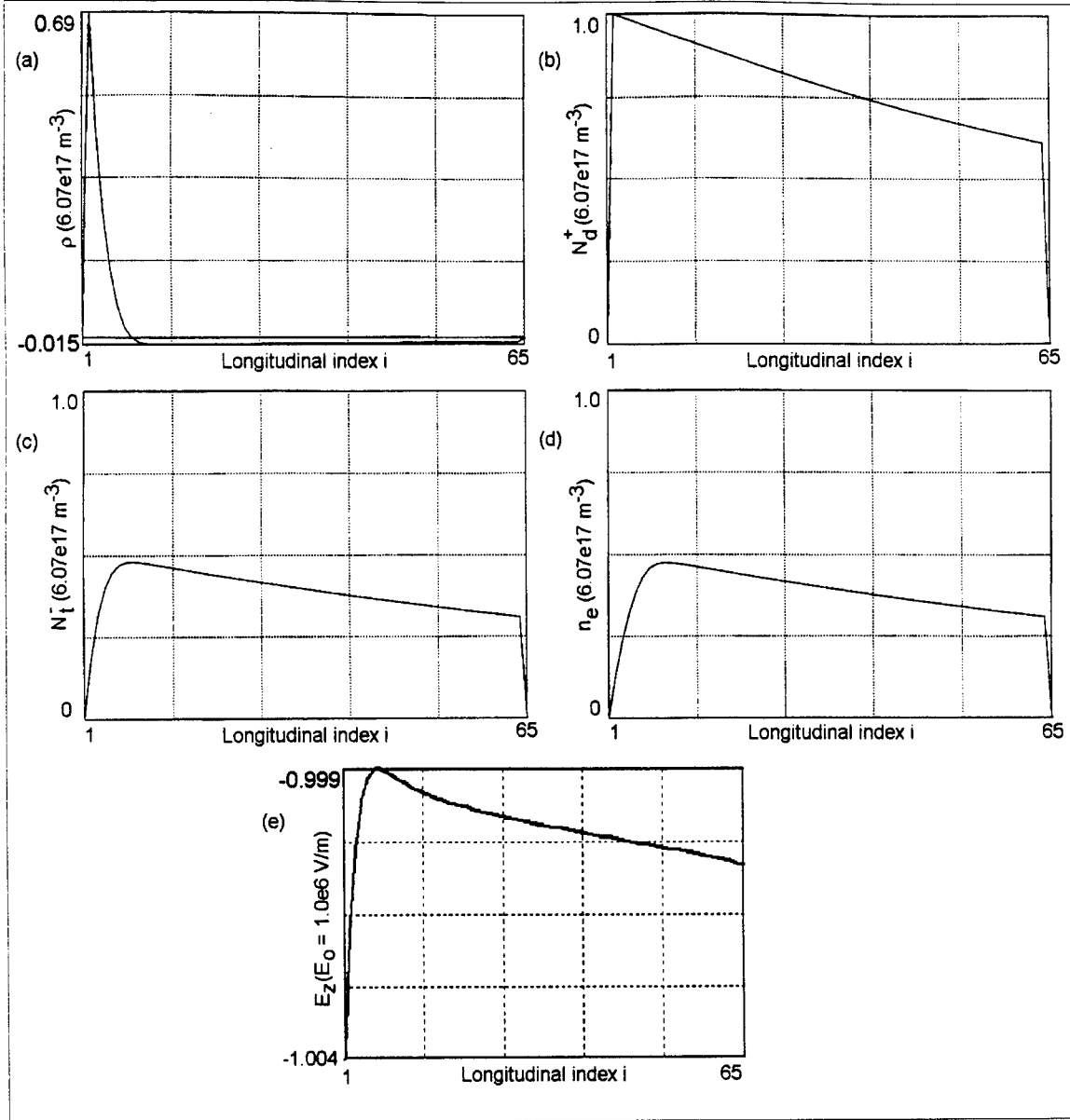


Figure 48. Longitudinal cross sections of the charge gratings at a peak in the input write-beam. (a) Net charge density,  $\rho(z,t)$ , (b) positive donor grating,  $N_d^+(z,t)$ , (c) negative trap grating,  $N_t^-(z,t)$ , (d) free electron grating,  $n_e(z,t)$ , and (e) longitudinal electric field,  $E_z(z,t)$ .  $t < \tau$ .

when every other quarter of the transverse field distribution, in the transverse direction, is negated (flipped upside-down). Therefore dominance can be expressed as

$$\delta(t) \equiv \frac{1}{m} \sum_{i=1}^m [c(x_i) \Delta \varphi(x_i, t)] = \frac{2\pi n_o^3 r_{41}}{m \lambda_r} \sqrt{\frac{2}{3}} \sum_{i=1}^m \left[ c(x_i) \int_0^d E_x(x_i, z, t) dz \right] \quad (42)$$

where  $m$  is the number of transverse points sampled;  $x_i$  is the value of the  $x$  coordinate at each of those sampled points; and  $\delta$  is dominance.

But how does dominance make the analysis easier? Note that in Figure 47 the positive charge peak near the cathode (and its transverse fields) creates a positive longitudinal subintegral in Equation (42) that contributes a positive value to  $\delta$  and that the negative charge region nearer the anode creates a negative longitudinal subintegral that contributes a negative value to  $\delta$ . If one divides the longitudinal integral of the transverse field into two subintegrals based on these regions, then  $\delta$  indicates which subintegral is bigger. A *positive* value for  $\delta$  indicates the region of positive charge near the cathode dominates the longitudinal integral, while a *negative* value for  $\delta$  indicates the negative region nearer the anode dominates the longitudinal integral. In this paper, the term p-dominance is used when the positive space charge region is dominant and the term n-dominance is used when the negative space charge region is dominant.

It can be shown that when the sign of the phase shift between the fast and slow axes changes, the sign of the output read-beam's electric field also changes. Thus a phase reversal in the output should correspond to a change in the sign of  $\delta$ . Also, since diffraction efficiency goes as the square of dominance, a phase reversal would correspond to a minimum in first order diffraction efficiency. Likewise, a maximum or minimum in  $\delta$  would correspond to a maximum or minimum in first order diffraction efficiency. Each of these relationships is observed in the numerical output. Thus the behavior of  $\delta$  can be used to predict the *qualitative* optical performance of the PRIZ in terms of first order diffraction efficiency.

### **Factors in Grating Dynamics**

So, if the factors which influence the evolution of the charge distributions can be related to the behavior of dominance, the optical behavior of the PRIZ can be qualitatively predicted and understood. The five factors chosen for this purpose are:

- 1) the longitudinal slope of the donor grating (absorption) (see Figure 48b),
- 2) the longitudinal separation between the donor and trap gratings (longitudinal drift),
- 3) the rate of growth of the trap gratings (effective trapping rate),
- 4) the transverse variation in the donor grating (write-beam modulation), and
- 5) the transverse distortion in the free electron grating (transverse drift).

Each factor is addressed in the following paragraphs.

**Longitudinal Slope of the Donor Grating (Absorption).** The longitudinal slope in the donor grating is caused by the absorption of photons from a write-beam with an exponential transmittance function (49:1) given by

$$I(z) = I_o e^{-\alpha z} \quad (43)$$

where  $I_o$  is the intensity incident to the crystal;  $z$  is the optical path length through the crystal; and  $I$  is the intensity of the beam at any location  $z$ . If transverse drift and the trapping time are not too large, the free electrons will not move far from their source (ionized donors), and the trap grating will have the same exponential slope as the ionized donor grating.

Thus, given two different absorption coefficients that might correspond to either two different write-beam frequencies or two different materials, one finds two different longitudinal slopes in the positive donor grating. In order to evaluate only the change in the exponential slope, assume that the intensity is adjusted so that  $I \cdot \alpha = \text{constant}$ . Then for two different absorption coefficients, the devices will both see the same number of absorbed photons at the cathode.

Now assume that the peak amplitudes of the positive donor and negative trap gratings are equal and that there is some amount of longitudinal separation caused by longitudinal drift of the electrons. Also simplify the shapes of the gratings by assuming that the exponential slopes can be represented by straight lines. Figure 49 shows a longitudinal slice (cross section at a point of peak input) through the donor and trap gratings for two cases of different absorption. The two lines in

each plot represent the amplitude of the donor (heavy line) and trap (thin line) densities, while the hatched regions (the space between the two lines) represent positive and negative space charge regions. A vertical line is added to the plots to separate the two charge regions. Note that in the first case, where the absorption coefficient is smaller, the net charge density is positive.<sup>28</sup> In the higher absorption case the net charge density is negative.

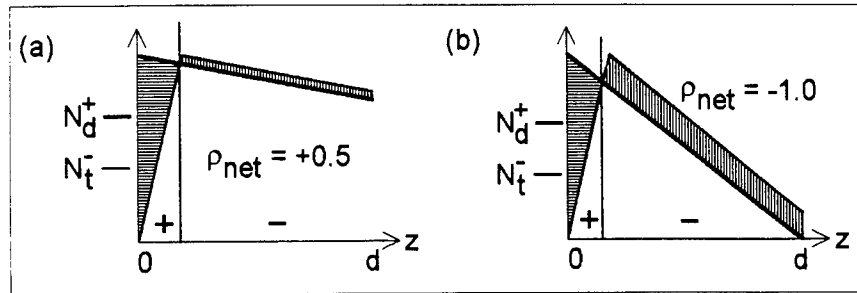


Figure 49. Longitudinal slope of positive donor grating for (a) low and (b) high absorption.  $I \cdot \alpha = \text{constant}$ .

Intuitively, the obvious step is to conclude that in the first case in Figure 49, the positive space charge region dominates while in the second the negative space charge region dominates. Although this method estimates net charge density and not the integral of the transverse field, one expects larger charges to create larger fields and hence the two quantities to have similar effects. Thus, Figure 49 suggests that as the absorption coefficient is increased, the dominance state of the crystal shifts towards n-dominance.

**Longitudinal Separation in Donor and Trap Gratings (Longitudinal Drift).** The second factor in grating dynamics is the longitudinal separation of the donor and trap gratings. The external field forces the free electrons towards the anode from their point of generation. This produces spatial separation between the donor grating and the trap grating. As the trapping time,

<sup>28</sup> The numbers for the ionized donor and trap gratings are actually densities. But these correspond to signed charge densities that can be added to each other. The net charge densities referred to in the figure are actually just relative numbers obtained by taking the difference in areas of the shaded positive and negative charge regions.



$\tau$ , increases, the electrons drift further before being trapped, and the longitudinal separation is increased. An increased trapping time might arise from a change in the energy level or density of traps. The longitudinal separation might also be changed by changing the drift velocity ( $\mu E$ ) through either the external voltage or the free electron's mobility.

Figure 50 shows the same representation of the two gratings as shown in Figure 49, but this time with the trapping time increased rather than the absorption coefficient. This results in an increased longitudinal separation between the trap and donor gratings without changing the longitudinal slope. By examining the net charge in the two cases, one notes that the dominance of the positive charge region increases. This suggests that the transverse fields will increase more in the positive space charge region, and one could expect a shift towards p-dominance as the trapping time increases or alternately as the spatial separation between the two net charge regions increases. Since this example does not suggest a change in the type of dominance (assuming the gentle longitudinal slope shown), one could go one step further and expect diffraction efficiency to increase as the trapping time increases.

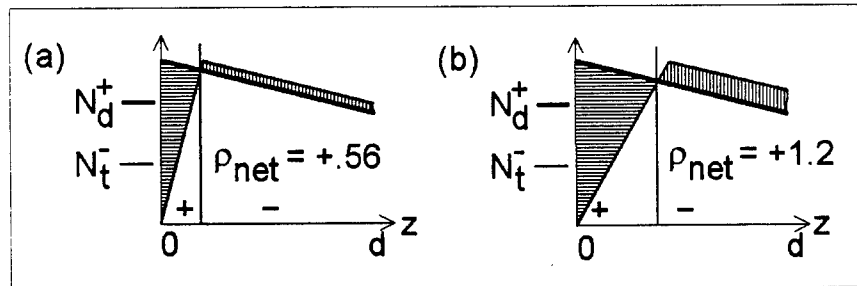


Figure 50. Spatial separation of donor and trap gratings for (a) short and (b) long trapping time.

**Growth Rate of the Trap Grating (Effective Trapping Rate).** The third factor in grating dynamics is the rate of change in the amplitude of the trap grating – the effective trapping rate. A change in the effective trapping rate might arise from an increase in the thermal ionization rate of the traps. This would increase the detrapping rate or alternately decrease the *effective*

trapping rate. In this case, the effective trapping rate is defined as the trapping rate (specified by the electron trapping time) minus the thermal ionization or detrapping rate. Further, assume that the analysis looks at the effects of this change over a long enough time that the increase in the free electron grating is negligible. Other factors such as trap-to-donor recombination, direct donor recombination, or photogeneration of electrons from traps by the read-beam could also change the effective trapping rate.

Figure 51 shows how decreasing the effective trapping rate reduces the amplitude of the trap grating without effecting the amplitude of the donor grating. The result is that the net charge shifts towards a more positive value. As seen above, this suggests a shift towards p-dominance.

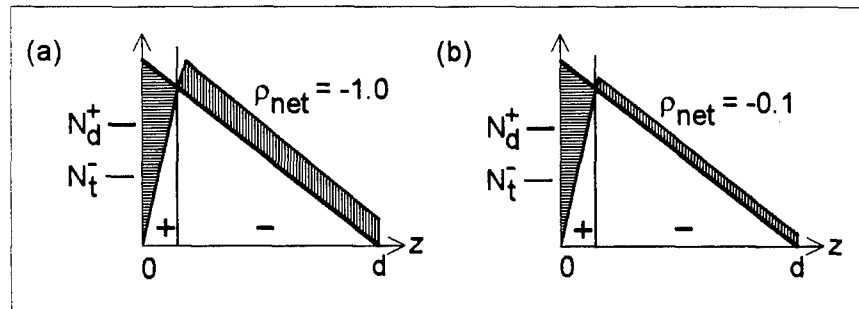


Figure 51. Effective trapping rate for (a) high and (b) low trapping rate.

**Transverse Variation in the Donor Grating (Write-beam Modulation).** The fourth factor is transverse variation in the amplitude of the donor grating. This variation reflects the input intensity distribution. A small modulation index reduces the variation and the resulting size of the fields; a large modulation index (or peak intensity in Equation (1)) increases the variation and the size of the transverse fields. Similarly, given a fixed modulation index (for a given spatial modulation frequency), increasing the peak intensity also increases the transverse variation.

Figure 52 shows a longitudinal slice of the donor and trap gratings for two simulations when only the peak input intensity of the write-beam has changed. Assume the spatial modulation frequency is constant in both cases, and the modulation index is one. Since only the intensity

changes (not the trapping time or absorption coefficient), one sees only an increase in the net positive charge region. The larger numbers of electrons create a correspondingly larger trap grating whose spatial separation from the donor grating has not changed (no change in  $\tau$ ). Since  $\alpha$  has not changed, there is no change in the longitudinal slope. Hence one expects to see a shift towards p-dominance as peak intensity is increased.

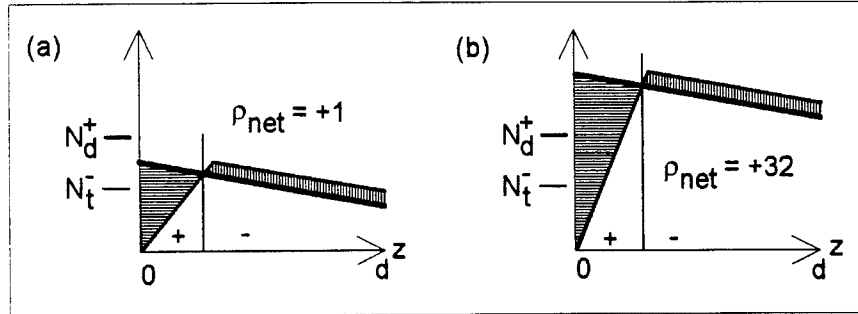


Figure 52. Transverse variation in the amplitude of the donor grating for (a) low and (b) high peak input intensity.

**Transverse Distortion in the Free Electron Grating (Transverse Drift).** The fifth factor discussed here is transverse distortion in the free electron grating from transverse drift. Transverse drift becomes important when the transverse fields from the local space charge provide the free electrons with significant transverse velocity components that distort the trap grating. If the electrons only moved in the longitudinal direction there would be no transverse drift and no transverse distortion of the free electron grating. A transverse cross section of a *distortion free* electron grating would look just like the donor grating. Of course the amplitudes would not be the same.

Figure 53 depicts two transverse slices through the crystal. The plots show relative shapes for one spatial period of the transverse write-beam grating, assuming two periods per length  $d$ . Note that the sinusoidal donor grating is simplified to a semi-circle. The plot shows roughly what happens to the free electron grating in the presence of transverse drift in either the positive or negative space charge regions. Where positive net charge peaks exist, the free electrons are forced

towards the peaks by the transverse fields. Where negative net charge peaks exist, the electrons are forced away from the peaks.

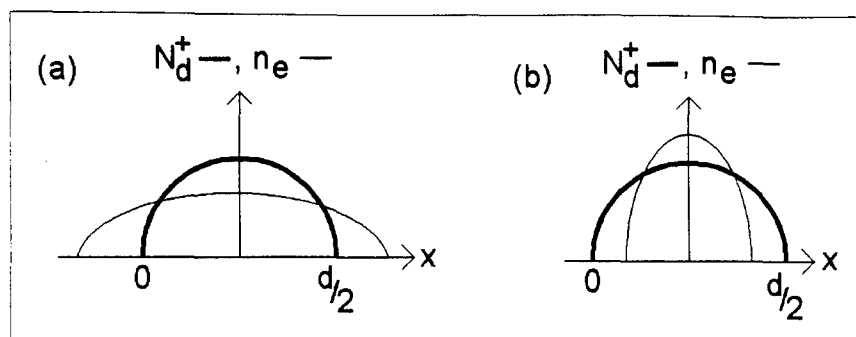


Figure 53. Transverse distortion in the free electron grating in (a) the negative space charge region and (b) the positive space charge region.

Since the trapping rate is proportional to the density of free electrons, the rate of growth of the trap grating is effected by the distortions. The trap grating grows faster at the positive peaks and in the valleys between the negative peaks. The trap grating grows slower at the negative peaks and in the valleys between the positive peaks. Thus distortion in both regions causes a slowing in the growth of the net charge peaks. In the negative space charge region, one expects a rise in the growth rate of the negatively charged valley floors that is equivalent to the fall in the growth rate of the negative peaks.

The size of any dominance shift due to distortion of the trap grating is very dependent upon the particular conditions encountered. It is not possible to predict a general trend for generic conditions. The usefulness of this factor only becomes apparent when explaining the observed peaks in diffraction efficiency and the self-erasure after those peaks.

Of course, the five factors described above are not an exclusive group. Other factors exist and are often significant. However, the use of these five factors provides a method for qualitative analysis that can greatly assist one's understanding of the dynamics of grating storage in the PRIZ and how those grating dynamics effect diffraction.

### Appendix C. Jones Matrix Derivation of Output Phase Shift

This appendix develops an expression for the output electric field via a Jones matrix derivation. The derivation includes the input and output polarizers and the photorefractive crystal. The results are applicable to any transverse location in the device, assuming the input is normal to the cathode.

Start by representing the electro-optic and polarization effects on the read-beam in terms of Jones matrices for Figure 54. Note that for simplicity, the axes shown here are not those used elsewhere in this paper; for the actual crystal and polarizer orientations, see the discussion of Figure 4 on page 11.

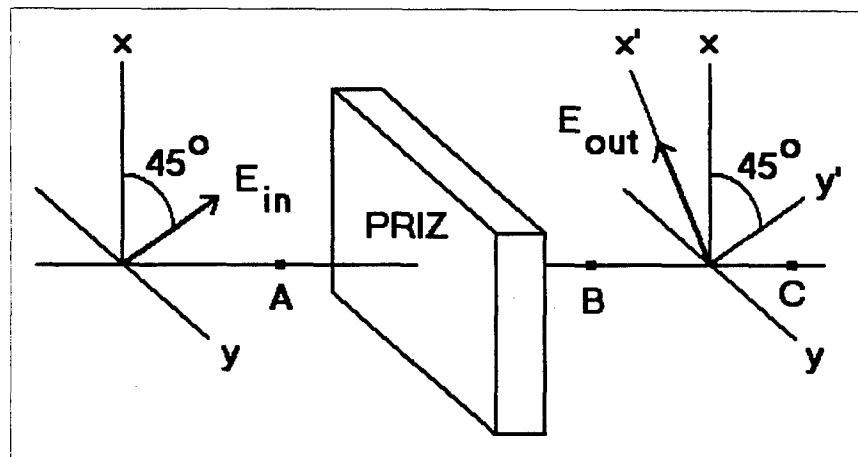


Figure 54. Device representation for Jones matrix calculations neglecting optical activity

Developing the equations for Figure 54 results in a generic expression for the output electric field after the output crossed polarizer at any transverse location. Assume the input read-beam is a normally incident plane wave linearly polarized in the  $x$ - $y$  coordinate system and represented by  $E_{in}$ , the electric field after the input linear polarizer. The  $x$  and  $y$  axes were chosen to correspond to the BSO crystal's slow and fast axes, respectively. At point  $A$ , the field's component values, assuming a unit magnitude and a rotation from either axis of  $45^\circ$ , are

$$E_{in} = \begin{bmatrix} \frac{1}{\sqrt{2}} \\ \frac{1}{\sqrt{2}} \end{bmatrix} \quad (44)$$

As the ray passes through the (111) oriented BSO, the electric field's components undergo fast and slow phase shifts represented at point *B* by the matrix

$$\begin{bmatrix} e^{i\varphi_s} & 0 \\ 0 & e^{i\varphi_f} \end{bmatrix} \quad (45)$$

The phase shifts  $\varphi_s$  and  $\varphi_f$  are described in Equations (14) and (15) respectively. The electric field then passes through the plane of the output crossed polarizer which is oriented in the new  $x'-y'$  coordinate system. This new system is rotated  $45^\circ$  from the input coordinate system. Thus the rotation matrix

$$\begin{bmatrix} \frac{1}{\sqrt{2}} & -\frac{1}{\sqrt{2}} \\ \frac{1}{\sqrt{2}} & \frac{1}{\sqrt{2}} \end{bmatrix} \quad (46)$$

changes the field representation to the new coordinate system at point *C*. Putting the elements together gives the Jones matrix

$$\begin{bmatrix} E_{out,\perp} \\ E_{out,\parallel} \end{bmatrix} \equiv \begin{bmatrix} E_{x'} \\ E_{y'} \end{bmatrix} = \begin{bmatrix} \frac{1}{\sqrt{2}} & -\frac{1}{\sqrt{2}} \\ \frac{1}{\sqrt{2}} & \frac{1}{\sqrt{2}} \end{bmatrix} \begin{bmatrix} e^{i\varphi_s} & 0 \\ 0 & e^{i\varphi_f} \end{bmatrix} \begin{bmatrix} \frac{1}{\sqrt{2}} \\ \frac{1}{\sqrt{2}} \end{bmatrix} = \frac{1}{2} \begin{bmatrix} e^{i\varphi_s} - e^{i\varphi_f} \\ e^{i\varphi_s} + e^{i\varphi_f} \end{bmatrix} \quad (47)$$

where  $\perp$  indicates the direction perpendicular to the input polarizer, and  $\parallel$  indicates a direction parallel to it. The Jones vector for the output field shows only the complex amplitudes of the field components (23:62). These complex amplitudes are not 'real' expressions of the wave, but rather representations of the relative phase between the components. Selecting the component of the

output in the direction of the crossed polarizer, and adding back in the time dependence of the field, gives the field after the output crossed polarizer.

$$E_{out}(x,t) \equiv E_{out,\perp}(x,t) = \frac{1}{2} \left( e^{i\Phi_s(x)} - e^{i\Phi_f(x)} \right) e^{-i\omega t} \quad (48)$$

where  $x$  is now the true transverse coordinate of the PRIZ shown in Figure 4 on page 11;  $t$  is time; and  $\omega$  is the frequency of the read-beam.

### ***Appendix D. Sensitivity Analysis***

The results of the sensitivity analysis were reported in the body of the dissertation in such as way as to explain intuitively and analytically how the device operated. However, the data can also be used to predict changes in output or device performance as a parameter is changed. Remember that the data presented below only applies to the local parameter space selected for the simulation. If a variable in that parameter space is changed, the device will not necessarily perform as shown in the plots. The following graphs show the peak first order diffraction efficiency for each variable (in units of  $\eta_0 = 1.5625 \cdot 10^{-4}$ ), the time that peak occurred (in ms) during continuous illumination, and the peak dominance ( $\times 10^{-2}$ ) in each run. The variation in output is usually not linear or even monotonic, therefore, the data is graphed rather than reduced to equation form. Also note that the charts were created in Mathcad™ where the subscript  $i$  simply refers to the index value of each matrix (variable) element; i.e., it can be ignored.

Figure 55 and Figure 56 show the sensitivity of the device to the absorption coefficient. Notice that diffraction efficiency goes through a minimum at the value that creates a zero dominance.



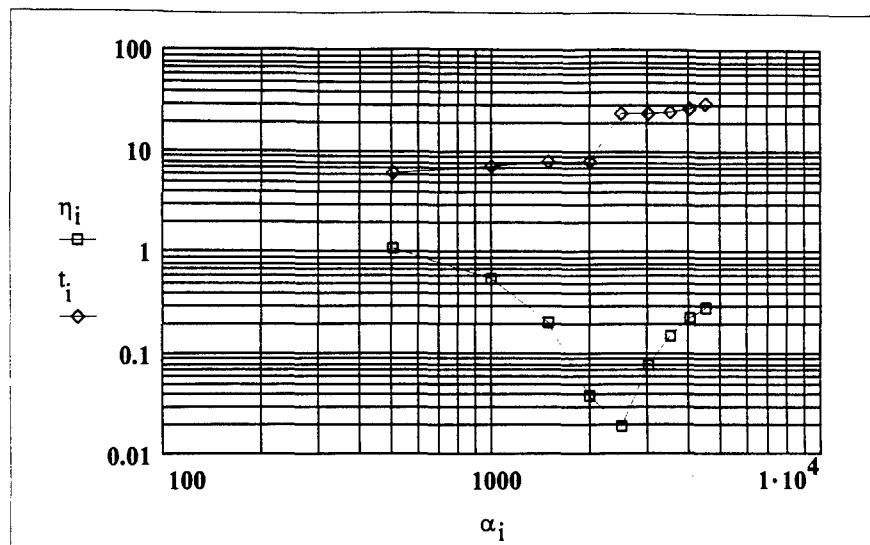


Figure 55. Diffraction efficiency and timing sensitivity to absorption coefficient,  $\alpha$  ( $\text{m}^{-1}$ ). (b26)

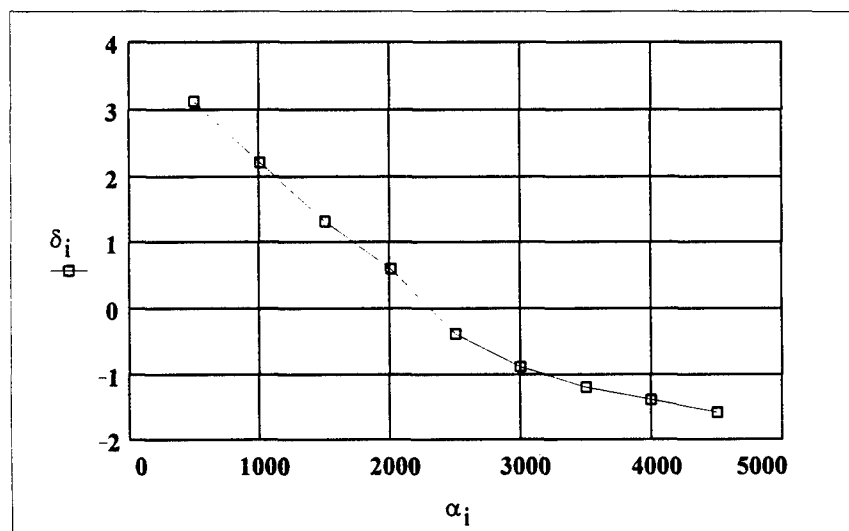


Figure 56. Dominance sensitivity to absorption coefficient,  $\alpha$  ( $\text{m}^{-1}$ ). (b26)

The sensitivity to trapping time at a low absorption coefficient, Figure 57 and Figure 58, also show a minimum corresponding to a dominance zero.

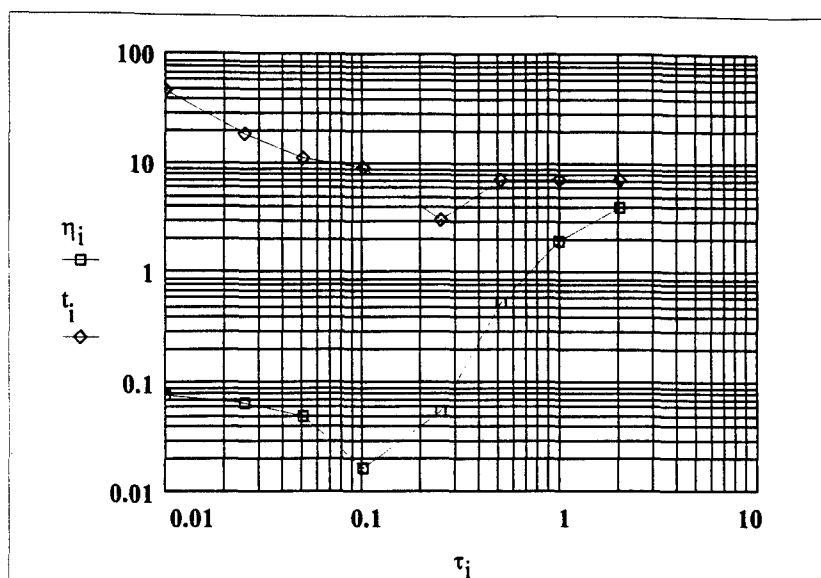


Figure 57. Diffraction efficiency and timing sensitivity to electron lifetime,  $\tau$  (ms), at  $\alpha = 1000 \text{ m}^{-1}$ . (b28)

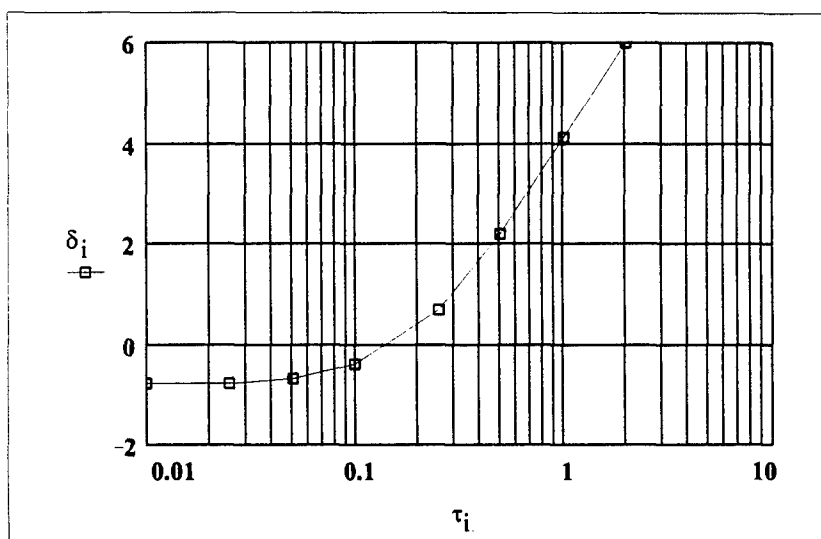


Figure 58. Dominance sensitivity to electron lifetime,  $\tau$  (ms), at  $\alpha = 1000 \text{ m}^{-1}$ . (b28)

At higher absorptions, Figure 59 and Figure 60, the minimum is barely achievable in the range of trapping times investigated.

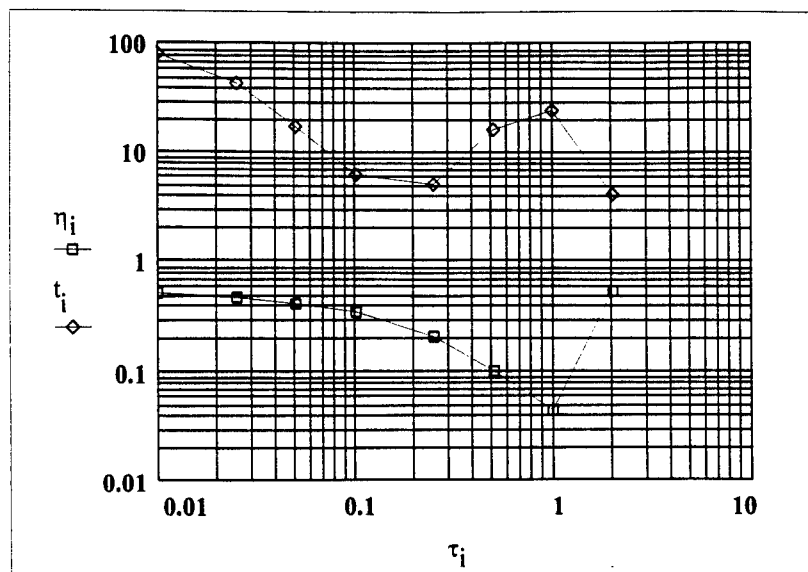


Figure 59. Diffraction efficiency and timing sensitivity to electron lifetime,  $\tau$  (ms), at  $\alpha = 3500 \text{ m}^{-1}$ . (b45)

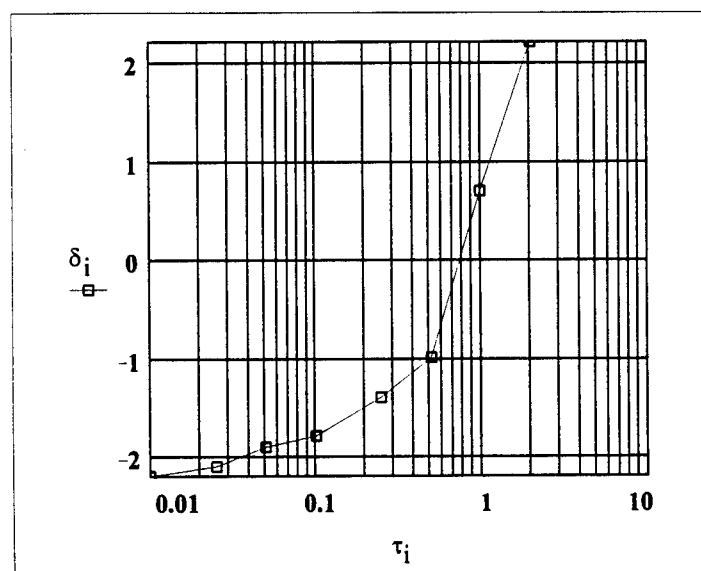


Figure 60. Dominance sensitivity to electron lifetime,  $\tau$  (ms), at  $\alpha = 3500 \text{ m}^{-1}$ . (b45)

A range of intensities at low absorption show a minimum corresponding to a zero dominance, see Figure 61 and Figure 62, at about  $1 \text{ W/m}^2$ . Notice that at the lower intensities, the time required to reach the peak becomes relatively long, seconds.

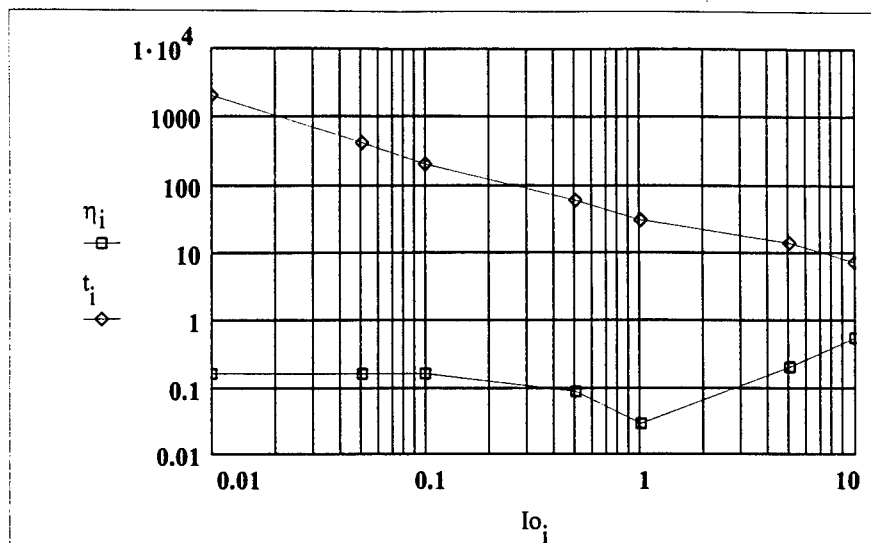


Figure 61. Diffraction efficiency and timing sensitivity to intensity,  $I_o$  ( $\text{W/m}^2$ ), at  $\alpha = 1000 \text{ m}^{-1}$ . (b29)

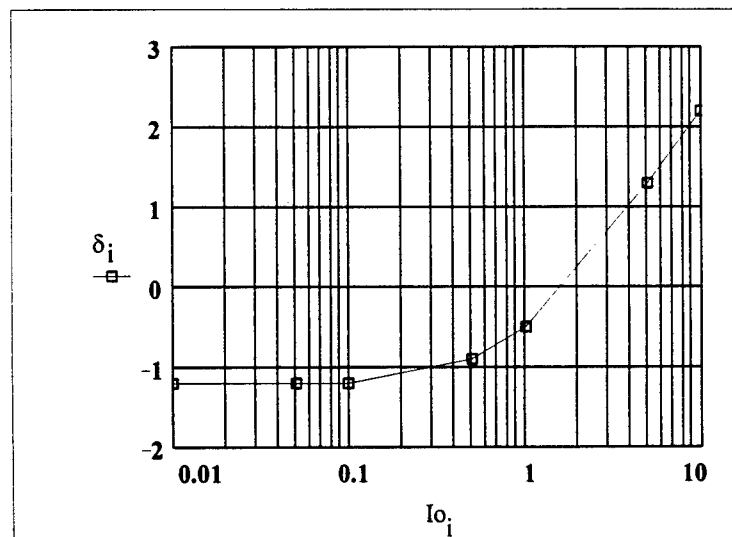


Figure 62. Dominance sensitivity to intensity,  $I_o$  ( $\text{W/m}^2$ ), at  $\alpha = 1000 \text{ m}^{-1}$ . (b29)

At higher absorption values, no zero dominance occurs in the tested range, see Figure 63 and Figure 64. The times required to reach peak output are slightly shorter at this absorption level.

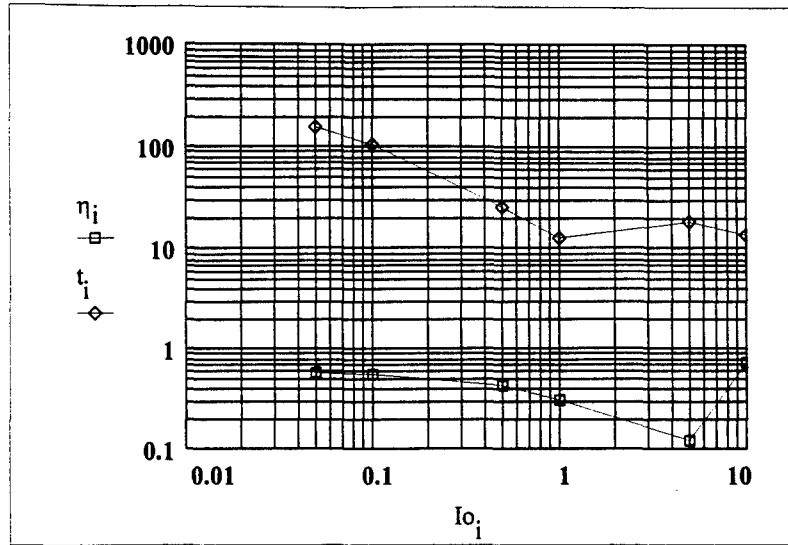


Figure 63. Diffraction efficiency and timing sensitivity to intensity,  $I_o$  ( $W/m^2$ ), at  $\alpha = 3500 \text{ m}^{-1}$ . (b43)

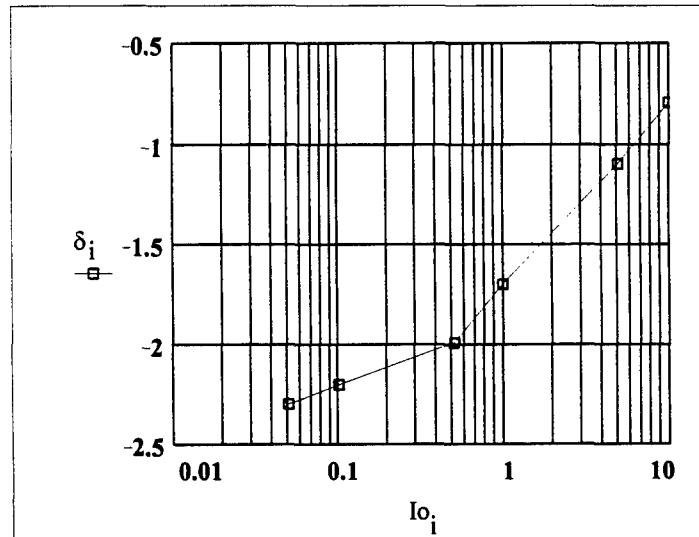


Figure 64. Dominance sensitivity to intensity,  $I_o$  ( $W/m^2$ ), at  $\alpha = 3500 \text{ m}^{-1}$ . (b43)

The device was very sensitive to mobility, see Figure 65 and Figure 66. The mobility range tested does not appear to be near a dominance zero.

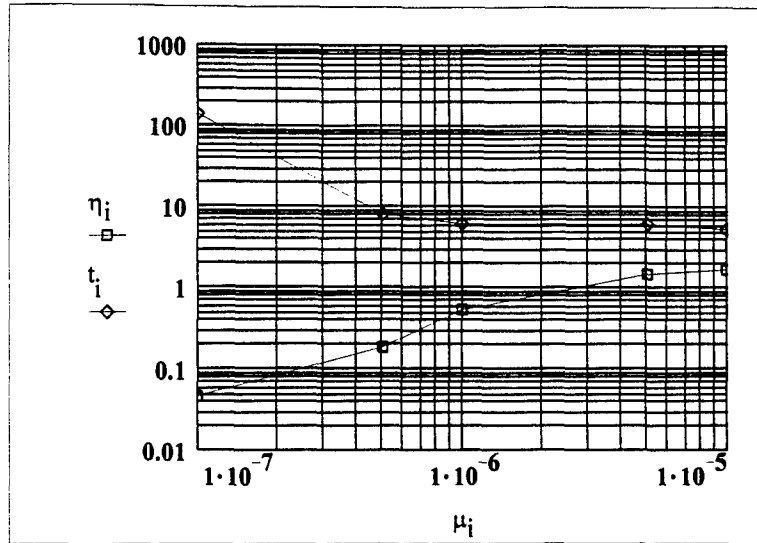


Figure 65. Diffraction efficiency and timing sensitivity to mobility,  $\mu$  (m<sup>2</sup>/V/s). (b30)

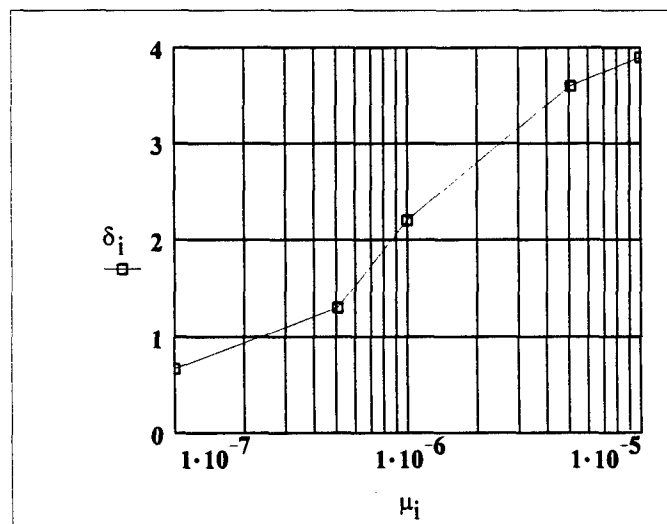


Figure 66. Dominance sensitivity to mobility,  $\mu$  (m<sup>2</sup>/V/s). (b30)

Figure 67 and Figure 68 show that at low absorption, the device is sensitive to detrapping time only at relatively short values.

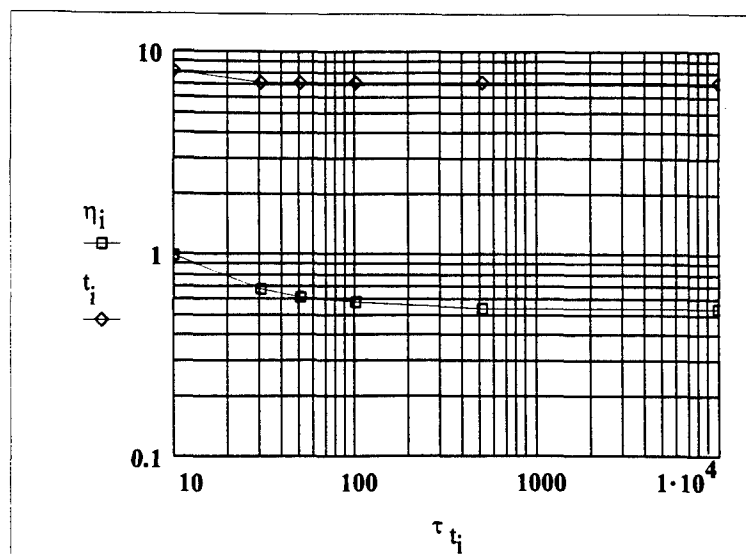


Figure 67. Diffraction efficiency and timing sensitivity to trap lifetime,  $\tau_t$  (ms), at  $\alpha = 1000 \text{ m}^{-1}$ . (b31)

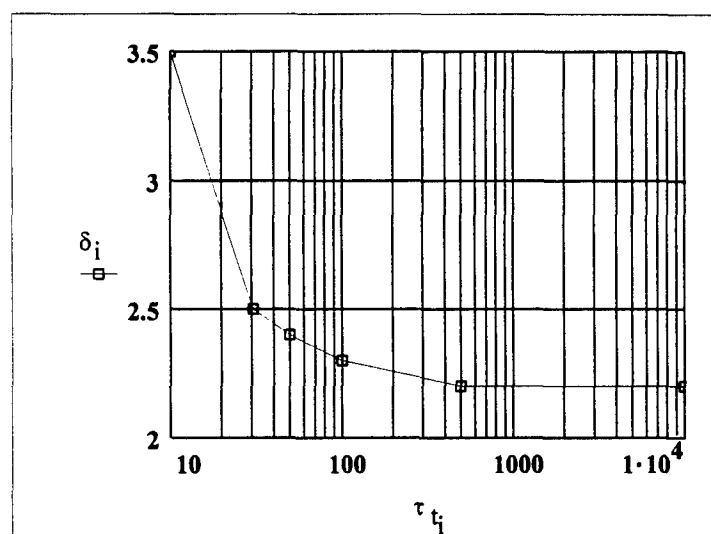


Figure 68. Dominance sensitivity to trap lifetime,  $\tau_t$  (ms), at  $\alpha = 1000 \text{ m}^{-1}$ . (b31)

At higher absorption levels, Figure 69 and Figure 70, the sensitivity to detrapping time is almost negligible.

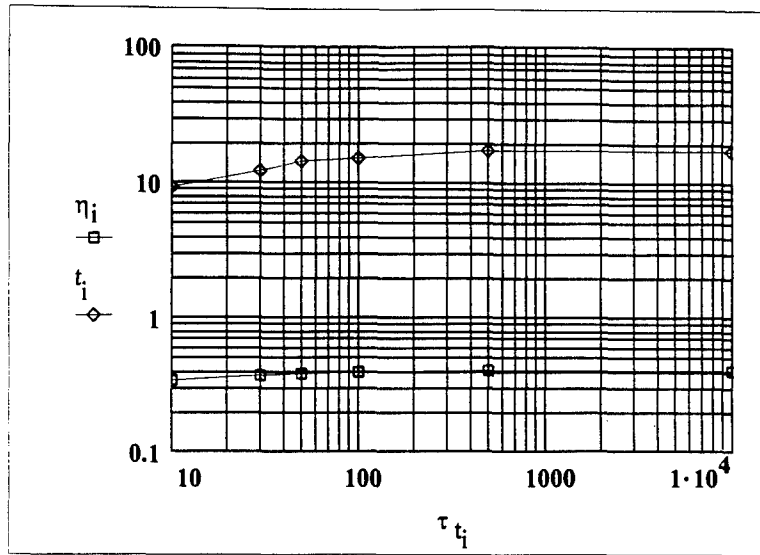


Figure 69. Diffraction efficiency and timing sensitivity to trap lifetime,  $\tau_t$  (ms), at  $\alpha = 3500 \text{ m}^{-1}$ . (b52)

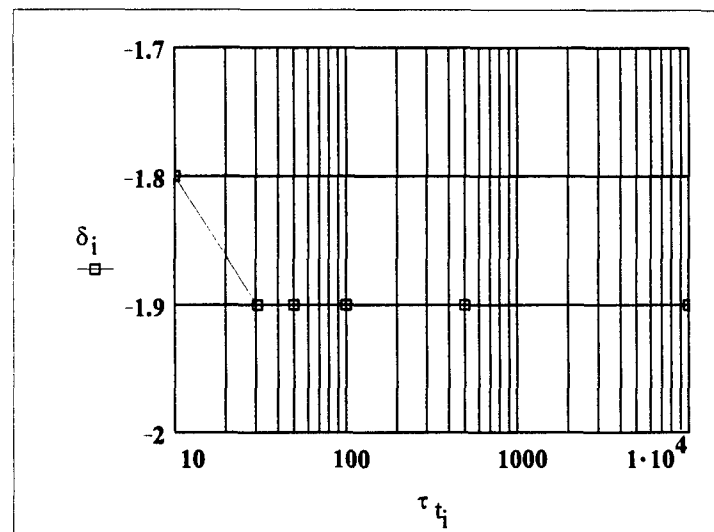


Figure 70. Dominance sensitivity to trap lifetime,  $\tau_t$  (ms), at  $\alpha = 3500 \text{ m}^{-1}$ . (b52)

The device shows a strong, exponential dependence on the applied voltage, see Figure 71 and Figure 72, when the device size is held constant. Most of the simulations in this dissertation were run at 1000 V.



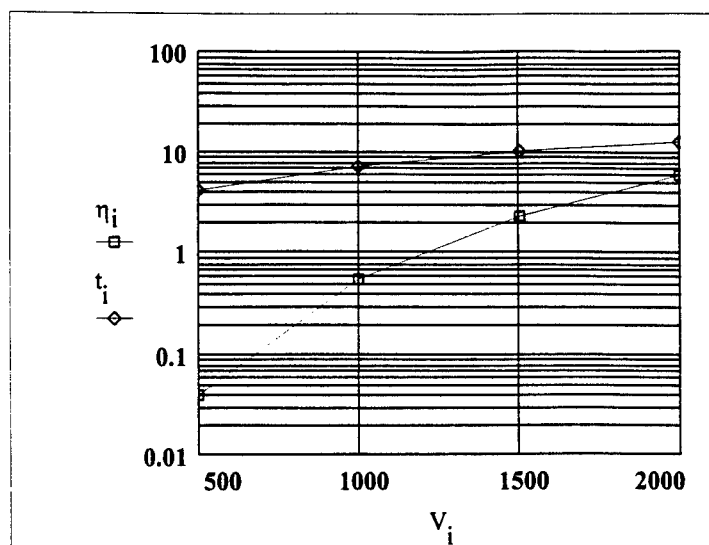


Figure 71. Diffraction efficiency and timing sensitivity to voltage,  $V$  (volts). (b42)

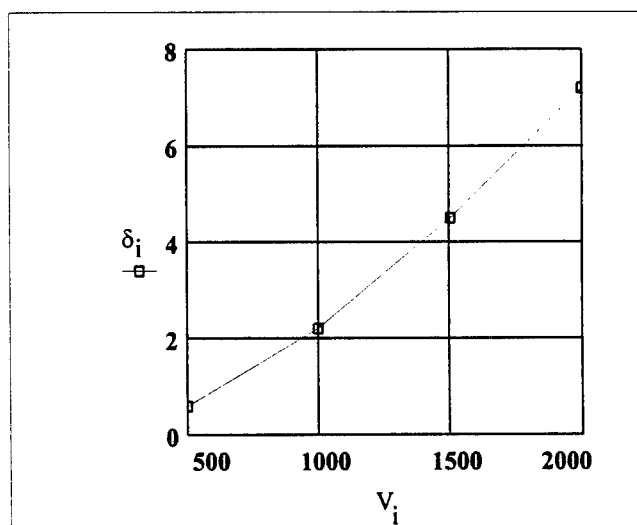


Figure 72. Dominance sensitivity to voltage,  $V$  (volts). (b42)

Figure 73 and Figure 74 show the magnitude of the output is very strongly dependent on the input modulation index. However, the timing of the peak output is only mildly dependent on this variable.

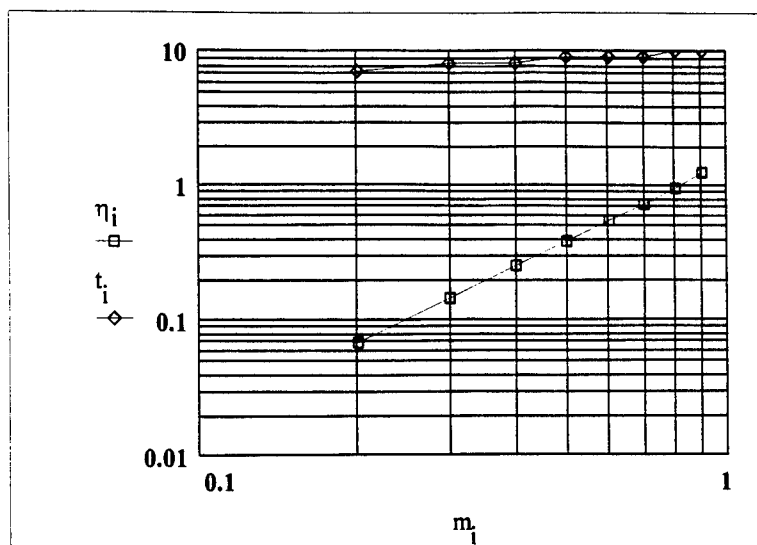


Figure 73. Diffraction efficiency and timing sensitivity to modulation index,  $m_i$ . (b37)

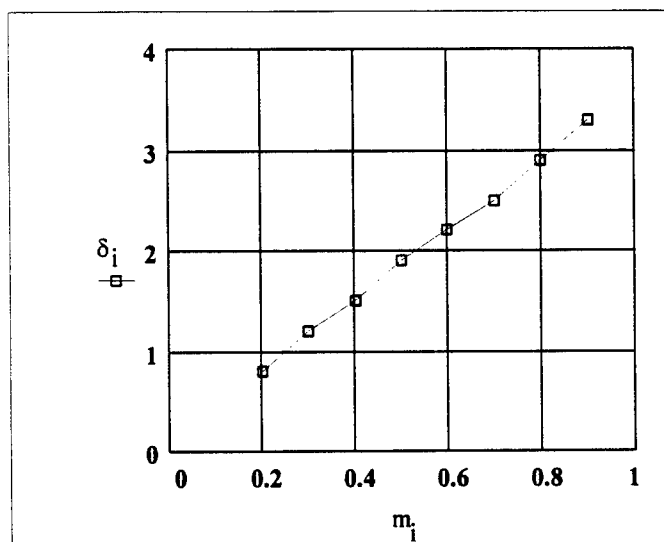


Figure 74. Dominance sensitivity to modulation index,  $m_i$ . (b37)

Figure 75 and Figure 76 show the device is very insensitive to the trap-to-donor recombination coefficient in the range tested. The logarithmic plots show almost no variation.

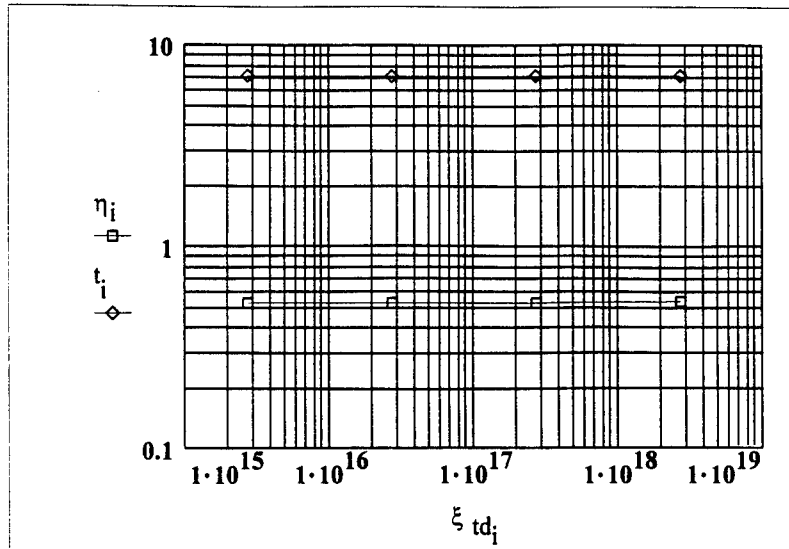


Figure 75. Diffraction efficiency and timing sensitivity to trap-to-donor recombination coefficient,  $\xi_{td}$  (s/m<sup>3</sup>). (b59)

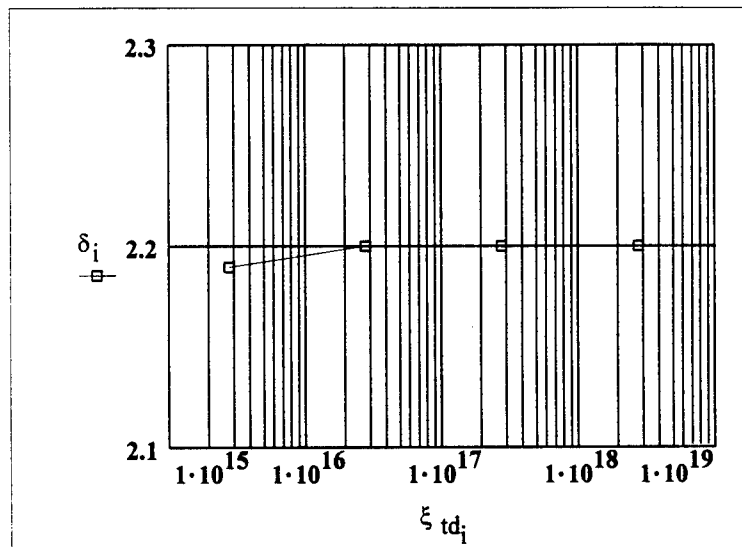


Figure 76. Dominance sensitivity to trap-to-donor recombination coefficient,  $\xi_{td}$  (s/m<sup>3</sup>). (b59)

Likewise, Figure 77 and Figure 78 show insensitivity to the donor recombination coefficient, again in the range tested. Remember that these plots are for continuous illumination simulations only.

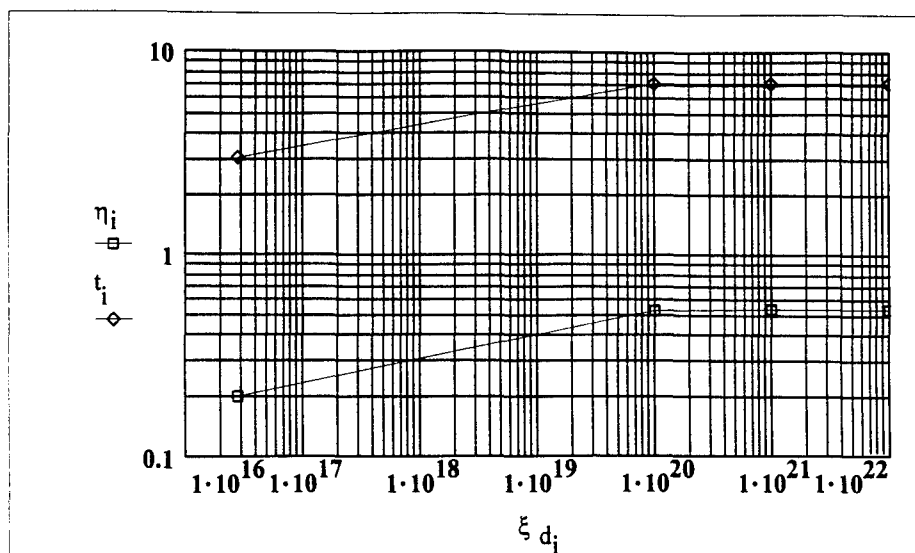


Figure 77. Diffraction efficiency and timing sensitivity to donor recombination coefficient,  $\xi_d$  (s/m<sup>3</sup>). (b60)

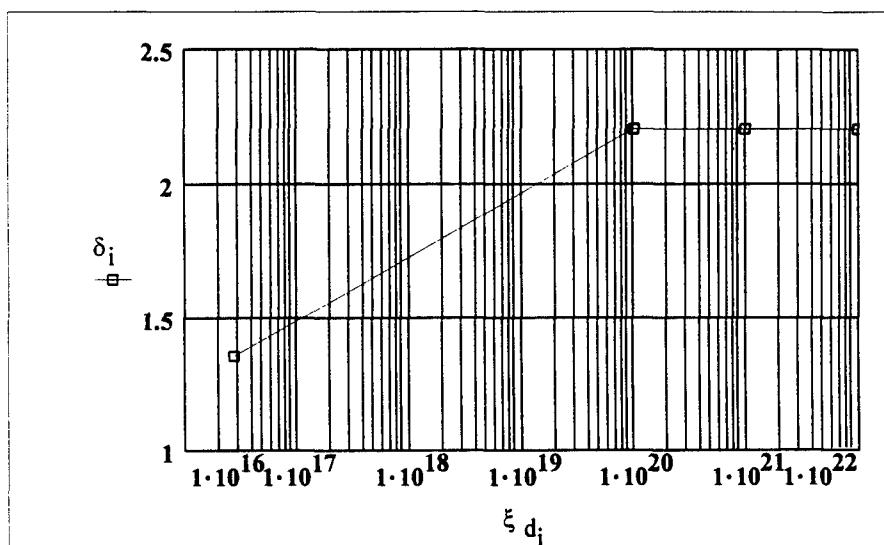


Figure 78. Dominance sensitivity to donor recombination coefficient,  $\xi_d$  (s/m<sup>3</sup>). (b60)

Finally, the injection coefficient, or cathode barrier, has a very strong effect on the peak diffraction efficiency and a relatively mild effect on its timing (see Figure 79 and Figure 80).

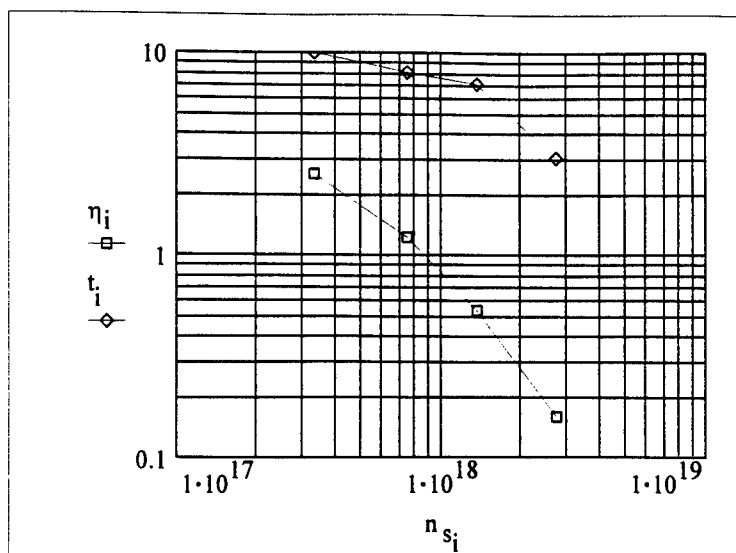


Figure 79. Diffraction efficiency and timing sensitivity to injection coefficient,  $n_s$  ( $m^{-3}$ ). (b66)

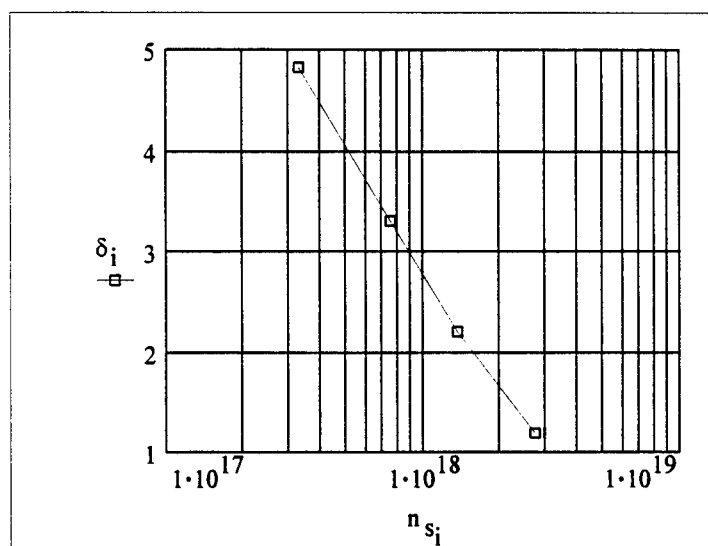


Figure 80. Dominance sensitivity to injection coefficient,  $n_s$  ( $m^{-3}$ ). (b66)

The device showed only a mild sensitivity to a very limited range of spatial modulation frequencies, see Figure 81. Fortuitously, a maximum in the output was found at about 3 lines/mm, very close to the standard 2 lines/mm used in most of the simulations. No plot of dominance is

provided since the code does not correctly calculate dominance at frequencies greater than 2 lines/mm.

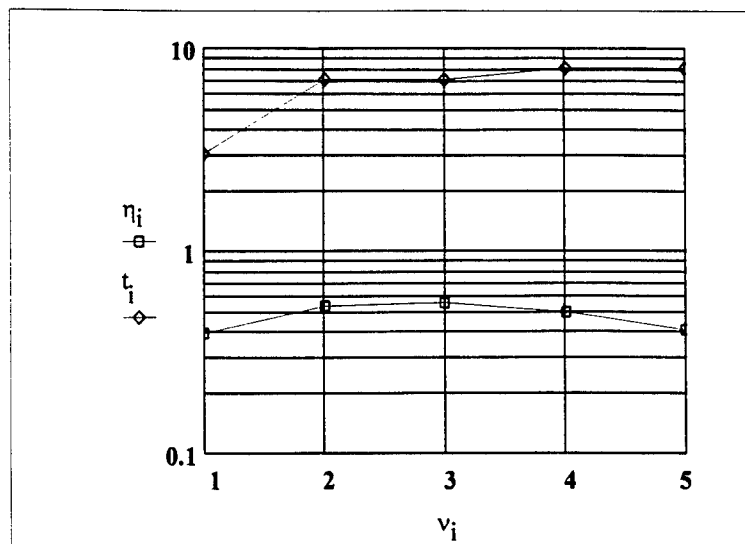


Figure 81. Diffraction efficiency and timing sensitivity to spatial modulation frequency,  $v$  (lines/mm). (b47)

## ***Appendix E. Abridged User's Guide***

This appendix is a brief user's guide. It shows how to install and operate the program and describes some of the potential pitfalls. This is not intended to be a full user's guide for a production software program. Rather, it is a sketchy introduction for the prospective researcher with some computer background in Windows and UNIX. The program is still in a very developmental stage. Comments in the code often refer to pages in the author's notebooks. Old code and options that did not work well or became unnecessary have often not been deleted and sometimes not even commented out. Thus, any option, flag, or parameter should be selected and used with extreme caution. It is strongly urged that new users familiarize themselves with the workings of the code as much as their computer backgrounds permit.

### **Introductory Comments**

Before discussing installation and the code, a few comments are provided to set the stage. First, the large floating point arrays led to a decision to select a compiler and language that allowed an 'unlimited' linear addressing space. The limited array sizes allowed by most 16 bit PC compilers were unacceptable. The choice was between programs for Unix or Windows NT™. Microsoft's 32-bit Visual C++™ compiler for the Windows NT operating system was selected. Early versions of the code suggested that runtimes on a 66 MHZ Intel 486/DX2 microprocessor would be acceptable. As the investigation continued, runtimes became excessive. However, by that point, the code for both the PRIZ simulation and the graphical presentation of the output were virtually complete on the Windows system. The decision was made to port the code to Unix. However, only the PRIZ simulation was completely portable. The graphics part of the code would

require a complete rewrite in some X-Windows™ system; time restrictions prevented the graphics port.

Thus, the current code actually consists of more than one program. The Windows NT program (priz2d.exe) is a full blown simulation with graphical output. Running the code requires a Win32s subsystem on any Windows operating system. Revising the code requires a 32-bit C++ compiler with Microsoft Foundation Class™ (MFC) support. The software *may* further be limited to printing graphics on a 600 dots-per-inch laser printer. Tests were not run on other printers.

The port to Unix only simulates the photoconductive stage of the PRIZ simulation. It uses the Free Software Foundation's GNU™ g++ and gcc compilers. Thus it is completely portable to any system with these compilers. That code, the executables priz2d or priz2do, creates a series of data files that contain the charge gratings at selected times. For example, the user might specify a simulation run from time 0 to 80 transit times (the time it takes an electron to longitudinally transit the crystal under only the external field) and output of the positive donor, filled trap, and free electron charge gratings once every transit time. The code then would create 80 data files.

The data files are binary, with values output as 'doubles', double precision floating point numbers that require 8 bytes each. If there are  $N^2$  interior points on the simulated grid, the output data file will contain  $3(N^2)$  doubles or  $24(N^2)$  bytes. Using Figure 82, the data is stored row after row, left to right and from the top down, with the organization at each grid point being  $N_d^+(x_j, z_i)$ ,  $N_t^-(x_j, z_i)$ , and finally  $n_e(x_j, z_i)$ .

To obtain graphical output, one at present must download the data files to a Windows system, and then rerun the simulation without redoing the Runge-Kutta calculations. The photoconductive portion of the simulation takes most of the time, with the Runge-Kutta routine using most of that. The nonlinear optics and diffraction portion of the simulation takes only a few minutes at most. Thus a rerun on Windows usually takes no more than 10 to 30 seconds.



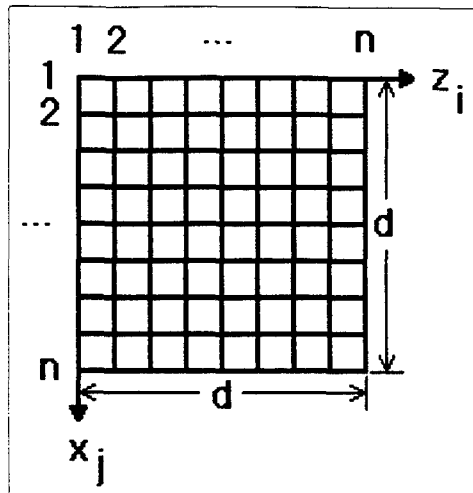


Figure 82. Grid to demonstrate data arrangement.

Unfortunately, the double format in the Unix compilers is not the same as that of the Windows compiler. The internal bytes in each of the doubles are reversed. Thus, the two programs can not directly read unaltered output from the other. This was fixed by doing two things. The binary parameter files (\*.a2d) that are used as input in the Windows system are converted to ASCII (\*.asc) via a short MS-DOS™ program, convert.exe, and then uploaded to the Unix system. This allows the user to start the Unix programs priz2d or priz2do. Once the simulation is finished, the data files (a2d\*.dat) are downloaded and then the eight bytes within each double are reversed by another short MS-DOS program, revorder.exe. Finally, the altered data files and the original parameter file are used to 'rerun' the simulation.

### Installation

To install the Windows version of the code, you need a Windows NT, Windows 95 or Win32s system with at least 8 Mbytes of RAM and about 3 Mbytes of hard disk space. The source and executables are supplied on one or more 3½ inch, high density floppies. They are compressed in a number of \*.zip files. From Windows run the "setup.exe" file to install and uncompress the files. You will be asked for a path for the new files. The recommended location is c:\priz2d, but

any new or old directory name will do. All files are placed in the selected directory, including \*.dll files. Your Windows directories and \*.ini files are not changed in any way. If you wish a desktop icon, you must install it yourself (see your Windows manual).

Installation problems are usually due either to lack of a recent (or compatible) Win32s subsystem for Windows 3.1+ systems or the wrong versions of msvcr20.dll. A new Win32s subsystem can be obtained from Microsoft's location on the major on-line services. As time passes, these subsystems may no longer be compatible with the compiled version of the program. The msvcr20.dll dynamic link library (and mfc30.dll) were provided with the Visual C++ compiler. The msvcr20.dll is system dependent, and you need different versions for Windows NT and Windows 3.11. No test has been made on Windows 95.

The UNIX code comes as source files and a makefile for two versions (with and without non-negative charge density enforcement). The files should be uploaded to your UNIX system and then compiled and linked with the make command. Your system must have gcc and g++ compilers. Executable code is also available. The current UNIX code is version 7.044 which is compatible with versions 7.046 and earlier Windows code.

To use the UNIX code from a Windows workstation, you also need the DOS programs convert.exe and revorder.exe. Convert.exe takes a \*.a2d file name as an argument and converts the binary file to ASCII. It produces a \*.asc file. Revorder.exe takes a binary \*.dat file and reverses the byte order of the C 'double' values. The original version of the \*.dat (bytes reversed) is deleted. These files create \*.asc parameter files required by the UNIX code and also converts the doubles from a UNIX to a Windows/PC format.

### **Running the Programs**

The suggested procedure is to create or modify a parameter file (\*.a2d) in the Windows program. Convert it to ASCII format (\*.asc). Upload the parameter file to the UNIX system.

Start the UNIX code in the same directory as the ASCII parameter file in background mode. After the UNIX code finishes running, download the data files the code created (\*.dat) to the Windows system and reverse the order of the bytes in each floating point double. Rerun the original parameter file (located in the same directory as the \*.dat files), and view the data on the Windows system.

To start the process, either click on the program icon you have created or double click on the priz2d.exe file in a file listing. Next, click on the FILE menu entry and then either NEW or OPEN, depending on whether you want to create or modify a parameter file. It is strongly suggested that you modify a previously used \*.a2d file. This will avoid old (possibly incorrect) default flag settings and material or device parameter combinations that will result in very long runtimes. Figure 83 shows the options to create a new parameter file. Note that AFIT-2D is the correct selection. The alternatives will create parameter files for additional simulations coded during this research. The alternatives are *not* described in this guide, but their use should be somewhat obvious to anyone who has read the text of the dissertation.

Once the user clicks okay, the parameter file is created with default values. Alternatively, selecting the OPEN menu entry results in a common file open dialog box as shown in Figure 84.

When the program opens the new or existing parameter file, the user sees two new icons in the main window and an open, empty child window. Each have the name of the parameter file that was opened. If a simulation is run (or rerun), the open window will show output graphics and one of the icons, a closed child window, will contain some parameter and program values for analysis purpose. The second closed window (icon) is just a simple notepad originally meant to hold comments about the parameter set. Recent changes to the code have not been tested with this

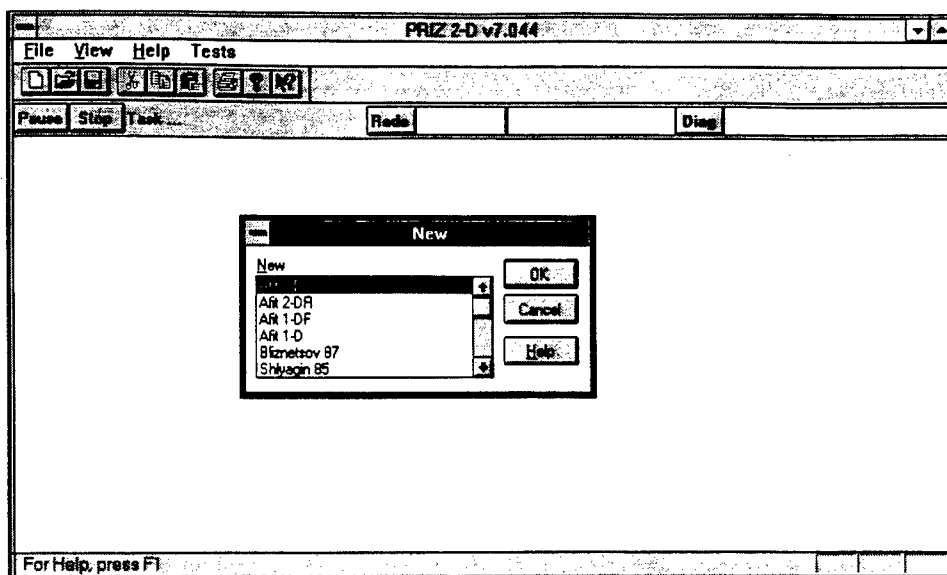


Figure 83. Creating a new parameter file

notepad. Hence, it is strongly recommended that it not be used.

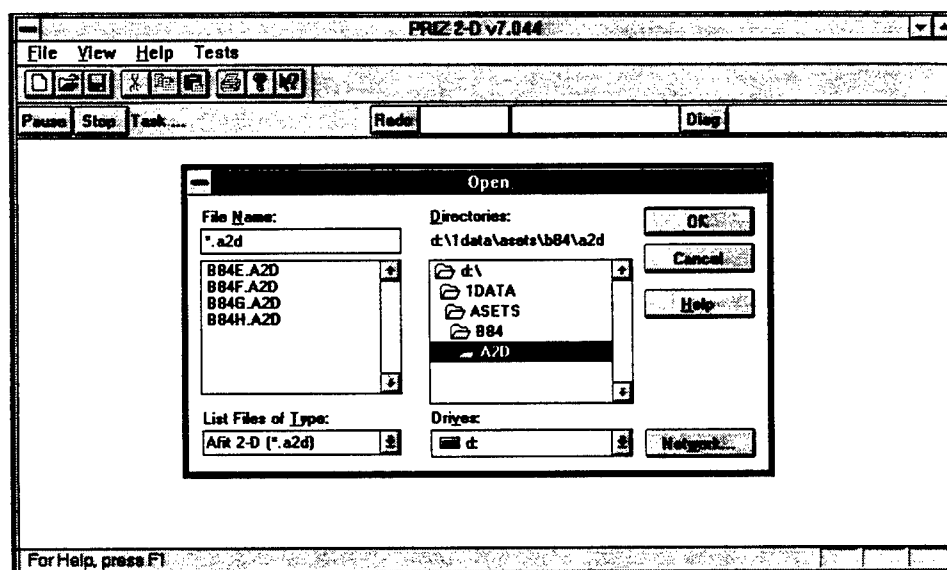


Figure 84. Opening an existing parameter file

Before initiating a run, the parameters are usually modified in the new or old parameter set. Figure 85 shows the dialog box used to modify the parameters or program flags. The user specifiable values are broken down into objects such as the PRIZ, the beam, 2-D plots, 3-D plots, program intervals, etc. The parameters corresponding to each object are shown in the parameter

list, with the value of a selected parameter shown in the value text box. Be sure to click the ACCEPT button after changing a parameter and before switching to a second object. All values should be entered in MKS units.

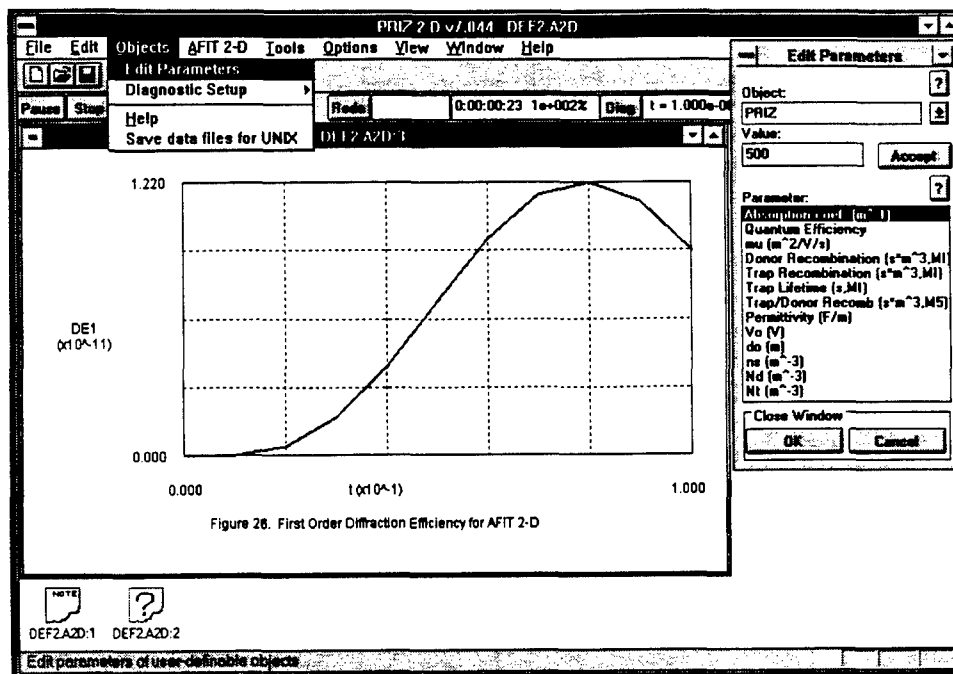


Figure 85. Editing model parameters and program flags

Once the parameters are correctly modified, save them to the same or a new parameter file. If you want to do a run under Windows, you are now ready. Figure 86 shows the RUN menu item in the AFIT 2-D menu. In the dialog box that shows up before the run starts, either enter file and directory names for the output data or else deselect the option to save the data. If you don't save the data, you can still view all of the plots until you exit the program.

If the user wants to run the simulation on the UNIX system, the parameter file (\*.a2d) should first be saved. Then go to a DOS or NT command line window, change to the directory containing convert.exe and your \*.a2d file, and then enter "convert filename.a2d". The filename should be the name of your parameter file, e.g., b87c.a2d. Convert will create an ASCII file called filename.asc, e.g., b87c.asc. Upload filename.asc to your UNIX directory, e.g. with FTP, being

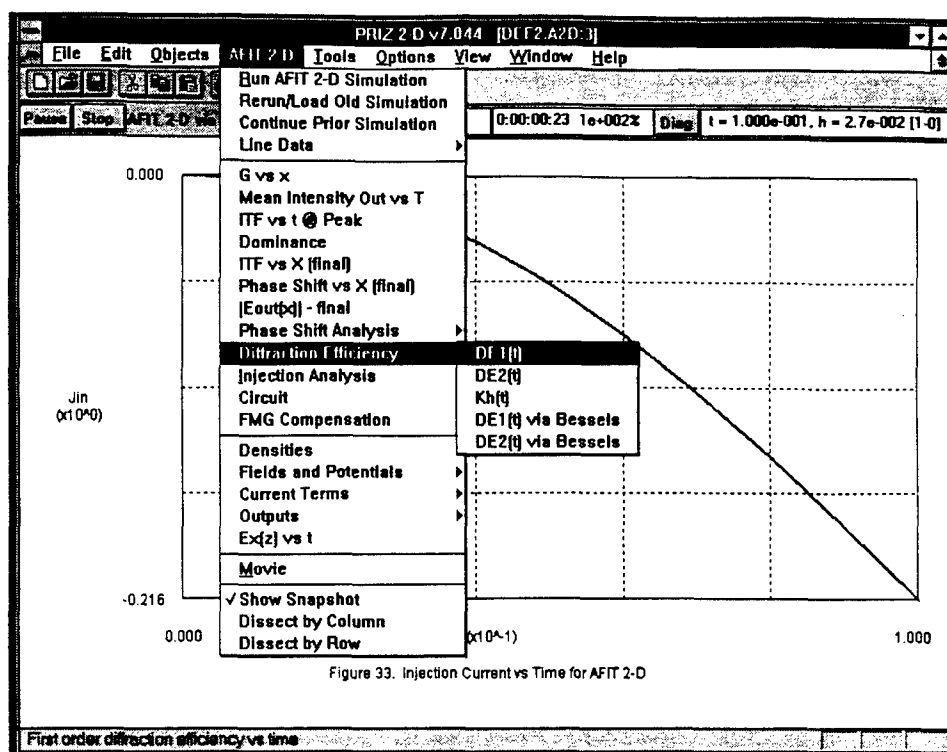


Figure 86. Menu to run the program and view the output

sure to identify the transmission as ASCII instead of binary.

Now log onto your UNIX system, perhaps with TELNET, and change to the directory containing the UNIX executable code (priz2d or priz2do) and the filename.asc file. Priz2d is the slower code and can be used when the write-beam is not turned off during a simulation. Priz2d ensures that charge densities remain positive; priz2do does not. Priz2do should be used whenever the write-beam is turned off in a simulation to avoid excessive slowdown. To run the program in the background, simply enter "priz2do filename.asc &". The "&" instructs UNIX to run the program in the background. You can safely log off and back on at some later time. A log file, priz2d.log, is updated at the end of each interval when a \*.dat file is saved. The information in priz2d.log is the percentage of simulation completed at a given date and time. Typically a run will take 40 minutes to 2 weeks. When the run is complete, a directory listing will show one data file per interval. For example, a listing might show: a2d0001.dat, a2d0002.dat, ..., a2d0080.dat.

The data files should be downloaded, in binary format, to a Windows PC directory. Since UNIX double format is reversed (byte by byte) from that used by Windows, each data file must be changed by "revorder a2d0001.dat" or a similar command from a directory containing both revorder.exe and the data files. A batch file can be easily created that does all 80 to 100 conversions from a single command.

Now move the original \*.a2d file to the directory where the reversed \*.dat files are located. Restart the PRIZ2D program and open the \*.a2d file. Now select RERUN from the AFIT 2-D menu (see Figure 86). Select one of the \*.dat files to identify the name and location of your \*.dat files (the program doesn't assume the \*.a2d and \*.dat files are in the same directory or that you only have one simulation in the directory). Clicking OK starts the simulation to rerunning. When it is completed, view any plots you like.

## Output

Once a Windows run or rerun is completed, there are numerous ways to look at a variety of data. Figure 86 shows the drop down menu from which the user selects the data to display. The various options on how to display the data can be found through exploration. This abbreviated version of the user's guide will present only a few of the options. The plots shown here are for a *very* brief run that does not create large transverse currents.

Charge densities can be shown either for the net charge or a particular species. After the simulation is run, you can only view the final 2-D distributions (or the 1-D output as a function of time). But if you save the data, you can quickly rerun a simulation specifying the plot(s) to be shown at the end of each interval. Figure 87 is an example of a final net charge density. Note that all values are in normalized units, while position is typically indexed by grid points: 0 to 64 or 1 to 65 for a 65 by 65 grid.

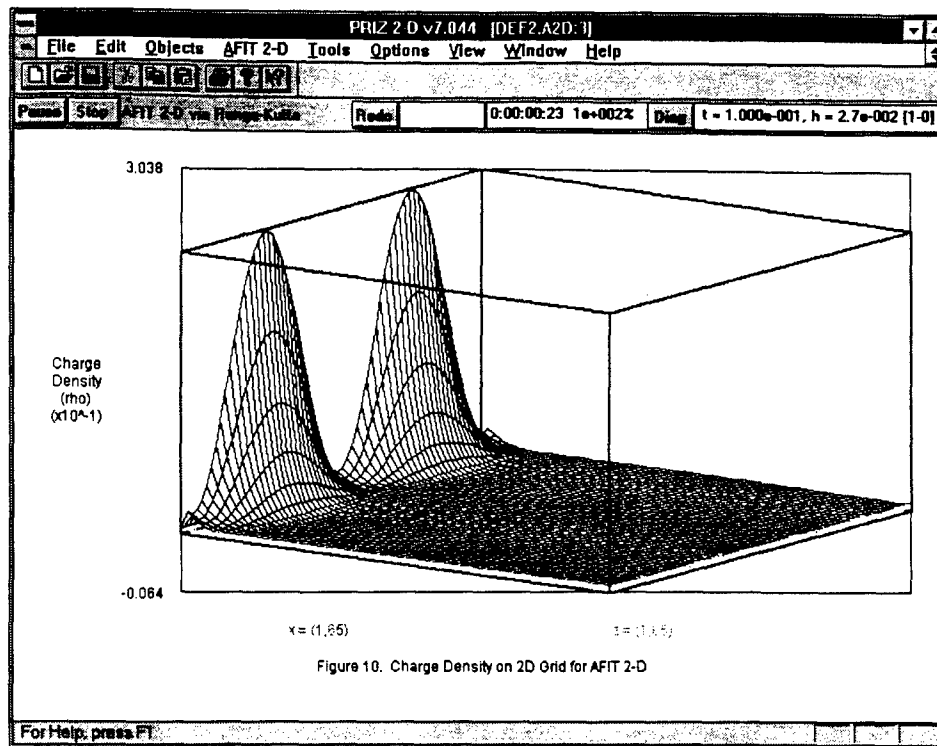


Figure 87. Net charge density vs position

Once charge densities are calculated, the program calculates electric fields. Figure 88 shows the transverse electric fields and Figure 89 shows the longitudinal fields. Figure 90 shows the slow index of refraction as a function of position. Using the transverse electric fields, the program calculates dominance as a function of time (see Figure 91).

The amplitude of the output electric field after the output polarizer, as a function of transverse position, is shown in Figure 92. Note the source of the asymmetry is addressed in Appendix G. The error is inherent in the Poisson solver and seems to be relatively large at the start of a run.

Finally, Figure 93 shows the output first order diffraction efficiency. Note that the square of dominance in Figure 91 is proportional to the diffraction efficiency in Figure 93.



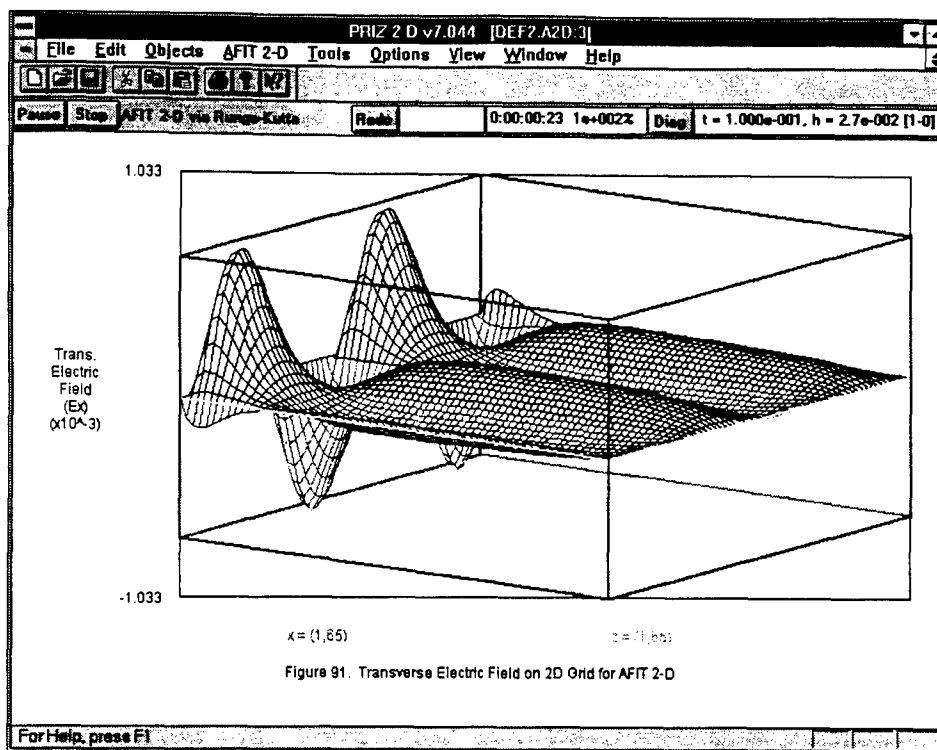


Figure 88. Transverse electric fields vs position

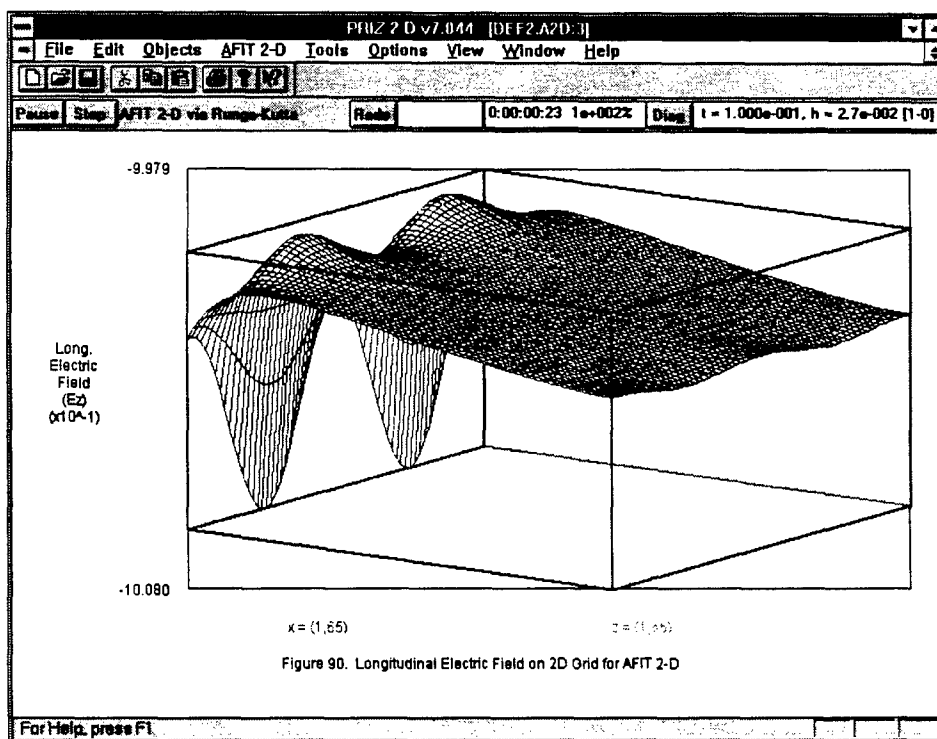


Figure 89. Longitudinal electric fields vs position

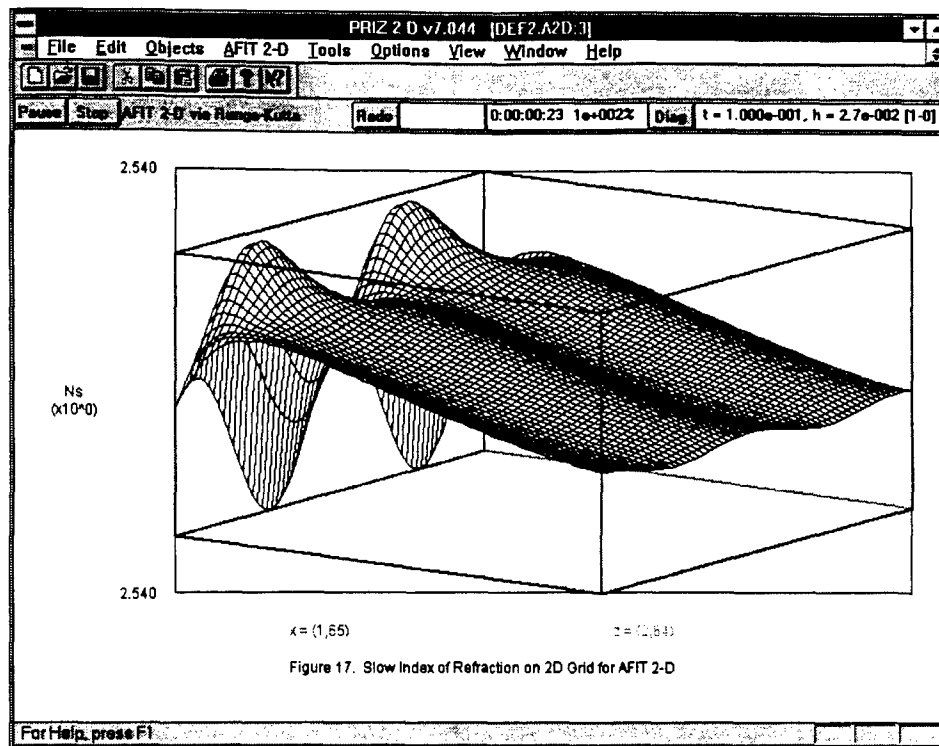


Figure 90. Slow index of refraction vs position

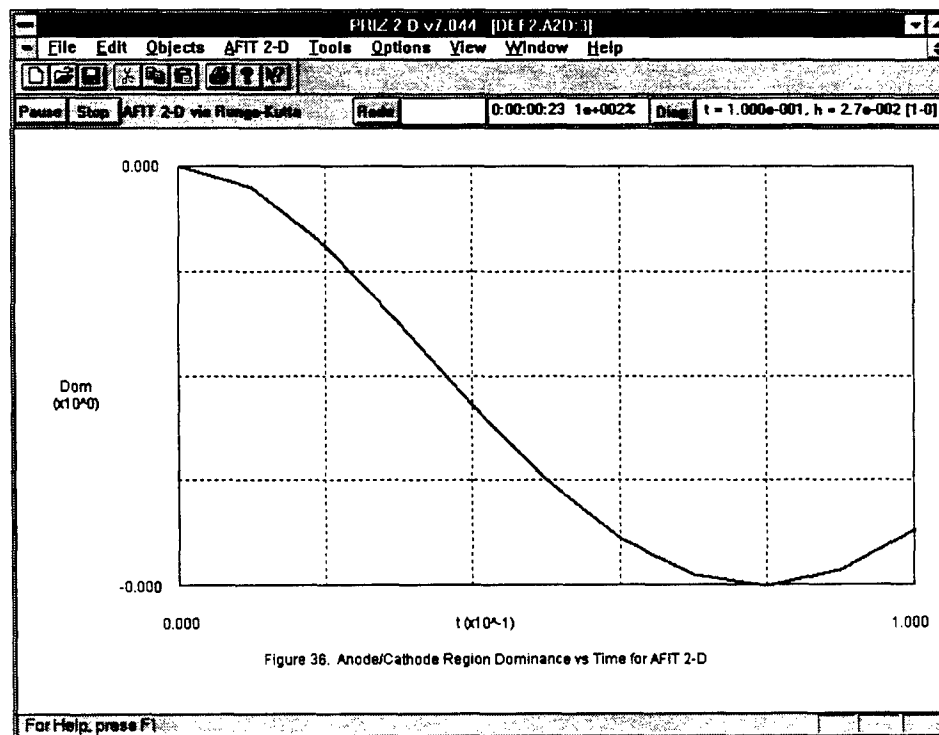


Figure 91. Dominance vs time

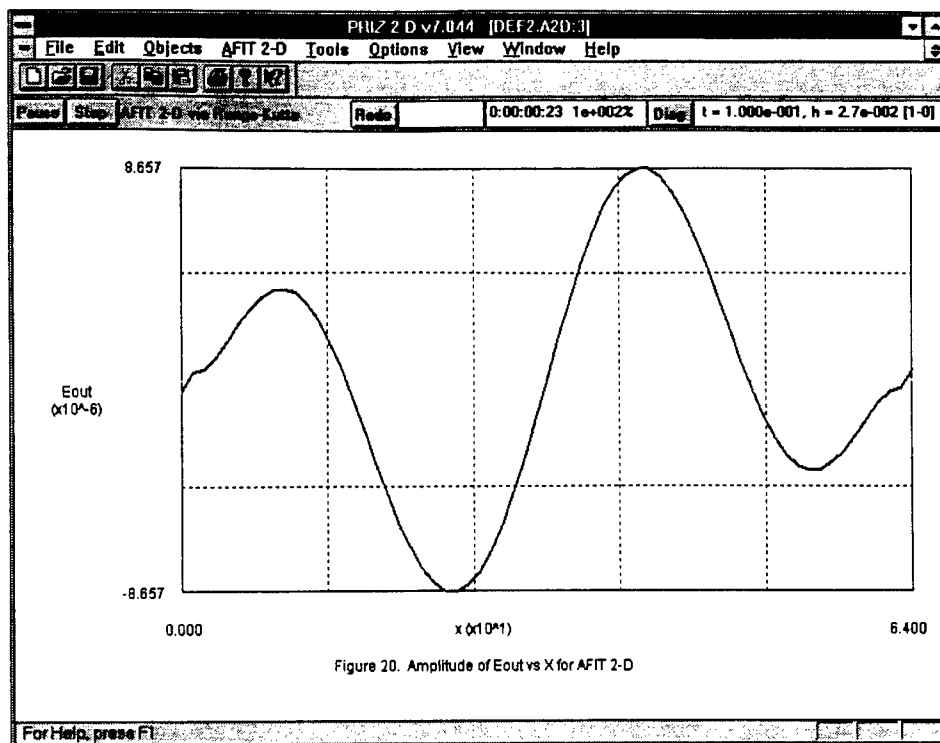


Figure 92. Amplitude of output electric field vs x

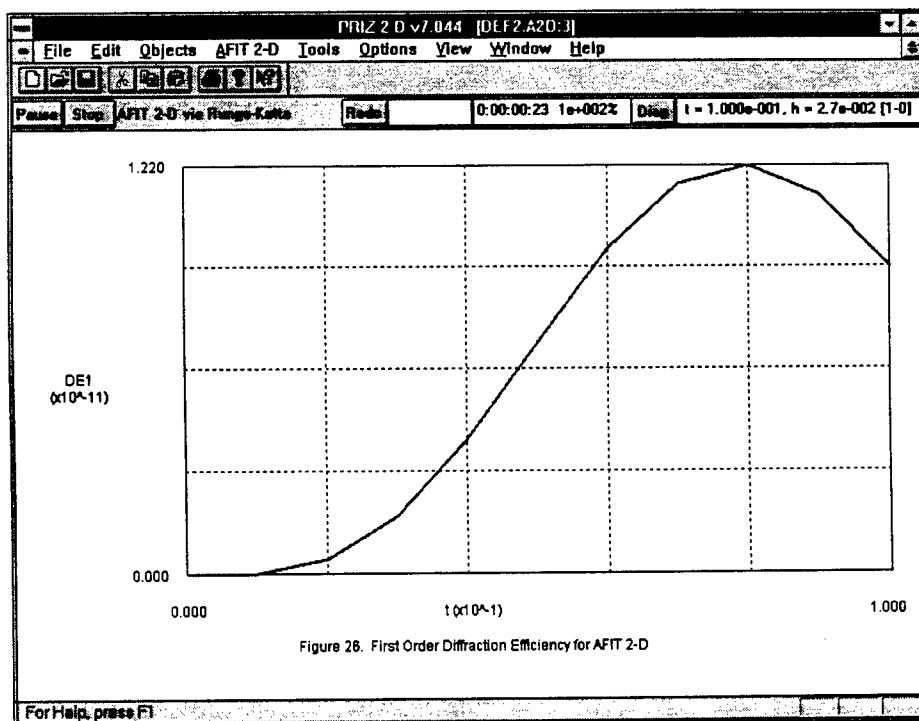


Figure 93. First order diffraction efficiency vs time

## **Pitfalls and Difficulties**

Mention was made of two simulation programs for UNIX, priz2d and priz2do. In some scenarios, such as small modulation indices or after turning off the write-beam, one finds localized, very low free electron densities. In these regions, it is possible for the approximations and discretizations in the simulation to drive the free electron density negative. This is physically impossible. The negative densities are very small, but over time, they can create localized, negative filled trap densities which are also physically impossible. The Windows version (priz2d.exe) and one of the Unix versions (priz2d) prevents the free electron density from going negative by artificially setting it to zero whenever the code tries to make it negative. However, this shows up as additional error to the Runge-Kutta ODE solver, which goes to smaller time steps and slows the program down. In some cases, the simulation slows almost to a dead stop.

Frequently, this extreme slowing occurs during simulations in which the write-beam is turned off. Since this was an important phase of the investigation, a second Unix program was developed, priz2do, where the free electron density was allowed any values the code specified. In essence, the user lives with localized, small, negative free electron densities. The error appears to be small. Whenever a simulation requires write-beam turn-off, priz2do is suggested.

The Windows code (priz2d.exe) also includes classes that reproduce the Russian analytical work and enhanced versions of the AFIT 1-D numerical model. Of course, this was not ported to the Unix versions.

The Windows code also allows the user to vary numerous internal flags that can solve the simulation using alternate algorithms. The recommended approach to use in specifying your parameter set and flags is to modify an existing \*.a2d file from this work. Before changing the flags, examine the help files and the code to see what they do. Changing the model parameters is straightforward and should not provide surprises except for extreme or unrealistic values. Such

values can slow down execution of the code when the Runge-Kutta routine reduces the time steps to handle increased rates of change in the charge species.

The Full Multi-Grid Poisson solver currently uses only a single point wrapping scheme to ensure periodicity. It also uses a five point approximation for the Laplacian of the potential. These approximations seem to produce small errors at the grid sizes used in this effort (see Appendices F and G).

Finally, with a parameter set that specifies a large, effective trapping rate, one may relatively quickly (depending on the intensity, absorption coefficient, etc.) observe localized saturation of the traps. If the user continues to run the simulation after that point, large oscillations in the output diffraction efficiency are observed. No attempt was made to determine whether this was a real phenomena or whether it was evidence that the simulation's approximations were becoming invalid.

### *Appendix F. Simulation Error*

As mentioned in the body of the report, there is some error in a typical 65x65 simulation, mostly because of the relatively coarse grid size chosen. This error should be kept in mind when using the simulation output for quantitative purposes.

The data in Table 5 was collected to determine the effect of varying the electric field update frequency and grid size on parameter set b55 (see Appendix A) during continuous illumination. The device behavior for this set displays a moderately large dominance. 'Normal' updates of the electric field (E) occur after the charge distributions are output by the Runge-Kutta routine at each small time step. 'Always' indicates that E is updated at the end of the much more frequent calculations of the rate equations within each Runge-Kutta step.

Table 5. Simulation error for continuous illumination and large dominance.(b55)

<u>Set</u>	<u>Grid</u>	<u>E update</u>	<u><math>\eta_1</math> max (<math>\eta_0</math>)</u>	<u>t @ <math>\eta_1</math> max (ms)</u>	<u><math>\eta_1</math> relative</u>
b55a	65x65	normal	0.530	7	1.065
b55b	129x129	normal	0.511	7	1.026
b55c	257x257	normal	0.498	7	1
b55d	65x65	always	0.526	7	1.056
b55e	129x129	always	0.510	7	1.024

Note that the time the output peaks does not vary at all, given a sample period of one transit time. Updating the electric field as often as possible, always, causes less than a 1% change in the size of diffraction efficiency. The behavior of the error does go down as the grid size goes up, but computer memory limitations prevented running simulations at higher grid sizes that could have provided a good bounds for the error. Figure 94 shows that the shapes of the diffraction efficiency curves are almost unchanged.

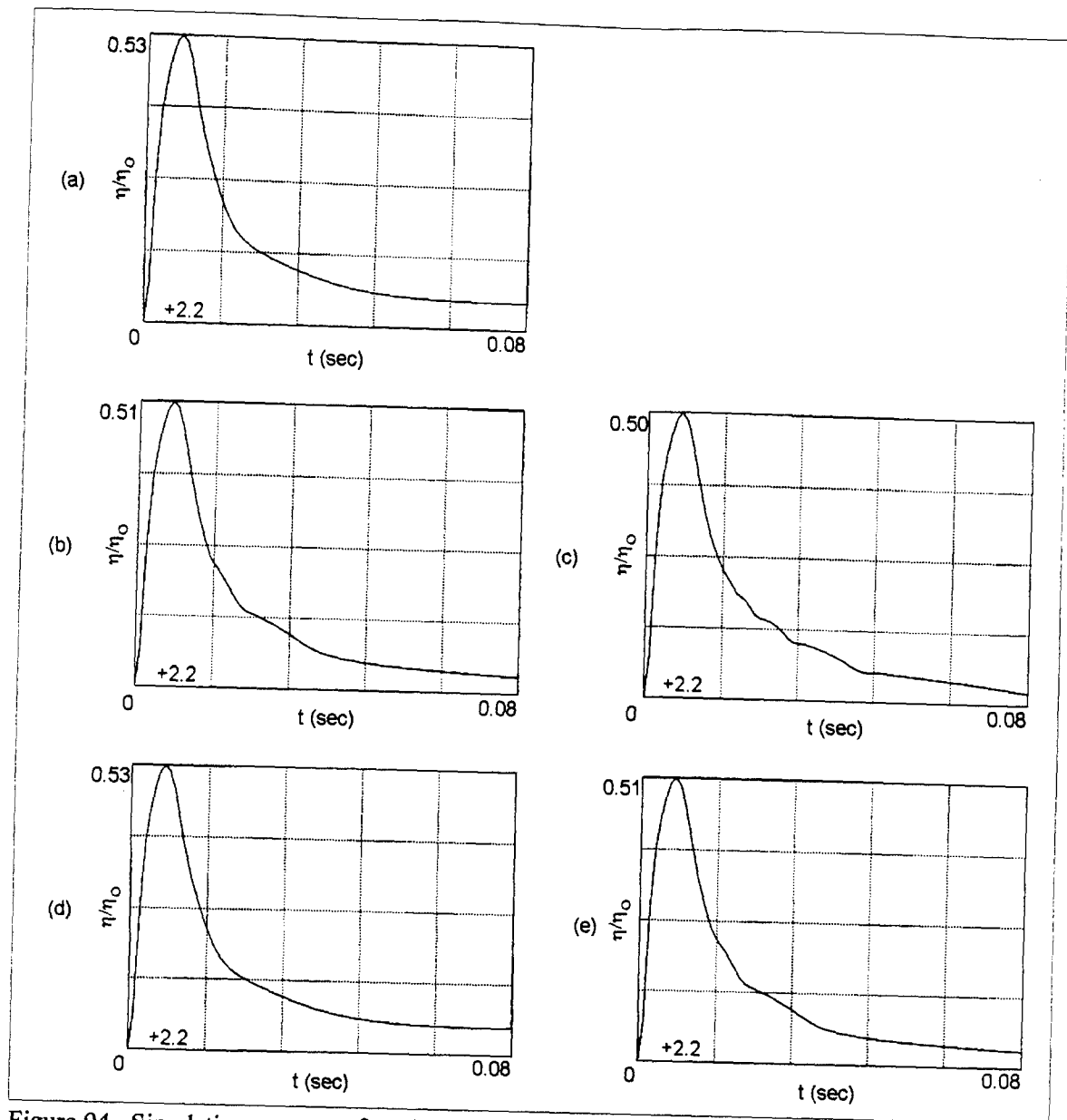


Figure 94. Simulation error as a function of grid size and frequency of electric field calculation for large p-dominance. Grid size and update frequency are (a)  $65^2$  and normal, (b)  $129^2$  and normal, (c)  $257^2$  and normal, (d)  $65^2$  and always, and (e)  $129^2$  and always. (b55)

Tests were also performed on a parameter set that showed only a small dominance. One expects coarse grid errors to be emphasized in this situation. Figure 95 shows that it is. The phase reversal actually disappears, and the size of the peak is different. Of course, for the same grid size,

the frequency of electric field update shows negligible effects. Additional simulations were not performed because of the lengthy runtimes involved.

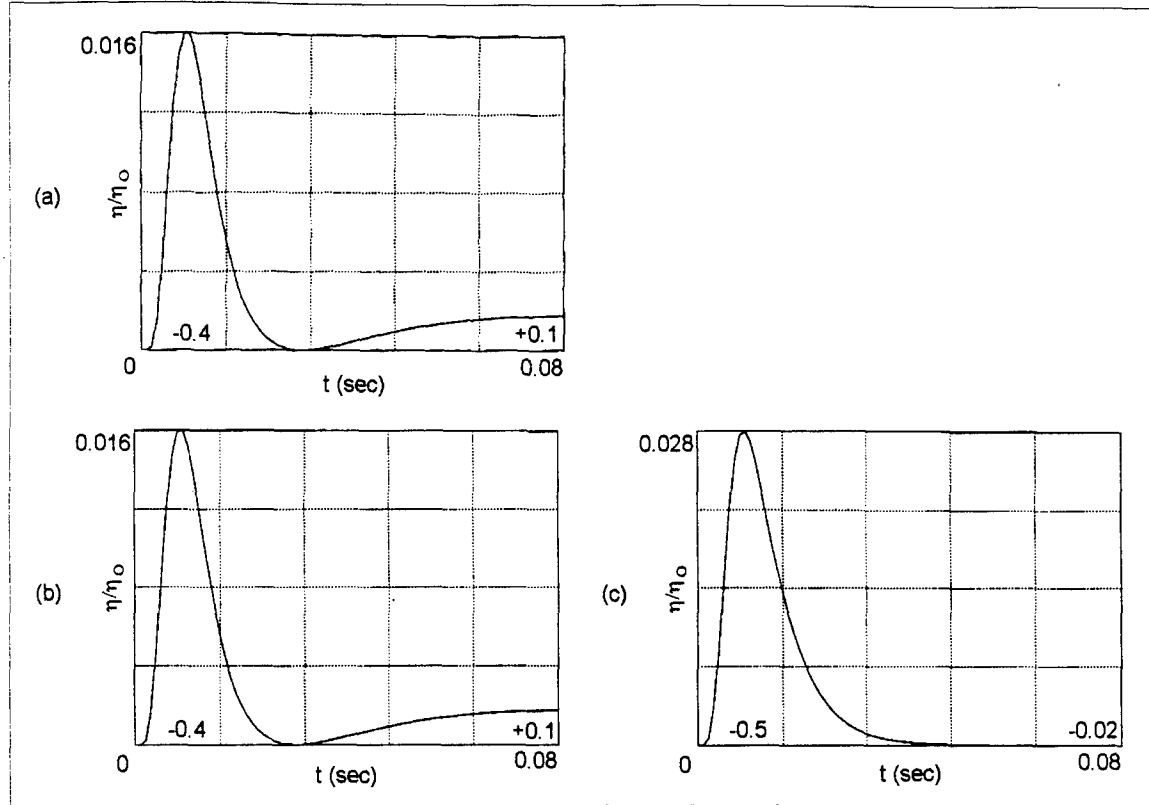


Figure 95. Simulation error as a function of grid size and frequency of electric field calculation for small  $n$ -dominance. Grid size and update frequency are (a)  $65^2$  and normal, (b)  $65^2$  and always, and (c)  $129^2$  and normal. (b28)

A final sequence of tests were performed on a parameter set that showed a small, slow reintensification after write-beam turnoff. Although one expects coarse grid errors to be emphasized after turnoff, Figure 96 shows only small changes. As usual, for the same grid size, the frequency of electric field update shows negligible effects. Additional simulations were not performed because of the lengthy runtimes involved.

The conclusion from the above studies is that unless the dominance state created during the run is small, there is only a small error due to grid size and an insignificant error due to



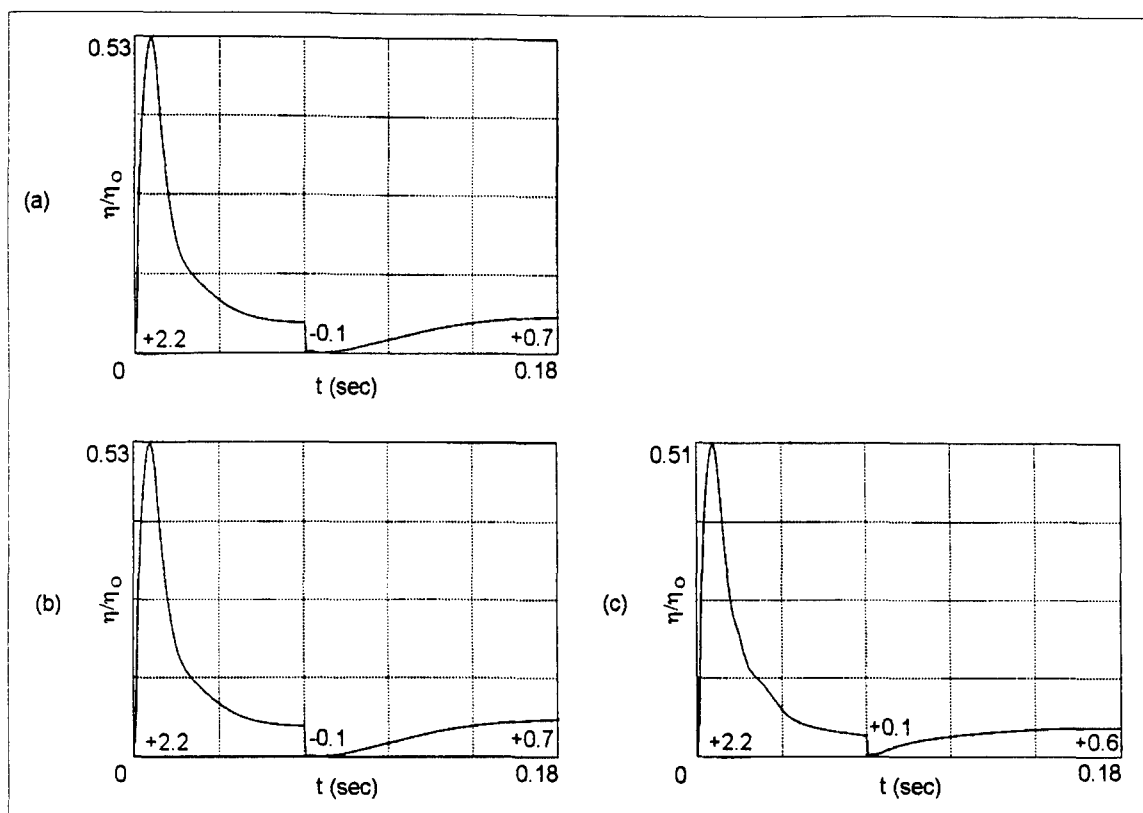


Figure 96. Simulation error as a function of grid size and frequency of electric field calculation for pulsed operation. Grid size and update frequency are (a)  $65^2$  and normal, (b)  $65^2$  and always, and (c)  $129^2$  and normal. (b32)

frequency of calculating the electric fields. If however, the dominance is small at peak diffraction efficiency, significant error is possible due to low grid resolution.

## *Appendix G. Asymmetry in Output*

During the simulations, it was noted that a slight asymmetry appeared in the output phase shift and the output electric field. This might be expected to result in some error in the first order diffraction efficiency. Therefore, the cause and effect were investigated.

The asymmetry is caused by a relatively small error in the Full Multi-Grid (FMG) algorithm and can be exacerbated by incorrect coding of the periodic boundary conditions in the FMG. The error in the FMG algorithm is likely due to several factors: (1) a 5-point formula limits the accuracy of a local approximation (solution), (2) the number of v-cycles (smoothing) is kept small, (3) the grid resolution is relatively coarse (65x65), and (4) floating periodic boundary conditions are imposed for two boundaries (see 30:871-882 and Chapters II and III).

The actual error in the FMG routine shows up as a lack of transverse periodicity in  $d/2$  for the output potential, where  $d$  is the breadth of the simulated (square crystal). Figure 97b shows the absence of periodicity for a brief run on a 33x33 grid that ends before significant transverse drift occurs. Figure 97a-c are transverse distributions at the sixth longitudinal gridpoint near the cathode. Figure 97d is the output field distribution that shows the suspect asymmetry. The input charge distribution is periodic in  $d/2$  in the transverse direction ( $x = 0, d/2, \text{ and } d$ ) and has roughly no longitudinal variation at the same  $x$  coordinates. Thus, one would expect the transverse distribution of the output potential to also be periodic in  $d/2$ . Instead, you get an error in the potential out of the FMG such as the worst case distribution shown in Figure 97b.

Notice that since the output distribution in Figure 97d is proportional to longitudinal integrals (sums) of the transverse fields such as those of Figure 97c, any asymmetry in the transverse fields is accentuated in the output. Since there is no obvious way to remove the errors in the FMG, there was no obvious way to quantify the error induced in charge transport by the

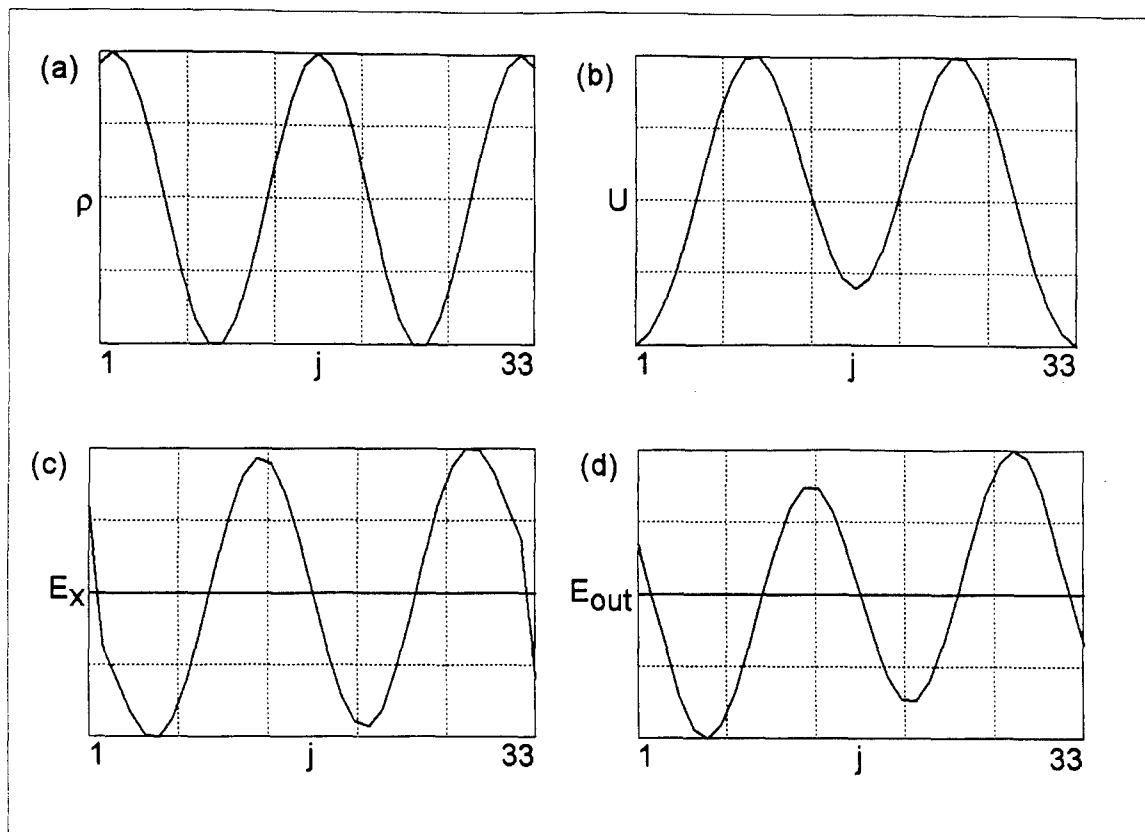


Figure 97. Transverse distributions in a brief simulation showing worst case error in potential. Plots (a) through (c) are taken at the sixth of thirty-three longitudinal points. The distributions are (a) the net charge density input to the FMG, (b) the potential output from the FMG, (c) the transverse fields calculated from the potential, and (d) the output field distribution proportional to the longitudinal integral of the transverse fields.

small error in the potential. Figure 97 is a worst case scenario, the simulations from the parameter sets used in the rest of this text show only a slight asymmetry. The associated small error in the potential in those simulations is assumed to have a very minimal impact on charge distribution.

But the direct effect of the asymmetry in the output field distribution, on diffraction efficiency, can be quantified. The effect of the asymmetry is equivalent to adding another frequency component to the output at a spatial wavelength two times that of the modulation wavelength of the write-beam input. Thus, the output based on first and higher harmonic frequencies of the input spatial modulation frequency are unaffected. The following analysis verifies this conclusion.

Figure 98 is the plot of the output electric field (after the output linear polarizer but before diffraction is applied in transmission to the far field) for a short worst case simulation such as in Figure 97.

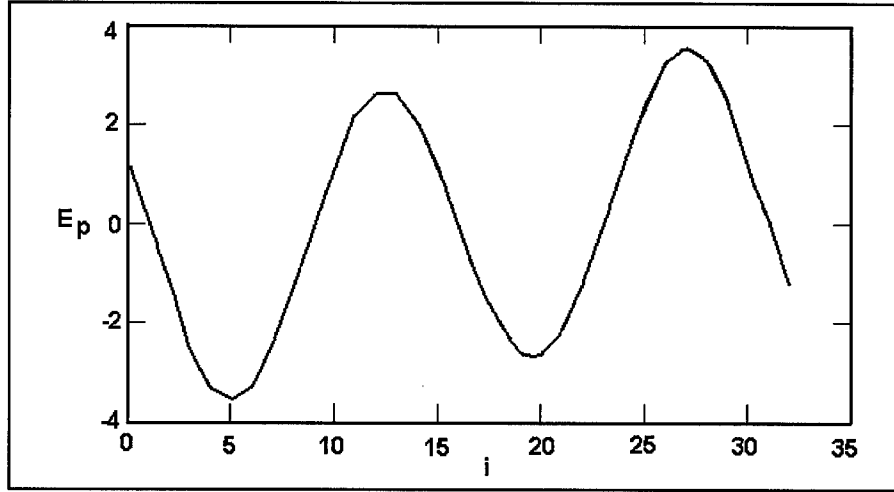


Figure 98. Output electric field versus transverse location showing typical amount of asymmetry. This corresponds to 33 transverse points and an input of 2 sine periods.

The addition of a frequency component at a wavelength twice that of the input can remove the asymmetry.

$$E_{mod} = E_{out} + 0.55 \sin\left(\frac{2\pi}{32}i\right) \quad (1)$$

where  $i$  is an index referring to the transverse location. This modification results in Figure 99.

The output of interest for this work is first order diffraction efficiency. Therefore, the amount of error introduced by the asymmetry of Figure 98 to the assumed correct output of Figure 99 must be determined. To do so, the discrete values plotted in Figure 98 and Figure 99 are input to a fast Fourier transform (FFT) to determine the diffraction pattern in the far field (scaled). This is the process performed in the code, of course only on one output. Figure 100 shows the FFT of Figure 98 and Figure 101 shows the FFT of Figure 99.

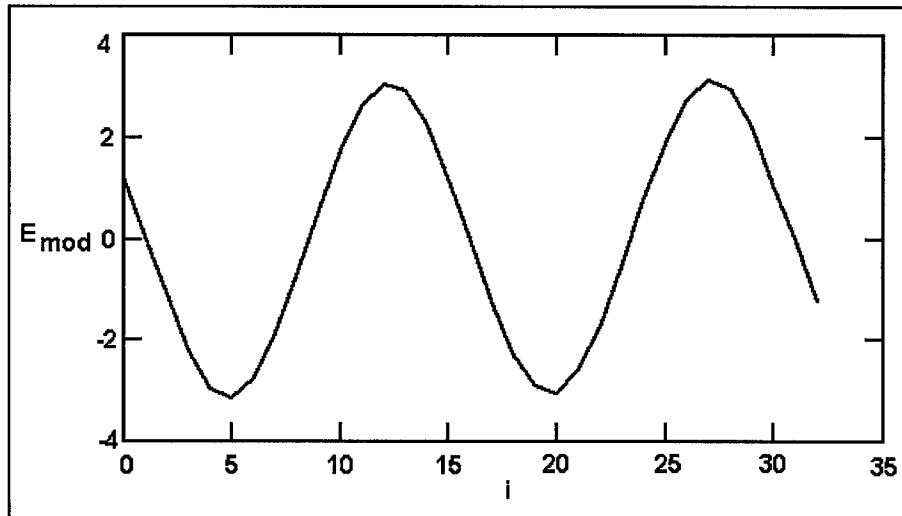


Figure 99. Output electric field (modified) versus transverse location. The asymmetry has been effectively removed.

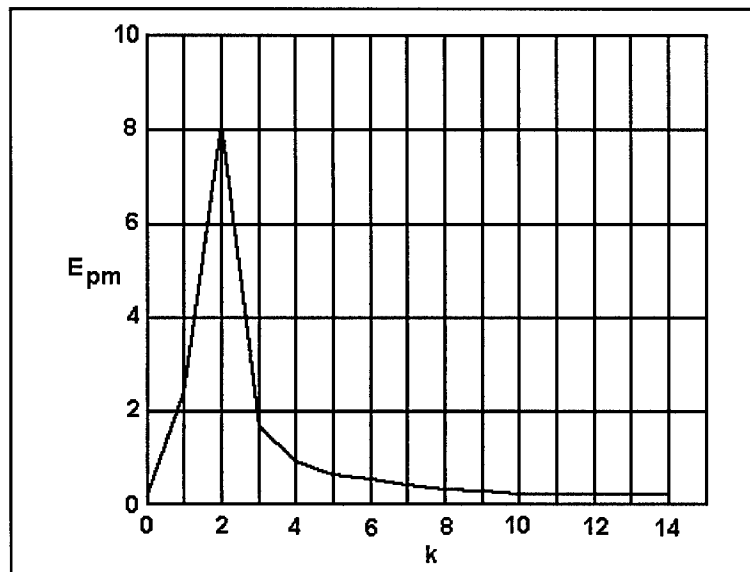


Figure 100. FFT of unmodified output electric field. First order output corresponds to  $k=2$ .

Note that the only difference between the graphs of Figure 100 and Figure 101 is the value at  $k=1$ , which corresponds to a wavelength equal to the width of the simulated region. The first order output at  $k=2$  is virtually unaffected (both values are 8.103). The conclusion is that the

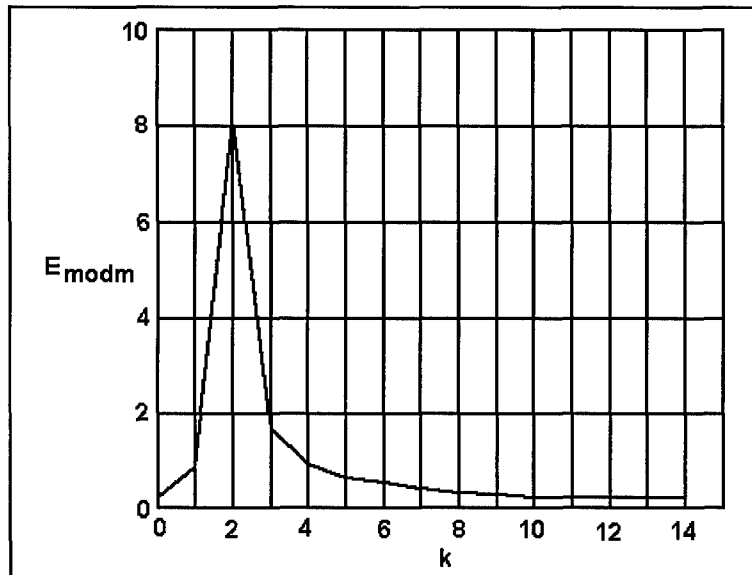


Figure 101. FFT of modified output electric field. First order output corresponds to  $k=2$ .

asymmetry introduced by the implementation of the transverse periodic boundary conditions does not significantly effect the first or lower order diffraction efficiencies.

## **Appendix H. Approximation to Diffraction Efficiency**

Although the numerical simulation can solve the equations in the mathematical model, there is some use for approximations in understanding dominance and how it relates to diffraction efficiency. Thus, the following derivation leads to an approximation for diffraction efficiency.

Chapter II on the mathematical model relates the approximation for diffraction efficiency developed here to the concept of dominance.

Substituting the expressions for the indices of refraction (Equations (14) and (13) on page 17) into the equations for the slow and fast phase shifts (Equation (15) on page 18) gives

$$\begin{aligned}\varphi_s(x,t) &= \frac{2\pi}{\lambda_r} \int_0^d \left[ n_o + \frac{n_o^3 r_{41}}{2} \sqrt{\frac{2}{3}} E_x(x,z,t) + \frac{n_o^3 r_{41}}{2\sqrt{3}} E_z(x,z,t) \right] dz \\ \varphi_f(x,t) &= \frac{2\pi}{\lambda_r} \int_0^d \left[ n_o - \frac{n_o^3 r_{41}}{2} \sqrt{\frac{2}{3}} E_x(x,z,t) + \frac{n_o^3 r_{41}}{2\sqrt{3}} E_z(x,z,t) \right] dz\end{aligned}\tag{50}$$

Now define expressions for the phase difference between the slow and fast phase shifts,  $\Delta\varphi(x,t)$ , and a new constant,  $\kappa$ .

$$\begin{aligned}\Delta\varphi(x,t) &\equiv 2 \cdot \frac{2\pi}{\lambda_r} \int_0^d \left[ -\frac{n_o^3 r_{41}}{2} \sqrt{\frac{2}{3}} E_x(x,z,t) \right] dz \\ \kappa &\equiv \frac{2\pi}{\lambda_r} \int_0^d \left[ n_o + \frac{n_o^3 r_{41}}{2\sqrt{3}} E_z(x,z,t) \right] dz = \frac{2\pi}{\lambda_r} \left[ n_o d - \frac{n_o^3 r_{41}}{2\sqrt{3}} V \right]\end{aligned}\tag{51}$$

With these expressions, one can redefine the slow and fast phase shifts as

$$\begin{aligned}\varphi_s(x,t) &= \frac{\Delta\varphi(x,t)}{2} + \kappa \\ \varphi_f(x,t) &= -\frac{\Delta\varphi(x,t)}{2} + \kappa\end{aligned}\tag{52}$$

Substituting these quantities into the expression for the output field (Equation (18) on page 20), and ignoring the  $e^{i\omega t}$  term, leads to

$$\begin{aligned}
 E_{out}(x,t) &= \frac{1}{2} \left( e^{i(\frac{\Delta\phi(x,t)}{2} + \kappa)} - e^{i(-\frac{\Delta\phi(x,t)}{2} + \kappa)} \right) \\
 &= \frac{1}{2} e^{i\kappa} \left( e^{i\frac{\Delta\phi(x,t)}{2}} - e^{-i\frac{\Delta\phi(x,t)}{2}} \right) \\
 &= e^{i\kappa} \sin\left(\frac{\Delta\phi(x,t)}{2}\right)
 \end{aligned} \tag{53}$$

or

$$|E_{out}(x,t)| = \sin\left(\frac{\Delta\phi(x,t)}{2}\right) \tag{54}$$

Now, if the phase difference  $\Delta\phi(x,t)$  is small, e.g.,  $\ll 1$  radian, then

$$|E_{out}(x,t)| \approx \frac{\Delta\phi(x,t)}{2} \tag{55}$$

and

$$E_{out}(x,t) \approx e^{i\kappa} \frac{\Delta\phi(x,t)}{2} \tag{56}$$

This approximation for the output electric field after the polarizer can be substituted into the expression for the nth order diffraction efficiency to get

$$\begin{aligned}
 \eta_n(t) &\approx \frac{1}{N^2} \left| F_{x,n,N} \left\{ e^{i\kappa} \frac{\Delta\phi(x,t)}{2} \right\} \right|^2 \\
 &\approx \frac{1}{N^2} \left| e^{i\kappa} F_{x,n,N} \left\{ \frac{\Delta\phi(x,t)}{2} \right\} \right|^2 \\
 &\approx \frac{1}{N^2} \left| F_{x,n,N} \left\{ \frac{\Delta\phi(x,t)}{2} \right\} \right|^2 \\
 &\approx \frac{1}{N^2} \cdot \frac{\Delta\phi_n^2(t)}{4}
 \end{aligned} \tag{58}$$



where  $\Delta\phi_n(t)$  is defined as the amplitude of the  $n$ th order output of the spatial FFT of the transverse distribution of the phase difference,  $\Delta\phi(x,t)$ . This expression states that the  $n$ th order diffraction efficiency is directly proportional to the square of the  $n$ th order phase difference. Of course, the intuitive understanding of the  $n$ th order phase difference is somewhat obscure.

Assume for now that most of the energy in the output phase shift is in the first order, which happens to be the component of interest in this work. If, over some time period of interest, the energy is nearly all in the first order, the shape of the transverse distribution of the phase difference changes little, and only the amplitude of the output varies. This time varying change in the amplitude of the distribution of the phase difference might be represented by a selected point on the distribution or by some average value. For this derivation, assume an average value of the magnitude of the phase difference is representative. Then one finds

$$\Delta\phi_1(t) \propto |\Delta\phi(x,t)|_{ave} \quad (58)$$

where the subscript *ave* indicates an average over the spatial coordinate  $x$  at any time  $t$ . Plugging this back into the previous equation gives

$$\eta_1(t) \propto (|\Delta\phi(x,t)|_{ave})^2 \quad (59)$$

This states that the first order diffraction efficiency is proportional to the square of some average value of the output phase difference when the output phase difference is much less than one radian and when the output phase difference's Fourier components, other than first order, are negligible. These conditions generally hold throughout this work, but were not apparent in the efforts of Shlyagin et al. (3).

The rough proportionality above could also be expressed in terms of transverse electric fields by substituting the expression for phase difference and removing constants.

$$\eta_1(t) \propto \left[ \left| \int_0^d E_x(\bar{x},t) dz \right|_{ave} \right]^2 \quad (60)$$

where again the *ave* indicates an average over the spatial coordinate  $x$ .

## *Bibliography*

1. Casasent, D., F. Caimi, and A. Khomenko, "Soviet Priz spatial light modulator", *Applied Optics*, 10(18): 3090-3092 (15 September 1981).
2. Casasent, D., F. Caimi, M.P. Petrov, and A.V. Khomenko, "Applications of the Priz light modulator", *Applied Optics*, 21(21): 3846-3854 (1 November 1982).
3. Shlyagin, M.G., A.V. Khomenko, V.V. Bryksin, L.I. Korovin, and M.P. Petrov, "Mechanisms of nonlinearity in a PRIZ space-time light modulator", *Sov. Phys. Tech. Phys.*, 30(1): 68-72 (January 1985).
4. Bliznetsov, A.M., V.V. Bryksin, L.I. Korovin, S.V. Miridonov, and A.V. Khomenko, "Injection mechanism of dynamic image selection in PRIZ space-time light modulators", *Sov. Phys. Tech. Phys.*, 31(6): 750-754 (July 1987).
5. Cook, Joseph W., *An Analysis of One-Dimensional Models of the Insulating and Conducting PRIZ*. MS thesis, AFIT/GEP/ENG/91D-2. School of Engineering, Air Force Institute of Technology (AU), Wright-Patterson AFB OH, December 1991.
6. Cushing, David A., *A Numerical Analysis of the Dynamics of PRIZ Operation*. MS thesis, AFIT/GEP/ENP/87J-1. School of Engineering, Air Force Institute of Technology (AU), Wright-Patterson AFB, OH, July 1987 (AD-A188853).
7. Saux, G.L. and A. Brun, "Photorefractive Material Response to Short Pulse Illuminations", *IEEE J. of Quantum Electronics*, QE-23 (10): 1680-1688 (October 1987).
8. Astratov, V.N., V.A. Li'inskii, and M.B. Mel'nikov, "Effect of preliminary optical excitation of traps on charge transfer in  $\text{Bi}_{12}\text{GeO}_{20}$  crystals", *Sov. Phys. Solid State*, 25 (7): 1244-1247 (July 1983).
9. Attard, Alfred E., "Fermi level shift in  $\text{Bi}_{12}\text{SiO}_{20}$  via photon-induced trap level occupation", *J. Appl. Phys.*, 71 (2): 933-937 (15 January 1992).
10. Attard, A.E. and T.X. Brown, "Experimental observations of trapping levels in BSO", *Applied Optics*, 25 (18): 3253-3259 (15 September 1986).
11. Attard, Alfred E., "Theory of origins of the photorefractive and photoconductive effects in  $\text{Bi}_{12}\text{SiO}_{20}$ ", *J. Appl. Phys.*, 69 (1): 44-55 (1 January 1991).
12. Petrov, M.P., A.V. Khomenko, V.I. Marakhonov, and M.G. Shlyagin, "Transients in a space-time light modulator", *Sov. Tech. Phys. Lett.*, 6 (4): 165-166 (April 1980).
13. Peltier, M. and F. Micheor, "Volume Hologram Recording and Charge Transfer Process in  $\text{Bi}_{12}\text{SiO}_{20}$  and  $\text{Bi}_{12}\text{GeO}_{20}$ ", *J. of Applied Physics*, 48(9): 3686-3690 (September 1977).

14. Bryksin, V.V., L.I. Korovin, and M.P. Petrov, "Linear operation of PRIZ space-time light modulators", *Sov. Phys. Tech. Phys.*, 29(8): 878-882 (August 1984).
15. Petrov, M.P., S.I. Stepanov, and A.V. Khomenko, *Photorefractive Crystals in Coherent Optical Systems*. Berlin: Springer-Verlag, 1965.
16. Owechko, Y. and A.R. Tanguay, Jr., "Theoretical resolution limitations of electrooptic spatial light modulators. II. Effects of crystallographic orientation", *J. Opt. Soc. Am. A*, 1(6): 644-652 (June 1984).
17. Bryksin, V.V., L.I. Korovin, M.P. Petrov, and A.V. Khomenko, "Dynamics of optical image formation in crystals with the aid of the internal transverse Pockel's effect", *Sov. Phys. Solid State*, 24(1): 82-86 (January 1982).
18. Bryksin, V.V. and L.I. Korovin, "Dynamics of the distribution of optically induced charges and electric fields in crystals", *Sov. Phys. Solid State*, 24(7): 1159-1162 (July 1982).
19. Bryksin, V.V., L.I. Korovin, and Y.I. Kuzmin, "Role of injection currents in the evolution of a photoinduced charge in photorefractive crystals", *Sov. Phys. Solid State*, 29(5): 757-761 (May 1987).
20. Reitz, J.R. and F.J. Milford, *Foundations of Electromagnetic Theory* (Second Edition). Reading, MA: Addison-Wesley Publishing Company, 1967.
21. Millman, Jacob. *Microelectronics*. New York: McGraw-Hill, 1979.
22. Bliznetsov, A.M., Y.I. Kuzmin, and A.V. Khomenko, "Investigation of reciprocity in the PRIZ space-time light modulator", *Sov. Phys. Tech. Phys.*, 33(3): 374-376 (March 1988).
23. Yariv, A. and P. Yeh. *Optical Waves in Crystals*. New York: John Wiley & Sons, 1984.
24. Boyd, R.W. *Nonlinear Optics*. Boston: Academic Press, Inc., 1992.
25. Petrov, M.P. and A.V. Khomenko, "Photorefractive Crystals in PRIZ Spatial Light Modulators", *Topics in Applied Physics*, 62: 325-352 (1989).
26. Feldman, A., W.S. Brower, Jr., and D. Horowitz, "Optical activity and Faraday rotation in bismuth oxide compounds", *Applied Physics Letters*, 16(5): 201-202 (1 March 1970).
27. Nye, J.F. *Physical Properties of Crystals*, Oxford: Clarendon Press, 1957.
28. Bryksin, V.V., L.I. Korovin, V.I. Marakhonov, and A.V. Khomenko, "Initial stage in the redistribution of photoinduced charges and electric fields in  $\text{Bi}_{12}\text{SiO}_{20}$ ", *Sov. Phys. Solid State*, 24(10): 1686-1689 (October 1982).
29. Gaskill, Jack D. *Linear Systems, Fourier Transforms, and Optics*. New York: John Wiley & Sons, 1978.

30. Press, W.H., S.A. Teukolsky, W.T. Vetterling, and B.P. Flannery. *Numerical Recipes in C* (Second Edition). Cambridge: Cambridge University Press, 1992.
31. Eads, C.L., A. Siahmakoun, and A.B. Western, "Bismuth silicon oxide as a holographic storage medium", *SPIE* 1779: 174-185 (1992).
32. Khomenko, A.V., N.N. Kovalev, and M.P. Petrov, "Recording of optical information in a  $\text{Bi}_{12}\text{SiO}_{20}$  PROM", *Sov. Tech. Phys. Lett.*, 2 (12): 432-433 (December 1976).
33. Petrov, M.P., V.I. Marakhonov, M.G. Shlyagin, A.V. Khomenko, and M.V. Krasinkova, "Use of PRIZ spatial modulator for information processing", *Sov. Phys. Tech. Phys.*, 25(6): 752-753 (June 1980).
34. Petrov, M.P., A.V. Khomenko, M.V. Krasinkova, V.I. Marakhonov, and M.G. Shlyagin, "The PRIZ image converter and its use in optical data processing systems", *Sov. Phys. Tech. Phys.*, 26(7): 816-821 (July 1981).
35. Petrov, M.P. and A.V. Khomenko, "Anisotropy of the photorefractive effect in  $\text{Bi}_{12}\text{SiO}_{20}$  crystals", *Sov. Phys. Solid State*, 23(5): 789-792 (May 1981).
36. Owechko, Y. and A.R. Tanguay, Jr., "Effects of crystallographic orientation on electrooptic spatial light modulator amplitude and phase responses", *Optics Communications*, 44(4): 239-242 (15 January 1983).
37. Bryksin, V.V. and L.I. Korovin, "Nonlinear theory of the dynamics of the distribution of an electric field in photorefractive crystals", *Sov. Phys. Solid State*, 25(1): 30-33 (January 1983).
38. Bryksin, V.V., L.I. Korovin, and V.I. Markhonov, "Effect of light absorption on the electric field distribution in  $\text{Bi}_{12}\text{SiO}_{20}$ ", *Sov. Phys. Tech. Phys.*, 9(6): 686-689 (June 1983).
39. Bryksin, V.V. and L.I. Korovin, "Role of nonlinear processes in determining the photoinduced charge near the surface of insulators", *Sov. Phys. Solid State*, 26(11): 2051-2057 (November 1984).
40. Bryksin, V.V. and L.I. Korovin, "Influence of light absorption on the dynamics of formation of optically induced charges", *Sov. Phys. Solid State*, 26(12): 2195-2199 (December 1984).
41. Bryksin, V.V., L.I. Korovin, M.P. Petrov, and A.V. Khomenko, "Theory of dynamic image selection in photorefractive media", *Sov. Phys. Solid State*, 24(2): 193-196 (February 1982).
42. Bryksin, V.V. and L.I. Korovin, "Role of injection currents in dynamic image selection under conditions nonlinear in the electric field", *Sov. Phys. Solid State*, 25(8): 1347-1351 (August 1983).

43. Attard, Alfred E., "Photoconductive and photorefractive effects in BSO", *Applied Optics*, 28 (23): 5169-5174 (1 December 1989).
44. Attard, Alfred E., "The role of traps in the restoration of faded holographic images in  $\text{Bi}_{12}\text{SiO}_{20}$ ", *J. Appl. Phys.*, 66 (7): 3211-3219 (1 October 1989).
45. Gardner, P.J. and T.E. Luke, "The spatial and temporal characteristics of the conducting PRIZ spatial light modulator", *Opt. Comm.*, 73 (1): 19-22 (1 September 1995).
46. Petrov, M.P., M.G. Shlyagin, N.O. Shalaevskii, V.M. Petrov, and A.V. Khomenko, "New mechanism for recording images in photorefractive crystals", *Sov. Phys. Tech. Phys.*, 30 (11): 1331-1332 (November 1985).
47. Hou, S.L., R.B. Lauer, and R.E. Aldrich, "Transport processes of photoinduced carriers in  $\text{Bi}_{12}\text{SiO}_{20}$ ", *J. Appl. Phys.*, 44 (6): 2652-2658 (June 1973).
48. Shields, D.M. and T.E. Luke, "Operation of a conducting PRIZ", *Opt. Comm.*, 55 (6): 391-392 (15 October 1985).
49. Bube, Richard H. *Photoelectronic Properties of Semiconductors*. Cambridge: Cambridge University Press, 1992.
50. Bryksin, V.V., V.S. Voloshin, and L.I. Korovin, "Transmission function of a PRIZ space-time light modulator", *Sov. Phys. Tech. Phys.*, 31(6): 609-614 (June 1986).
51. Bryksin, V.V., L.I. Korovin, M.P. Petrov, and A.V. Khomenko, "Characteristics of diffracted waves after passage through an inhomogeneous electrooptic and gyrotropic crystal", *Sov. Phys. Tech. Phys.*, 33(4): 440-445 (April 1988).
52. Bryksin, V.V., L.I. Korovin, and M.P. Petrov, "Influence of the inhomogeneous Pockels effect on the propagation of light waves in crystals", *Sov. Phys. Tech. Phys.*, 33(9): 995-999 (September 1988).
53. Stepanov, S.I. and V.V. Kulikov, "Dynamic image recording in  $\text{Bi}_{12}\text{SiO}_{20}$  crystals", *Sov. Phys. Tech. Phys.*, 28(11): 1384-1386 (November 1983).

## *Vita*

Major Gary D. Barmore [REDACTED] He graduated from Purdue University in 1978 with a Bachelor of Science degree in physics. He worked at McDonnell-Douglas Astronautics as an associate engineer from 1978 to 1980 when he entered Washington University School of Law. Major Barmore interrupted his studies to enter the Air Force; he received his commission in February of 1982 as a distinguished graduate of Officer Training School. The Air Force then sent him to Louisiana Tech University where he received a Bachelor of Science degree in electrical engineering in 1983. His next assignment was as an engineer and then chief of the Satellite Systems Division of the NAVSTAR/Global Positioning System Joint Program Office. In 1987 he entered the graduate electro-optics program at the Air Force Institute of Technology (AFIT) and received a Master of Science degree in Electrical Engineering in 1988. He was then directed to duty at the Foreign Technology Division where he analyzed foreign command, control, and communications (C<sup>3</sup>) systems. In 1992 he returned to AFIT and began his doctoral studies. In July of 1995 he began his current assignment as Deputy Director, Surveillance and Photonics Directorate, Rome Laboratory.

*Address:*

Gary D. Barmore  
1004 Franklin Street  
Rome, NY 13440

REPORT DOCUMENTATION PAGE			Form Approved OMB No. 0704-0188	
Public reporting burden for this collection of information is estimated to average 1 hour per response, including the time for reviewing instructions, searching existing data sources, gathering and maintaining the data needed, and completing and reviewing the collection of information. Send comments regarding this burden estimate or any other aspect of this collection of information, including suggestions for reducing this burden, to Washington Headquarters Services, Directorate for Information Operations and Reports, 1215 Jefferson Davis Highway, Suite 1204, Arlington, VA 22202-4302, and to the Office of Management and Budget, Paperwork Reduction Project (0704-0188), Washington, DC 20503.				
1. AGENCY USE ONLY (Leave blank)	2. REPORT DATE September 1996	3. REPORT TYPE AND DATES COVERED Doctoral Dissertation		
4. TITLE AND SUBTITLE  A 2-D NUMERICAL SIMULATION AND ANALYSIS OF A SIMPLE BAND MODEL FOR THE PRIZ SPATIAL LIGHT MODULATOR		5. FUNDING NUMBERS		
6. AUTHOR(S)  Gary D. Barmore, Major, USAF				
7. PERFORMING ORGANIZATION NAME(S) AND ADDRESS(ES)  Air Force Institute of Technology 2750 P Street WPAFB OH 45433-6583		8. PERFORMING ORGANIZATION REPORT NUMBER  AFIT/DS/ENP/96-05		
9. SPONSORING/MONITORING AGENCY NAME(S) AND ADDRESS(ES)  MR JAMES CUSACK CHIEF, PHOTONICS DIV ROME LAB/OCP 26 ELECTRONIC PARKWAY ROME NY 13441		10. SPONSORING/MONITORING AGENCY REPORT NUMBER		
11. SUPPLEMENTARY NOTES				
12a. DISTRIBUTION/AVAILABILITY STATEMENT  Approved for public release; distribution unlimited		12b. DISTRIBUTION CODE		
13. ABSTRACT (Maximum 200 words)  This dissertation discusses the development of and analyzes the first complete, 2-D numerical simulation of the PRIZ. The simulation is based upon a simple band model of the PRIZ: a single donor, a single trap, and free electron carriers. Modeled mechanisms include photogeneration, energy level transitions, injection, drift currents, diffusion currents, photorefractive and diffraction. The model goes beyond the previous charge and field dynamics of 1-D numerical models to include optical effects, and it eliminates the oversimplifications and assumptions used in earlier mathematical models with closed solutions. Sensitivity analyses and selected simulations provide a better understanding of the dynamic imaging phenomena. The device output depends on the relative dominance or strength of the fields in the positive or negative space charge region. Transverse drift is as important as charge mirror imaging and injection current in determining peak output and self-erasure. The simulations show a broad range of unreported behavior both before and after write-beam turnoff, including sharp transients; reintensification with and without phase reversals; and even strong intensification after a turnoff. Finally, the 2-D model is shown to be a reasonable representation of the PRIZ by comparing simulated output with experimental data from the literature.				
14. SUBJECT TERMS  Spatial light modulator, photorefractive material, Pockels effect, transverse linear electro-optic effect, BSO			15. NUMBER OF PAGES 206	
			16. PRICE CODE	
17. SECURITY CLASSIFICATION OF REPORT Unclassified	18. SECURITY CLASSIFICATION OF THIS PAGE Unclassified	19. SECURITY CLASSIFICATION OF ABSTRACT Unclassified	20. LIMITATION OF ABSTRACT  UL	